CR 151619

LAMONT-DOHERTY GEOLOGICAL OBSERVATORY

OF COLUMBIA UNIVERSITY

PALISADES, NEW YORK

LUNAR HEAT-FLOW EXPERIMENT

*

F I N A L T E C H N I C A L R E P O R T

NASA Grant NAS 9-6037

CU-4-77

Name of Principal Investigator: Dr. M. G. Langseth

Period Covered by the Report: 6/6/1966 - 6/30/1975

*

September, 1977

LUNAR HEAT-FLOW EXPERIMENT

*

F I N A L T E C H N I C A L R E P O R T

NASA Grant NAS 9-6037

CU-4-77

*

Name of Principal Investigator: Dr. M. G. Langseth

Period Covered by the Report: 6/6/1966 - 6/30/1975

*

Name and Address of Grantee Institution:

Lamont-Doherty Geological Observatory
of Columbia University
Palisades, New York 10964

***

Credits

This report was prepared by Marcus G. Langseth and Stephen J. Keihm. The description of the heat-flow instrumentation and lunar surface drill development in the Appendices has been taken, in large part, from earlier reports by personnel at Arthur D. Little, Inc., Bruce Smith of the Aerospace Systems Division of the Bendix Corporation and the Martin Marietta Corporation. Annette Trefzer, in addition to the typing of the manuscript and the drafting of many of the figures, has contributed significantly to the organization and proofing of the report. Kenneth Peters helped proofread the text and made important improvements. Ana Maria Draganović drafted many of the figures in Chapter V.

*****

TABLE OF CONTENTS

*

*

I. SUMMARY OF PRINCIPAL SCIENTIFIC RESULTS FROM THE LUNAR HEAT-FLOW EXPERIMENT

The Apollo Lunar Heat-Flow Experiment was conceived to make direct observations of the rate of heat loss through the surface of the moon at the Apollo landing sites. Two of these experiments were emplaced successfully during the Apollo program: one at Hadley Rille (Apollo 15) and the other at Taurus Littrow (Apollo 17). A third experiment was flown on Apollo 13, but when the mission was aborted en route it never reached the moon. A fourth instrument was installed at Apollo 16, but a broken cable between the central transmitting station and the heat-flow experiment rendered it useless. The principal components of the experiment were probes, each with twelve thermometers of exceptional accuracy and stability, that recorded temperature variations at the surface and in the regolith down to 2.5 m. The Apollo 15 experiment recorded temperatures for a period of four and a half years and the Apollo 17 probes, which were still returning accurate results when the instrument was turned off, recorded four years and ten months of lunar surface and subsurface temperatures. These data provided a unique and valuable history of the interaction of solar energy with lunar surface and the effects of heat flowing from the deep interior out through the surface of the moon. The interpretation of these data resulted in a clearer definition of the thermal and mechanical properties of the upper two meters of lunar regolith, direct measurements of the gradient in mean temperature due to heat flow from the interior and a determination of the heat flow at the Apollo 15 and Apollo 17 sites (see Table 1 for values of significant new observations that resulted from the experiment.)

Surface Temperatures and the Nature of the Shallow Regolith

Surface thermometers of the heat-flow experiment provided a complete history of the surface variation of temperature during the observation period. Two important discoveries stemmed from the interpretation of these results:

1) A 30 to 35° difference in mean temperature occurs across the upper few centimeters of the regolith because, in this relatively fluffy layer, radiative heat transfer predominates. At lunar noon, nearly 70% of the

TABLE 1: Values of Major Parameters Measured by the Lunar Heat-Flow Experiment

DATUM	Hadley Rille	Taurus Littrow
Mean surface temperature, °K	207	216
Maximum mean subsurface temperature of undisturbed regolith, °K	253.0 (1.38m)	256.7 (2.34m)
Thermal conductivity of the surface layer $mWm^{-1}-°K^{-1}$ (at 120°K)	1.2 ± 0.03	1.5 ± 0.03
Average conductivity below 10 cm, $mW-m^{-1}-°K^{-1}$	10 ± 10%	15 ± 10%
Depth at which lunation fluctuations fall to 1% of surface value, m	0.29	0.33
Depth at which annual fluctuation falls to 1% of surface value, m	1.35	1.48
Mean vertical temperature gradient (most reliable probe) °K/m	1.85	1.35
Observed surface heat flow mW/m^2	21	16
Correction applicable to the observed heat flow due to terrain	<4%	-10%

heat transfer in this layer occurs by particle to particle radiation.

2) The thermal response of the regolith to variations in solar radiation, due to eclipses, rotation of the moon on its axis, and the eccentricity of its orbit about the sun, is well described by a simple two layer model of the upper 2.5 m of the regolith, which is comprised of a thin (2-3 cm) surface layer of low density (1.1 - 1.2 gm/cc) very fine material of extremely low conductivity (0.9-1.6 mW/m°K). This layer overlies a higher density (1.75 - 2.10 gm/cc) tightly compacted layer of fines which have a quite uniform conductivity of 10 to 15 mW/m°K. The thermal conductivity of the deeper layer was determined by careful analysis of the downward propagation of long-term surface variations of temperature, such as the annual variations and disturbances caused by the visits of the astronauts to the sites. The value of conductivity inferred for this deeper layer is considerably higher than can be achieved by compaction of lunar soils in the laboratory, suggesting that on the moon soils below a few centimeters have been compacted into a mechanical configuration that has evolved over millions of years which cannot be duplicated in the laboratory. This characterization of the lunar soil layer will be important when the time comes to establish bases or scientific stations on the lunar surface.

The Temperature Gradient and Heat Flow

The increase of mean temperature with depth, due to heat flow from the interior, varied between the four sites, due to local disturbances and regional variations in surface heat flow. The average gradient observed was 1.6 °K/m. This value is in agreement with the vertical temperature gradients deduced from radiotelescope observations of long wavelength radiation from the whole disk of the moon. The observed increase in brightness temperature with wavelength when combined with the electromagnetic properties measured on Apollo soil samples, indicate a gradient of 1.5 to 2.0 °K/m. The significance of this agreement is that it indicates that the mean of the four Apollo measurements is probably representative of the nearside of the moon.

The observed mean gradient of 1.6°K/m and the thermal conductivity of the regolith below 3 cm combine to yield a heat flow of 17 mW/m^2 with an estimated uncertainty of 20%. How representative this value is of the true

average heat loss from the moon is difficult to say with so few data that vary so widely. There are some lines of evidence that suggest it may be quite representative. The large variations of heat flow which are observed over the surface of the earth are mainly associated with the boundaries of converging and diverging lithospheric plates. The lithosphere of the moon, on the other hand, is rigid and static so that variations associated with tectonics are unlikely. Regional variations in heat flow on the moon are more likely associated with variations in abundance of long-lived radioactive isotopes of potassium, thorium and uranium. These isotopes were mobilized by the igneous activity that formed the lunar crust and flooding of the mare basins. Orbital gamma-ray observations, global photomapping and Apollo samples allow some estimate of the variability of heat flow. Our analysis suggests that this variability is small. It is described in Section VI-4. Lastly, a critical analysis of crust and mantle temperatures that would be implied by a heat flow between 12 and 18 mW/m^2 gives values that are in good agreement with seismic and magnetic data that depend on mantle temperatures. The heat-flow result implies temperatures within a few hundred degrees of melting at depths of about 300 km.

For a planet as small as the moon, much of the heat associated with accretion will have escaped during its 4.5 b.y. history; consequently, most of the heat escaping through the surface at present is produced by radioactive isotopes in the interior. Thus, the moon is close to steady state. If we assume that this is the case for the moon, then the observed heat-flow value would require a uranium content of approximately 30-45 x 10^{-9} g/g which is consistent with the results of more detailed thermal models. This amount is similar to that estimated for the mantle of the earth.

PAPERS AND REPORTS BASED ON THE

LUNAR HEAT-FLOW EXPERIMENT

Clark, S.P., Jr. (1965) Some calculations pertaining to the feasibility of measuring lunar heat flow: Final Report contract NASA NSG-400: Yale University

Clark, S.P., Jr. (1967) The in situ measurement of lunar thermal conductivity, Interim Report, NASA

Horai, K., J.L. Winkler, Jr., S.J. Keihm, M.G. Langseth and J.A. Fountain (1977) Thermal conductivity of two Apollo 17 drill core samples 70002 and 70006; A preliminary result: Proc. Lunar Sci. Conf. 8th Houston, Texas, in press

Keihm, Stephen J. and Marcus G. Langseth, Jr. (1973) Surface brightness temperatures at the Apollo 17 heat flow site; Thermal conductivity of the upper 15 cm of regolith; Proc. Lunar Sci. Conf., 4th; in, Geochim. et Cosmochim. Acta Suppl. 4, p. 2503-2513

Keihm, Stephen, J. and Marcus G. Langseth (1975) Microwave emission spectrum of the moon; Mean global heat flow and average depth of the regolith; Science, v. 187, p. 64-66

Keihm, Stephen J. and Marcus G. Langseth (1975) Lunar microwave brightness temperature observations reevaluated in the light of Apollo program findings; Icarus, v. 24, p. 211-230

Keihm, Stephen and Marcus Langseth (1976) Lunar heat flow data analysis and the feasibility of a Mars penetrator heat flow measurement; in, FY 1976 Progress Report on a Feasibility Study Evaluating the Use of Surface Penetrators for Planetary Exploration, by M.B. Blanchard, V.R. Oberbeck et al., NASA Techn. Memorandum TMX-73, 181, Appendix F, p. 109-132

Keihm, Stephen and Marcus G. Langseth (1977) Modeling studies for a Mars penetrator heat-flow measurement; Columbia University Techn. Rpt. CU-1-77

Keihm, S.J. and Marcus G. Langseth (1977) Lunar thermal regime to 300 km; Proc. Lunar Sci. Conf. 8th, Houston, Texas, in press

Keihm, S.J., K. Peters, M.G. Langseth, Jr., and J.L. Chute, Jr. (1973) Apollo 15 measurement of lunar surface brightness temperatures; Thermal conductivity of the upper 1 1/2 meters of regolith; Earth and Planet. Sci. Lett., v. 19, p. 337-351

Kleven, L., L. Lofgren and P. Felsenthal (1970) A rugged, stable differential platinum resistance thermometer; The Rev. Sci. Instru., v. 41, n. 4, p. 541-544

Kleven, L., L. Lofgren and P. Felsenthal (1971) Unique platinum resistance temperature sensors for the lunar heat flow measurements; Proc. 5th Symposium on Temperature

Langseth, M.G., Jr. (1968) The lunar heat flow experiment; American Astronautical Society; Advanced Space Experiments Conference, AAS 68-207

Langseth, M.G., Jr., S.P. Clark, Jr., J.L. Chute, Jr., S.J. Keihm and A.E. Wechsler (1972) Heat flow experiment; in, Apollo 15 Preliminary Science Report, Section 11, NASA SP-289, U.S. Govern. Printing Off., Wash. D.C., p. 11-1 to 11-23

Appendix: Equilibration of an infinitely long cylinder in a homogeneous medium by conduction (same publication as above); p. 11-21 to 11-23

Langseth, M.G., Jr., S.P. Clark, Jr., J.L. Chute, Jr., S.J. Keihm and A. E. Wechsler (1972) The Apollo 15 lunar heat-flow measurement; in, The Moon, v. 4, p. 390-410

Langseth, M.G., Jr., S.P. Clark, Jr., J. Chute, Jr., and S.J. Keihm (1972) The Apollo 15 lunar heat flow measurement; in, Thermal Characteristics of the Moon, ed. John W. Lucas; in, Progress in Astronautics and Aeronautics, v. 28, Chapter 2D, p. 205-212, The MIT Press, Cambridge, Mass.

Langseth, M.G., Jr., E.M. Drake, D. Nathanson and J.A. Fountain (1972) Development of an in situ thermal conductivity measurement for the lunar heat flow experiment; in, Thermal Characteristics of the Moon, ed. John W. Lucas, in, Progress in Astronautics and Aeronautics, v. 28, Chapter 2C, p. 169-204, The MIT Press, Cambridge, Mass.

Langseth, Marcus G. and Stephen J. Keihm (1974) In situ measurements of lunar heat flow; Proc. Soviet-American Conference on, The Cosmochemistry of the Moon and Planets; held in Moscow, USSR on June 4-8, 1974; Preprint, The Lunar Sci. Inst., Houston; J.H. Pomeroy, Techn. ed.

Langseth, M.G., Jr., S.J. Keihm and J.L. Chute, Jr. (1974) Heat flow experiment in, Apollo 17 Preliminary Science Report, Section 9, NASA SP-330 U.S. Gov't Print. Off., Wash. D.C., p. 9-1 to 9-24

Langseth, Marcus G., Stephen J. Keihm and Kenneth Peters (1976) Revised lunar heat-flow values; Proc. Lunar Sci. Conf.7th, v. 3, p. 3143-3171

Langseth, M.G., K.A. More and W.E. Johnson (1968) An experiment to measure heat flow from the interior of the moon; Bendix Techn. Jour. v. 1, n. 1, p. 33-43

Langseth, M.G., F.E. Ruccia and A.E. Wechsler (1974) Thermal conductivity of evacuated glass beads: Line source measurements in a large volume bead bed between 225 and 300 K: in, Heat Transmission Measurements in Thermal Insulations; ASTM STP 544: Amer. Soc. Testing and Materials p. 256-274

Langseth, M.G., Jr., A.E. Wechsler, E.M. Drake, G. Simmons, S.P. Clark, Jr., and J. Chute, Jr. (1970) Apollo 13 lunar heat flow experiment; Science, v. 168, p. 211-217

Peters, Kenneth and Marcus G. Langseth (1975) Lunar heat flow experiment: Long term temperature observations on the lunar surface at Apollo sites 15 and 17; Tech. Rpt., n. 3, Cu-3-75; NAS 9-6037

Smith, B.D. (1971) The lunar heat flow experiment; Bendix Technical Journal v. 4, n. 2, p. 64-80

***

II. EARLY ORGANIZATION OF THE APOLLO LUNAR HEAT-FLOW EXPERIMENT

Even though, in concept, the heat-flow experiment was simple, it in fact applied physical principles that have been well understood for more than a century, the development of any Apollo experiment was a complex undertaking, usually involving hundreds of persons, a dozen or more corporations and several branches of NASA. Because of this complexity, this history will not attempt to cover every event or person involved. There were many activities about which I am totally unaware and that only a long research effort could uncover. The purpose of this section is rather to record the interesting and sometimes instructive story of the twisting path the development of our experiment followed. It will, in some cases, describe the results of efforts which were eventually discarded for one reason or another, and consequently will not appear in any scientific report.

The importance of knowing the total loss of heat energy from the surface of a planet has long been recognized as an important constraint in thermal history and total average composition of that planet. Important papers by Urey (1957), Levin (1962), MacDonald (1959) and others during the 1950's and early 60's used mathematical thermal models of evolution of the moon to explore the consequences of certain origins (hot or cold accretion), age (the same as the solar system, or younger) or composition (chondritic or otherwise) on the present state of the moon. These models predict a present day heat flow from the moon against which measurements could be compared, which provide a direct test of any of the hypotheses of evolution and composition. Thus, the value of surface heat flow is a fundamental planetary quantity like mean density or moment of inertia, that provide clues to the composition and internal distribution of properties in a planet.

Determining the rate of heat loss from the moon did not have to await lunar landings. Theoretically, the average heat flow can be measured from earth, using radiotelescopes. Telescopic IR measurements from earth and

measurements of thermally generated microwave emission spectra, particularly as a function of solar phase, were one of the primary sources of information on the detailed nature of the lunar surface, before close-up photography became available from spacecraft. Except for the very near surface optical characteristics of the lunar surface, the thermal properties, temperature, thermal conductivity, density and heat capacity of the lunar surface layer were better known than any other physical properties. Telescopic thermal observations on the moon were the only source of information on the nature of the subsurface.

Interpretation of microwave and infrared observations are strongly limited by the uncertainty of the electrical properties of the lunar surface, by the low level signals at long wavelengths, and by the uncertainty of the distribution of thermal properties with depth. Consequently, the reliability of estimates of heat flow based on these observations is not good, and the possibility of making in-situ determinations of surface heat flow on a landing mission would help resolve many of these uncertainties.

It is not known exactly who first proposed that a measurement of the rate of heat loss from the moon should be made as part of the scientific effort of the Apollo Lunar Landing Program. During the early planning phase of Apollo, NASA sponsored many studies, some by scientific groups working in NASA, some by industrial groups and some by academic scientists to recommend science programs that might be carried out when the Apollo lunar landings were achieved. Reports of these studies usually contained a 'shopping list' of experiments and measurements that could be performed on the lunar surface. Some thermal measurements were usually included on such lists, usually surface temperature and surface thermal properties. A few proposed trying to measure heat flow from the moon.

My first exposure to the concept of lunar heat-flow measurements came via a phone call from Dr. Paul Lowman at the Goddard Space Center in Maryland. Paul asked simply how difficult would it be to measure heat flow through the surface of the moon.

Soon afterward, in 1964, I was asked to join a small ad hoc committee to address the problems of in situ thermal measurements on the lunar surface The membership of this committee consisted of Arthur Lachenbruch

of the U.S. G.S. in Menlo Park, California; Sydney Clark of Yale University; Richard Von Herzen, then with Scripps Institution of Oceanography; and myself. It was a good mix; the two first mentioned were experienced with continental heat flow determinations, while Von Herzen and I were actively making heat flow measurements in the seafloor. The first meeting of this group took place in Washington. Sydney Clark's first comment was that the only worthwhile thermal measurement would be that of heat flow from the lunar interior. We all concurred and the remainder of this meeting was devoted to learning more about how and when the first Apollo missions would take place, the nature of the lunar surface, and the most feasible approach to measuring heat flow.

Richard Von Herzen's term on the committee was short-lived as he accepted a position with UNESCO in Paris. Later in 1964, a conference in Houston at the Manned Spacecraft Center brought all the ad hoc committees representing many other scientific disciplines together. Lachenbruch, Clark, and I spent most of our time at this meeting considering techniques for measuring lunar heat flow. The most straightforward approach to determine the flux through the lunar surface layer or lunar soil is by direct measurements of the temperature gradients and the thermal conductivity of the soil. Because the measurements would have to be made very close to the lunar surface, it was early recognized that the heat flow might be seriously disturbed by near-surface effects and, consequently, it was proposed that numerous (ten or more probes) be used to measure the flux.

An alternative technique we considered was to set up heat flux meters on the lunar surface. These meters would consist of thin circular disks (or blankets) made of material of very low but known thermal conductivity. If the ratio of the disk radius to thickness was 50 to 1 or greater, the mean temperature difference across the disk would provide a measure of mean heat flow. As in the case of the probes, several 'heat-flow meters' would have to be set up to measure and, it was to be hoped, average the local near surface variability.

Sydney Clark was the principal author of a joint proposal to study methods for making measurements of surface heat flow on the lunar surface. NASA gave a grant to Yale and Lamont-Doherty Geological Observatory of Columbia University to carry out these studies in response to this proposal. Arthur Lachenbruch

did not wish to continue active participation in the proposed program because of the responsibilities he already had at U.S.G.S. However, subsequent to the meeting at the Manned Spacecraft Center, he contributed a short report on the effects of surface temperature variations on measurements of heat flow.

Under this grant, Sydney Clark carried out two analytical studies, the first addressed the problem of how to measure the very low level heat flow escaping from the moon in the midst of the large periodic variations of temperature at the surface produced by the moon's diurnal cycle, and the feasibility of using the heat-flow meter or blanket approach to measuring the surface heat flow. The results of this study were summarized in the final report of NSG-400 of Yale University (1965). One principal conclusion was that the 'blanket' method of measuring lunar heat is not feasible because of the necessity of closely matching the local albedo and because a blanket' which would effectively alter periodic fluctuations, would take a prohibitively long time to come to equilibrium with steady-state surface conditions.

It is interesting to note that the blanket technique had a far more serious problem which was not fully appreciated until later. Linsky (1966), Watson (1964) and others had pointed out the importance of radiative heat transfer in evacuated powders. The radiative component depends strongly on temperature and, as a result, behaves nonlinearly. A rectifying effect occurs that produces a net transfer of heat energy into the subsurface during the lunar day, which must be balanced by a steady mean outward flux. This effect, which is confined to the upper few cm, can induce steady-state fluxes that are ten or more times greater than the flux from the interior. Thus, a direct measurement of the flux at the surface would not have been representative of the heat flow from the interior. Our subsequent measurements on the moon showed that this heat flux induced by the nonlinearity of radiative heat transfer in the lunar soil is very large. For example, a temperature differential of 40°C was induced over a few cm of near-surface material at the Apollo 15 site.

A second study carried out by S. Clark investigated techniques of measuring thermal conductivity with a probe inserted into the lunar soil. The results are summarized in an Interim Report under Grant NGR -07-004-039 at Yale University. This report formed the basis of the technique that was eventually used to make in situ conductivity measurements on the moon. The method proposed consisted of a cylindrical ring source of heat and a temperature

sensor placed within the heater, or at some distance from the heater, along the probe. A finite difference thermal model was used by Clark to investigate the problems interpreting the temperature change with time, in terms of the thermal conductivity of the surrounding material. This work showed that a reasonable determination of the thermal conductivity could be obtained by curve fitting, although it was clear that the thermal linkages and properties of the probe and its contact with the lunar medium had to be well known.

During the same period, scientists at Arthur D. Little, Inc. (ADL) of Cambridge, Massachusetts, in particular, Peter Glaser and Alfred Wechsler, had proposed a number of experiments to measure radiative and thermal properties of the lunar surface as well as surface temperature as part of the Apollo program. ADL has been engaged in a study of the characteristics of the lunar surface layer under contract to NASA. In the spring of 1965, Peter Glaser visited Lamont-Doherty Geological Observatory to discuss ADL's interest in working with us on lunar thermal experiments. This was the beginning of a cooperation that survived through the entire program.

1965 Summer Studies & the LSEP Concept. During the summer of 1965, NASA and the National Academy of Sciences (NAS) sponsored two formative workshops, one at Falmouth, Massachusetts and the other at Woods Hole, Massachusetts. The purpose of both studies was to help NASA formulate a firmer set of scientific objectives and priorities for the Apollo lunar program. S. Clark and I participated in the Falmouth study.

Among the geophysical experiments proposed to be carried out on the moon, a direct measurement of heat flow had a high priority. One of the most important concepts to emerge from the study was that of the Lunar Science Experiments Package (LSEP). This concept recommended a single transmitter and power supply to be set on the lunar surface, to which various arrays of experiments could be connected. This concept was accepted by the Apollo program planners and, with the addition of an 'A' for Apollo, became the ALSEP science stations that were eventually set at five locations on the lunar surface (see NASA Special Report, NASA SP-88, 1965).

At these meetings, NASA management also selected experiment teams for those experiments that had been given a high priority. The heat-flow experiment team named included Marcus G. Langseth as Principal Investigator and Sydney Clark as Coinvestigator. During the meeting, Gene Simmons,

a scientist interested in geothermal problems at Southern Methodist University, asked to be included in the team and was accepted. It was recommended by the NAS panel meeting at Woods Hole, that this team work closely with ADL scientists in developing the experiment. These decisions were the basis of a contract between NASA and L-DGO to help in the development of a lunar heat-flow experiment for Apollo.

One further outcome of the Falmouth meeting had an important effect on the subsequent technique to measure heat flow. It was recognized that, to avoid the large surface fluctuations, it would be necessary to implant the probes to measure the temperature gradient and thermal conductivity deep in the lunar soil. Because of the uncertain penetrability of the lunar surface layer, it was recommended that a portable, astronaut-operated drill be developed to assure deep burial of the probes even in hard rock. Thus, the development of a hard rock drill (soon to be designated as the ALSD, Apollo Lunar Surface Drill), became a part of the Lunar Heat Flow Experiment.

Organization for Flight Experiment Development

By 1966 NASA was firmly committed to the ALSEP scientific stations as part of the Apollo lunar landing sites. An ALSEP Management Office was established at the Manned Spacedraft Center; experiment teams, each headed by a principal investigator were established, and means of communication and coordination between the growing number of elements in the program were developed.

The first task was to select an ALSEP system contractor who would be responsible for the overall management of the development, testing, manufacture, flight qualification and flight support for the ALSEP system, from among proposers from major aerospace corporations. The field was soon narrowed to three; namely, the Bendix Aerospace Corporation of Ann Arbor, Michigan; Space General in Los Angeles, California; and, TRW, also in the Los Angeles area. It seemed as though there were an interminable series of meetings at which we listened politely to long engineering and management presentations of their development programs. In the process we learned a whole new language and we offered criticism and evaluation where we could. The eventual winner of the competition was the Bendix Corporation, Aerospace Systems Division.

At the experimental level competition was equally vigorous and diverse. A subcontractor to develop each ALSEP experiment had to be chosen. Four companies were being considered to develop the Heat Flow Experiment, Arthur D. Little, Texas Instruments, Bendix and Teledyne Corporation. It was difficult at the time

to evaluate the proposals submitted by these companies, because the heat-flow experiment design was at the conceptual stage. There was no precedent for such an instrument and it had to operate in the lunar subsurface environment which was poorly defined. Consequently, it was decided to go with the group that had the greatest experience in original thermal design and knowledge of the characteristics of the lunar surface. The obvious choice was Arthur D. Little, Inc. (ADL) of Cambridge, Massachusetts. There was a protracted negotiation between the National Aeronautical Space Administration, the Lamont-Doherty Geological Observatory of Columbia University, Arthur D. Little Co. Inc. and the Bendix Corporation over the responsibility for the overall integration of the heat-flow instrument. I personally favored having Arthur D. Little Inc. assume that role, which meant that the Arthur D. Little Inc. would deliver a complete instrument subsystem to be 'plugged' into the ALSEP. I did not have my way. The final decision made the Bendix Corporation the principal contractor and Arthur D. Little a subcontractor to Bendix, with a primary responsibility for instrument development and the manufacture of the heat-flow subsurface heat-flow probes, which were the primary components of the experiment. Gulton Industries Incorporated of Albuquerque, New Mexico was chosen to develop the electronic circuitry. This award was given on the basis of a critical circuit design which automatically compensated for drifts in the offset and gain in the necessary amplifiers and the A-D converters needed to measure temperature. The circuit design and its application to the measurement of temperature difference was primarily due to Jay Cox of Gulton Industries.

The Drill

For most of the conceptual designs of the experiment a drill, capable of penetrating the lunar surface, would be needed. NASA decided to manage this development outside of the ALSEP contract. There were two companies vying for the contract; The Martin Marietta Company of Baltimore, Maryland and the Northrop Corporation of California. The Martin Marietta Company had earlier experience developing space tools for NASA, inclucing a surface drill, and the Northrop Corporation was involved in a deep lunar drill development (deeper than 100 feet). The Martin Marietta Company won the contract.

Nearly all of 1966 was spent on the process of reviewing proposals, making site visits and contract negotiations; in summary, selecting the

industrial members of the heat -flow experiment development team. The complete team was defined by the end of the year.

References

Clark, S.P., Jr. (1965) Some calculations pertaining to the feasibility of measuring lunar heat flow: Final Report contract NSG-400 , Yale Univ.

Clark, S.P., Jr. (1967) The in situ measurement of lunar thermal conductivity; Interim Report, NASA NGR 07-0-004-039, Yale University.

Linsky, J.L. (1966) Models of the lunar surface including temperature dependent thermal properties; Icarus, v. 5, p. 606

MacDonald, G.J.R., (1959) Chondrites and chemical composition of the earth; in Researches in Geochemistry, ed. P.H. Abelson; Wiley & Sons, N.Y., p. 476

NASA Special Report (1965) NASA SP-88

Urey, H.C. (1957) Boundary conditions for theories of the origin of the solar system; in, Physics and Chemistry of the Earth, Volume 2, p. 46-76

Watson, K. (1964) Thermal conductivity of selected silicate powders in vacuum from 150° - 350°K; Ph.D. thesis, California Institute of Technology

ORGANIZATION OF THE LUNAR HEAT-FLOW EXPERIMENT TEAM

Scientific Investigators

Principal investigator - M.G. Langseth, Lamont-Doherty Geological Observatory of Columbia University

Coinvestigators - S.P. Clark, Jr., Yale University
J. L. Chute, Jr. - Lamont-Doherty Geological Observatory of Columbia University
S.J. Keihm - Lamont-Doherty Geological Observatory of Columbia University
M.G. Simmons, Massachusetts Institute of Technology

Prime Contractor for the Heat-Flow Experiment

Bendix Corporation, Aerospace Systems Division, Ann Arbor, Michigan

Principal Personnel

K. Peacock, R. Gilson, Wm. Johnson and B. Smith

Responsibilities

Heat-flow experiment subsystem integration; integration of the heat-flow experiment with the ALSEP system; design and fabrication of the thermal housing for the heat-flow experiment; and, testing of the subsystem for flight qualification and acceptance.

Principal Subcontractors

Arthur D. Little, Inc., Cambridge Massachusetts

Principal Personnel

A. Wechsler, P. Glazer, E. Drake, F. Ruccia, D. Nathanson, R. Sanborn, E. Boudreaux, P. Felsenthal.

Responsibilities

Design and fabrication of the heat-flow probes, testing and calibration of heat-flow probes; and theoretical studies of the probe performance.

Gulton Industries, Albuquerque, New Mexico

Principal Personnel

J. Cox, J. Mason, R. Maschoff, R. Carlson

Responsibilities

Design, fabrication and testing of the electronics subsystem

Rosemount Engineering Company, Minneapolis, Minnesota

Principal Personnel

L. Lofgren, L. Klaven

Responsibilities

Design, fabrication, calibration and performance testing of all platinum resistance thermometers used in the heat-flow experiment

Lunar Surface Drill Prime Contractor

Martin Marietta Corporation, initially at Baltimore, Maryland and later at Denver, Colorado

Principal Personnel

D. Crouch and Wm. Britten

Subcontractors

Black and Decker Manufacturing Company, Baltimore, Maryland

*

III . CONSTRAINTS OF THE CONCEPTUAL DESIGN OF THE HEAT-FLOW EXPERIMENT

The principal constraints on the conceptual design of the experiment were:

1) The mechanical properties of the lunar surface layer;
2) the thermal properties of the lunar surface layer and its heat budget;
3) the weight and dimensional constraints of the spacecraft; and,
4) the limitations of astronaut activity on the lunar surface.

Since our knowledge of the subsurface was limited, we decided to make the experiment in such a way that reliable results could be obtained over as wide a spectrum of mechanical and thermal properties as possible. What follows is a summary of the status of information about these constraints when the design was started.

Numerical Properties

Some indications of the physical characteristics of the lunar soil has been inferred from the thermal and optical response of the lunar surface to solar radiation decades before the Apollo program. The facts that, at noon the moon's surface temperature was nearly that required for radiative steady state, and the rapid cooldown after sunset, or during an eclipse, indicated that the surface layer had an extremely low thermal inertia $(K\rho c)^{1/2}$ (Wesselink, 1948 and Jaeger, 1953). Microwave observations throughout a lunar day indicated that subsurface materials to a depth of several centimeters had a very low conductivity as well (Piddington and Minnett, 1949). The highly insulating thermal properties of the lunar surface could be best explained if the surface material was finely powdered material in a vacuum. Photometric observations of low albedo, peaking of brightness at zero phase and low polarization also indicated that the lunar surface was covered nearly everywhere by extremely fine powders (e.g. Hapke, 1971).

Further verification of the dusty nature of the lunar surface came with the Ranger missions. High resolution photographs showed that topography at the smallest scale was rounded and smoothed by a blanket of material that prevailed everywhere except over fresh craters. The ranger photographs also

revealed that the lunar mare surfaces were peppered everywhere by craters up to 30 meters in size (see, Ranger VIII and IX, Technical Report # 32-800, p. 161-170). This observation suggested the mare surfaces had been hit everywhere at least once by objects large enough to create craters twenty to thirty meters in diameter. Such craters would be from three to six meters deep, based on experiments in materials simulating these thought to exist on the lunar surface. If craters this deep, or deeper, had excavated material during a hypervelocity impact, then the surface layer of the moon would consist of fine fragments and rock debris to at least these depths.

The Surveyor Missions provided the first eye level view of the lunar surface. These views showed several meter-sized boulders and numerous smaller rock fragments strewn over the lunar surface. (Surveyor Project Final Report, Part II. Technical Report 32-1265 JPL).

The Surveyor Missions also provided the first direct information on the distribution of grain sizes in the near surface layer of the regolith. These distributions were found to vary from site to site; but, in general, only 1% of the volume was comprized of fragments ten centimeters or larger in diameter. (Figure III-1).

The soil mechanics experiments which were flown on some of the Surveyor Missions could perform simple mechanical tests on the soil to a depth of several centimeters. The tests showed the soil to have little cohesion and a density of about 1.5 gm/cm^3. However, trench digging experiments showed the resistance of the soil to penetration increased at depths of five to ten centimeters.

Thermal Properties

Infrared and microwave observations of the lunar surface had provided much information on the thermal properties and temperatures of the regolith. Observations of the temperature drop of the lunar surface during a total eclipse indicated the thermal inertia of the very near surface material is about 7.7×10^{-4} cal $cm^{-2} sec^{-1/2} {}^\circ K^{-1}$. At 200°K, this corresponds to a conductivity of 4×10^{-6} cal $cm^{-1} sec^{-1} {}^\circ K$, or 1.5×10^{-5} W $cm^{-1} {}^\circ K^{-1}$, assuming $\rho c = 0.16$ cal $cm^{-3} {}^\circ K$. The surface temperature decay curve during the lunar night however was best fit by a thermal inertia of 1.25×10^{-3}, which corresponds to a conductivity at 200°K of 7.7×10^{-6} cal $cm^{-1} sec^{-1} {}^\circ K^{-1}$, or 3.2×10^{-5} Watt $cm^{-1} {}^\circ K^{-1}$. These results are extracted from a summary given by Shorthill (1972).

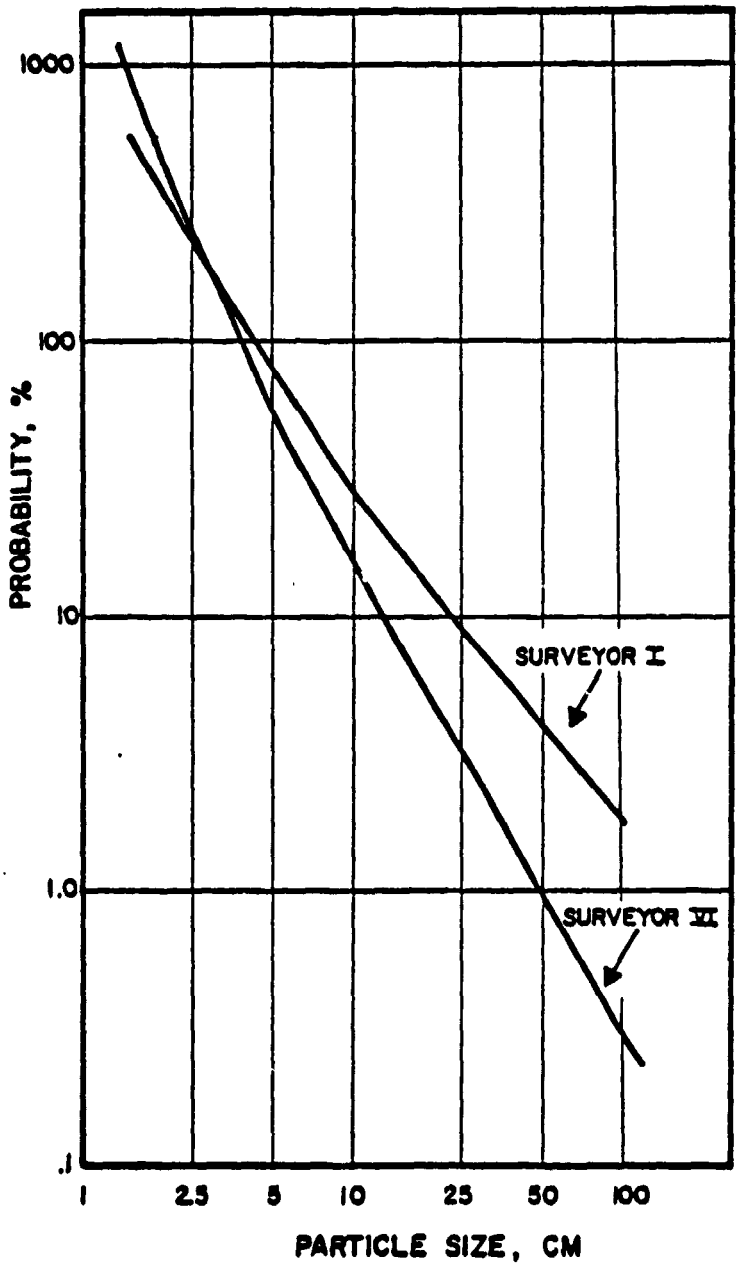
1000
100
10
1.0
.1
PROBABILITY, %
SURVEYOR I
SURVEYOR III
1
2.5
5
10
25
50
100
PARTICLE SIZE, CM

Figure III-1

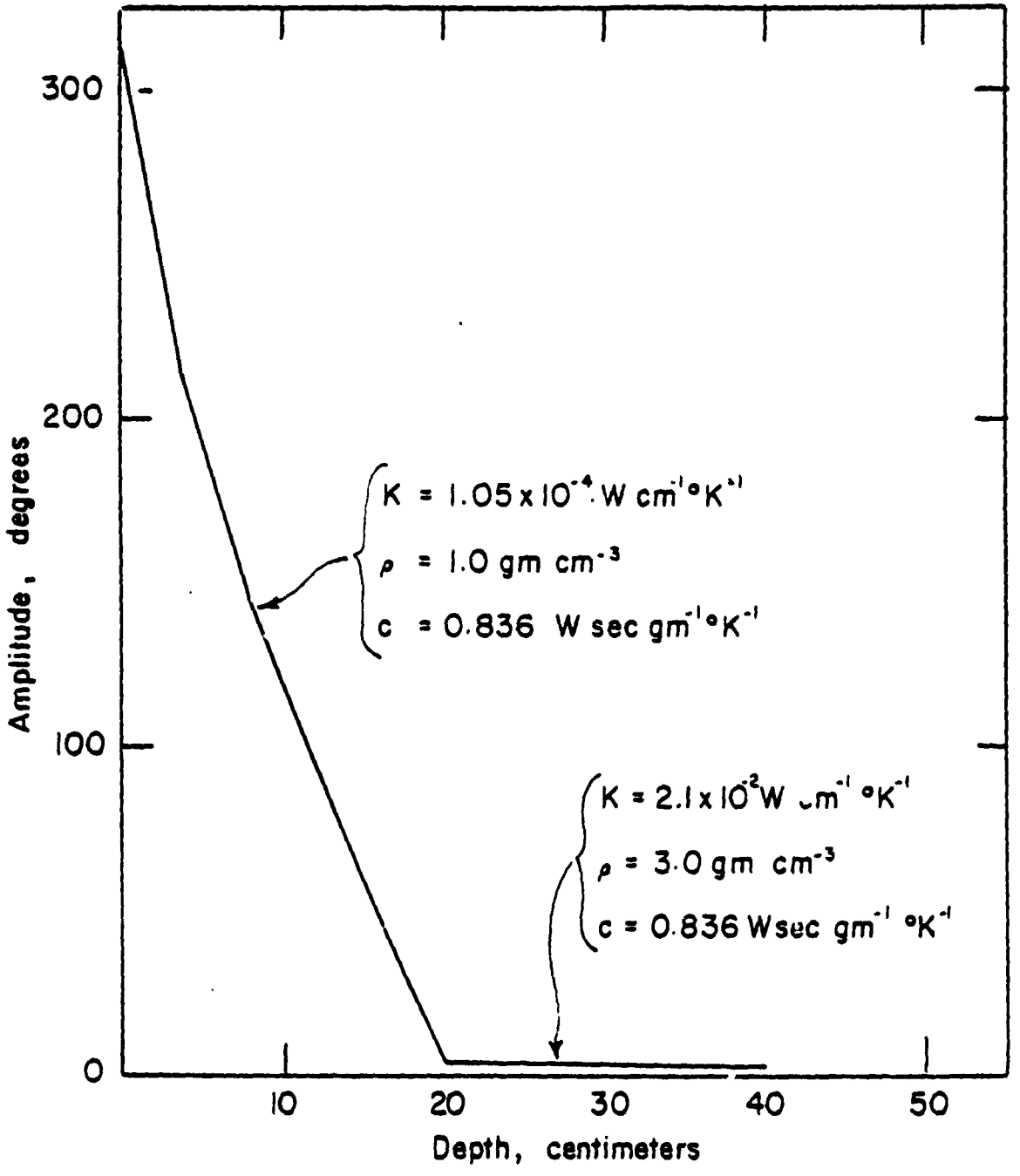

Effect of properties of the surface material on amplitudes.

Figure III-2

The difference in the thermal inertia between the two types of observations; the eclipse with an umbral period of about three hours and the lunar nighttime of about 350 hours, resulted from an increase in thermal conductivity with depth.

High resolution infrared scans of the lunar surface showed certain areas that remained relatively hot during an eclipse. These became known as hot spots and generally coincide with the location of large fresh craters. It is now generally agreed that these anomalies are due to higher abundance of solid rock fragments around these craters. The solid rocks have much greater thermal inertias (about 4.5×10^{-2} cal $cm^{-2} sec^{-1} °K^{-1}$) than the typical regolith. However, before the Surveyor program the nature of these hot spots was debatable.

The heat budget: The thermal properties from remote measurements permitted calculations of the transient and steady state heat budget in the regolith. Rather conservative limits on physical properties were assumed for such calculations based on the high variability of the properties observed over the surface.

Periodic variations, due to the lunation cycles, were of primary concern. At the surface they had a peak to peak amplitude of nearly 300°K, but with the generally low thermal conductivities the resulting thermal wave propagating downward into the subsurface would be rapidly attenuated. An example computed by Clark (1965) is shown in Figure III-2). The model is a 20 cm layer with a thermal inertia of 2.24×10^{-3} cal $cm^{-2} °K^{-1} sec^{-1/2}$ over solid rock of basaltic composition. It is clear that the amplitude is reduced to only a few degrees, 20 cm below the surface.

There is also an annual variation in mean temperature due to the eccentricity of the earth-moon systems' orbit about the sun. The amplitude of this variation is about 3°K peak to peak; however, the attenuation factor is 3.5 times lower, so that some variation due to this annual cycle might be observed at depths of a meter or more.

Steady State Gradient Due to Heat Flow: The bases for estimating the value of the gradient in mean temperature with depth resulting from heat flow from the lunar interior were:

1) Microwave observations of brightness temperature gradient and models of the thermal evolution of the moon, based on cosmologically reasonable abundances of heat-generating long-lived radioactive isotopes.

2) The range of estimates of thermal conductivity which takes into account the observations described above and also the possibility that a significant increase in the total amount of solid rock fragments below depths of tens of centimeters could significantly increase the conductivity there.

Microwave observations were interpreted by Troitsky (1965) to indicate that heat flow from the moon was similar to that observed for the earth (i.e. 6.3 μW cm^{-2}). We took this value as an upper limit. For the lower limit, we used a chondritic model of the moon, with a uranium abundance of only 11 ppb and an initial temperature near zero °C (see, for example, Reynolds et al., 1972 , who gives a value of about 1.0 μw cm^{-2} for such a model).

The range of conductivities of the regolith was taken to be 2 x 10^{-5} W cm^{-1} $°K^{-1}$ to 4.2 x 10^{-4} W $cm^{-1}°K^{-1}$ (see, for example, Langseth et al., 1968). The high upper limit reflected uncertainties as to the conductivity below 20 cm. When these two ranges are combined, the range of expected gradients resulting from heat flow from the interior of the moon is 2.4 x 10^{-3}°K/cm to 0.314°K/cm or, in terms of the temperature difference expected over a one meter depth interval, 0.24 °K to 31.4 °K.

Steady State Gradient Associated with the Radiative Heat Transfer in the Upper Regolith: Linsky, 1966 pointed out the possibility of a substantial temperature gradient in the upper few centimeters of the lunar surface material due to the strong temperature dependence of finely divided particulate material in vacuum. This dependence results from the prominent role of radiative heat exchange between the individual particles. Evacuated powders as a consequence, transfer heat far more efficiently at high temperature than at low temperature. This nonlinear behavior results in a net flux of heat into lunar regolith during the lunation cycle which must be counterbalanced by a steady temperature gradient to maintain the overall energy balance. The consequences of this behavior of lunar surface material are important to the design of the heat-flow experiment. Firstly, the mean temperature gradient in the uppermost layer (0-10 cm) will be due to the nonlinearity of heat transfer and not to the heat flux from the interior. As we noted earlier, this phenomenon rules out the use of a surface blanket or wafer-type heat flow meter. Secondly, any change in the radiative properties of the near surface layer will cause a change in the subsurface temperature because there is a reasonable chance that the ratio of

radiative to conductive heat transfer will have been changed.

It should also be noted that this effect would have important consequences for the interpretation of microwave observations from any planetary body that has a powdery surface and a very tenuous atmosphere

Space Constraints

One of the most significant constraints placed on the experiment's design was the size of the compartment in which the instrument was to be stowed during the flight to the moon. The maximum length of an object to be placed in the compartment was about 63 cm. This meant that any probe we wished to emplace to depths greater than 60 cm had to be folded, collapsed, or taken apart to be stowed.

The large accelerations the instrument would encounter during launching of the Apollo rocket, due to vibration and shock, were another important consideration. Most accurate temperature sensors suffer shifts in their calibrations when they are subjected to large accelerations.

Less demanding constraints, as far as design was concerned, were the maximum weight of about 4.5 kg, the maximum of peak power allowed which was 9 watts, and the range of temperatures that the experiment would experience 90°K to 400°K.

Astronaut Surface Activity

The disturbance of a dust covered lunar surface by an astronaut as he is setting up experiments on the surface can have a profound effect on the subsurface thermal regime. The footprints and the dust kicked up by walking change the surface radiative properties (the surface albedo and the IR emissivity) and the thermal inertia. These changes in surface properties could cause a change in surface temperature and consequently, a change in heat flow through the subsurface. These changes take years to propagate down to the depth of a meter or more.

Other design considerations had to take into account that the astronaut would be greatly encumbered by his spacesuit. In particular, the gloves greatly reduced the manual dexterity as compared to the use of the bare hand. Additional considerations were: that the deployment of the experiment on the surface had to be accomplished in the shortest possible time in order to maximize the number of tasks the astronauts could accomplish during their brief stay.

References

Clark, S.P., Jr. (1965) Some calculations pertaining to the feasibility of measuring lunar heat flow: Final Report contract NASA NSG-400, Yale University

Hapke, B. (1971) Optical properties of the lunar surface; in, Physics and Astronomy of the Moon, ed., Z. Kopal, Chapter 5.

Jaeger, J.C. (1953) The surface temperature of the moon; Austral. J. Phys., v. 6, p. 10-21

Langseth, M.G., K.A. More and W.E. Johnson (1968) An experiment to measure heat flow from the interior of the moon; Bendix Tech. Jour., v. 1, n. 1, p. 33-43

Linsky, J.L. (1966) Models of the lunar surface including temperature dependent thermal properties; Icarus, v. 5, p. 606

Piddington , J.H. and H.C. Minnett (1949) Microwave thermal radiation from the moon; Austral. J. Sci. Res., Ser. A2, p. 63

Ranger III and IV (19) Technical Report # 32-800, p. 161-170

Reynolds, R.T., P.E. Fricker and Audrey L. Summers (1972) Thermal history of the moon; in, Thermal characteristics of the Moon; ed. J.W. Lucas; Progress in Astronautics and Aeronautics, v. 28, p. 303-337, Chapter 4a, The MIT Press, Cambridge, Mass.

Shorthill, R.W. (1972) The infrared moon; A Review; in, Thermal Characteristics of the Moon; ed. J.W. Lucas; Progress in Astronautics and Aeronautics, v. 28, Chapter 1a; p. 3-49, The MIT Press, Cambridge, Mass.

Surveyor Project Final Report, Part II: Science Results; Technical Report 32-1265; NASA-JPL (1968

Troitsky, V.S. (1965) Investigation of the surface of the moon and planets by the thermal radiation. Radio Sci., v. 69D, p. 1585-1611

Wesselink, A.J. (1948) Heat conductivity and nature of the lunar surface material; Bull. Astronomical Inst. Netherlands, v. 10, n. 390, p. 351-363

*

IV. FLIGHT HISTORY OF APOLLO HEAT-FLOW EXPERIMENT

Apollo program plans called for the heat-flow experiment to be flown on Apollo missions 13, 15 and 16. Mission 13 never landed on the lunar surface because of the explosion of the oxygen tank in the CSM fuel cell. After many months of preparation with James Lovell and Fred Haise, the commander and lunar module pilot on the mission, it was very disappointing to have our first flight instrument burn up as the lunar module reentered the atmosphere over Australia. In retrospect, a heat-flow measurement at the Fra Mauro site (the Apollo 13 target site) would have been very valuable. Later orbital data showed this region to have the highest surface abundance of long-lived radioisotopes; thus, a measurement there would have provided a valuable end point for a heat flow and surface heat production correlation. Secondly, we would have had an earlier indication of the problems of drilling the regolith and could have been better prepared for the later missions.

Apollo 15 - Hadley Rille

The time was too short between the Apollo 13 and 14 missions to reconfigure the Apollo 14 ALSEP to carry the heat-flow experiment. Consequently, our first opportunity to emplace the experiment on the lunar surface came with the Apollo 15 mission to Rima Hadley.

Both astronauts worked to set up the ALSEP station and array of experiments, however. Drilling the holes and emplacing the heat-flow probes was the task of David Scott, the mission commander. The drilling proceeded badly. After the first meter of penetration, Commander Scott reported that the drilling was getting 'stiff' and downward progress stopped. He managed to drill two sections of the borestem down to a depth of about one meter, and to continue an additional section of borestem would have to be added. To disconnect the drill power head from the drillstring required a counterclockwise twist of the head relative to the drillstring to release a collet over the tapered upper joint. However, there was no sufficient counter torque on the stem to release the collet. With great difficulty Dave Scott managed to put a wrench

on the stem. The struggle was painful to watch, the spacesuit made the stooping and bending movements extremely difficult. It was only the physical strength and persistence of Dave Scott that allowed him to accomplish the task. After adding two more sections, Scott managed to continue penetrating to a total depth of 170 cm. By this time he was applying his full lunar weight to the powerhead and the drill's motor was stalling. At this point, it was decided to remove the powerhead and insert the first heat-flow probe, even though the bit was still one meter above the target depth. Again, it was extremely difficult to get the collet to release its grip on the upper taper joint; but, again Scott succeeded after a cumbersome struggle.

After the emplacement of the first probe, it was decided to go ahead and turn on the experiment. This would allow us to see if the experiment was working properly before expending the valuable time and astronaut effort on completing the drilling for the second probe. It operated perfectly.

The second drill hole was started, but immediately the same difficulties were encountered. The science team in the ALSEP room decided to call a stop to deployment of the heat-flow experiment until the second EVA. The powerhead was left on the drillstem after penetrating about one meter.

Between EVA's there were hasty conferences at mission control to try to diagnose the problems of the drill based on performance. The concensus of opinion was that Scott was applying too much downward force on the drill and not allowing the drilled material to clear out of the hole. Before the second EVA Scott was advised to try to hold the drill back, to actually pull up if necessary to help clear the cuttings.

Soon after the second EVA began, Scott resumed the task of drilling. He tried to restrain the downward progress of the drill, but commented that the stem seemed to be augering deeper into the regolith. At one point in the drilling, there was a noticeable release of torque and Scott commented that it had freed. Later, analysis of the films and the photographs showed that the drillstem had actually parted at one of the joints below the surface and, therefore, the stem attached to the powerhead no longer had a bit. Even without the bit, the drill continued to penetrate twerty to thirty additional centimeters and then stalled. We decided to halt the drilling at that point. Scott had the same difficulty removing the powerhead as before, but finally managed it. The second probe was inserted, but when it reached the bottom of the hole, the top of the probe still protruded. Commander Scott felt that there was some obstruction in the hole, but a rapid miscalculation on earth

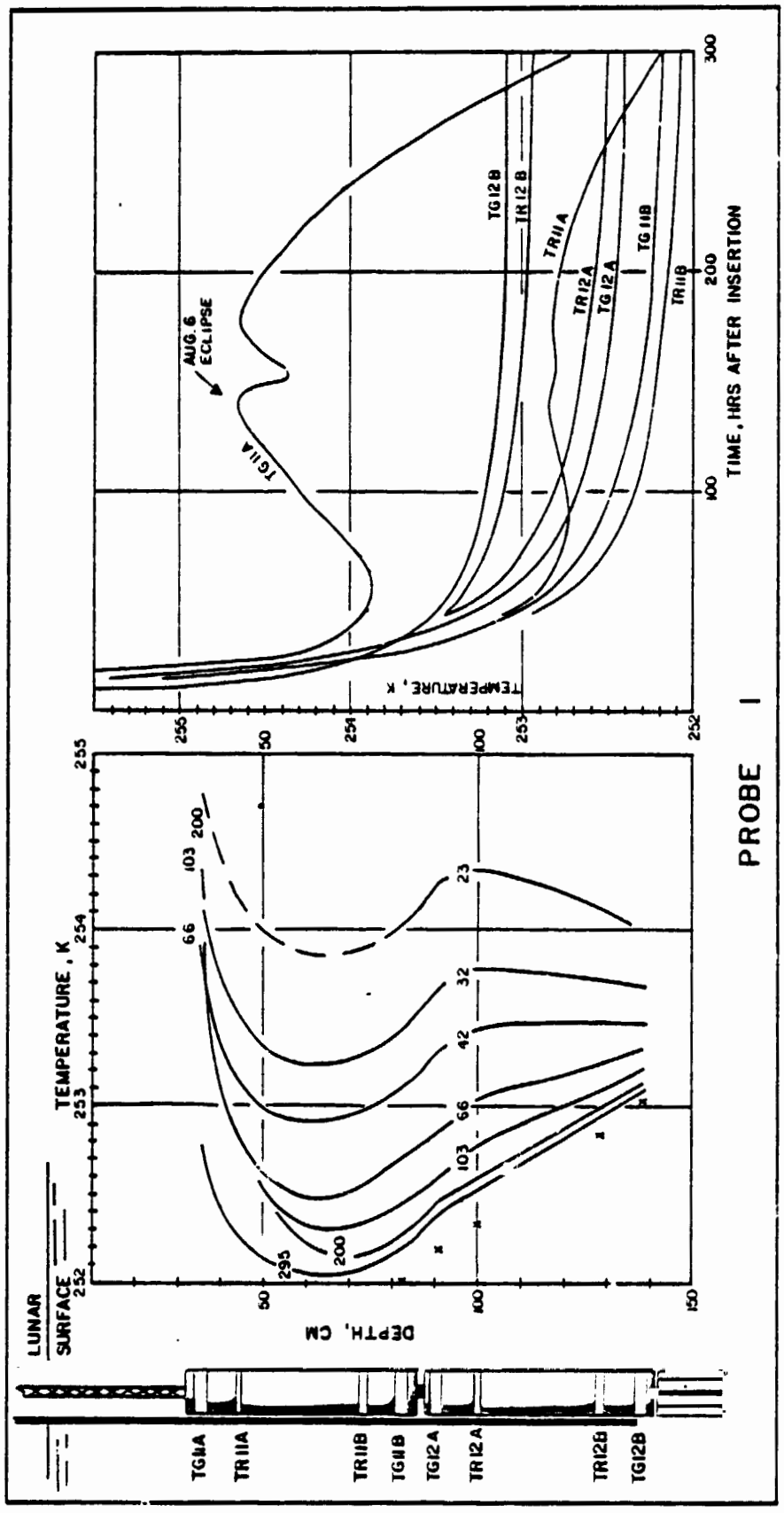

Temperature histories of the sensors on probe 1 during the first 300 hours after emplacement. The subsurface geometry of the probe and temperature as a function of depth are shown on the left. Temperature as a function of time is shown on the right.

Figure IV-1

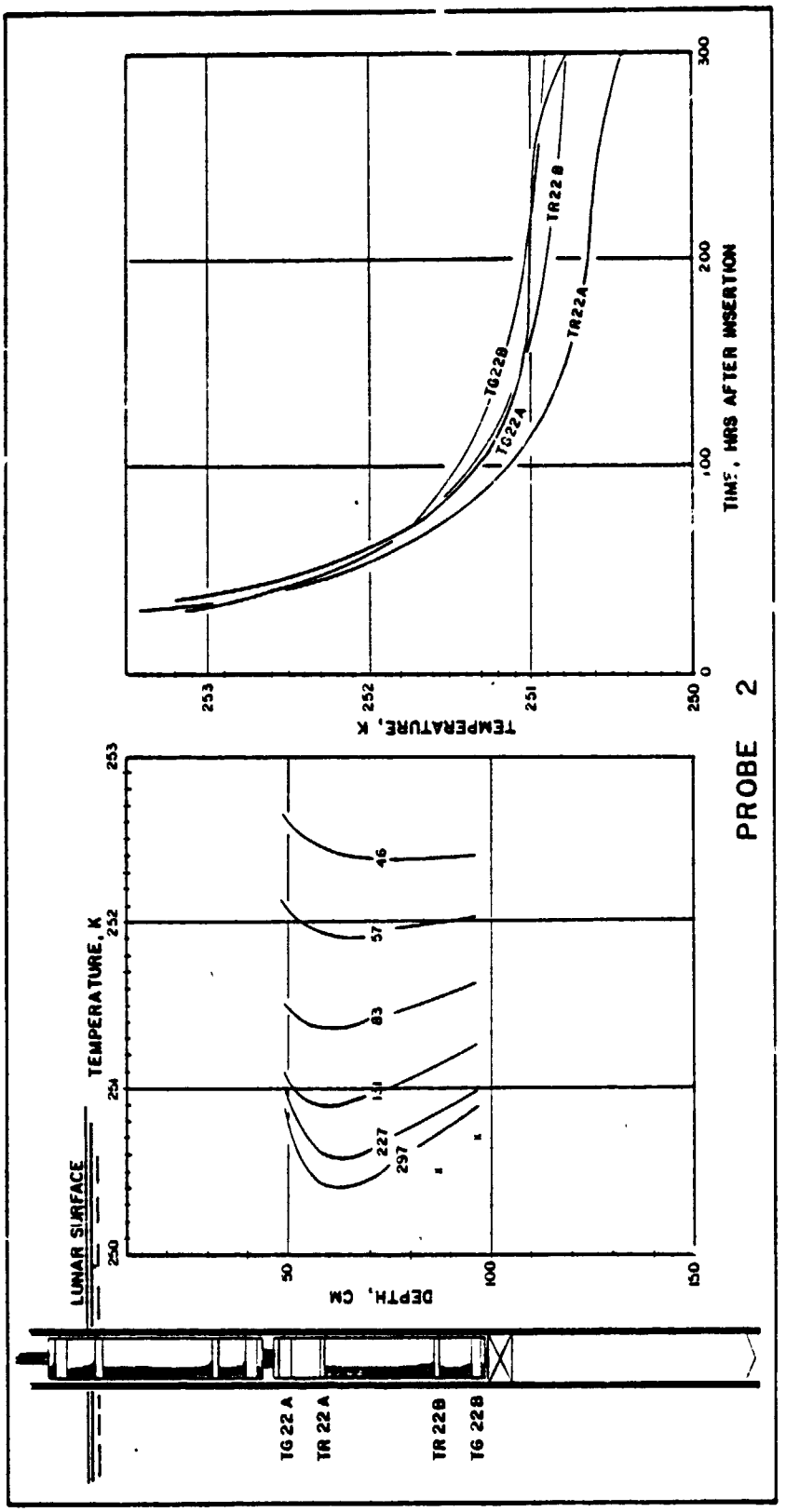

Temperature histories of the sensors on probe 2 during the first 300 hours after emplacement. The subsurface geometry of the probe and temperature as a function of depth are shown on the left. Temperature as a function of time is shown on the right.

Figure IV-2

assured him that everything was as expected.

It was abundantly clear that the drill that we had designed to penetrate the lunar regolith was not up to the task; nonetheless, we had thermometers buried in the subsurface. The deepest was buried to a depth of 137 cm. This depth was sufficient to assure an accurate measurement of the subsurface temperature gradient. In Figures IV-1 and IV-2 we show the evolution of the temperature versus depth profiles measured by the probes, for the first 300 hours after emplacement. Notice that, the initial temperature profiles of both probes decreased with depth; but, as the probe slowly equilibrated with the surrounding regolith, a gradient of nearly 1.7°C/m was established in the lower 70 cm of the hole. It took more than a month for the probe to fully equilibrate, which attests to the extremely low thermal conductivity of the regolith . A feature of the early temperature profiles of probe 1 was very pertinent to the drilling problem. The thermometers adjacent to the tapered joint show high temperature indicating a high frictional heating at this point.

The Deep Core Sample

The lunar drill was also used on Apollo 15 to obtain a deep core about two and a half meters long. Scott again operated the drill and it penetrated the regolith quite readily. The difficulties came when the drill was to be extracted. Scott simply could not get the drill to pull up despite applying power; which, if the drill were held steady, would help clear cuttings out of the hole. Instead, the drill tended to twist itself farther down. Finally with great effort and Jim Irwin's help the two pulled the drill up.

Later analysis of the core samples showed that the material at depths greater than two meters had lain undisturbed for a half billion years.

Diagnosing the Drill Problem

The problem with the drill was simple. The subsurface of the regolith was much denser than we had supposed. The regolith, at least to a depth of a few meters, is mainly composed of extremely fine dust of rocky and glassy fragments; yet it is packed so densely that it cannot be further compressed without great effort. This character of the lunar soil layer required that all of the drill cuttings pass up alongside the drill stem to the surface. The bulges in the stem at each joint prevented this; and, consequently, the drill was augering its way into the moon as Dave Scott had noted. We had

mistakenly assumed, based on models of the lunar surface layer, that the cuttings could be easily compressed into the adjacent material.

The poor performance of the drill on the Apollo 15 mission could be completely explained by this hypothesis and it was demonstrated by running tests in a test bed of highly densified basalt powder. During these tests, the drill would penetrate beautifully until a joint entered the soil. Then the penetration slowed and eventually the motor stalled.

The problem was solved by changing the design of the joint so that there was no bulge and so that the spiral fluting that moved the cutting up the hole continued through the joints. To do this, we had to bond titanium joints onto the ends of the composite borestems. At the same time, we lengthened each section so that fewer joints were required. We adjusted the lengths so that no thermometer was immediately adjacent to a titanium joint. The redesigned drill stem drilled the high density basalt powder model easily. A redesign of the wrench that decoupled the powerhead from the borestem was also needed to make it easier for an astronaut to use. To overcome the problem of retrieving the deep drill core an extractor, with a greater mechanical advantage, was designed. All of these modifications were made, tested and flight rated in the eight month interval between Apollo 15 and 16.

Apollo 16 - The Highland Site

Charles Duke, the lunar module pilot on the Apollo 15 mission was active in the redesigning and retesting of the drill. Being taller than John Young, the commander of Apollo 16, Charlie was assigned the drilling task, since it was easier for him to manage the long first section. Charlie was a perceptive engineer and helped greatly with all the phases of the modifications to the drill.

The drilling went perfectly for the first heat-flow hole. Each section sank slowly, but surely into the regolith. However, as Duke was inserting the first probe, John Young who was busily engaged in setting up other experiments of the ALSEP array, caught the flat cable that connects the heat-flow experiment to the ALSEP central station over his boot. Before he felt the tug of the cable, or before any word of warning could be relayed from the ground, the cable snapped rather easily at the connector that plugged into the central station.

John Young apologized dejectedly when he discovered the heat-flow cable had become completely torn off. Charlie Duke grumbled about the time wasted in drilling the hole and inserting a probe that would never be used. Upon closer inspection, the astronauts found that the cable had torn off cleanly and squarely right at the outermost clamp of the astromate plug, the connector to the ALSEP transmitter (see Section III). Strain relief had not been provided for a tearing motion. The outer rim of the clamp from which the cable emerged had a sharp square corner that undoubtedly helped in starting the tearing action. The tensile strength of the cable was sufficient to withstand almost any imaginable tug that an astronaut might apply. Because of the soft nature of the lunar surface and the poor downward visibility of the astronaut that the helmet afforded there was a good likelyhood that they could trip over one or more of the many wires that radiated out from the central station. The cables and plugs were designed to withstand this eventuality. It was another design failure that completely negated all of the heat-flow team's preparation for the mission.

There was a faint ray of hope. The cable was torn so cleanly that there was a possibility it could be repaired. Thus, between the first and the third EVA's we began a nonstop effort to discover a way to remake the twenty or more electrical connections. If the 'Astromate Connector' could be disconnected from the central station, if the probe could be pulled out of the borestem without damage, if the whole experiment could be bagged and carried back into the LEM, if the tools existed to open the clamp, if the insulation on the flat cable could be removed to expose the surface of the ribbons of copper conductor without damaging them, if the cable could be inserted back into the plug so that most of the contacts were good, and if the repaired experiment could be set up on the lunar surface, the heat flow experiment could be saved.

A Possible Repair of the Apollo 16 Accident

Developing a fix was an all-out effort. NASA assigned its 'Tiger Team' to the problem. The principals were Don Arabian and Fred Haise. Haise donned his space suit to determine whether the 'Astronaut Connection' could be disconnected from the central station. It could be done if the station housing were tilted backward and the astronaut virtually got down on all fours. The rest of us worked on ways of stripping the insulation away from the conductors on the ribbon cable. Any sharp edged tool could be used as long as one were

patient enough. However, it was not certain what tools the astronauts had on board the lunar module. Each astronaut carried a discretionary packet of things not inventoried. There was some hope that either Duke's or Young's packet contained a sharp edged tool. Another possibility was to use one of the lunar rocks. The harder breccias were an ideal abrasive, so that they could be used much like a coarse whetstone. By rolling ribbon cable over a hard mandrel and rubbing firmly, but carefully, with a flat side of a stone the insulation could be removed with only slight damage to the copper conductor inside.

By 7 a.m. the next morning, a procedure had been written and Don Arabian was talking Fred Haise through a simulation of the repair. After the simulation the repaired plug was tested and most, but not all, of the contacts were good. However, enough were good to give useful temperature data thanks to considerable redundancy in the use of the conductors. The amazing thing to me was that, while the enthusiasm and energy of most of us seemed to flag through the wee hours of the morning, Arabian and Haise seemed to gain in strength. By 8 a.m. they were working with the vigor most of us had started with twelve hours earlier. I later learned that Arabian had been up the two preceding nights working on the problem of the errant thruster controls in the command module that nearly cancelled the Apollo 16 lunar landing.

At about 9 the next morning, an ad hoc board consisting of top members of the Apollo Program Directorate convened. Arabian presented the procedure for carrying out the repair. There were many attractive reasons for trying it. Firstly, it would be a convincing demonstration of the valuable role men play in space missions. The repair would have strong public relations appeal, especially the possibility of using lunar material to do it. The heat-flow program had the highest priority of all the ALSEP experiments, so that one of the principal objectives of the mission would have been saved. This was the last chance to get a heat-flow measurement in the highland areas during the Apollo Program.

But, the reasons for not trying the repair were stronger. To gather up the experiment at the end of EVA 2 would cut about a half hour of time from other parts of the science program. Another hour at the start of EVA 3 to set the repaired experiment back up would have precluded the trip to North Crater, a primary geological target of the mission. The probability of a successful

repair was not very high, so that all this time could conceivably be wasted. Most importantly however, was the fact that the repair to the cable had to be done inside the lunar module and it would cut into the rest time of Charles Duke and John Young between EVAS 2 and 3. After EVA3 they would have to perform the critical launch from the lunar surface and rendezvous without rest.

On balance then, it was clear that the correct decision was to forsake the heat-flow experiment. This decision Rocco Petrone made unequivocably after lengthy discussion and consideration of all sides.

Apollo 17 - Taurus Littrow

In contrast to the Apollo 15 and 16 problem the operations involved with setting up the experiment at the Apollo 17 site of Taurus Littrow went smoothly. Each borestem was drilled to its prescribed depth and the probes installed. The operation of the experiment system was perfect and it continues to work as of 1976 with virtually no failures. The only degradation in performance is noise that appears on the thermocouple channels during the lunar morning (see Section V).

By the end of the Apollo Program, there were two working heat-flow experiments operating on the lunar surface, one at Rima Hadley with the probes buried to shallower than planned depths, and the other at Taurus Littrow, which is set up as planned. The shallow depth of burial at Apollo 15 proved eventually to be beneficial. The four and a half years recording lunar temperatures at relatively shallow depths has provided an excellent record of long-term temperatures in the moon's subsurface. The first major failure in the Hadley Rille experiment occurred in December of 1975, four and a half years after installation.

V. EXPERIMENTAL RESULTS

A. SURFACE TEMPERATURES AND THE NATURE OF THE SHALLOW REGOLITH

1. Surface Temperature Deductions

At each of the heat-flow stations, sections of the electronics' cable containing one or more thermocouples of $\pm$ 0.5°K accuracy were deployed above the lunar surface. These thermocouples are in radiative balance with the lunar surface, the solar flux and space and hence provide a measurement of the surface brightness temperature. At the Apollo 15 site, a total of five thermocouples (two at the probe 1 station; three at probe 2) were exposed above the lunar surface between the protruding borestem and the heat-flow electronics' station. Because of poorly defined orientation and an unknown amount of lunar dust coverage, interpretation of the daytime thermocouple data in terms of surface temperature could not be accomplished with less than 20°K uncertainty. However, since daytime surface temperatures are primarily controlled by the solar albedo, theoretical models taking into account latitude and previous albedo estimates were used to supplement the nighttime data and calculate the mean surface temperature over a lunation.

At the Apollo 17 site, each of the probes was deployed to the nominal depth of 2.3 m, resulting in the placement of two above surface thermocouples (one at each station), approximately 15 cm from the top of each borestem. Improved determination of orientation allowed noontime temperature estimates of $\pm$7°K accuracy.

Fortunately, more accurate measurements of surface temperature could be made during the lunar night, when cable orientation and surface solar albedo can be neglected. The cooldown response of the surface in the absence of solar flux is controlled primarily by the thermal properties of the upper 5-15 cm of the regolith and can, therefore, be utilized to deduce a thermal property profile for the near surface layer.

In the absence of solar flux, the radiative balance of each thermocouple can be expressed as:

$$a\rho c \frac{\delta T_c}{\delta t} = \alpha_{dir} \cdot F \cdot \varepsilon_m \sigma T_m^4 - 2\varepsilon_c \sigma T_c^4 \qquad \text{(V-A-1)}$$

were a = cable radius,

ρc = volumetric heat capacity of cable,

α_{cir} = infrared absorptivity of cable,

ε_c = emissivity of cable,

ε_m = emissivity of lunar surface,

F = view factor of thermocouple element to the surrounding topography,

σ = Stefan-Boltzman constant; and,

T_c, T_m = cable and lunar surface temperature respectively.

Except for periods of rapid temperature change (such as during an eclipse, or immediately following lunar sunset), the finite time constant of the cable may be neglected and Equation V-A-1 may be reduced to the following expression for T_m.

$$T_m = \left[\frac{2\,\varepsilon_c}{F\,\alpha_c\,\varepsilon_m}\right]^{1/4} \cdot T_c \qquad \text{(V-A-2)}$$

The primary sources of error in calculation of surface brightness temperatures using Equation V-A-2 derive from uncertainties of the radiative properties of the cable and topographic effects. During eclipses and immediately following lunation sunset, errors in the determination of $\delta T_c/\delta t$ must also be taken into account.

Radiative properties of the thermocouple cable, ε_c and α_{cir}, as well as the term accounting for the cable's thermal mass, $a\rho c$, were determined experimentally by Clifford Cremers of the University of Kentucky on a sample piece of thermocouple cable. Values of $a\rho c$ were also checked by an evaluation of cable component properties. Values of ε_c and α_{cir} were adjusted to account for partial cable covering by lunar fines as was indicated by the different temperatures reached by the five thermocouples at the Apollo 15 site at the end of lunar night. More detailed descriptions of the surface temperature analysis can be found in Keihm et al. (1973) and Keihm and Langseth (1973).

2. Temperature Dependence of the Surface Layer thermal Conductivity

A major result of the surface temperature measurements at Hadley Rille and Taurus Littrow was the calculation of the mean lunation temperatures: 207 $\pm$ 7°K at Apollo 15 and 216 $\pm$ 5°K at Apollo 17. The lower mean temperature at the Apollo 15 site is due primarily to the early morning shadowing effect

produced by a topographic high to the east of that site. The mean surface temperatures observed are 35-40°K lower than the equilibrium temperatures measured at meter depths. Only a small part of this mean temperature rise (no more than 5°K) can be accounted for by the temperature gradient produced by the measured heat flow. The mean temperature rise is due mainly to the non-linear effects of radiative heat transfer within the highly porous dust layer about 2-3 cm thick at the surface. During the warm lunar day heat is transferred more effectively into the lunar surface than it can be transferred out during the cold lunar night. To conserve net flux over a lunation, a mean-temperature gradient is established mainly confined to the porous surface layer. The size of this gradient is largely a function of the relative contributions of the radiative and conductive components of the effective thermal conductivity. Because most of the total mean-temperature difference takes place in the upper few centimeters, the relative contribution of the radiative and conductive terms can be determined unambiguously only in this region. If one characterizes the conductivity temperature dependence by the Linsky (1966) parameter,

$$R_{350} = K_r\ (350)/K_c$$

where K_r is the radiative component, and K_c is the conductive component, the observed mean temperature gradients at Hadley Rille and Taurus Littrow require $R_{350} = 2.5 - 3.0$ and $R_{350} = 1.7 - 2.2$ respectively. These values indicate a somewhat larger radiative component then that inferred from measurements of returned lunar fines (Cremers and Birkebak, 1971 and Cremers and Hsia, 1973) and suggest that thermal properties in the low density surface layer are a strong function of in situ grain-contact configuration.

3. Thermal Response During the Lunar Night

As discussed earlier, the surface temperature response in the absence of solar radiation is primarily a function of the shallow regolith thermal properties: ρ, the density; c, the specific heat; and k, the thermal conductivity. Variations with depth and temperature can also be constrained by the nature of the surface cooldown. Matching of the postsunset surface temperatures was reduced to the selection of an appropriate conductivity

function, k(z,T), by utilizing other data to constrain the density profile and temperature dependence of the specific heat. Density profile selection appropriate to each site was based on soil mechanics data provided by J.K. Mitchell (personal communication) for Apollo 15 and D. Carrier (personal communication) for Apollo 17. The specific heat as a function of temperature was modeled by a least square fit to the data of Robie et al. (1970) on Apollo 11 fine samples. Similar measurements on Apollo 15 soil sample 15301,20 and Apollo 16 soil sample 60601,31 by Hemingway et al. (1973) yielded nearly identical values of specific heat versus temperature as the Apollo 11 sample. Since the ratio of the radiative to conductive component of the thermal conductivity was constrained by the observed mean temperature gradient discussed earlier, only the conductive component, K_c, remained to be varied as a function of depth to fit the cooldown surface data. One dimensional finite difference models were utilized to fit the nighttime data. Figure V-A-1 shows the fits to the nighttime surface cooldown data along with the derived mean conductivity profiles (solid curve in inset). In both the Apollo 15 and 17 models, a low conductivity layer of about 2 cm thickness, with 210°K conductivities between 0.9 and 1.5 x 10^{-5} W/cm^{-}°K was required to fit the steep drop in surface temperature for the first 40-60 hours following sunset. The Apollo 15 model then required a steep, but not discontinuous, rise in conductivity with depth, to a value of $\sim$ 0.8 x 10^{-4} w/ cm^{-}°K at a depth of 10 cm, to produce the increased flattening of the surface cooldown curve through the lunar night. The Apollo 17 model, however, required a much sharper jump in conductivity at a depth of 2-3 cm to produce the abrupt flattening of the cooldown curve at 10° phase past sunset characteristic of the Taurus Littrow site. The required increase in conductivity with depth from 3-15 cm is slight enough that the Apollo 17 model may be considered essentially a two layer model. Conductivity values of 1.2 - 1.3 x 10^{-4} are required below 5 cm. For both the Apollo 15 and 17 sites, the conductivities inferred at depths of 10-15 cm are in excellent agreement with the values deeuced from the annual wave data for the deeper regolith.

The principal advantages of the heat-flow experiment surface temperature measurements was the ability to measure local temperatures immediately

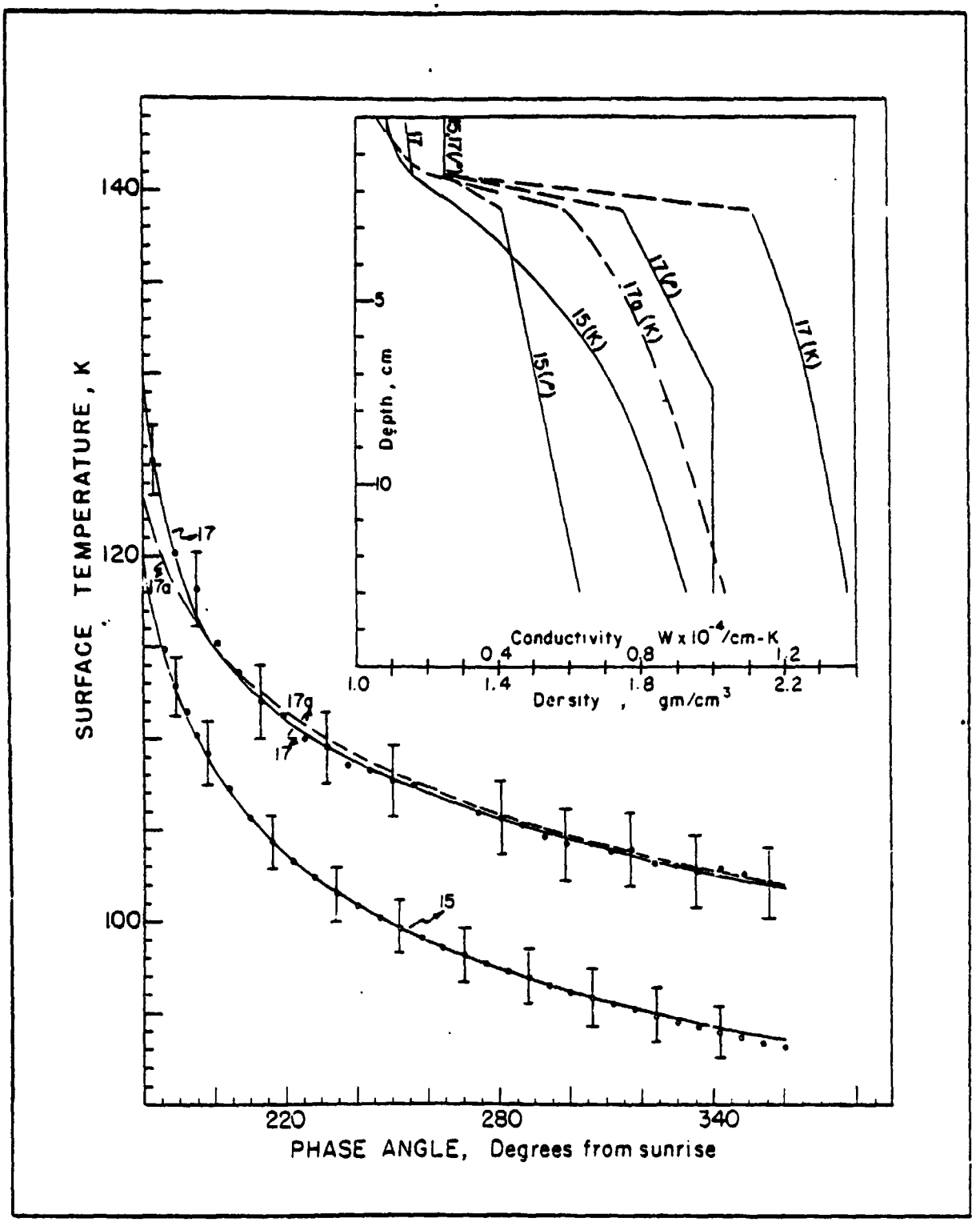

Surface temperatures during the lunar night at the Apollo 17 (solid dots) and Apollo 15 (open circles) heat flow sites. Vertical bars are estimated errors. The continuous curves are theoretical curves derived from the thermal property models shown in the inset.

Figure V-A-1

following sunset. The conductivity models inferred from the data are in essential agreement with earlier models based on earth-based infrared brightness temperature measurements. However, the greater detail of thermal property determination could only be accomplished with the addition of precise postsunset data. Measurements of $\pm$ 2°K accuracy within the first 10-20 hours after sunset are critical to an unambiguous modeling of the near surface thermal property profile. For example, as shown in Figure V-A-1, slight (2°K) changes in the nighttime cooldown curve within 40 hours following sunset can lead to relatively large changes in the derived conductivity profile (compares curves 17 and 17a).

4. Thermal Response During Eclipse

Because of the relative short duration, surface cooling during periods of partial or total solar eclipse are controlled primarily by the first centimeter of the surface layer. At the Apollo 15 site, surface temperatures were computed from the thermocouple data for the complete eclipse of August 6, 1971. Umbral surface temperatures of $\pm$ 5°K accuracy were obtained. (The decrease in accuracy relative to lunation nighttime temperature is due to uncertainties in the calculation of $\delta T_c/\delta T$ which must be included during the rapid temperature variations of an eclipse; see Equation V-A-1). The conductivity of the upper centimeter was varied in the one-dimensional models until agreement with the umbral surface temperatures was obtained. The preeclipse temperature profile was computed from the thermal property profile deduced from the lunation cooldown and has little effect on the eclipse deductions. Surface temperatures and feasible conductivity model fits for the August 6, 1971 eclipse at the Apollo 15 site are shown in Figure V-A-2. The resulting best fit conductivity function for the upper centimeter yielded:

$$K_s(T) = 0.67 \times 10^{-5} + 0.42 \times 10^{-12} T^3$$

indicating at 210° conductivity 1.05×10^{-5} w/cm°K, in agreement with the lunation results for the near surface layer. The accuracy of deduced umbral surface temperatures led to an uncertainty of $\pm$ 20% for the conductivity fits. A similar analysis in a total eclipse at the Apollo 17 site also yielded a surface conductivity in agreement with the lunation cooldown data.

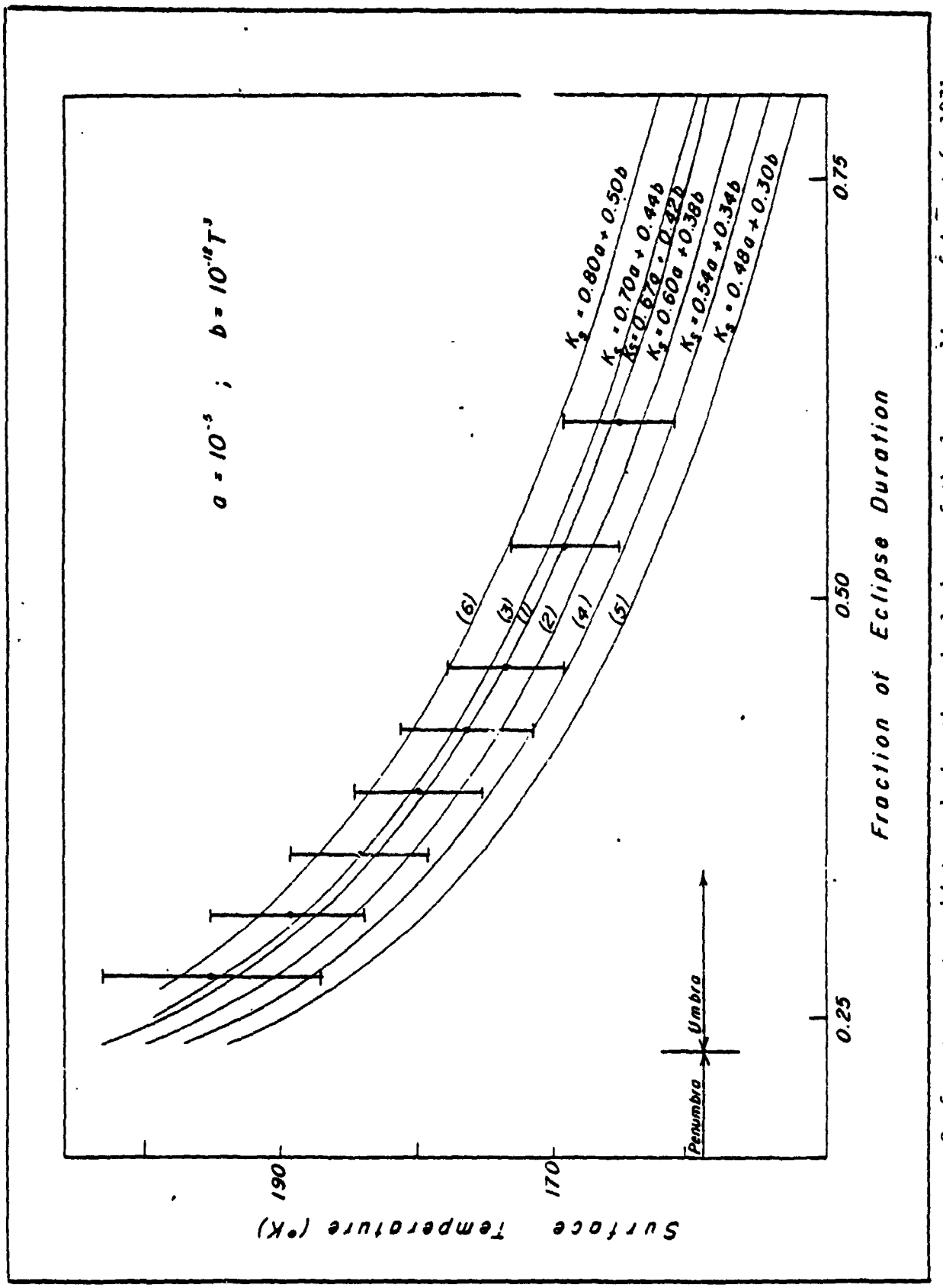

Surface temperature history during the umbral phase of the lunar eclipse of August 6, 1971. The vertical bars span a range of two standard deviations centered at the reduced surface temperature measurement. The solid lines represent computer generated models characterized by conductivity functions, $k_s(T)$, for the two centimeter.

Figure V-A-2

5. Comparison With Laboratory Measurements

Laboratory measurements of the thermal properties of returned regolith samples provide a direct comparison with the in situ measurements from the heat-flow sites. The most striking result of these measurements both for small samples of lunar soil and intact core tube samples, is the rather narrow range of conductivity values obtained. Small soil and sample measurements (Cremers et al., 1970; Cremers and Birkebak, 1971; Cremers, 1972; and Cremers and Hsia, 1973), utilizing the line heat source technique, yielded conductivities in the range 0.5 -3.0 x 10^{-5} w/cm^{-}°K over a temperature range between 100 and 400°K. All samples were characterized by increasing conductivity with temperature. The relative contribution of the radiative term to the effective conductivity was characterized by R_{350} [= K_r (350)/K_c] values between 0.5 and 1.5, approximately a factor of two less than that deduced in situ. Most of the measurements were done at low bulk densities (∿1.3 gm/cm^3). However, measurements at densities as high as 1.9 (characteristic of the deeper regolith) did not yield significantly different results.

Conductivity measurements of unopened core-tube regolith samples have been made using a new radiative flux technique (Horai et al., 1977). By conducting the measurements with minimal disturbance to the cores, it was hoped that the thermal conductivity characteristic of in situ regolith could be obtained. However, for the two Apollo 17 drill cores 70002 and 70006, preliminary results yielded conductivities in the range 1.8 - 3.6 x 10^{-5} w/cm^{-}°K, in close agreement with the line source laboratory results. The Apollo 17 drill-core samples contained material from 1-3 m depths below the lunar surface with bulk densities of 1.74 - 1.80 gm/cm^3. The large discrepancy between the laboratory measurements and the in situ results at depths greater than 10 cm suggests that the deeper lunar regolith possesses an intragranular thermal contact that has been enhanced by mechanical stress over millions of years of meteoritic impact. Only the near surface layer (0-2 cm), which has been overturned on a much more rapid time scale, exhibits the low conductivities obtained for the returned samples. At greater depths, whatever long-term mechanical process is involved, conductivities 3-5 times the laboratory results occur. The annual wave and transient deductions, as well as the short term

in situ conductivity experiments and surface temperature cooling histories, could not be accounted for by a regolith characterized by the laboratory conductivity results at depths greater than 10 cm. These results emphasize the importance of in situ measurements for reliably assessing the near-surface thermal regimes of other planetary bodies.

References

Cremers, C.J. (1972) Thermal conductivity of Apollo 14 fines; Proc. Lunar Sci. Conf. 3rd, p. 2611-2617

Cremers, C.J. and R.C. Birkebak (1971) Thermal conductivity of fines from Apollo 12; Proc Lunar Sci. Conf. 2nd, p. 2311-2315

Cremers, C.J., R.C. Birkebak and J.P. Dawson (1970) Thermal conductivity of ines from Apollo 11; Proc. Apollo 11 Lunar Sci. Conf., p. 2045-2050

Cremers, C.J. and H.S. Hsia (1973) Thermal conductivity and diffusivity of Apollo 15 fines at low density; Proc. Lunar Sci,Conf.4th , p. 2459-2464

Hemingway, B.S., R.A. Robie and W.H. Wilson (1973) Specific heats of lunar soils, basalt, and breccia from the Apollo 14, 15, and 16 landing sites between 90 and 350°K. Proc. Lunar Sci. Conf. 4th, p. 2481-2487

Horai, K., J.L. Winkler, Jr., S.J. Keihm, M.G. Langseth and J.A. Fountain (1977) Thermal conductivity of two Apollo 17 drill core samples 70002 and 70006: A preliminary result ; Proc. Lunar Sci. Conf. 8th, Houston, Texas; in press

Keihm, S.J. and M.G. Langseth, Jr. (1973) Surface brightness temperatures at the Apollo 17 heat flow site; Thermal conductivity of the upper 15 cm of regolith; Proc. Lunar Sci. Conf., 4th, in, Geochim. et Cosmochim. Acta Suppl. 4, p. 2503-2513

Keihm, S.J. , K. Peters, M.G. Langseth, Jr., and J.L. Chute, Jr. (1973) Apollo 15 measurement of lunar surface brightness temperatures; Thermal conductivity of the upper 1 1/2 meters of regolith; Earth and Planet. Sci. Lett., v. 19, p. 337-351

Linsky, J.L. (1966) Models of the lunar surface including temperature dependent thermal properties; Icarus, v. 5, p. 606

Robie, R.A., B.S. Hemingway and W.H. Wilson (1970) Specific heats of lunar surface materials from 90 to 350°K, v. 167, p. 749-750

V-B. OBSERVED TEMPERATURE HISTORIES IN THE SUBSURFACE AND ON THE SURFACE

Temperature sensor locations and final subsurface emplacement geometries are shown in Figure V-B-1. The accuracies and resolution of each of the sensors were given in Section III-B. Figure V-B-2 presents a three and one half year history of temperatures at some representative sensors. Four distinct temporal components are evident.

1) We see initial cooldown of the probe and borestem after emplacement of the probes showed that the initial temperatures were 295 - 305 °K. Cooling to ambient regolith temperatures is rapid at the start; however, full equilibration requires nearly three lunations as Figure V-B-2 shows.

2) We see a diurnal component on sensors within 80 cm of the surface. Below 80 cm, the nearly 300°K peak-to-peak surface variation is attenuated to a level below the noise of the absolute temperature measurement. Close examination of the Apollo 17 sensors shows a small variation with a diurnal period. This variation is not due to heat transfer downward in the borestem, but induced by the electronic circuitry which is apparently slightly temperature sensitive (see Section III-B). Two notable features of the diurnal variation are the high frequency content of the variations and the fact that they are nearly in phase with the surface variation. These features indicate that the predominant mode of heat transfer is radiative transfer along the borestem.

3) We see an annual temperature variation, which is most clearly seen by the Apollo 15 thermometers at 45 and 59 cm. As will be discussed in detail later, this variation is propagated downward through the regolith and its amplitude and phase lag are not strongly affected by the presence of the borestem and probes.

4) All sensors show a slow increase in temperature with time. The shallowest sensor begins to detect this increase after a few lunations, whereas the deepest sensors, for example those at Apollo 17 deeper than 150 cm, begin to detect the rise after a year. This component of the temporal variation is due to an increase of a few degrees K in surface temperature around the borestem caused by the astronaut's footsteps. Notice the substantial difference in this effect between probe 1 and probe 2 at the Apollo 17 site.

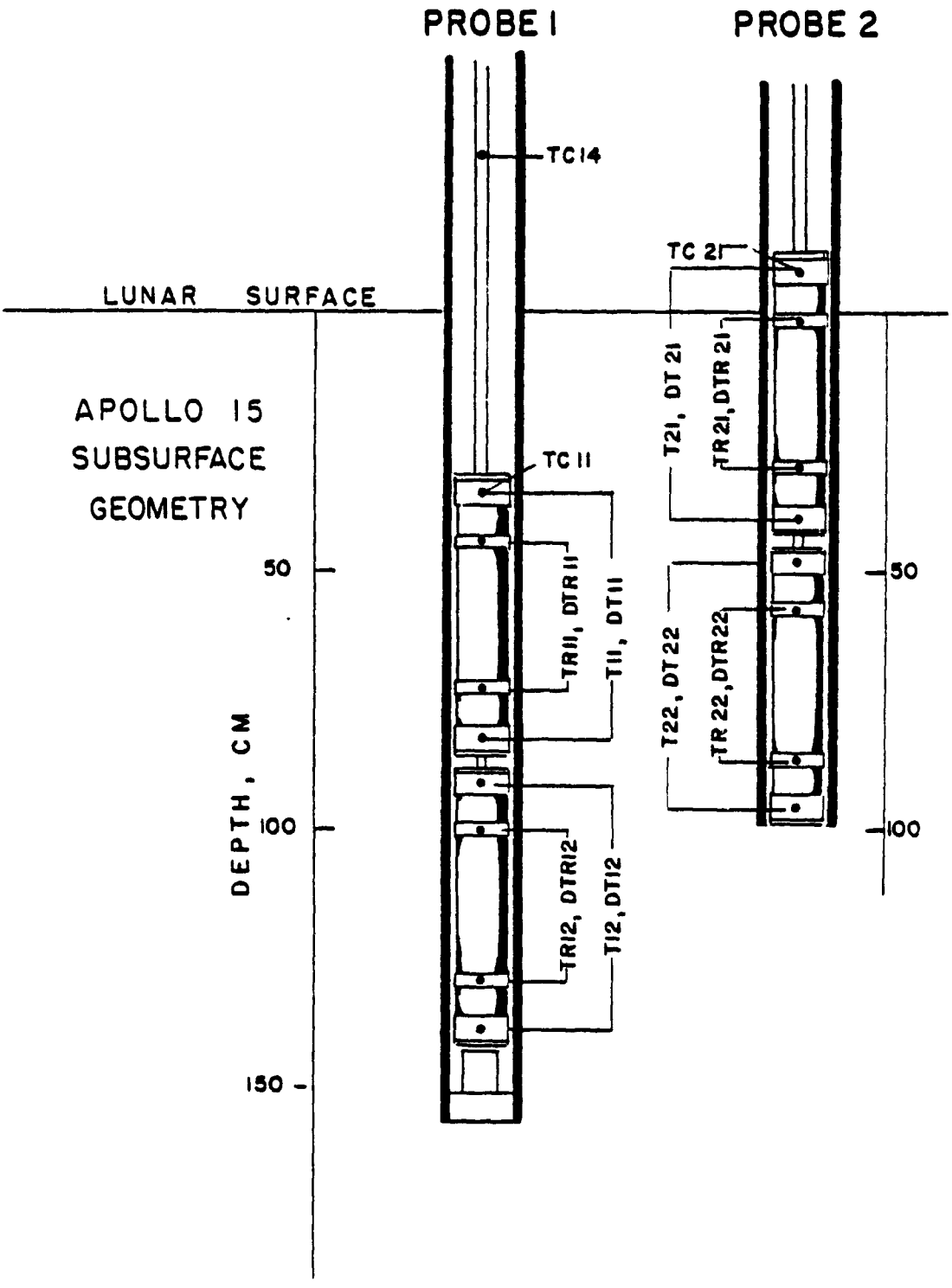

Configuration of the heat-flow probes in the lunar regolith. Additional details about the heat-flow instrumentation may be found in Langseth et al. (1974)

Figure V-B-1a

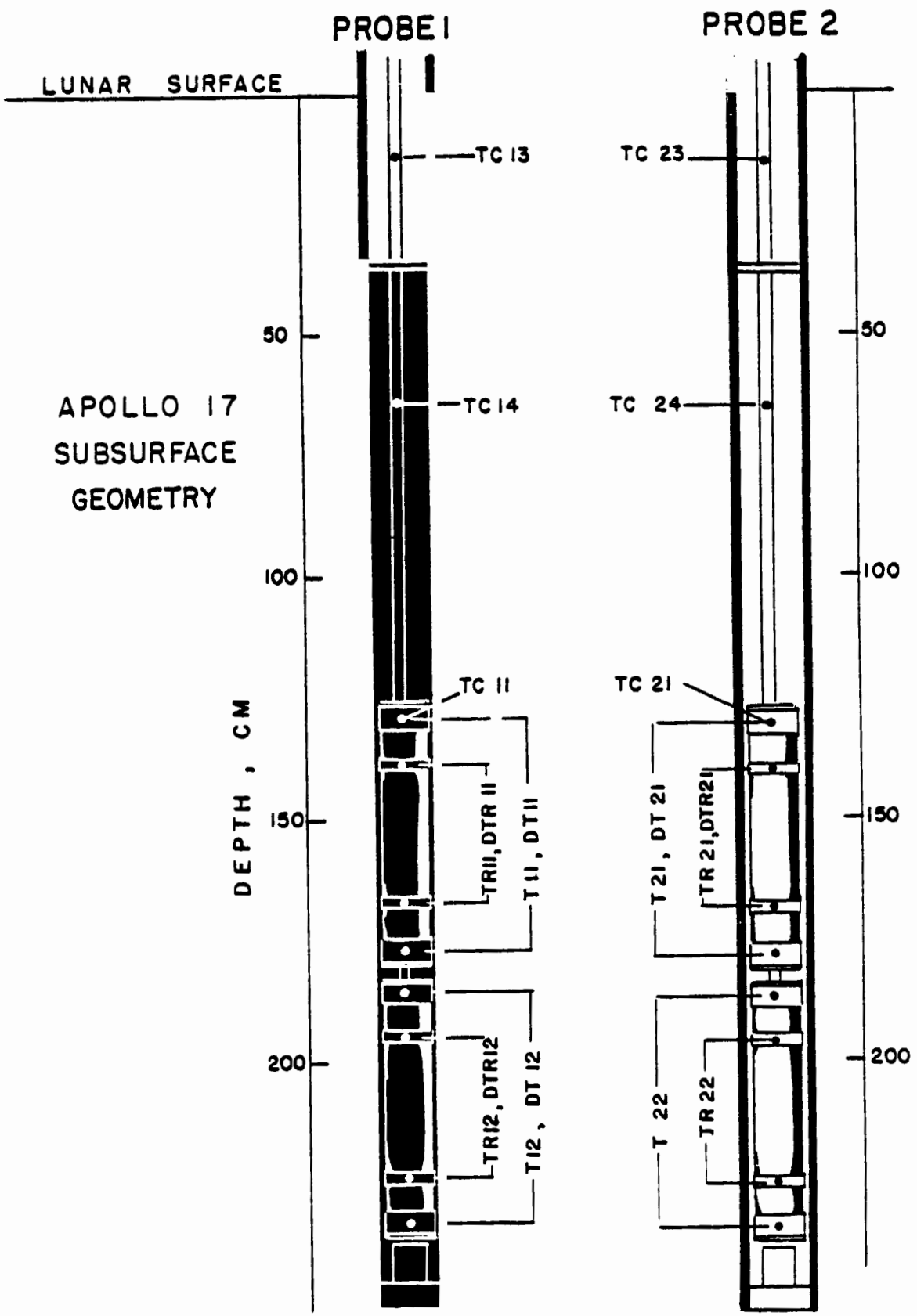
PROBE 1
PROBE 2
LUNAR SURFACE
APOLLO 17
SUBSURFACE
GEOMETRY
DEPTH , CM
50
100
150
200
TC 13
TC 14
TC 11
TR11, DTR 11
T 11, DT 11
TR12, DTR12
T12, DT 12
TC 23
TC 24
TC 21
T 21, DT 21
TR 21, DTR21
T 22
TR 22

Figure V-B-1b

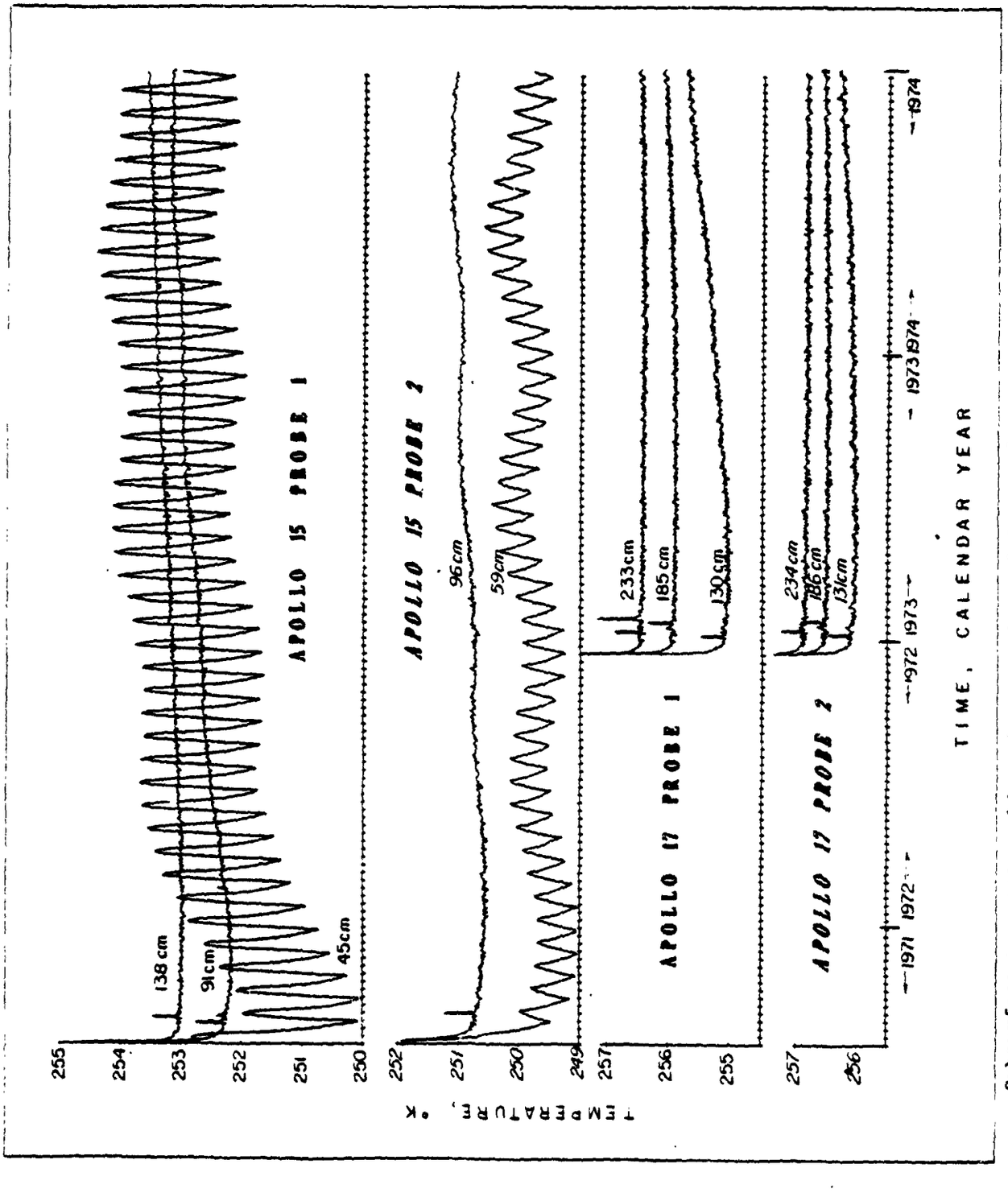

Subsurface temperature histories covering a 3.5 yr period of representative sensors on the four heat-flow probes. Initial cooldown of the probes after insertion can be seen at the start of each history. The small spikes in the first 60 days result from the short-term conductivity experiments.

Figure V-B-2

In Figure V-B-(3-14) are shown temperature records of principal sensors the first and last lunations observed on the surface. Figure V-B-1 (a & b) gives the sensor designations used to identify each curve. The records show many interesting details.

At the Apollo 15 site five of the thermocouples are in parts of the cables that are hanging above the lunar surface and are exposed to the full solar flux. The sixth, TC14, is inside the part of the borestem projecting above the surface. During the first lunation, shortly after the experiment is turned on, there is an abrupt change in temperature of all exposed thermocouples and TREF (which is the sensor on the thermal plate of the electronics). This results from realignment of the electronics and the probe I cable during EVA 2 and the insertion of probe 2 which was done on EVA 2 (see Section IV).

An eclipse occurred during this lunation which is clearly seen by all thermocouples. The abrupt fall of temperatures is repeated at sundown. There is a pronounced decrease in cooling rate at about 140°K, which is due to radiation from surrounding topography which is still sunlit. The slow warming of the thermocouples before dawn is probably due to a similar effect. However, at Hadley Rille the topography west of the experiment is much lower than that east of the experiment which explains the difference in magnitude of the effect between post sunset and predawn parts of the record.

Relatively low temperatures observed by TC12 and TC13 at probe 1 during the morning are due to partial shadowing by the very small scale surface roughness and the fact that the cable is nearly aligned with solar radiation in the morning. Similar effects are seen to reduce temperatures at probe 2 thermocouples during the evening. Large dips in temperature occur when the borestem shadow crosses the section of cable containing the thermocouple.

The records of subsurface thermometers, during the first lunation at Apollo 15, show in more detail the initial cooldown of the probes and the diurnal variation of temperature. The topmost sensor TG 11A actually shows a drop in temperature during the eclipse. This is because the sensor is radiatively coupled to the top of the borestem where the temperature drops nearly 200°K during the eclipse. The effects of two thermal conductivity measurements made late in the lunar night of the first lunation are also noticeable.

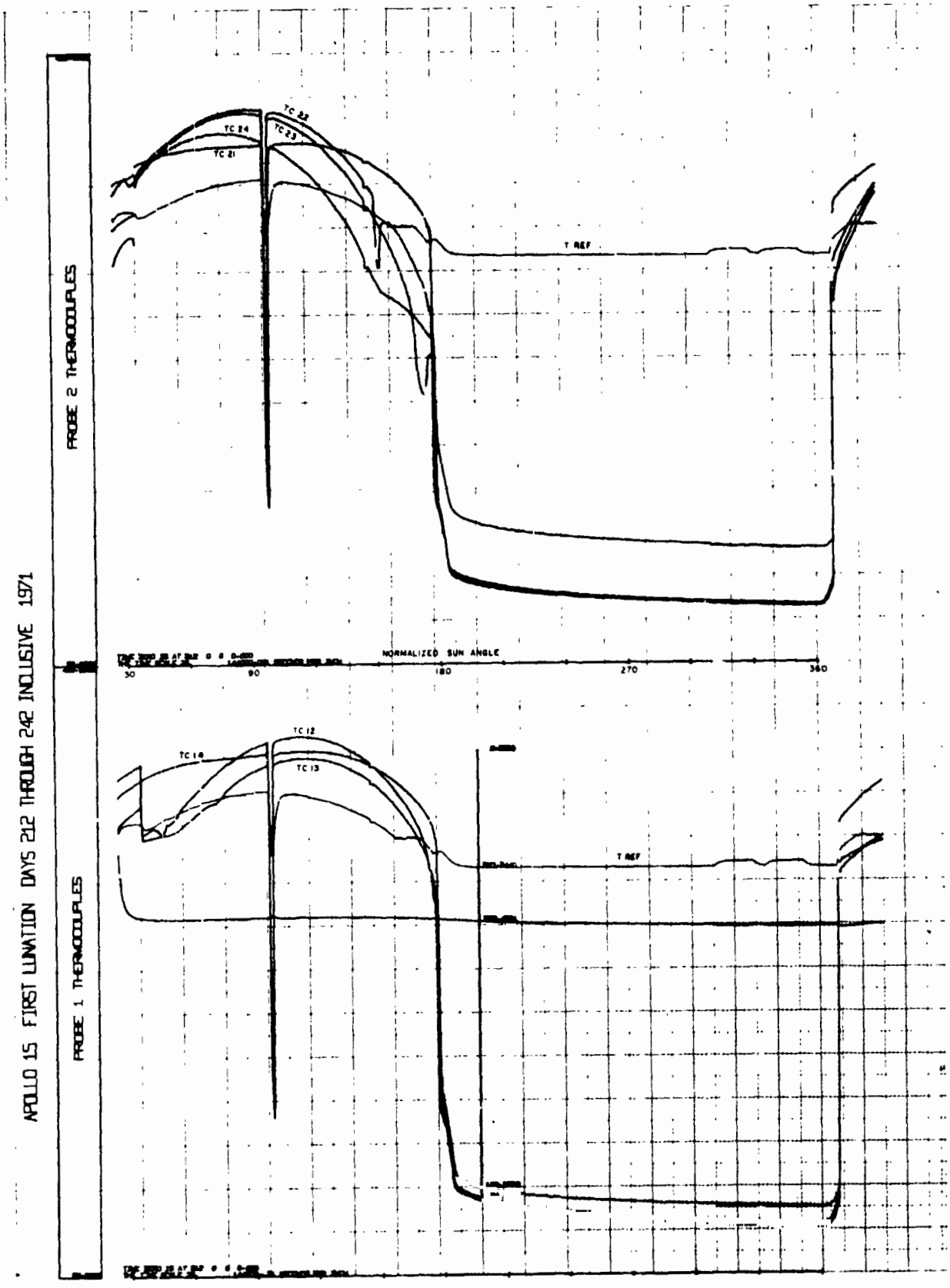

Figure V-B-3

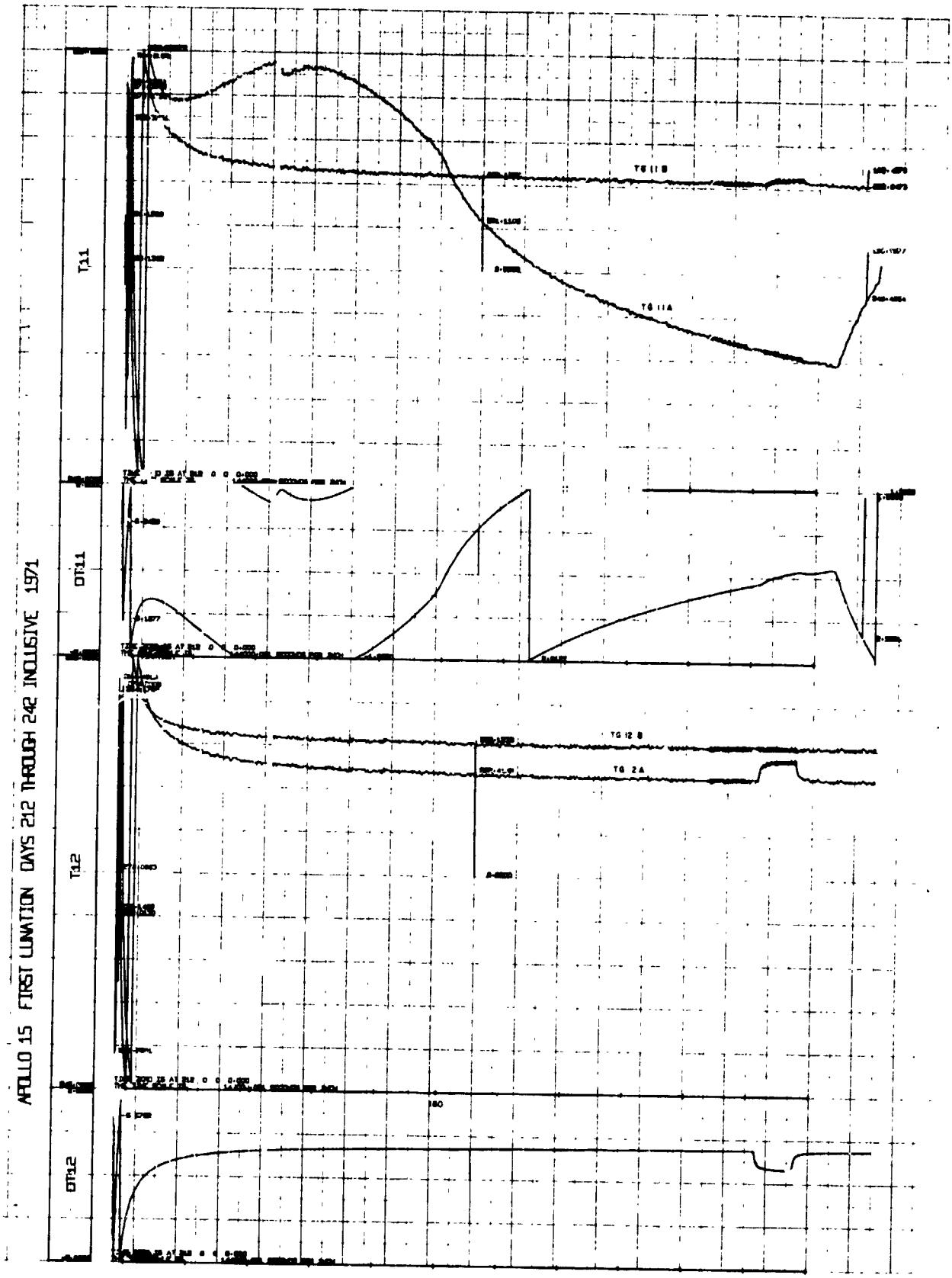
APOLLO 15 FIRST LUNATION DAYS 212 THROUGH 242 INCLUSIVE 1971
T11
DT11
T12
DT12
TG 11 B
TG 11A
TG 12 B
TG 2A
180

Figure V-B-4

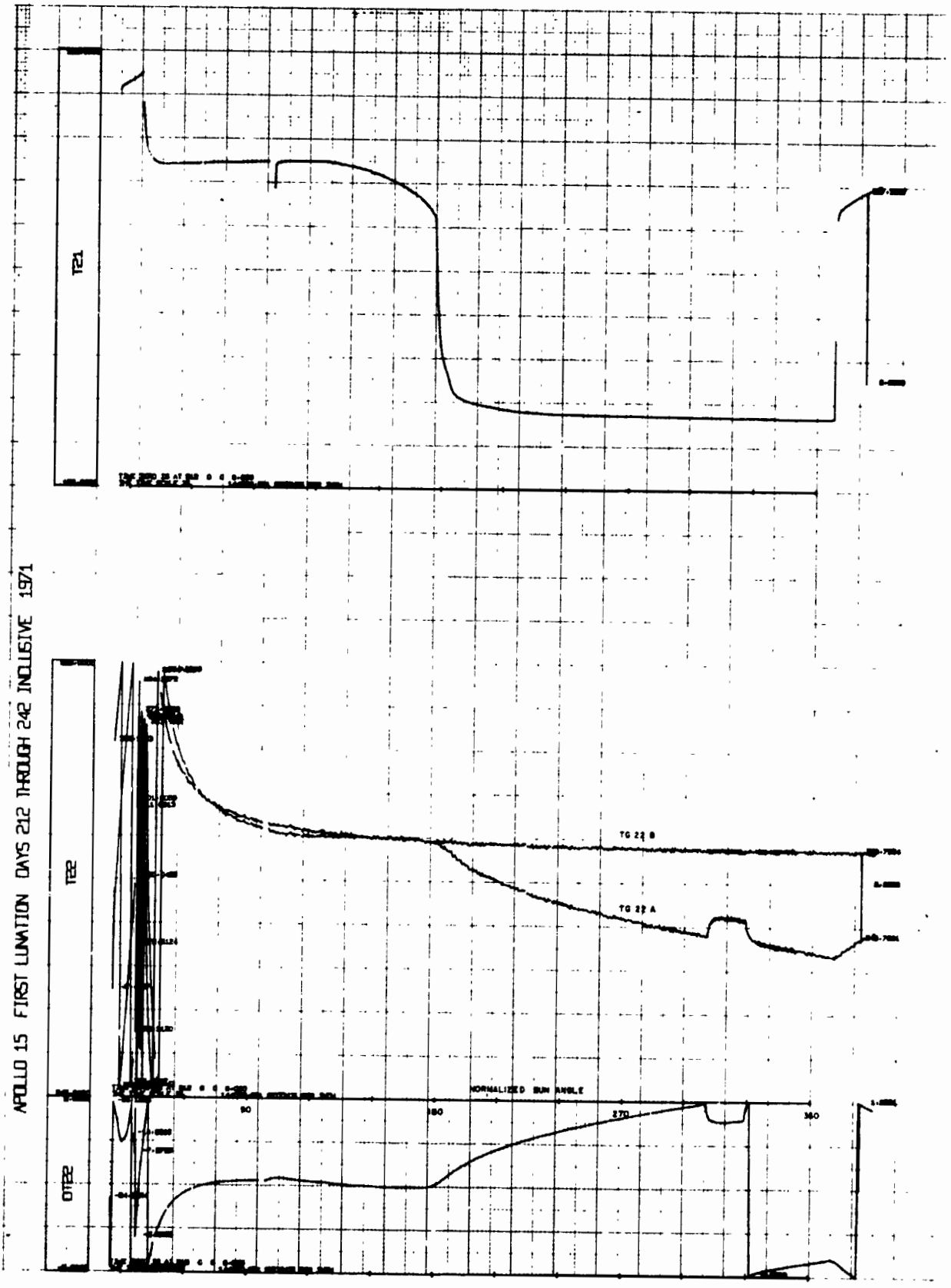
APOLLO 15 FIRST LUNATION DAYS 212 THROUGH 242 INCLUSIVE 1971
TE1
TE2
DTE2
TG 22 B
TG 22 A
NORMALIZED SUN ANGLE
90
180
270
360

Figure V-B-5

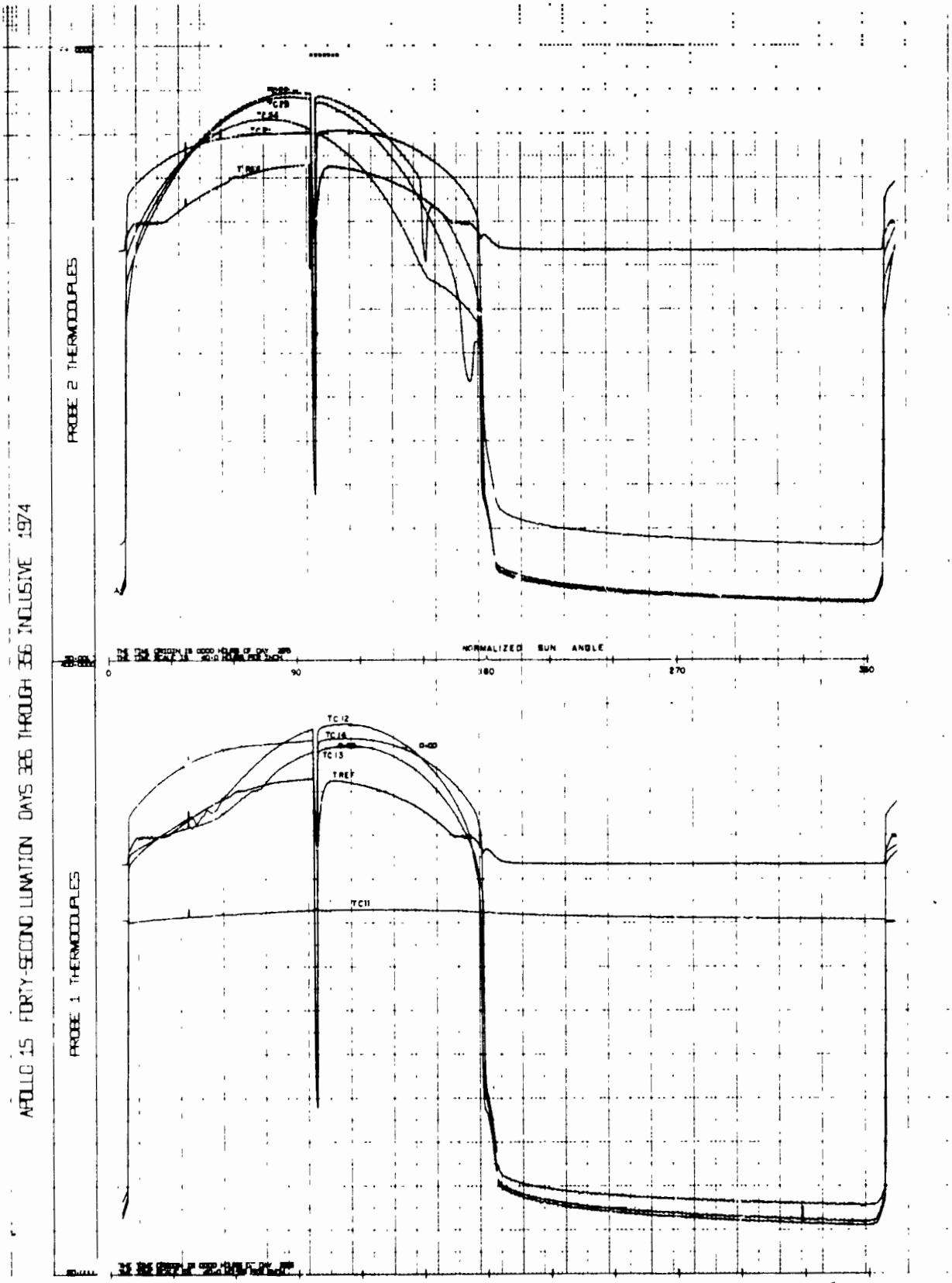
APOLLO 15 FORTY-SECOND LUNATION DAYS 336 THROUGH 356 INCLUSIVE 1974
PROBE 2 THERMOCOUPLES
PROBE 1 THERMOCOUPLES
NORMALIZED SUN ANGLE
0
90
180
270
360
TC12
TC13
TREF
TC11

Figure V-B-6

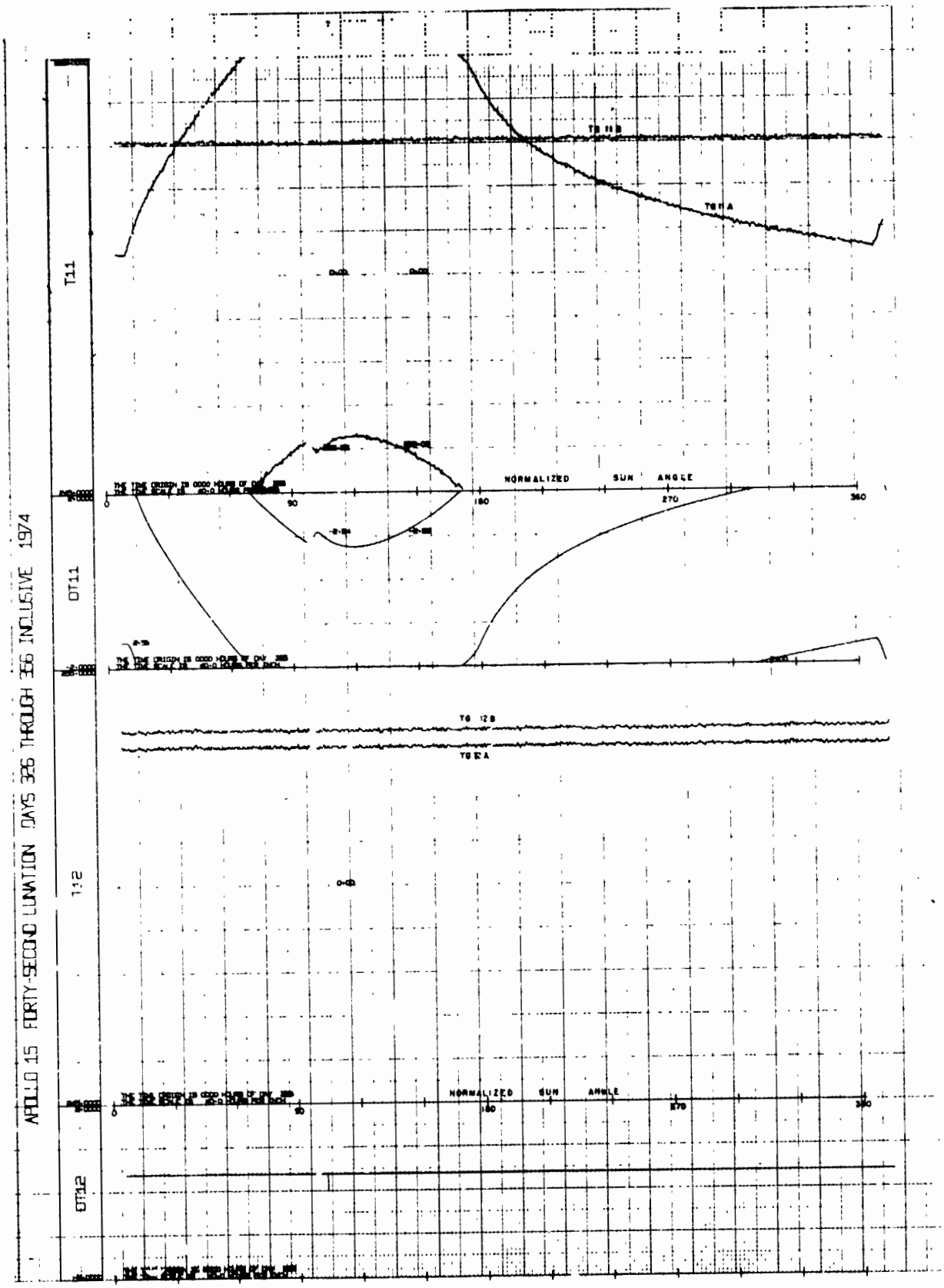
APOLLO 15 FORTY-SECOND LUNATION DAYS 326 THROUGH 356 INCLUSIVE 1974
T11
DT11
T12
DT12
NORMALIZED SUN ANGLE
90
180
270
360
TG 11 B
TG 11 A
TG 12 B
TG 12 A

Figure V-B-7

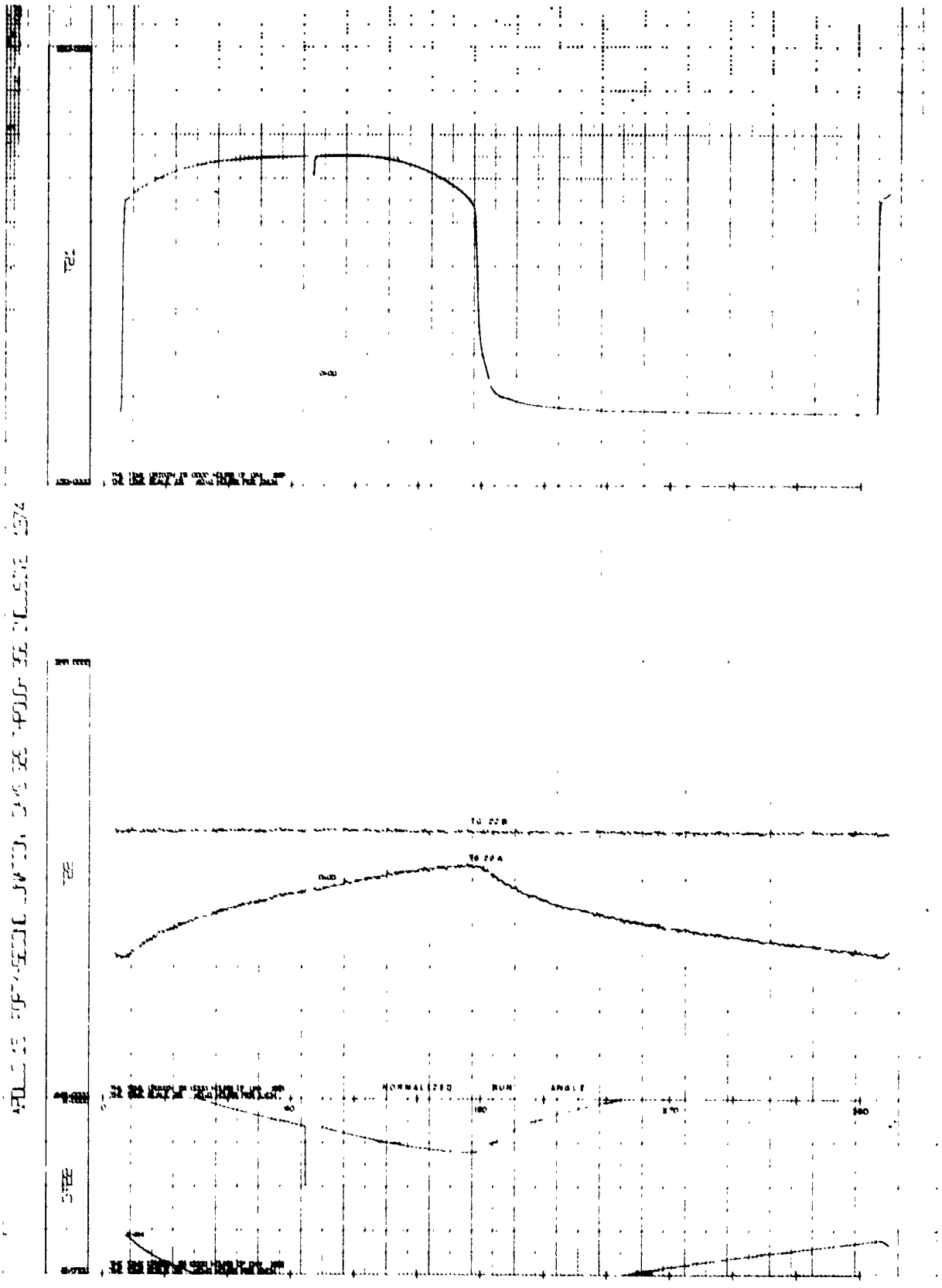

Figure V-B-8

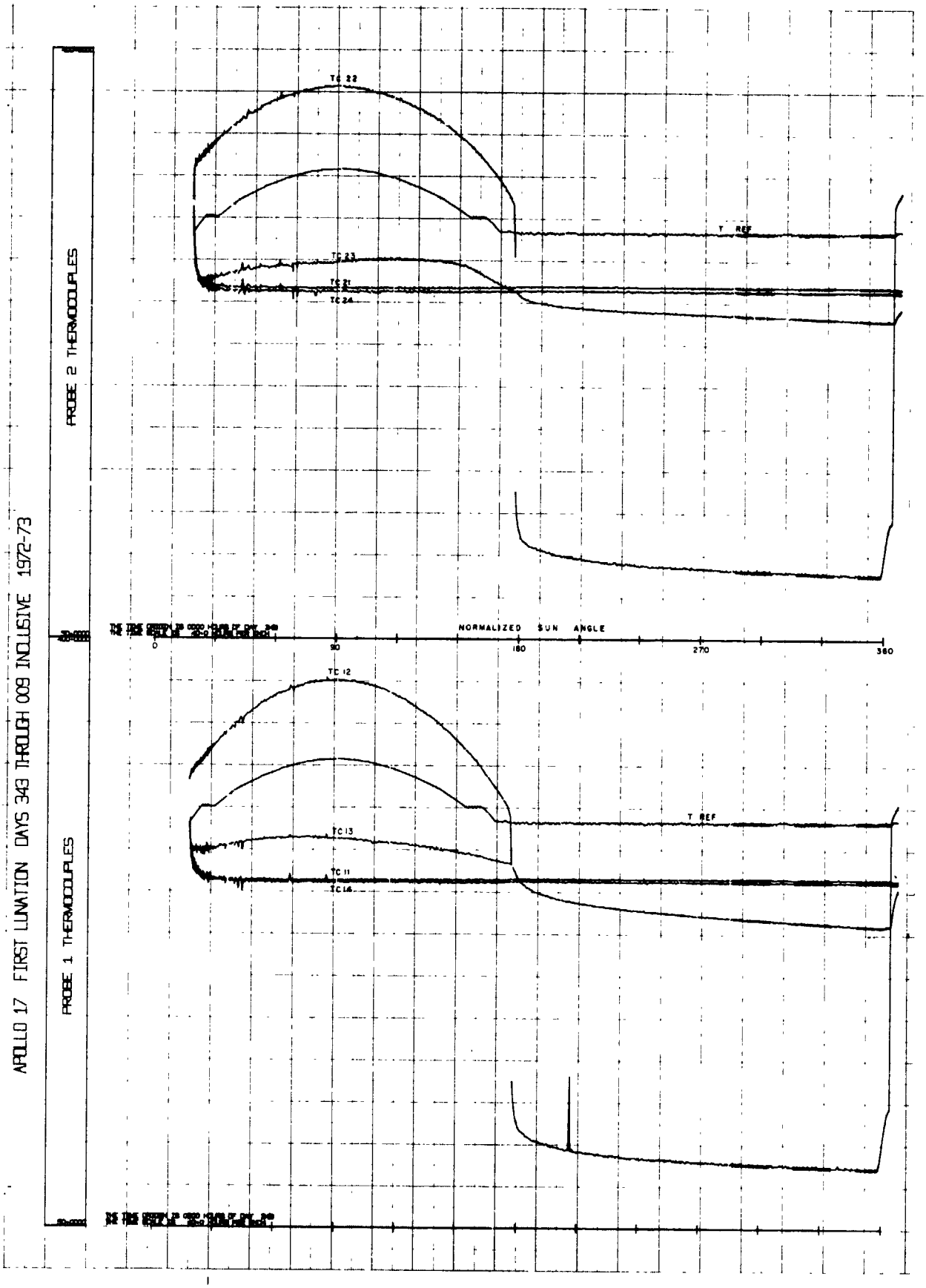
APOLLO 17 FIRST LUNATION DAYS 343 THROUGH 009 INCLUSIVE 1972-73
PROBE 2 THERMOCOUPLES
TC 22
T REF
TC 23
TC 21
TC 24
NORMALIZED SUN ANGLE
0
90
180
270
360
PROBE 1 THERMOCOUPLES
TC 12
T REF
TC 13
TC 11
TC 16

Figure V-B-9

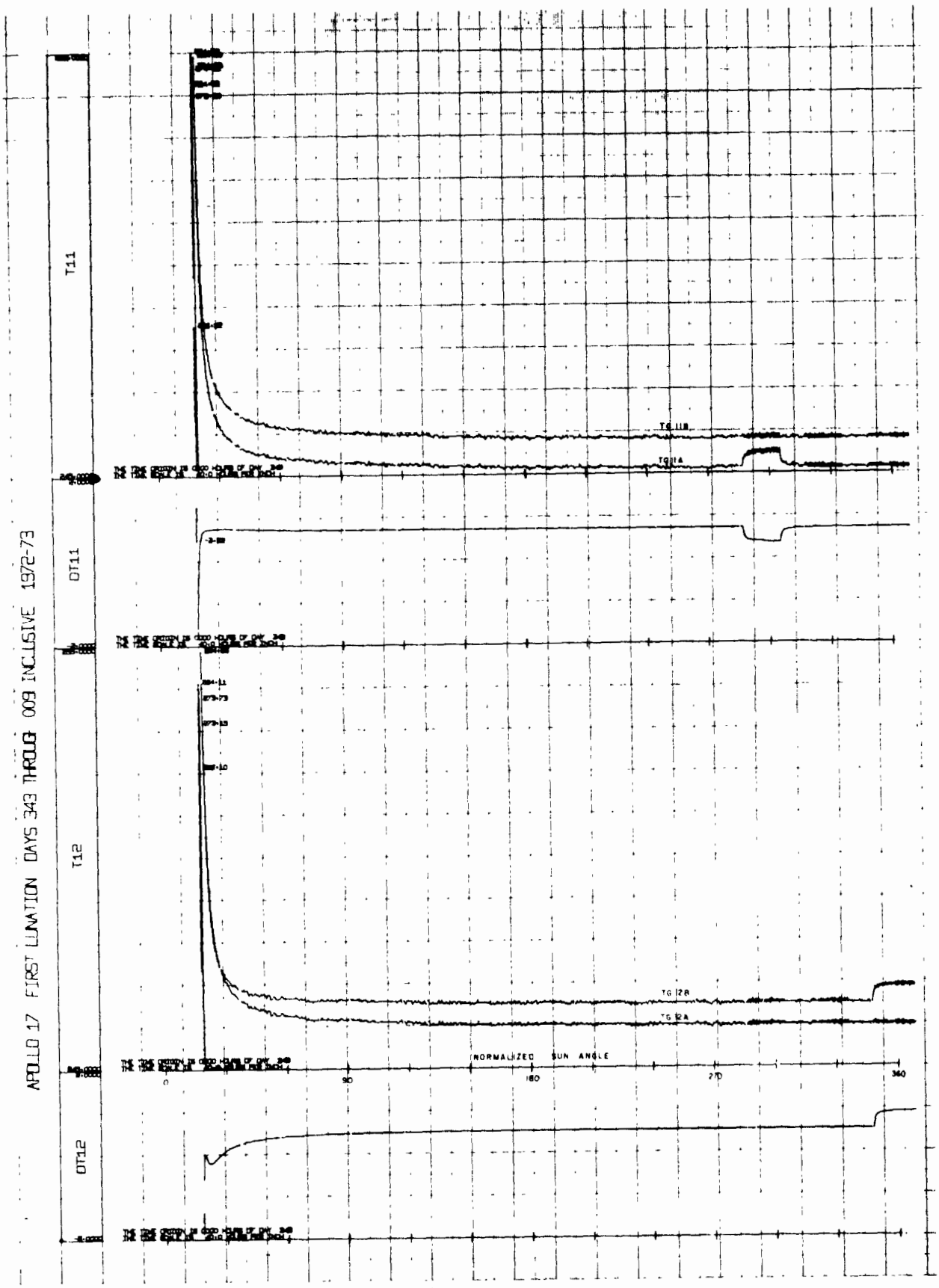
APOLLO 17 FIRST LUNATION DAYS 343 THROUGH 009 INCLUSIVE 1972-73
T11
DT11
T12
DT12
TG 11B
TG 11A
TG 12B
TG 12A
NORMALIZED SUN ANGLE
0
90
180
270
360

Figure V-B-10

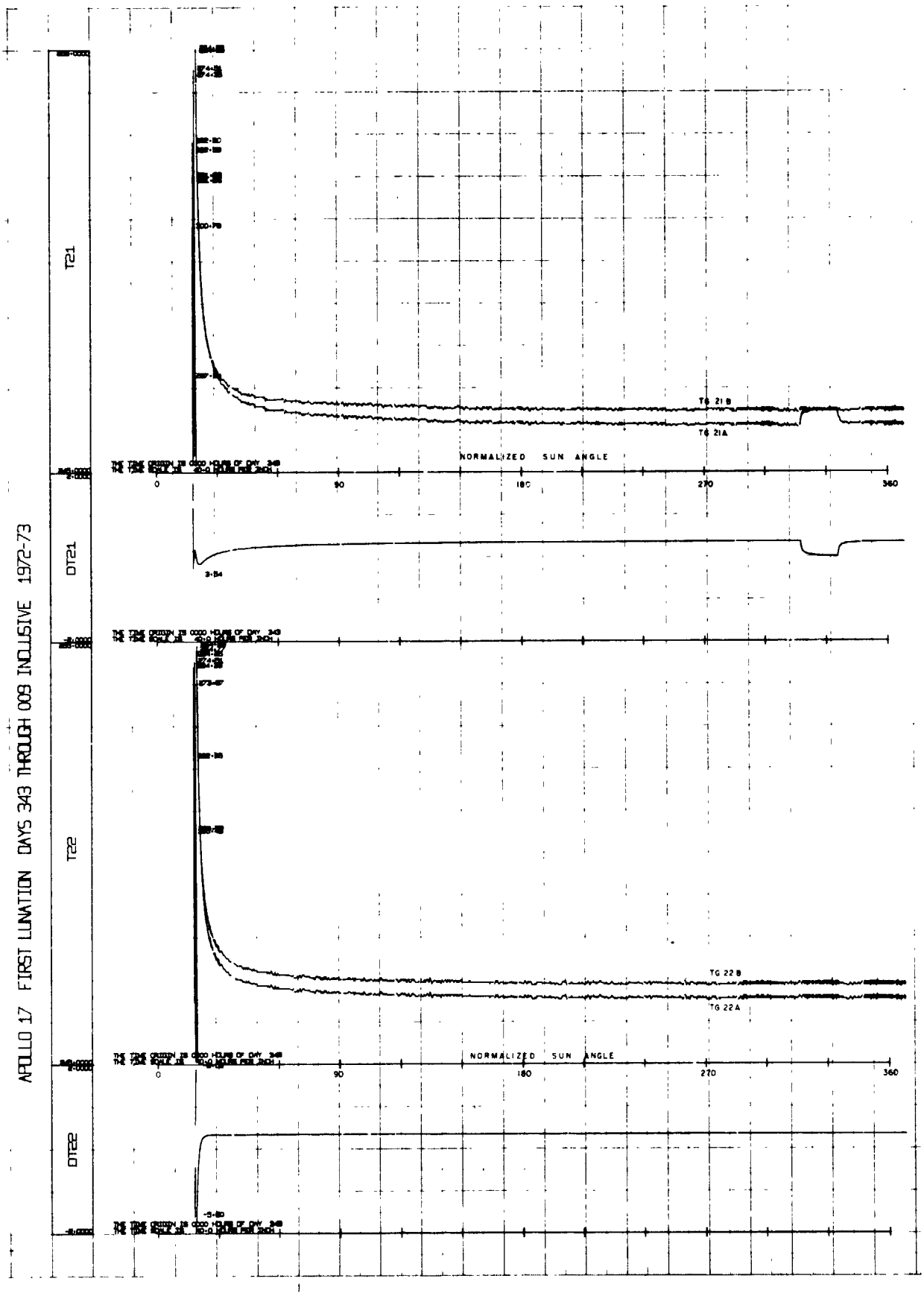

Figure V-B-11

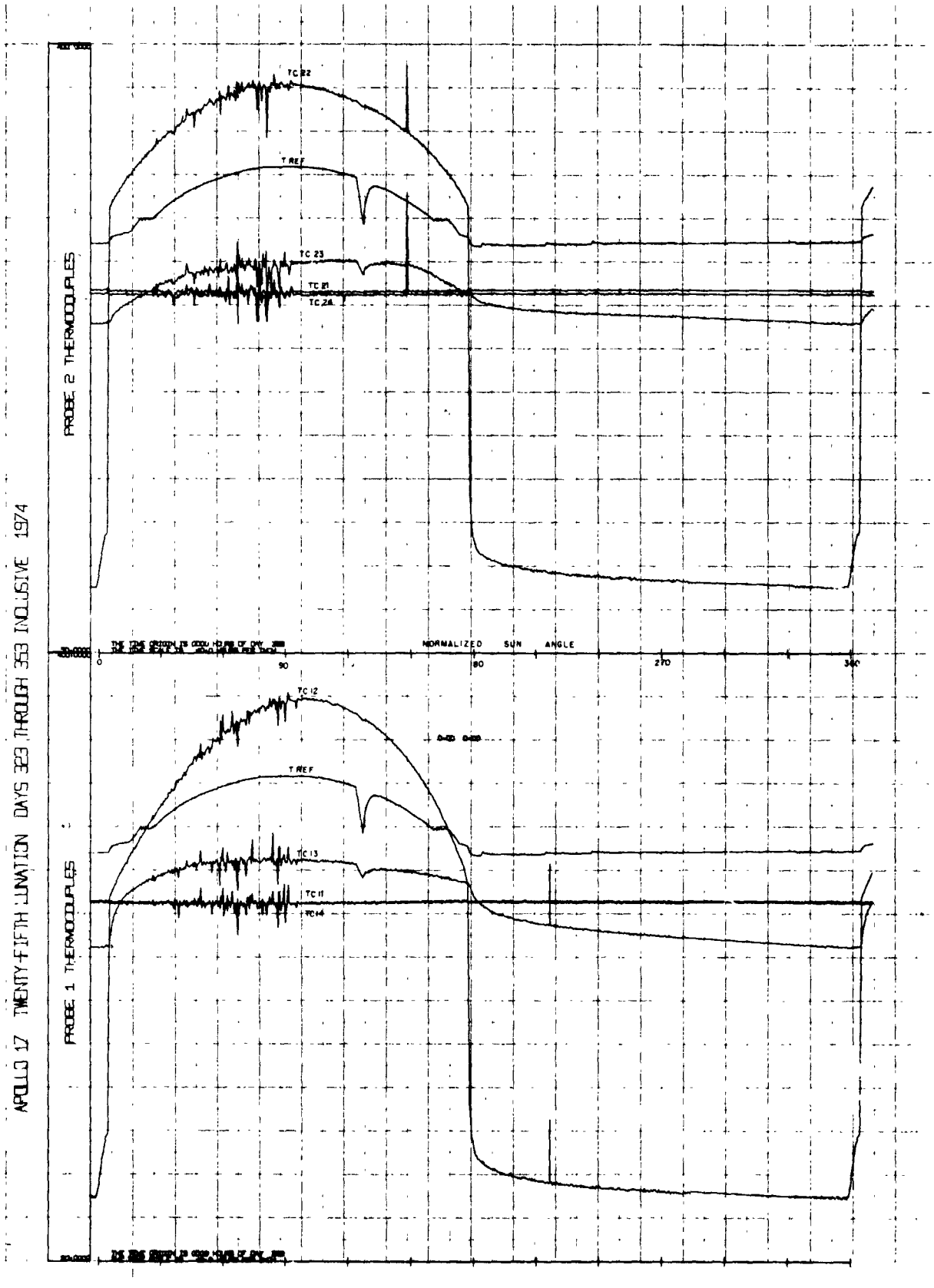
APOLLO 17 TWENTY-FIFTH LUNATION DAYS 323 THROUGH 353 INCLUSIVE 1974
PROBE 2 THERMOCOUPLES
TC 22
T REF
TC 23
TC 21
TC 24
NORMALIZED SUN ANGLE
0
90
180
270
360
PROBE 1 THERMOCOUPLES
TC 12
T REF
TC 13
TC 11
TC 14

Figure V-B-12

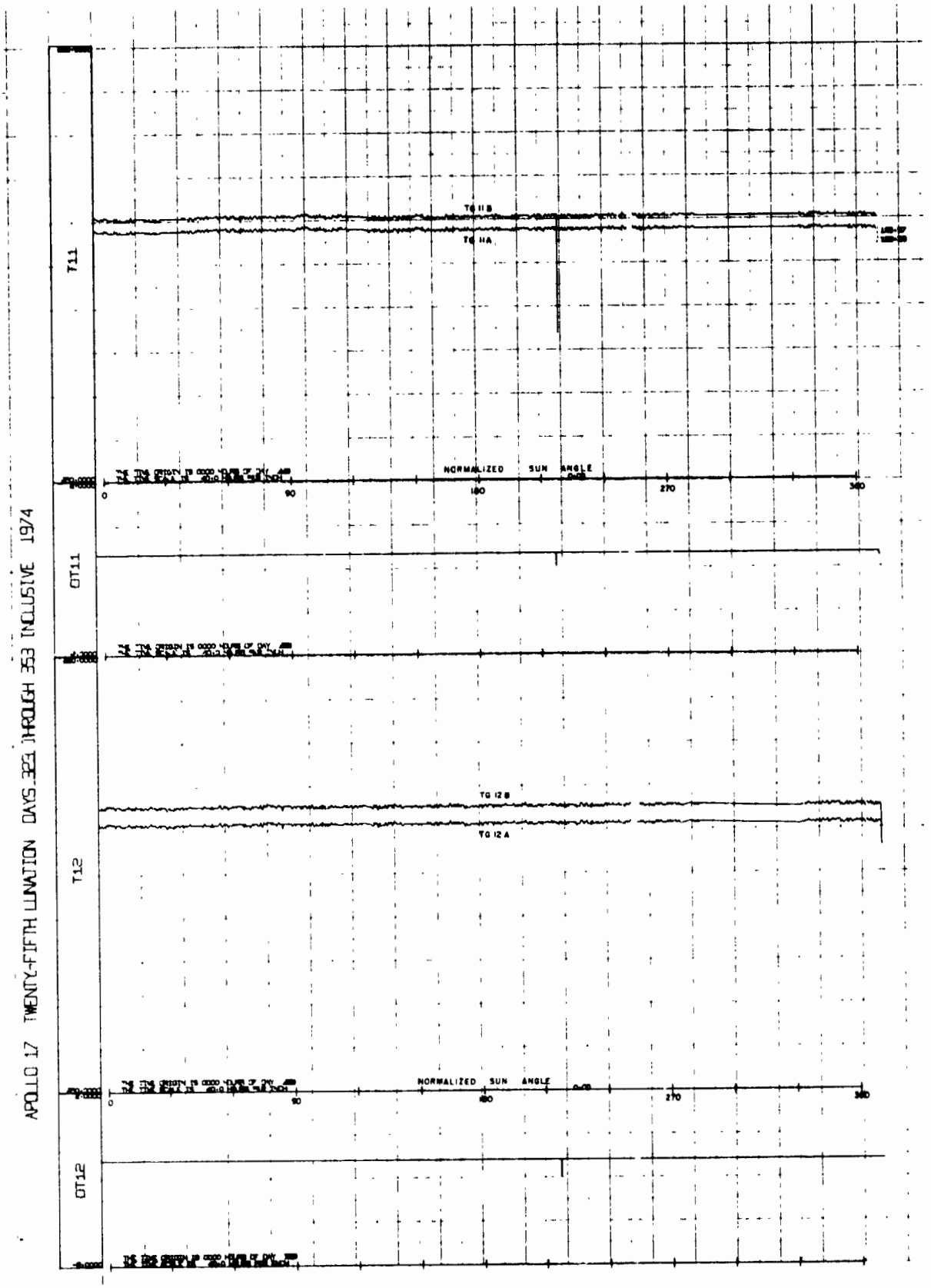
APOLLO 17 TWENTY-FIFTH LUNATION DAYS 323 THROUGH 353 INCLUSIVE 1974
T11
TG 11B
TG 11A
NORMALIZED SUN ANGLE
0
90
180
270
360
DT11
T12
TG 12B
TG 12A
NORMALIZED SUN ANGLE
0
90
180
270
360
DT12

Figure V-B-13

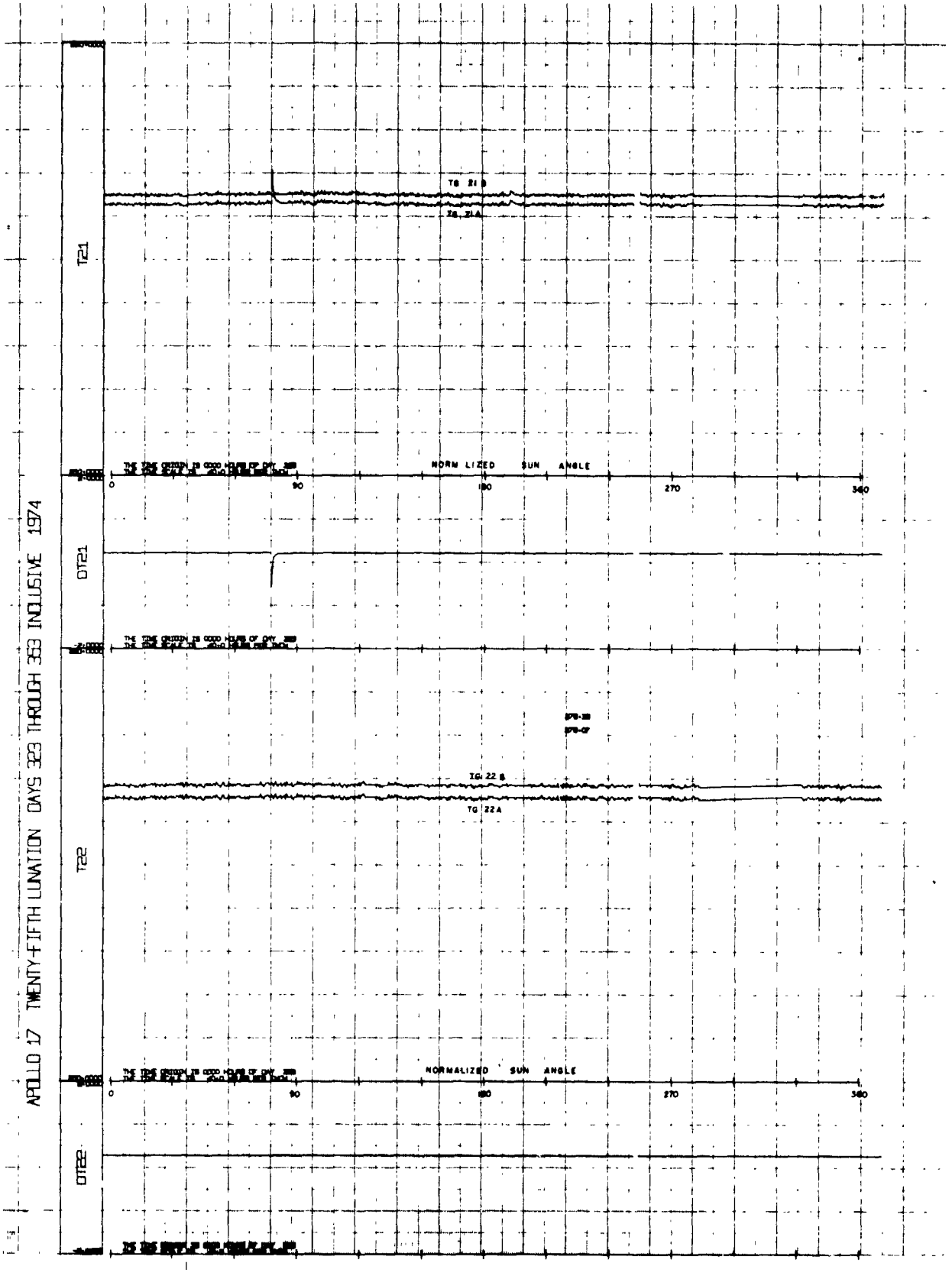
APOLLO 17 TWENTY-FIFTH LUNATION DAYS 323 THROUGH 353 INCLUSIVE 1974
T21
DT21
T22
DT22
TG 21 B
TG 21 A
NORM LIZED SUN ANGLE
TG 22 B
TG 22 A
NORMALIZED SUN ANGLE
0
90
180
270
360

Figure V-B-14

The records from the 42nd lunation at Apollo 15 show that an eclipse also occurred. Notice that many of the small details noted three and a half years earlier are still repeated.

The records from the Apollo 17 probes show quite different temperature variations during a lunation because of the deeper probe depths. Only one thermocouple at each probe, TC12 and TC22, are exposed above the surface. The cables emerging from the top of the borestem were purposely aligned north and south, resulting in a far more symmetrical temperature history during the lunar day.

TC 13 and 23 are buried about 15 cm below the lunar surface (see Figure V-B-1b). A 50°K peak to peak diurnal variation in temperature is observed. This is much greater than would be observed if the periodic surface variation was propagating downward by conduction alone. These sensors have a relatively strong radiative link with the top of the borestem which is further evidenced by the synchronousness of the variations with solar phase. Both temperature records on thermocouples at the 15 cm level are asymmetric relative to solar noon, but each in an opposite sense to the other. The reason for this is not known for certain, but is believed to be related to the different orientations of a reflecting shield placed on top of the borestem.

The thermocouple at 65 cm below the surface records a variation that is barely preceptible at the scale of the plots. In large part this variation is an artifact.

The source of this artifact has been traced to copper/Kovar (Cu/KO) junctions in each thermocouple's electronic circuit, which are mounted on a circuit board in the electronic's housing. The areas of the circuit boards where these junctions are located have variable temperature during a lunation cycle and, consequently, introduce a varying EMF at the input to the data sensing circuitry which is extraneous. This source of error in the thermocouple measuring circuits has been thoroughly analysed and is reported in a Bendix Corporation Aerospace Systems Division Technical Memorandum ASTIR TM30/31 by B.D. Smith. This analysis allows the thermocouple temperature to be corrected so that absolute temperature can be determined to $\pm$ 0.26°K. The data shown in the figures has not been corrected.

Another problem with the Apollo 17 thermocouple observations is seen in the 25th lunation data. A large $\pm$ 15°K noise appears only during the lunar morning, starting after the solar phase reaches 30°. This obviously is a

thermally induced noise but its source has not been ascertained. This noise appeared during the 2nd lunation, and appears at a lower level during the 1st lunation.

The records of subsurface temperatures at Apollo 17 are monotonous compared to the Apollo 15 observations. The initial cooldown is clearly seen during the first lunation; subsequently, the only discernible variation is due to electronically induced noise.

References

Smith, B.D. (1973) Report on the Apollo 17 heat flow experiment thermocouple error investigation. Bendix Aerospace Systems Division Technical Memorandum ASTIR TM 30/31

Langseth, M.G., Jr., S.J. Keihm and J.L. Chute, Jr. (1974) Heat flow experiment; in, Apollo 17 Preliminary Science Report, Section 9, NASA SP-330, U.S. Gov't Pinrt. Off., Wash. D.C., p. 9-1 to 9-24

V-C. THERMAL PROPERTIES OF THE DEEPER REGOLITH

Through fortuity as well as design, measurements of the surrounding regolith thermal properties were provided by analysis of four distinct components of transient temperature histories recorded by the subsurface sensors of the heat-flow experiments. Preliminary estimates were provided within the first sixty days following the experiment emplacement by analysis of the relatively short-term transients produced by probe regolith equilibration and the activation of small probe heaters. Because of the small amount of heat dissipation involved, the early measurements characterized the thermal peoperties of primarily the first few centimeters of material adjacent to each borestem. After two or more years of data were available at each probe site, analysis of long-term temperature variations, characteristic of a much larger volume of surrounding regolith material, were used to refine and revise the early thermal property estimates. The long period transients resulted from annual variations in the solar flux at the lunar surface and reequilibration of the local subsurface thermal regime following astronaut-induced alteration of the thermal and radiative properties of the surface layer.

The present section is devoted to a description of the methods of analysis utilized for the regolith thermal property estimates based on four distinct components of transient temperature variations observed at the heat-flow stations. Particular emphasis is placed on details of the long-term analysis, upon which the final heat-flow values were based. At the end of the section, a comparison and discussion of the different thermal property deductions is presented.

1. Short-term Measurements

a. Initial Probe-Borestem Equilibration

When the borestem was drilled into the soil and the probe inserted, both were at temperatures considerably higher than their subsurface surroundings. The higher temperatures resulted from the temperature of these components above the surface before emplacement and from heat generated during drilling. Because of the complexity of the drilling process, it was difficult to estimate the amount of heat dissipated and the distribution of heat along the borestem.

Measurements made within minutes after the probes were inserted showed that the probes were approximately 40 to 50 °K warmer than the surrounding undisturbed lunar soil. Because of the very low thermal conductivity of the lunar soil, this heat was dissipated very slowly. Even after 45 days, some of the thermometers indicated continued cooling.

In general, the rate of equilibration of each probe sensor to the surrounding lunar medium depends on several different parameters, including thermal and geometrical properties of the probe/borestem system, thermal properties of the adjacent lunar medium, the thermal contact between the borestem and the adjacent zone of disrupted lunar material, and the total heat energy excess of the system upon completion of drilling. For long times (t>20 hr) after the probes were inserted, however, the probe sensor temperatures above equilibrium depended essentially on two quantities, the total initial energy excess per unit length of the system ΔE and the thermal conductivity of the adjacent regolith k_m.

$$T_p(t) - T_\infty = \Delta E/4\pi k_m t \qquad (C\text{-}1)$$

where $T_p(t)$ is a probe sensor temperature at time t since emplacement and T_∞ is the equilibrium sensor temperature.

The form of equation (C-1) has been verified by finite difference models and by analytical solution appropriate to simplified distribution of ΔE between the probe and borestem. The analytical solution, which takes the form of equation (C-1) for long times, is described in detail in the appendix of Langseth et al. (1972).

Estimates of the regolith conductivity k_m made from the long-time cooldown data using equation (C-1) once a value for ΔE was assumed. Because of the uncertainties of the contribution of the drilling process to the total excess heat energy, two different assumptions were made in regard to the ΔE term. First, it was assumed that drill heating effects were negligible and that all excess heat energy initially resided in the probe and borestem. The probe and borestem were assumed to be at the same initial temperature T_o after drilling, as measured by the probe sensors. For this assumption, the initial energy excess can then be expressed simply as

$$\Delta E = \left(S_p + S_b \right) \cdot \left(T_o - T_\infty \right) \qquad (C\text{-}2)$$

where S_p and S_b are the heat capacities per unit length of the probe and borestem, respectively. The resultant problem has an analytical solution that was used to determine regolith conductivity estimates from the cooldown data. These assumptions constituted the minimum initial energy case.

For a maximum initial energy estimate, it was assumed that a 2.2 mm thickness of disrupted lunar material had received enough heat during the drilling process to attain an initial temperature equal to that of the probe and borestem. The 2.2 m contact zone thickness was chosen to correlate with the difference in drill bit radius and borestem radius. The subsequent cooldown problem was then solved, assuming radial heat dissipation, by using a finite difference model. The curve matching procedure was performed for times >20 hr when all parameter effects, with the exception of k_m, were negligible; that is, when equation (C-1) was valid.

The cooling histories for all subsurface sensors that were not affected by diurnal variations were analyzed to estimate the thermal conductivity of the surrounding regolith for the two limiting estimates of initial temperature. Results have been tabulated in Langseth et al., 1972, 1973 and are presented with the other conductivity measurements in Figure V-C-16 of this report.

b. Heater-activated conductivity measurements

Following substantial equilibration of the probe-borestem systems to the surrounding regolith thermal regimes, active conductivity measurements were made using the thousand Ohm heaters that surrounded each of the gradient sensor housings. The experiments could have been operated in either of two modes by energizing the heaters at 0.002 or 0.5 W, depending on the conductivity of the surrounding regolith. Because of the low conductivities inferred from the cooldown analysis only the lower power was used at both heat-flow sites. The discussion is therefore confined to this mode.

After each heater was energized, the temperature rise at the gradient sensor enclosed by the heater depended in a complex way on the thermal properties of nearby probe components, borestem, and lunar material, as well as the contact zones between these elements. A detailed finite difference model of the conductivity experiment at each heater location was used to interpret the temperature history of the gradient sensor in terms of the conductivity of material external to the borestem. Numerical model computations, laboratory experiments, and lunar experiments indicated that, for times >20 hr, the temperature rise $\Delta T(t)$ was well defined by the simple relationship

$$\Delta T(t) = c_1 \ln (t) + c_2 \qquad \text{(C-3)}$$

where c_1 and c_2 are constants. The form of equation (C-3) is the same as that for a heated infinite cylinder in an infinite homogeneous medium after many time constants, indicating that axial gradients at the heater location are quite small and that the principal heat dissipation at long times takes place in the adjacent regolith.

For an infinite cylindrical source

$$c_1 = Q/4\pi k_m \qquad \text{(C-4)}$$

where Q is the power per unit length in W/cm. Thus, c_1 depends solely on the heater power per unit length and on conductivity. The constant c_1 can be determined easily because it is the slope of the temperature rise curve when plotted versus ln t; therefore, cylindrical sources are often used as a practical technique for measuring conductivity.

Conductivity was determined from lunar experiments by comparing observed slopes on a logarithmic time scale with values of c_1 calculated with the finite difference models. Parametric studies, in which certain thermal properties were varied singly in the numerical model, showed that for times >20 hr, c_1 was very nearly insensitive to changes in pc of the surrounding medium, changes in borestem conductance, and changes in the thermal links between the probe and borestem and the borestem and lunar medium. However, c_1 was sensitive to changes in conductance in the probe body, which could alter the flow of heat from the heater axially along the probe. Assumptions of thermal properties in the numerical models that influence axial heat transfer along the probe were probably the largest source of error in the heater activated conductivity determinations.

Active conductivity measurements were carried out at all subsurface gradient sensors free of large diurnal variations within the first sixty days following deployment of each heat-flow station. Heaters were sequentially energized for periods of 36 hours or more and local conductivity estimates were made by matching long-time slopes of the gradient sensor temperature rise with predictions of the finite difference models. Small transients due to incomplete initial cooldown equilibration or slight diurnal effects were accounted for by

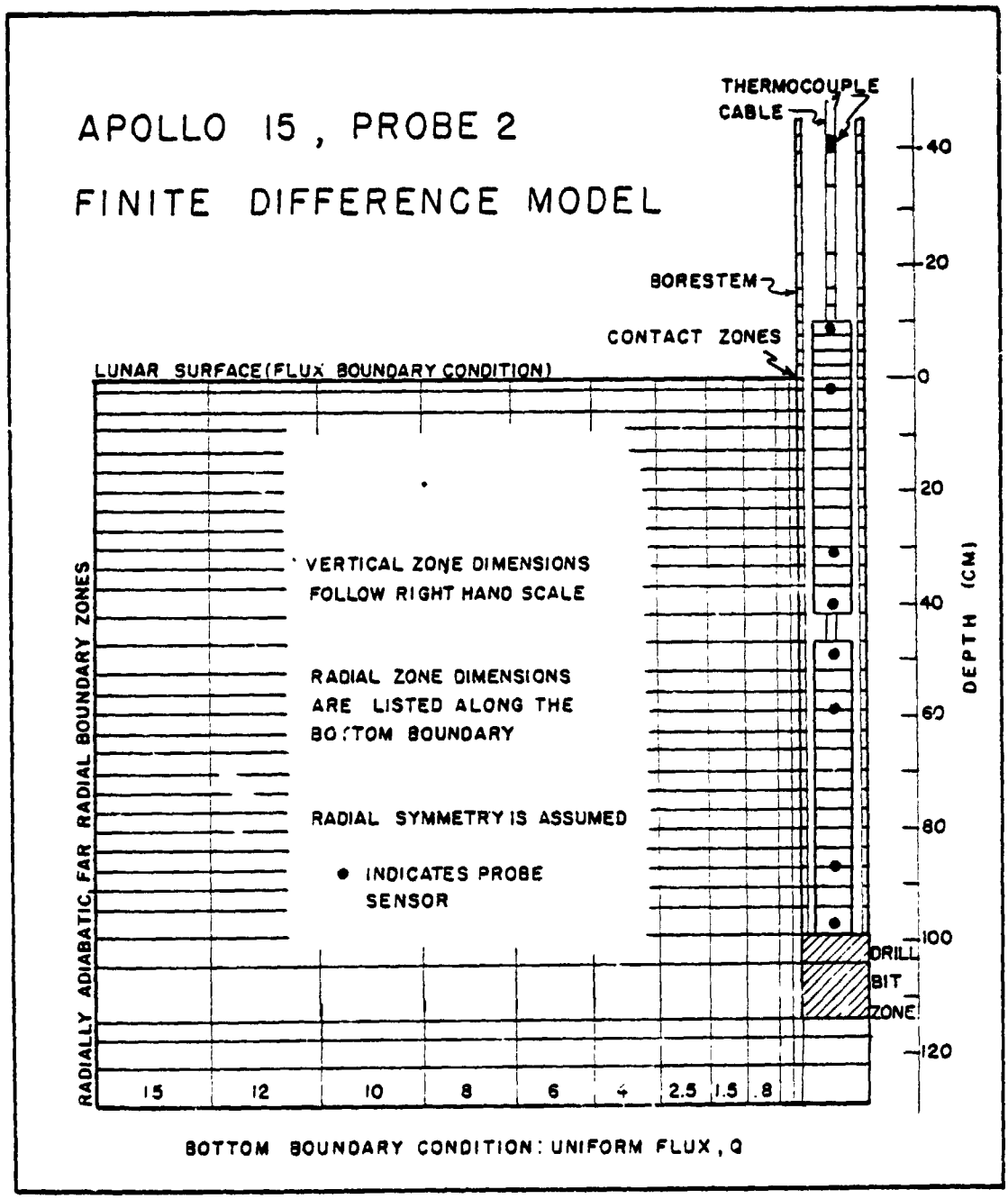

Schematic of Apollo 15 probe 2 numerical model

Figure V-C-1

extrapolation of trends observed immediately prior to heater turn-on. The absolute level of observed temperature rise at a given heater location was utilized to estimate the contact resistance between the borestem and adjacent regolith by comparison with the finite difference models. Examples of the curve matching exercise and subsequent thermal property results can be found in Langseth et al., 1972, 1973. The heater activated conductivity results are included in Figure V-C-16 of this report.

2. Long-Time Temperature History Analysis

a. The Probe-Borestem-Regolith Numerical Model

It became increasingly apparent with the return of temperature data from the Apollo 15 heat-flow probes that the exchange of heat within the probe-borestem regolith system would require careful analysis before much of the data could be utilized. Because of the shallow emplacement of both heat-flow probes only the lower section of probe 1 was deployed deep enough to be free of measurable diurnal variations. The presence of significant higher frequencies and the absence of a discernible phase lag, which characterized the probe diurnal variations, implied the importance of radiative transfer along the probe-borestem axis (significant annual temperature variations were observed at all sensors. In addition, thermocouple measurements within the borestem section protruding above the surface indicated that the diurnal variation at the top of the borestem differed significantly from the lunar surface diurnal response in amplitude, frequency composition and average temperature over one lunation. Thus, to interpret the time varying data in terms of regolith thermal properties and the steady-state regolith gradient, detailed numerical models of both the probe 1 and probe 2 in situ geometries were developed, including both conductive and radiative heat exchange. A schematic of the probe 2 model is shown in Figure V-C-1. Vertical dimensions are to scale. Radial dimensions are indicated along the bottom boundary. Radial symmetry is assumed. Within the regolith thermal properties are modeled as both temperature and depth dependent. Lateral variation of properties is limited to the contact zone adjacent to the borestem. A fixed finite value of conductivity is used to evaluate conductive exchange vertically along the borestem walls. Distinct conductivities are assigned to each of the probe nodes for evaluation of axial conductive exchange. The variation of conductivity along the probe depends on the number of electrical

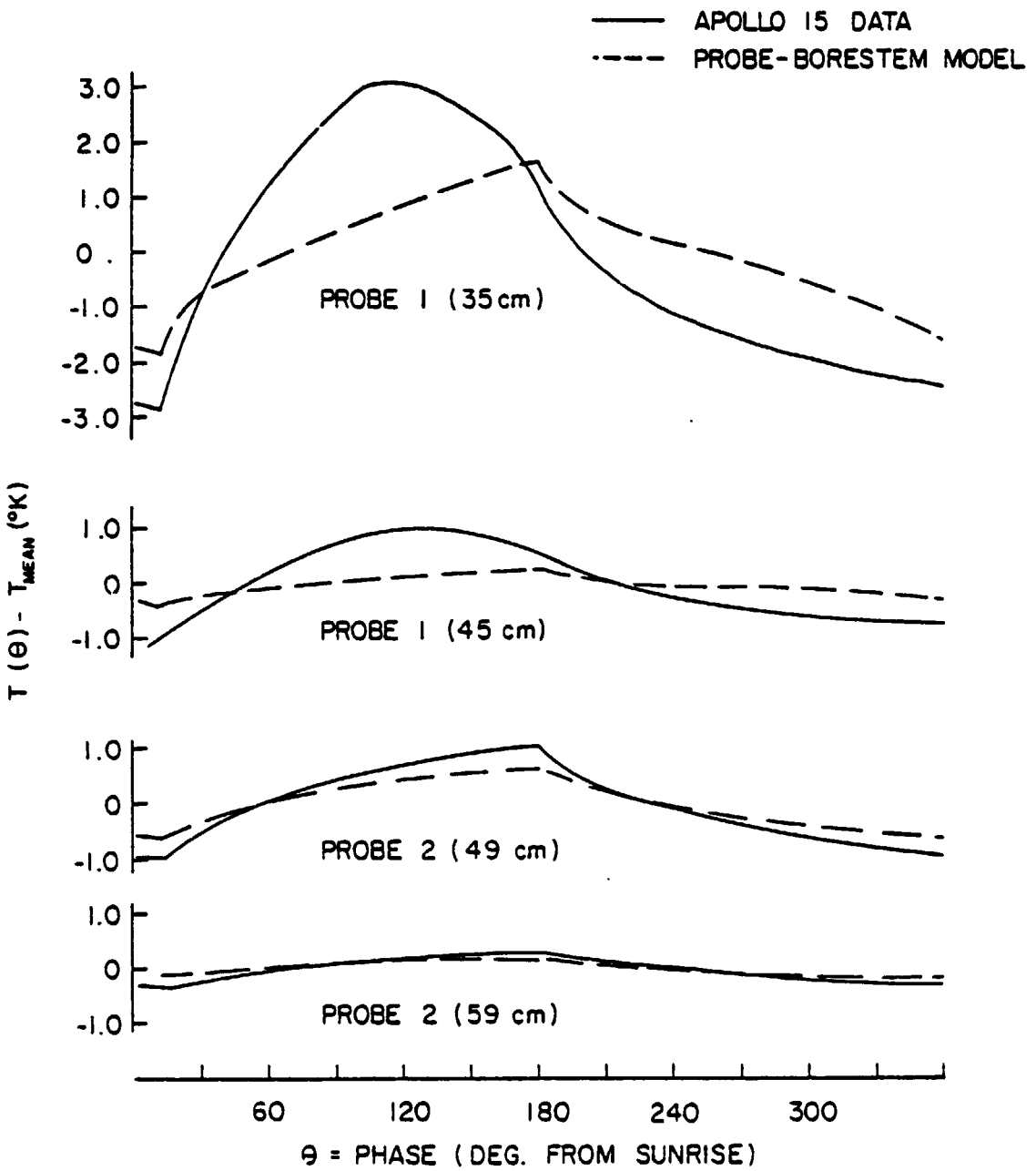

Comparison of diurnal variations observed in the Apollo 15 subsurface data and produced by the numerical models at comparable sensor depths.

Figure V-C-2

connections within a particular probe zone. The zones corresponding to the large platinum resistance thermometer locations, at either end of each probe section, are nearly ten times as conductive as other probe zones. Heat capacitance variation is accounted for in a similar way.

Blackbody radiative exchange takes place at the surfaces of all borestem, probe and cable zones. View factors between all radiating zones are calculated based on the formulas found in Hottel and Sarofim (1967) for concentric cylinders. The surface boundary condition balances the outgoing flux, solar insolation and the temperature gradient at the surface. A similar flux balance equation governs the heat balance of the exposed borestem zones. At the bottom boundary, 15 cm below the deepest drill bit penetration, a constant heat flux is assumed. At the far radial boundary, lateral heat flux is set to zero.

The computation scheme utilizes forward difference equations which essentially assume a steady flux across each node boundary over the time step of about 100 sec. The general formulation of the difference equation is outlined in Appendix A. Temperature dependent thermal properties are recomputed after each time step. Initial conditions were established by running one dimensional regolith models with the same vertical zone sizes, thermal properties and solar insolation function as the complete model until a periodic steady state solution was achieved. In this way, predeployment regolith temperatures were established. The regolith thermal property profile used was based on the preliminary in situ conductivity measurements and near surface (0-15 cm) conductivity deductions inferred from the measured temperature histories (see Langseth et al., 1972; Keihm et al., 1973). Temperature dependence of regolith conductivity was derived from the measured mean temperature difference between the surface and the shallowest probe sensor at 35 cm. The density profile was based primarily on the core tube measurements of Carrier et al. (1973). Specific heat variation with temperature was modelled as a polynomial fit to the data of Robie et al. (1970). It is to be emphasized that the principal objective of the two dimensional models was an attempt to understand the complex thermal interaction of the probe-borestem system and surrounding regolith and subsequently to interpret sensor temperature variations with time and depth in terms of the regolith variations and thermal properties. For this reason, uncertainties in the choice of regolith thermal properties were of secondary importance. The

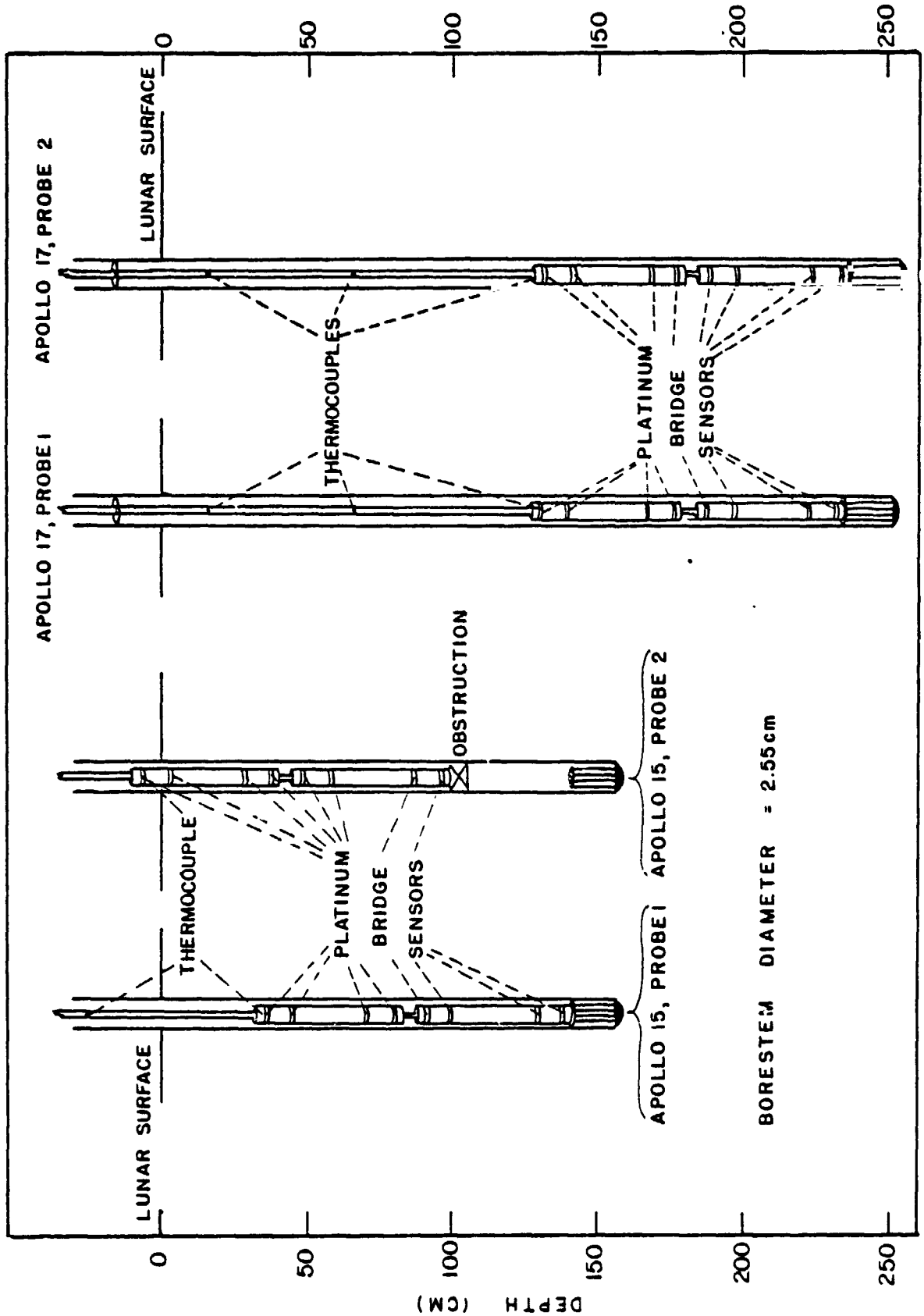

Schematic of final probe emplacement geometries at the Apollo 15 and 17 heat-flow sites

Figure V-C-3

primary question was to what extent did the probe-borestem thermal linkages modify the temperature regime which it was designed to measure.

The first models runs were carried through three lunations with no annual component present in the solar insolation function. The purpose of these initial runs were twofold: first, to test the model's capability of reproducing the diurnal characteristics of the real time data, and, second, to examine the feasibility of interpreting the diurnal variations and time averages of the actual data in terms of regolith thermal properties and gradients. Comparisons with the lunar data containing significant diurnal variations is shown in Figure V-C-2. Note the difference in shape between the probe 1 and probe 2 lunar data. The modelling results simulate the high frequency content of the probe 2 data but do not compare well with the smoother, more surface-like response of the probe 1 data (Differences in amplitude between the modeling results and the lunar data indicate that our original choice of regolith thermal properties based on active conductivity experiments required adjustment. However, the matching of diurnal amplitudes observed at various depths along the probe by varying the regolith conductivity is neither a straightforward nor unambiguous process. In fact, it will be shown in the next section that the regolith conductivity must be lowered to raise the model's diurnal amplitudes to the level observed at depth. This result agrees with the later analysis of the long-term data.) The probe 1 and 2 geometries differed only in depth of probe emplacement and in the presence of a disk shaped radiation shield made of reflective material above probe 1 within the borehole (Figure V-C-3). Both of these differences have been accounted for in the probe 1 and 2 models, yet the thermal model of the probe 1 response is essentially similar to that at probe 2. Various model parameters were adjusted in an attempt to reproduce the shape of the probe 1 diurnal data. These included varying the reflectivity of the radiation shield, the borestem-regolith contact resistance and the borestem and regolith conductivity. Yet, the shape of the modelled diurnal response remained essentially unchanged - a steady rise in temperature from sunrise throughout the lunar day with a sharp transition to cooling immediately after sunset. The lack of a significant morning phase lag and the absence of afternoon cooling indicate that the probe sensors are responding primarily to diurnal pulse propagation down the probe-borestem hole rather than the diurnal response of the adjacent regolith. In large measure this

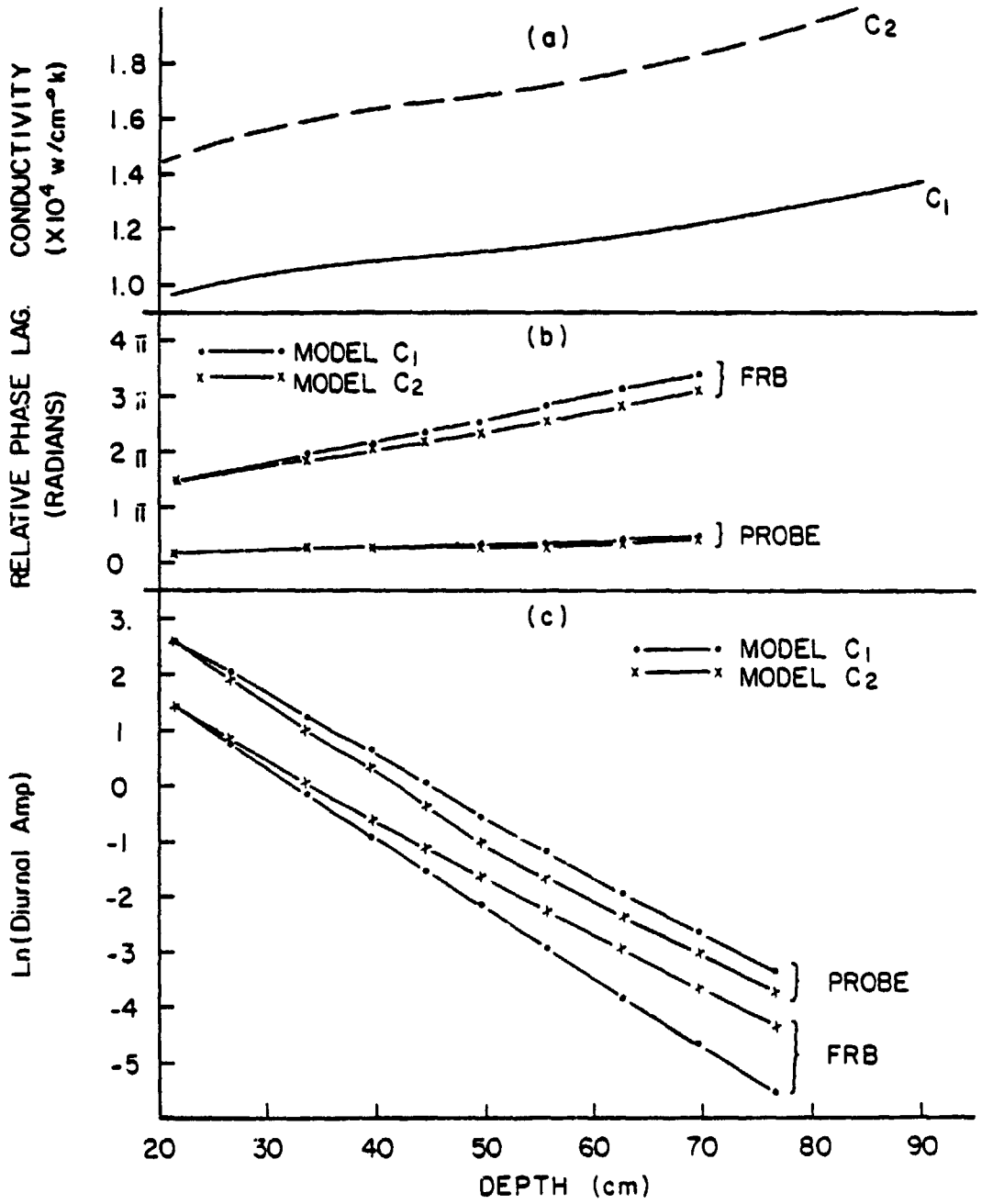

Comparison of diurnal phase lags and amplitudes for undisturbed regolith (FRB) and probe sensors using two different regolith conductivity profiles in the Apollo 15 probe numerical model.

Figure V-C-4

heat transfer is by radiation along the tube. Unlike the lunar surface, the protruding borestem maintains a nearly constant high temperature during the lunar day due to the orthogonality of the borestem-lunar surface orientation. Daytime flux into the protruding borestem derives both from direct solar heating and radiation from the lunar surface. The solar contribution maximizes near sunrise and sunset while the heat emitted by the surface peaks near noon. The summing of these effects results in the approximate constancy of daytime protruding borestem temperatures, which serve as a hot source for the axial pumping of heat downward during the day. Radiative transfer explains the nearly immediate response of the probe sensors at sunrise. Both radiation and borestem wall conduction subsequently deliver heat to the probe sensors from the protruding borestem 'reservoir' throughout the lunar day; at sunset, the borestem cools almost immediately as the opposite process takes place.

The question remains as to why the probe 1 sensor's diurnal response more closely resembles the regolith diurnal variation than the probe 2 data or the modelling results for either probe. One feasible explanation is that the reflective plate which caps each borestem appears from photographs to be somewhat tilted up at the probe 1 site, possibly resulting in radiation from the lunar surface being reflected directly into the probe 1 borehole. This could explain the early afternoon peaking of probe 1 sensor temperatures since they would be more directly coupled with actual surface temperature variations than the probe 2 sensors or either model.

b. Probe-Regolith Coupling: Diurnal Variations

It is apparent from the data shown in Figure V-C-2 that the axial thermal linkages of the probe-borestem system contribute to the character of the probe sensors' diurnal variations. To assess the effects of regolith thermal properties on the probe response, models were run with different regolith thermal properties for three lunations each. Although this is not normally enough time for a periodic steady-state solution to be obtained, it is sufficient to estimate the effects of regolith properties on probe diurnal response. Results are shown in Figure V-C-4. For each of the two models shown, the diurnal temperature variations of all probe and far radial boundary (undisturbed) regolith nodes were Fourier analyzed, using the second and third lunations of the three lunation computer runs, to yield the amplitude and relative phase lag of the diurnal components. Models C1 and C2 differed only in regolith thermal

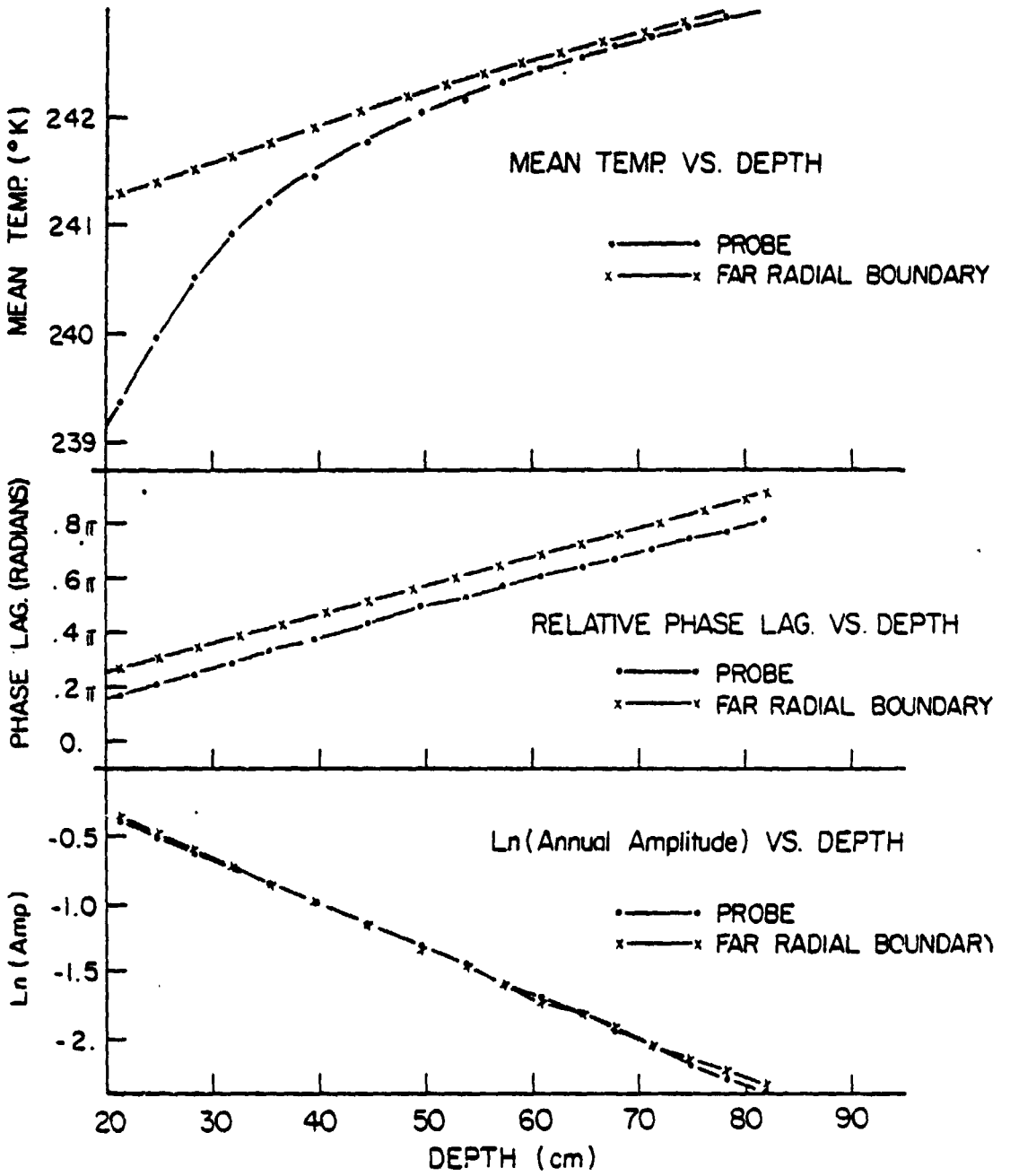

Comparison of mean temperature, annual phase lag and annual amplitude between undisturbed regolith (FRB) and probe as computed from 2.2 year run of the Apollo 15 probe 2 numerical model.

Figure V-C-5

conductivity below 20 cm: $K_2(x) = 1.5\ K_1(x)$ for $x > 20$ (Figure V-C-4a). Note in Figure V-C-4b the suppression of the diurnal phase lag with depth as sensed by the probe. This results directly from the radiative coupling of the subsurface probe and the above-surface borestem section. The increased conductivity model does suppress the phase lag even further; however, the resolution of average regolith conductivity based on the probe phase lag data is much less than that implied by the undisturbed regolith zones.

Figure V-C-4c illustrates most clearly the importance of the probe-borestem thermal linkages in determining the probe's diurnal response. At the lunation frequency, the regolith acts primarily as a medium into which the diurnal wave disperses by conduction effectively lowering the probe diurnal response for higher regolith conductivity. Thus, we see that the diurnal amplitude response of regolith and probe are essentially negatively coupled in that a higher regolith conductivity results in larger diurnal variations within the regolith (lower attenuation) but reduced variations within the probe (higher attenuation). This effect dominates at all depths below 20 cm, but quantitatively depends in a complex manner on the amplitude and phase correlation between the probe and regolith variations at a given depth. For these reasons, the utilization of probe diurnal variations as an accurate means to estimate regolith thermal properties had to be abandoned.

c. Probe-Regolith Coupling: Annual Variations in Mean Temperature Profile.

Previous models, both analytic and numerical, had been utilized to examine the effect of the relatively high conducting probe-borestem system upon the local regolith steady-state gradient. It was found that for depths at which diurnal variations were negligible, the gradient as measured by the probe differed from the undisturbed local regolith value by less than 5%. However, the shallow emplacement at the Apollo 15 site did result in significant diurnal variations at four of the working probe sensors and the question of how reliably the time average probe temperature profiles reflected the regolith gradient required investigation. Of prime importance was the effect of the mean temperature difference between the lunar surface and the protruding borestem section and the resultant equilibrium thermal regime in the subsurface.

In addition to the shallow sensor diurnal components, annual temperature variations were detected in the long-term data at all but the deepest probe 1

sensors. Once again, correlation between regolith annual variations and thermal properties demanded investigation. To examine the correlation of both the shallow sensor mean temperature gradient and the measured annual variations with the comparable temperature components in the undisturbed regolith, the probe 2 numerical model was run with the nominal thermal property profile for a simulated period of 2.2 years. The run of over 27 lunations was required to achieve a satisfactory periodic steady-state solution for the probe-borestem-regolith thermal regime and to allow an accurate Fourier analysis to obtain the annual components. Diurnal and annual components were identified using the same finite Fourier transform technique as was employed for the actual lunar data. Both probe nodes and far radial boundary nodes (undisturbed by the probe presence) were analyzed. Probe and regolith comparison of mean temperatures, phase lag, and annual amplitude profiles are shown in Figure V-C-5. The large offset in mean temperature (Figure V-C-5a) at depths less than 50 cm results directly from the mean temperature difference between the protruding borestem and the lunar surface. Only at depths below significant diurnal variations ($\leq 0.05°K$) does the regolith temperature regime totally constrain the probe gradient. Sensors in the region of significant diurnal variation can be corrected using the probe models. These corrections have been applied to both the probe 1 and probe 2 shallow sensor data based on the results shown in Figure V-C-5a.

Figures V-C-5 b and c illustrate the excellent probe-regolith coupling for the long period annual component upon which the subsequent revision of regolith thermal conductivity and heat flow was based. The nearly constant offset in phase between the probe and undisturbed regolith is established close to the surface and does not affect the subsurface conductivity deductions which are constrained only by the rate of phase change with depth. The probe and regolith annual amplitude components can be considered virtually identical at all depths if allowances are made for the uncertainties present in the Fourier transform analysis. These results, when compared with the near absence of , or negative probe-regolith coupling, for diurnal variations shown in Figure V-C-4a are indicative of the frequency dependence of the probe-regolith coupling for periodic temperature variations. At frequencies as high as the diurnal, axial heat transfer by radiation and probe-borestem conduction is a primary factor in controlling the subsurface probe response.

The high frequency of the lunation cycle mitigates the effect of temperature variations within the adjacent regolith which are thermally coupled to the probe-borestem system only by the highly insulating lunar soil. Annual variations, on the other hand, are of such low frequency that at any given time during the year, a near equilibrium thermal regime is established in which the probe temperatures are almost totally constrained by the adjacent regolith temperatures. These modelling results provided the basis for a reevaluation of the regolith thermal conductivity from the Apollo 15 and 17 annual wave data.

Formulation of the Finite-Difference Scheme for the Probe-Borestem-Regolith Numerical Model

The computational scheme utilized assumes that all thermal properties and node temperatures remain constant over one time step. The temperature change at any given node over the time step is then simply the total heat flux across all node boundary surfaces multiplied by the time step and divided by the heat capacity of the node.

$$\Delta T_i = \frac{\Delta t}{V_i \rho_i C_i} \cdot \sum_{j=1}^{N_i} F_{ij} \tag{1A}$$

where Δt is the time step.

V_i, ρ_i, C_i are the volume, density and heat capacity of node i, and F_{ij} is the flux into node i across its jth boundary, summed over each of its N_i boundaries.

In the cylindrical coordinate system, for an interior node with no free surface boundaries, Equation 1A can be expressed as:

$$\Delta T_{i,j} = \frac{\Delta t}{(V\rho C)_{i,j}} \cdot \left[\frac{T_{i-1,j} - T_{i,j}}{(RR)_{i-1,j}} + \frac{T_{i+1,j} - T_{i,j}}{(RR)_{i,j}} + \frac{T_{i,j-1} - T_{i,j}}{(RV)_{i,j-1}} + \frac{T_{i,j+1} - T_{i,j}}{(RV)_{i,j}} \right] \tag{2A}$$

where $(RR)_{i,j}$ is the thermal resistance in the radial direction between node centers i,j and i + 1,j and $(RV)_{i,j}$ is the thermal resistance in the vertical direction between node centers i,j and i,j +1.

The thermal resistances can be calculated from the node geometry under the assumption of constant flux over the duration of the time step.

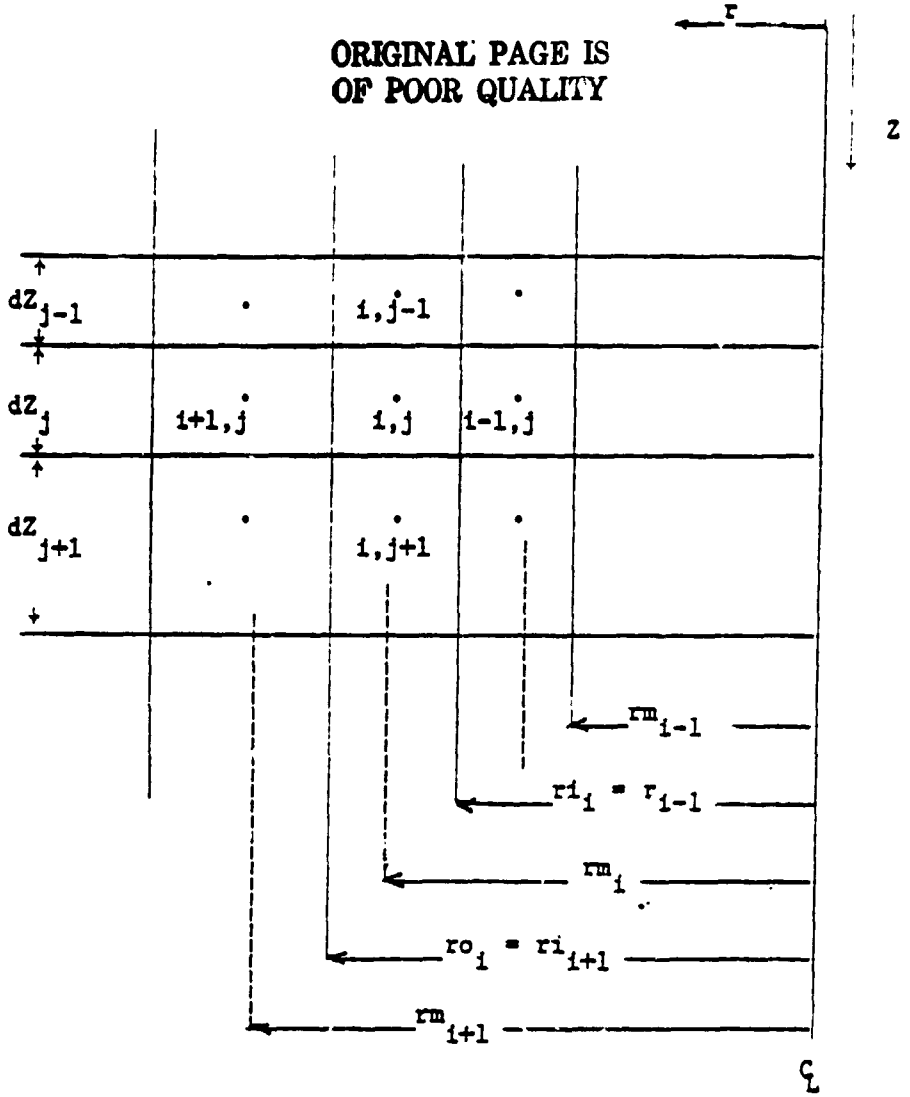

In the radial direction,

$$F_{i-1,j\rightarrow i,j} = \frac{2\Pi \cdot DZ_j \cdot (T_{i-1,j} - T_{i,j})}{\frac{Ln\,(\frac{ro_{i-1}}{rm_{i-1}})}{K_{i-1,j}} + \frac{Ln(\frac{rm_i}{ri_i})}{K_{i,j}}} \qquad (3A)$$

$$\pm RR_{i-1,j} = \frac{Ln(\frac{ro_{i-1}}{rm_{i-1}})}{2\Pi \cdot DZ_j K_{i-1,j}} + \frac{Ln(\frac{rm_i}{ri_i})}{2\Pi \cdot DZ_j K_{i,j}} \qquad (4A)$$

Similarly

$$RR_{i,j} = \frac{Ln\,(\frac{ro_i}{rm_i})}{2\Pi \cdot DZ_j K_{i,j}} + \frac{Ln\,(\frac{rm_{i+1}}{ri_{i+1}})}{2\Pi \cdot DZ_j K_{i+1,j}} \qquad (5A)$$

In the vertical direction,

$$F_{i,j-1\leftrightarrow i,j} = \frac{\Pi\,(ro_i^2 - ri_i^2) \cdot (T_{i,j-1} - T_{i,j})}{DZ_{j-1} / (2K_{i,j-1}) + DZ_j / (2K_{i,j})} \qquad (6A)$$

$$\updownarrow RV_{i,j-1} = \frac{DZ_{j-1} / (2K_{i,j-1}) + DZ_j / (2K_{i,j})}{\Pi(ro_i^2 - ri_i^2)} \qquad (7A)$$

Similarly,

$$RV_{i,j} = \frac{DZ_j / (2K_{i,j}) + DZ_{j+1} / (2K_{i,j+1})}{\Pi\,(ro_i^2 - ri_i^2)} \qquad (8A)$$

At the lunar surface, the flux boundary condition is:

$$K_s \left(-\frac{\delta T}{\delta Z}\right)_{z=o} = \varepsilon\sigma T_s^4 - (1 - A) \cdot I\,(t) \qquad (9A)$$

where ε is the infrared surface emittance

σ is the Stefan-Boltzmann constant

A is the solar albedo: and,

I(t) is the time dependent solar flux.

Equation (9A) is expressed in finite-difference form for each of the lunar surface zones by using the approximation:

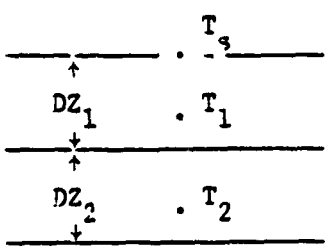

$$\left(\frac{\delta T}{\delta Z}\right)_{z=o} = \frac{2\,(T_1 - T_s)}{DZ_1} - \frac{DZ_1\left(\frac{2(T_2 - T_1)}{DZ_1 + DZ_2} - \frac{2(T_1 - T_s)}{DZ_1}\right)}{2\,DZ_1 + 2\,DZ_2} \qquad (10A)$$

With the substitution of (10A) into (9A), the non-linear surface boundary condition can be solved iteratively for T_s using the Newton-Raphson method.

For the borestem, probe and cable nodes which possess free boundary surfaces, radiative exchange is calculated with all other line of sight node surfaces by assuming unit emittance and utilizing computed direct exchange areas based on the concentric cylinder formulae given in Hottel and Sarofim (1967). The net radiative flux into all such node surfaces is then calculated (utilizing the temperature distribution at a given time step) and substituted in Equation 1A.

d. Filtering and Smoothing Techniques: Identification of the Annual Components

Revised diffusivity values resulting from analyses of the two and three and a half year subsurface temperature histories at the Apollo 17 and 15 sites have been published (Langseth et al., 1976). In this section we describe in more detail the filtering, smoothing and curve fitting techniques utilized in the long-term analyses.

The primary tool used for component separation (diurnal, annual, transient and noise) was a finite Fourier transform computer program. The program required as input 2^n equally spaced (in time) data points with n any integer. The temperature history data were converted to this form by linear interpolation between adjacent data. At the Apollo 15 gradient sensors, 4096 (n = 12) data points were utilized over approximately a three year window. For the ring bridge sensors, 512 (n = 9) data points were input into the transform program. In all cases, the output consisted of $2^n - 1$ pairs of the cosine and sine components.

At the Apollo 15 site, a two step transform process was used. First, a data window of exactly 38 mean synodic periods was transformed, utilizing the available data up to December 31, 1974 (Step 1). This transform window encompassed over three years of data but excluded the first few lunations following deployment to minimize the initial condition effects. Representative spectra are shown in Figure V-C-6. (see Figure V-C-8 for the time series data). At the shallowest sensors (TR11A, TG22A), significant diurnal harmonics can be clearly seen at frequencies six to eight times the lunation fundamental (n = 38). Significant nonrandom power is also present at near diurnal frequencies due to the variation in the synodic period throughout the year. At a deeper sensor such as TG11B, diurnal components are still significant, although strongly attenuated relative to the shallower depths. At the deepest sensors (such as TG22B) the barely discernible diurnal component probably results from a day-night offset in the electronic's calibration.

The large low frequency components are primarily the signature of the long-term transient rise present at all sensors. At the n = 3 harmonic, significant power is produced by the annual component, especially at the

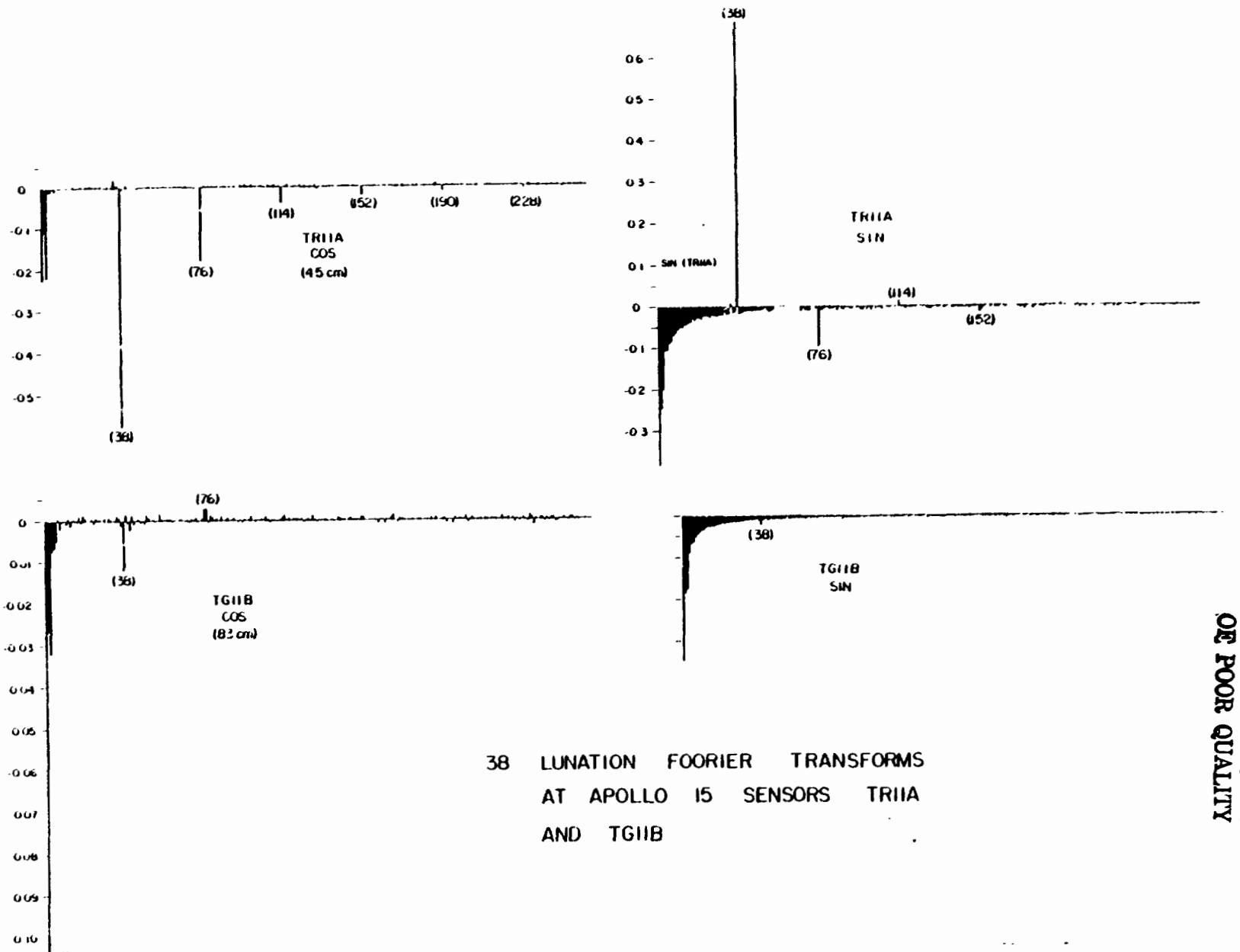

Figure V-C-6

Fourier spectra produced by 38 lunation transform of the Apollo 15 probe subsurface data at TR11A and TG11B

shallower sensors (For a 38 lunation transform window, the precise annual frequency would be at n = 3.07). Since the purpose of the long-term analysis was the precise identification of the annual components and pure transient response, the spectra such as shown in Figure V-C-6 were smoothed to eliminate the diurnal components and minimize the high frequency noise. For this purpose, the high frequency components (n > 12), excepting the diurnal and surrounding frequencies, were fitted with analytic expressions consistent with the general trends of the sine and cosine high frequency components. For the sine components an exponential decay function of the form

$$S(n) = S_0 e^{-\alpha n}$$

was utilized. For the cosine component, note that the high frequency noise has a definite positive bias. This property is a characteristic of the discrete Fourier transform utilized. The high frequency cosine noise averages to zero asymptotically with the number of data points used in the transform. For this reason, a linear fit to the n > 12 harmonics was employed. An example of the spectrum filtering fit, utilized for TR11A, is shown in Figure V-C-7. Note the absence of the diurnal and near diurnal components which were not used in the fits. The cosine fit (a small positive constant) shows that the transient power is contained primarily in the low cosine frequencies. As pointed out earlier, the non-zero high frequency noise average is an artifact of the Fourier transform computation technique. The experimental decay fit to the high frequency sine components is compatible with the theoretical spectrum of an idealized transient response (discussed in the next section). Also shown in Figure V-C-7 is the inversion of the filtered transform showing the time series data smoothed and free of the diurnal components. These smoothed data were then transformed using a window exactly three years long (Step 2). This spectrum is shown on the right. The component at n = 3 contains power both from the annual variation and the long-term transient. Separating the two contributions was the primary goal of the long-term analysis. At the shallower sensors, such as TR11A (45 cm), the annual and transient contribution are of comparable magnitude and a good first approximation of the annual component can be obtained by interpolating for the n = 3 transient contribution from the surrounding spectra which re-

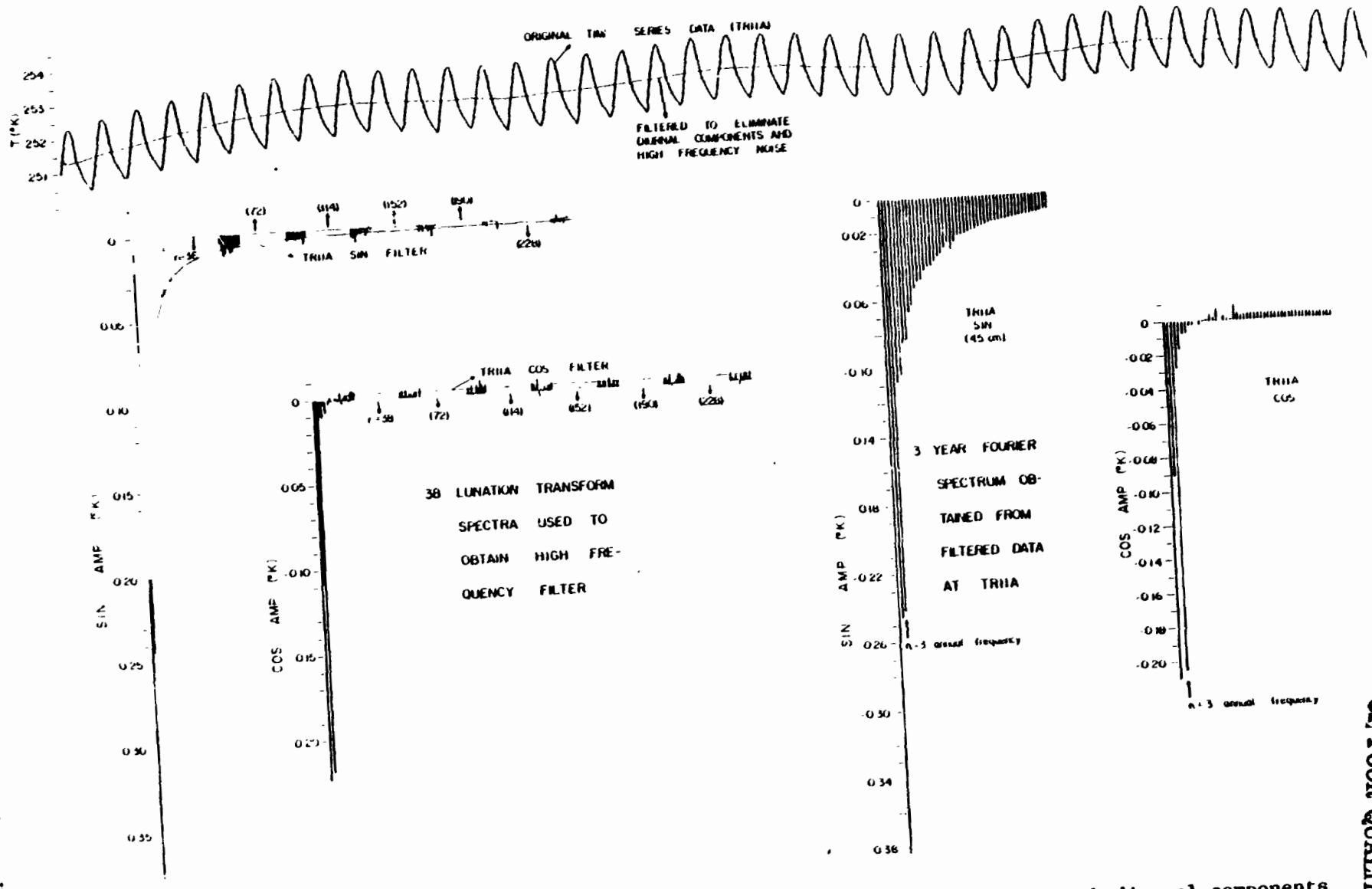

Figure V-C-7

Smoothed 38 lunation spectra for Apollo 15 TR11A. Inversion to time domain with diurnal components and high frequency noise removed is shown at top. Subsequent 3 year spectrum of the filtered real time data is shown at right

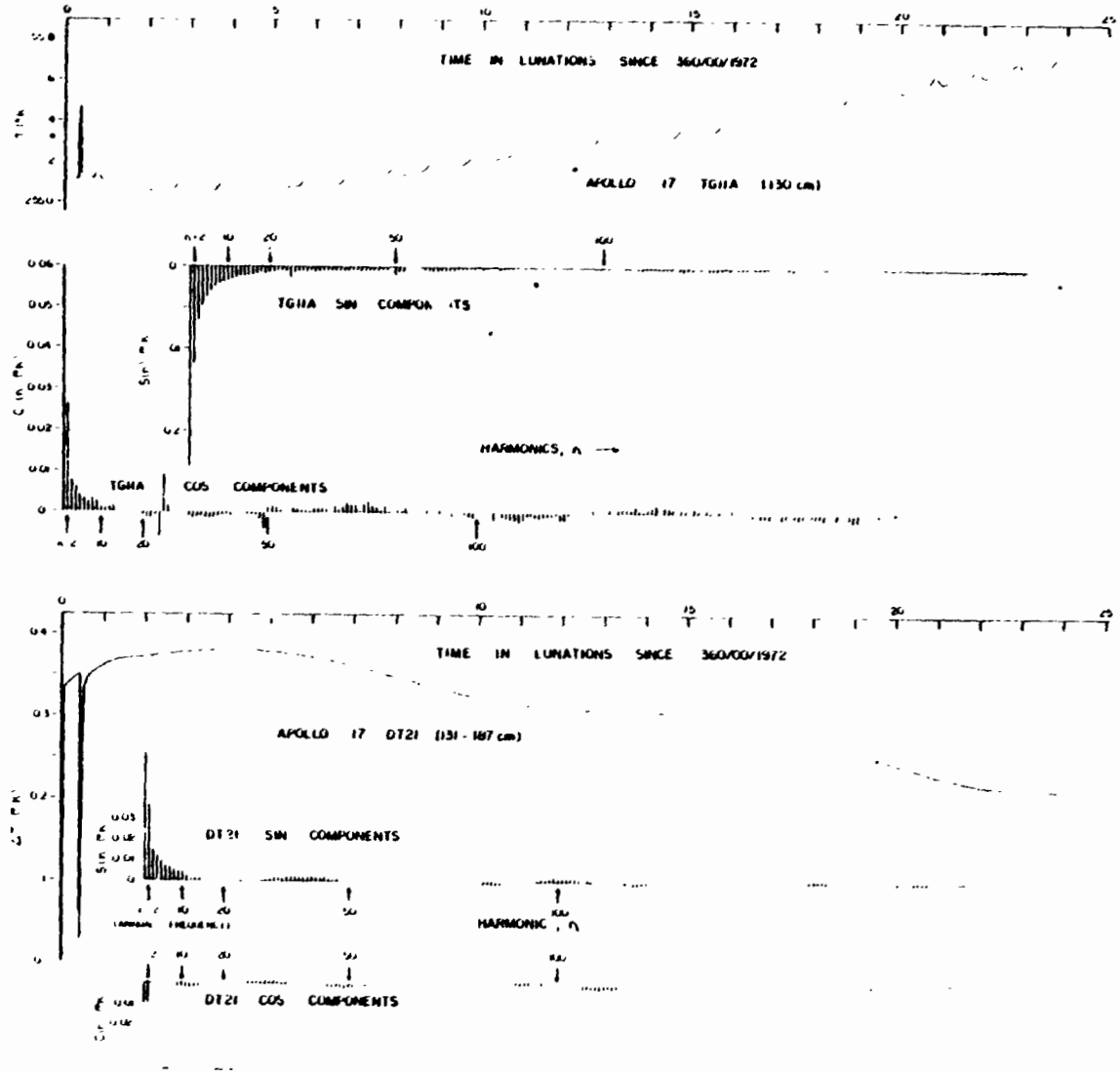

Figure V-C-8

Real time data and two year frequency spectra from Apollo 17 TG11A and DT21 data

present transient power only (see the three year transform of Figure V-C-7). At the deeper sensors,however, the transient contribution at the annual frequency is many times larger than the annual component itself, and interpolative techniques cannot always be used. For example, at the Apollo 17 site, the shallowest probe sensors were at a depth of 1.3 m. Discernible annual variations were present in the real time data, but did not stand out clearly from the transient background in the frequency spectrum. This is illustrated in Figure V-C-8 which shows the time and frequency domain data at the Apollo 17 absolute temperature sensor TG11A and the more accurate temperature difference data at DT21. Note that only two years of data were available for frequency analyses. Thus, the fundamental annual component lies at the n = 2 harmonic of the transform. The primary difficulty is caused by the large amplitude at the n = 1 frequency due to the aperiodic transient. The shape of the transient background spectrum is too irregular near the n = 2 annual frequency to allow a reliable interpolation to eliminate the transient contribution. (The modulation of the spectra seen at higher frequencies is a result of the short term conductivity experiments characterized by the spikes within the first lunation of the time history data. The diurnal components seen in the absolute temperature data at TG11A result from a day-night bias in the electronics calibration and do not represent a real penetration of the diurnal wave to a 130 cm depth.) The most precise method for separating the annual components from the transient background is an examination by eye of the filtered real time data. First, any diurnal variations, if present, and the high frequency noise were filtered out as described previously. The resulting real time data containing only transient and annual components were then replotted on as large a scale as the residual noise level permitted. An initial estimate of the sine and cosine annual components was then made by interpolation and the temperature history data replotted with the assumed annual components subtracted out. The resultant plot was then carefully examined by eye for any discernible annual periodicity remaining. This process was repeated for various values of assumed annual components until no annual fluctuation could be detected in the replotted data. The resolution of the trial and error method at representative sensors of varying precision is illustrated by the test models shown in Figures V-C-9 through V-C-12. In all cases, the vertical scale refers to the filtered data with no annual component removed. If feasible, initial estimates of the sine and cosine components

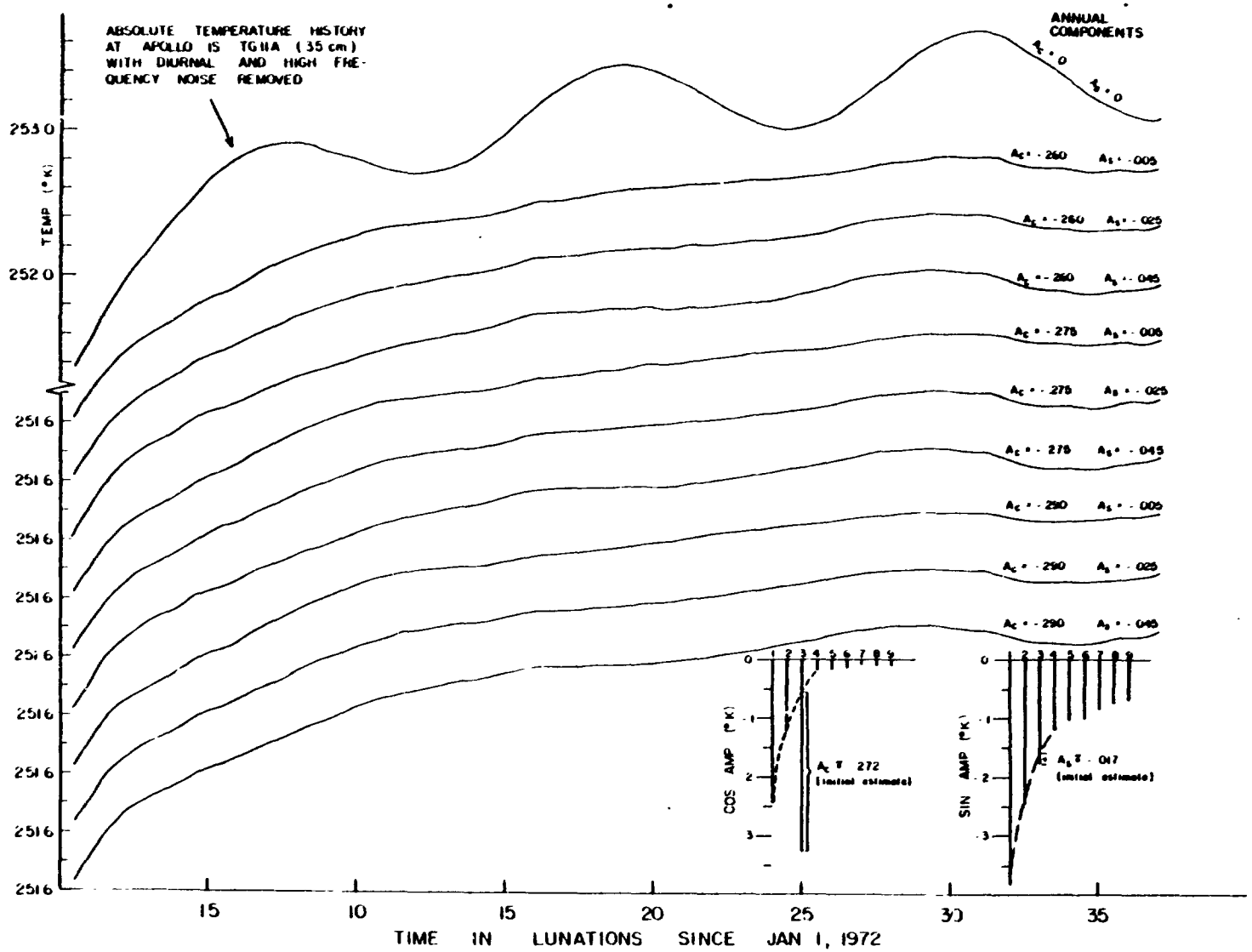

Smoothed real time data with various annual components removed:
A15 TG11A

Figure V-C-9

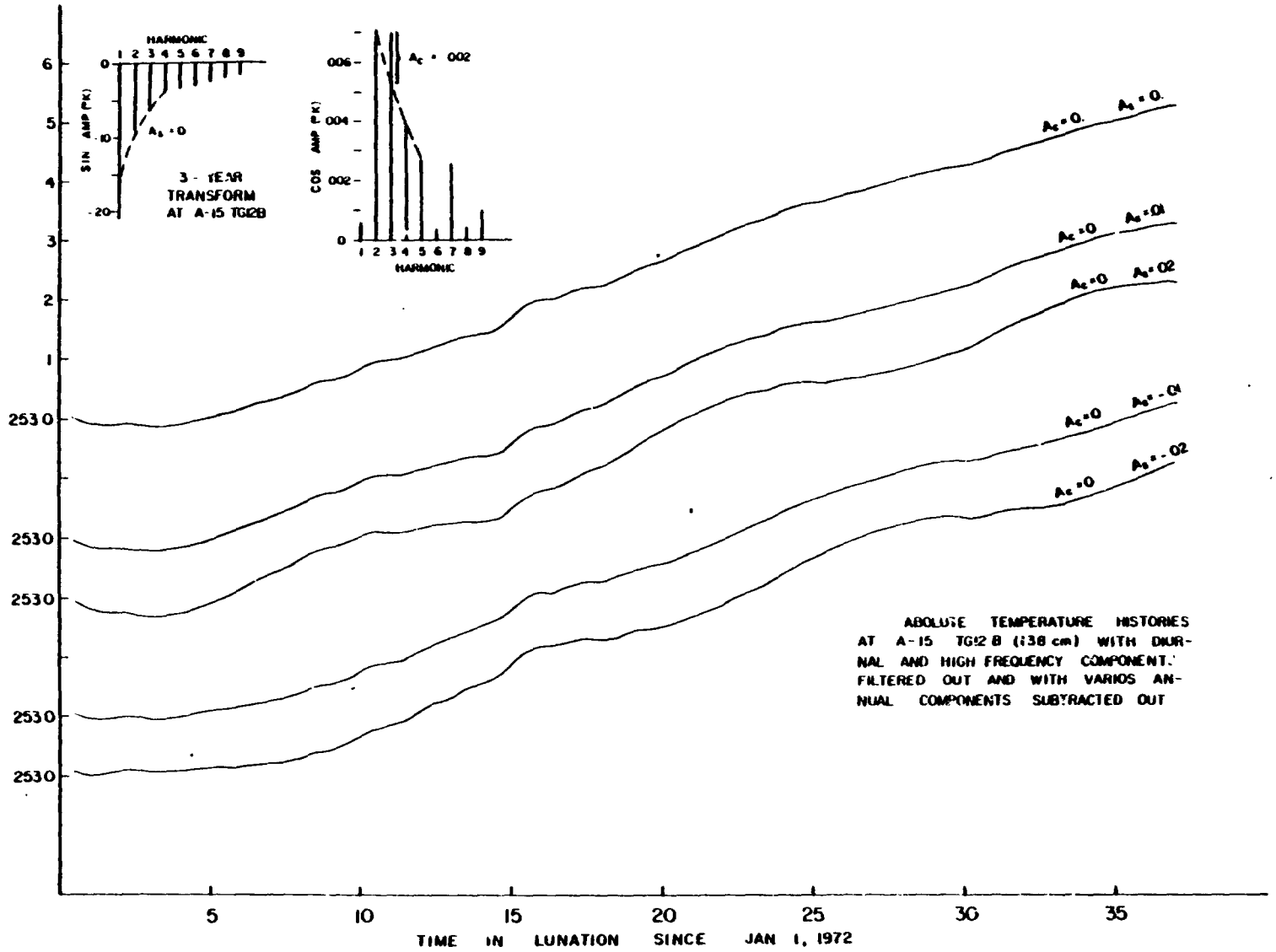

Figure V-C-10

Smoothed real time data with various annual components removed:
A15 TG12B

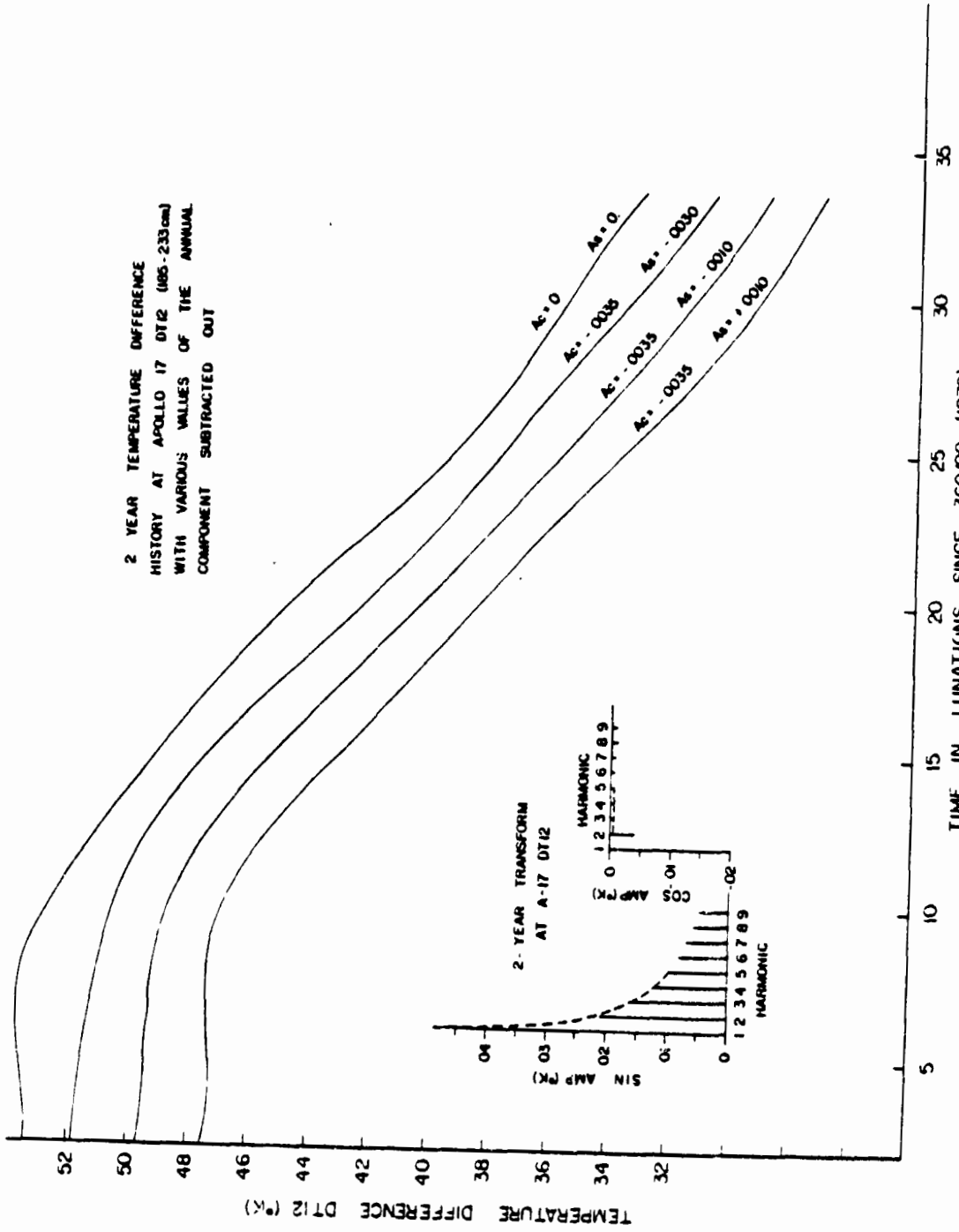

Smoothed real time data with various annual components removed
A17 DT12

Figure V-C-11

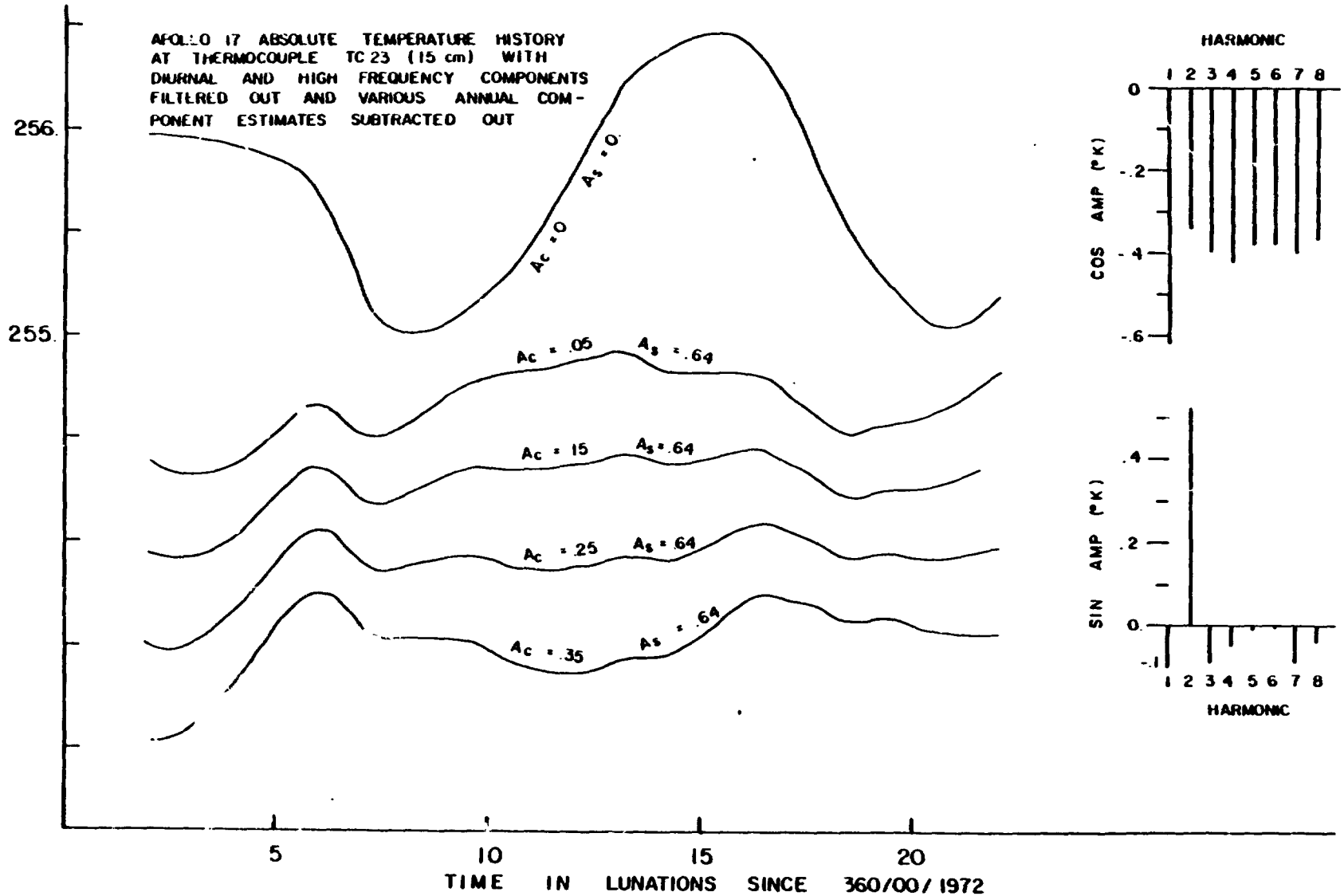

Figure V-C-12

Smoothed real time data with various annual components removed: A17 TC23

are made by interpolating from the surrounding pure transient components of the frequency spectrum. For example, at the shallowest Apollo 15 probe sensor (TG11A, Figure V-C-9) the three year spectrum exhibits a distinctive cosine component at the n = 3 annual frequency, most of which is due to the annual periodicity. An interpolation from the su rounding frequencies (n = 1,2) yields an initial estimate of Ac $\tilde{=}$ - 0.272; As $\tilde{=}$ - 0.017. Further refinement is obtained by replotting the real time data with a feasible range of annual components subtracted. On the scale shown, annual fluctuations can be discerned by eye in all cases except for Ac = - 0.260; As = 0.005 and Ac = -0.275; As = - 0.005. (Irregularities of non-annual frequency result from the filtering techniques described earlier used to eliminate the diurnal components and minimize the high requency noi). Further resolution of the annual components by plotting on expanded scale resulted in final estimates of Ac = - 0.265 ($\pm$ 0.010) and As = - 0.005 ($\pm$ 0.010) for TG11A.

Limitations of the 'eyeba ing' technique are illustrated in Figure V-C-10. Initial spectrum interpolation estimates indicate that the annual component is very near zero (<0.010) at the depth of TG12B (138 cm). (Note the difference in scales for the sine and cosine spectra). Inspection of the real time data confirms the spectrum indications. The subtraction of any sine component larger than |0.01| results in an easily discernible annual variation while no such variation can be seen in the time history data assuming zero annual component. F.r this reason, further resolutions obtained by eyeballing on expanded scale resulted in the establishment of an upper bound for the annual component of |Ac| < 0.003; |As| < 0.005. Note that this resolution is an order of magnitude below the noise level of the absolute temperature data.

At the Apollo 17 site, the increased emplacement depths severely limited the usefulness of the absolute temperature data for the determination of annual components. Only the uppermost probe sensors (130 cm exhibited annual variations detectable within the absolute temperature noise ($\pm$ 0.05°K). To obtain annual components at other depths, both the more accurate temperature difference (DT) data and the shallowest (15 cm) thermocouples were examined. Analysis for the Apollo 17 DT12 gradient sensor is shown in Figure V-C-11. At the time of analysis, 2.7 years of Apollo 17 data were available. Thus, the Fourier analysis was done over a two year window and the real time data were inspected with various annual components removed over the full 2.7 years. From the spectra, it can be seen that a cosine component of approximately -0.0035 is required. Because of the shape of the sine spectrum, the sine

TABLE V-C-1

Annual Components at A-15 and A-17 Subsurface Sensors

	Depth	A_s	A_c	$\sqrt{A_s^2 + A_c^2}$
Apollo 15, Probe 1	35	-0.005	-0.290	0.290
	45	-0.064	-0.170	0.182
	73	-0.075	-0.010	0.076
	83	-0.057	-0.008	0.058
	91	-0.037	+0.009	0.038
	101	-0.030	+0.012	0.032
	129	<0.01	<0.01	--
	139	<0.01	<0.01	--
Apollo 15, Probe 2	49	-0.265	-0.150	0.305
	59	-0.140	-0.170	0.220
	87	+0.015	-0.075	0.076
	97	+0.025	-0.050	0.056
Apollo 17, Probe 1	15	0.63	0.53	0.82
	130	-0.020	0.006	0.021
	186	-0.0012	-0.0036	0.0038
Apollo 17, Probe 2	15	0.64	0.15	0.66
	131	-0.014	-0.008	0.016
	187	-0.0009	-0.0020	0.0022

component cannot be directly estimated. The real time test plots show the resolution available for sine components ranging from -0.003 to + 0.001. Even on the limited scale of Figure V-C-11, it can be seen that a value of As $\geq$ 0.001 is required to eliminate a discernible annual variation. Further eyeballing analysis on expanded scale yields Ac = - 0.0036 ($\pm$ 0.0002) and As = - 0.0012 ($\pm$ 0.0002). Again, the resolution obtained is an order of magnitude increase over the accuracy of the data. The temperature difference annual components were assumed to be representative of the annual variation at the top gradient sensor (185 cm). This is equivalent to assuming zero annual variation at the lower gradient sensor, a justifiable assumption in view of the low thermal diffusivity of the lunar regolith.

The Apollo 17 thermocouple data TC23 (15 cm), shown in Figure V-C-12, are accurate only to $\pm$ 0.5°K. However, at the 15 cm depth, the annual component is large enough to permit a good first estimate from the two year spectra. The time series data shown have been filtered to remove a diurnal component and to minimize the thermocouple noise. Cosine component resolution is illustrated. Further trial and error analysis on expanded scale yielded Ac = 0.18 ($\pm$ 0.03) and As = 0.64 ($\pm$ 0.04)°K.

Annual components at all analyzed Apollo 15 and 17 sensors are presented in Table V-C-1 . Resultant bulk regolith conductivity estimates based on the annual amplitude depth attenuation are discussed in Langseth et al. (1976) and at the end of this section

e. Annual Wave Diffusivity Deductions

For a medium of uniform thermal properties the amplitude of a harmonic temperature variation at the surface attenuates with depth with a decay constant $\beta = \sqrt{\omega/2\kappa}$, where ω is the fundamental frequency and κ the thermal diffusivity (Carslaw and Jaeger, 1959). For the lunar situation, departures from homogeneity occur primarily at shallow depths (less than 10 cm). At these depths, non-linearities produced by the strong temperature dependence of thermal properties must also be considered. However, all probe sensors over which temperature gradient measurements were made lie at least 35 cm below the surface. At these depths, diurnal variations are less than 6°K and the temperature dependence of thermal properties need not be considered. In addition, if one measures the attenuation from one sensor to the next, the resultant diffusivity estimate will represent, to first order, an effective bulk diffusivity between the two sensor depths, regardless of the properties of near-surface layers.

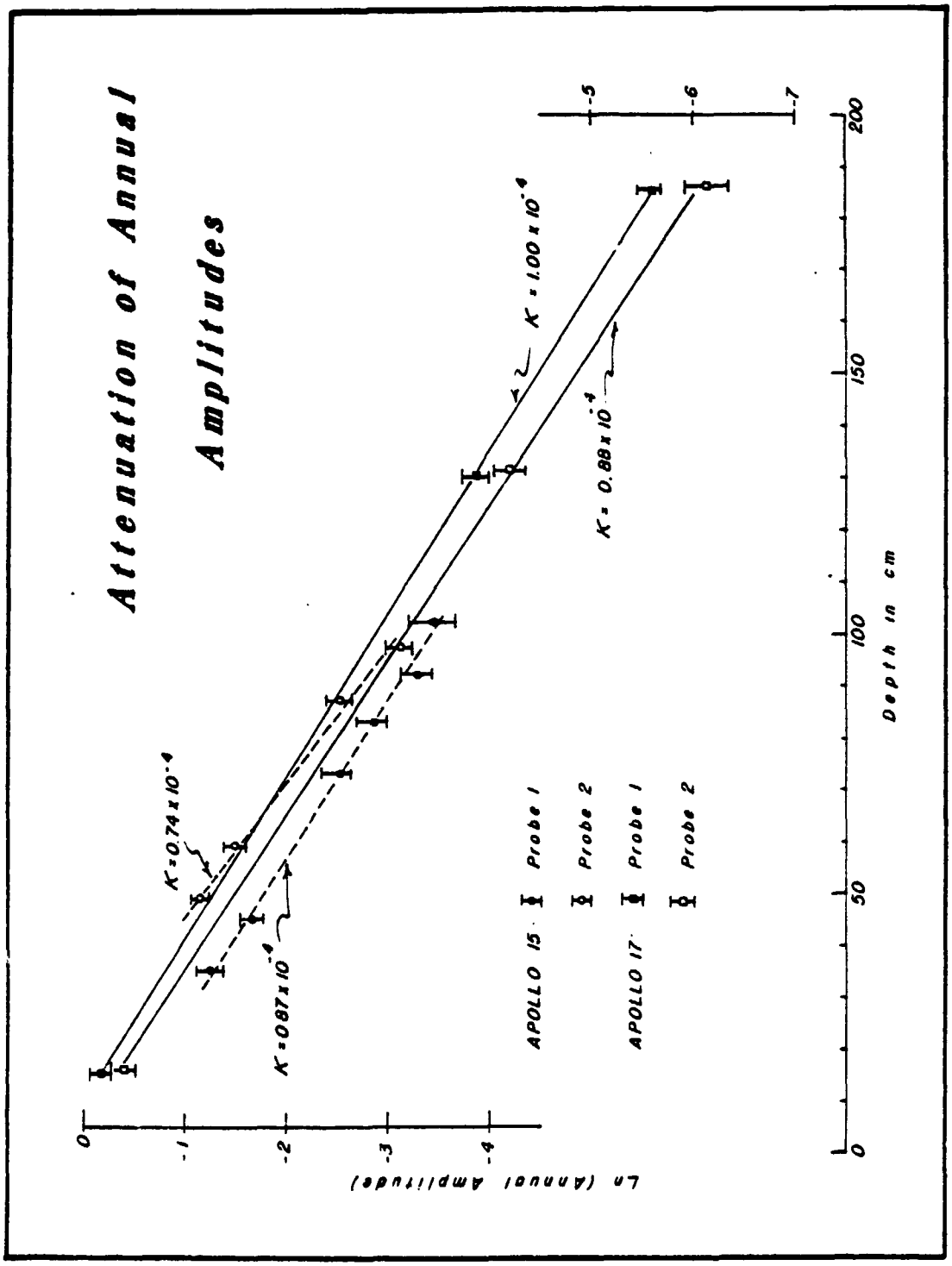

Exponential decay fits to annual emplitude data at A15 and 17

Figure V-C-13

Figure V-C-13 shows the attenuation of annual temperature variations with depth at the Apollo 15 and 17 sites. Within the accuracy of the amplitude determinations, linear fits to the exponential attenuations were made, with the best filling attenuation curves shown in the figure. The range of acceptably fitting curves corresponds to a range of diffusivities of $\pm$ 0.08 x 10^{-4}. The sparseness of the data from the Apollo 17 site is due to the relatively deep probe emplacement depths. Annual wave amplitudes could be resolved only for the absolute temperature histories of the top probe sensors. Amplitudes at depths of nearly 2 m were derived from the more accurate temperature difference data with the assumption that all annual variations were due to variations in the upper sensor temperature. The shallowest Apollo 17 data points, at 15 cm, were calculated from thermocouple temperature histories. The narrow range of linear fits again supports the assumption of regolith thermal property homogeneity at depths below 10 cm.

f. Theoretical Fits to the Long-Term Transients

Following subtraction of our best estimates of annual components from the time series data, the remaining transient histories, propagating downward from the disturbed surface region, were analyzed to provide an additional estimate of the bulk regolith thermal properties.

In actuality, the region of perturbed mean surface temperature is made up of a patchwork distribution of footprint indentations, scuffed surface fines and some undisturbed surface elements within a few meters of each probe. The relative contribution of each disturbed surface element to the subsurface transient behavior will depend on the solid angle subtended at a given probe depth by that surface element:

$$dT = \frac{B}{2\pi} \left| \frac{\sqrt{Z^2 + r^2}}{\sqrt{\pi \kappa t}} \cdot e^{-\frac{(Z^2 + r^2)}{4 \kappa t}} + \operatorname{erfc}\left(\frac{\sqrt{Z^2 + r^2}}{2\sqrt{\kappa t}} \right) \right|_{d\Omega} \qquad (1)$$

(Lachenbruch, 1957)

In the above equation dT is the temperature change at probe depth Z and time t due to a temperature change B over a surface element subtending solid angle $d\Omega$ at depth Z and located a lateral distance r from the probe axis. The regolith thermal diffusivity, κ, is assumed uniform. Erfc is the complimentary

error function. Equation (1) indicates that at the shallower probe depths, transient disturbance will be weighted most heavily by the disturbed surface elements nearest the probe axis. At greater depths, the probe axis proximity of disturbed surface elements will be less of a factor in their relative effect on the subsurface transient response.

Because the actual distribution of disturbed surface elements is unknown, we have fitted the subsurface transient histories to an idealized transient function appropriate to a uniform disk shaped surface disturbance of temperature magnitude B and radius R centered at the probe axis. For this model integration of Equation (1) yields

$$\Delta T\,(z,t) = B\left[\operatorname{erfc}\left(\frac{Z}{2\sqrt{\kappa t}}\right) - \frac{Z}{\sqrt{Z^2+R^2}}\operatorname{erfc}\left(\frac{\sqrt{Z^2+R^2}}{2\sqrt{\kappa t}}\right)\right] \qquad (2)$$

where ΔT is the total transient effect at time t and probe depth Z due to the uniform disturbance of magnitude B and radial extent R. It is to be noted that the fitted diffusivity parameter, κ , represents a bulk or average value between the surface and a given probe sensor depth. At both heat flow sites, however, the linearity of the mean temperature profiles and exponential annual amplitude attenuations indicate nearly uniform bulk thermal properties at probe depths. Only the upper surface layer (2-10 cm) varies significantly with depth. One would therefore anticipate that the transient diffusivity fits should approach the annual wave results for the deeper probe sensors.

In the fitting of Equation (2) to the probe transient histories, time t = 0 (onset of 'instantaneous' change in the local near surface temperature) was taken to occur at the end of the first lunar night following deployment. In actuality, the establishment of the perturbed regions' mean surface temperatures takes place over the course of the first lunation cycle following probe emplacement. Earlier t = 0 times were tested (for example, immediately following the early morning deployment and at the first sunset) for the Apollo 15 transient fits to assess the effect of the zero time choice on resultant diffusivity deductions. In no case did the results yield diffusivities differing by more than $0.1 \times 10^{-4}\,cm^2/sec$. At the deeper sensors, the effects of zero time choice were even less.

In our early transient fits (Langseth et al., 1976) the transients for a particular probe were required to yield a constant value of the parameters B

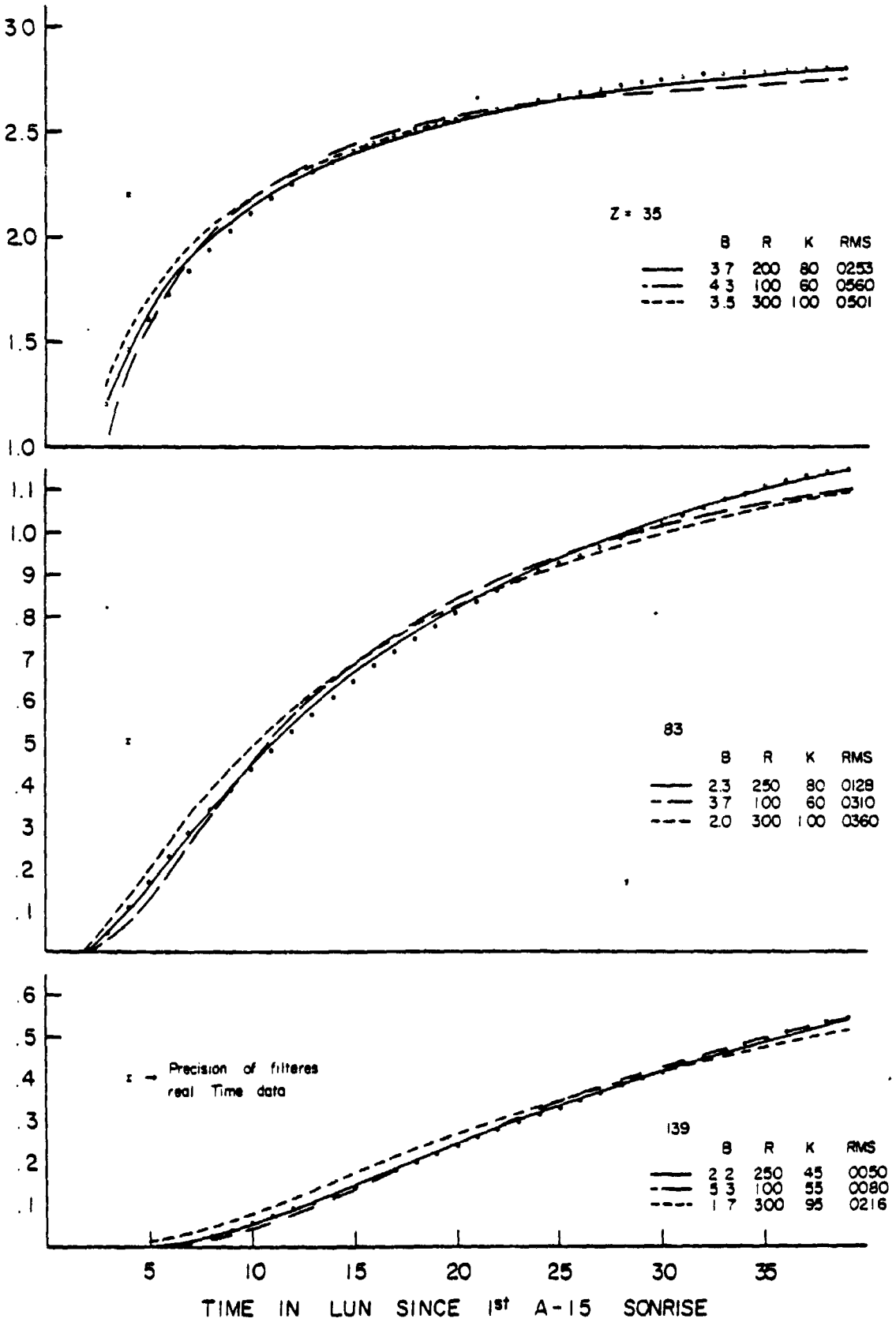

Fits to the astronaut induced transient component at representative A-15 sensors

Figure V-C-14

and R as well as a depth profile of average diffusivity, $\kappa(z)$. This was based on the assumption that the disturbed region approximation represented by a 'best' choice (in the least squares sense) of B and R in Equation (2) should apply equally well at all sensor depths. This, however, need not be the case. One would expect that the region of astronaut disruption be concentrated within about one meter of the probe during the drilling of the hole. At distances greater than one meter, disruption occurs less frequently with the result that the angle averaged mean temperature change will decrease with distance from the borehole site. Thus, due to the solid angle effect expressed in the weighting Equation (2), shallower sensor transients will be more strongly affected by the near hole surface disturbance, while at deeper sensors, the more extensive disturbed region will bear more nearly equal weight for the transient response. For the refined transient fits, therefore, we have allowed depth variation of the best fitting disturbed region parameters B and R within constraints which will be described further on.

Representative examples of the refined transient fits are shown in Figures V-C-14 and 15. The theoretical transient shown are meant to illustrate the sensitivity of the fits to the diffusivity parameter alone. Each transient was fit in the least squares sense for the parameters B and R for diffusivities of 0.40, 0.45... 1.5×10^{-4}. Values of R were restricted to $100 \leq R \leq 300$ cm at 50 cm intervals. The solid curves indicate the best fit obtainable by varying all three parameters. The dashed and dotted curves are the best fits obtainable using κ values $\pm 0.2 \times 10^{-4}$ from the optimum allowing further variation in B and R. At the Apollo 15 site (Figure V-C-14), residuals in the range 0.005 - 0.025°K were obtainable by optimization of all three parameters. Varying κ by $\pm 0.2 \times 10^{-4}$ from its optimum value, and then optimizing B and R increased the residuals by a factor of 2-3 in most cases. At the deepest sensor (139 cm) comparable fits could be obtained for $\kappa = 0.50 - 0.80 \times 10^{-4}$ (RMS $\leq$ 0.015). However, the lower range of these satisfactory diffusivity values (0.50-60) can be eliminated by the criteria that the average disturbance magnitude, B, cannot exceed that determined for the shallowest sensor. As discussed earlier, the shallowest sensor's transient response is heavily weighted toward the near-hole region of maximum disturbance. We, therefore, impose the additional constraint that the effective B value appropriate to the deeper sensors (which are sensitive to a greater extent of disturbed surface elements) must be less than, or equal to, that determined for the shallowest sensor at a particular probe site.

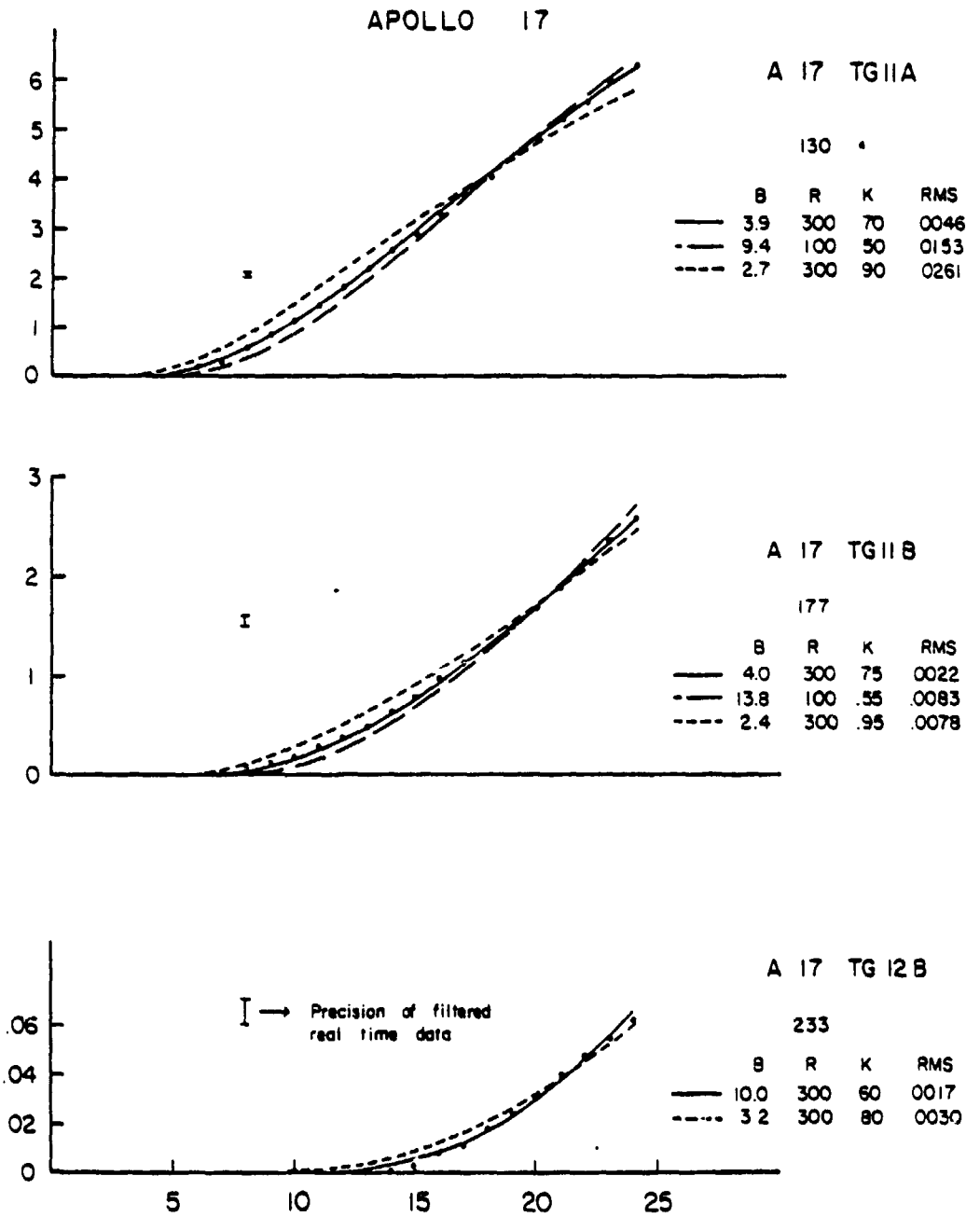

Fits to the astronaut induced transient component at representative A-17 sensors

Figure V-C-15

TABLE V-C-2 Theoretical Transient Fits

Sensor	Depth (cm)	κ_2 ($\times 10^4$ cm^2 sec)	R (cm)	B (°K)	RMS (°K)	κ-Range
A p o l l o 15 (Probe 1)						
TG 11A	35	0.75	200	3.73	0.0221	0.65-0.90
TR 11A	45	0.85	250	3.12	0.0161	0.75-0.95
TR 11B	73	0.85	300	2.25	0.0063	0.75-0.90
TG 11B	83	0.85	300	2.20	0.0140	0.65-0.95
TG 12A	91	0.80	300	2.20	0.0173	0.70-1.00
TR 12A	101	0.90	300	2.00	0.0112	0.75-1.00
TR 12B	129	0.80	300	1.97	0.0052	0.65-0.85
TG 12B	139	0.75	300	2.20	0.0070	0.60-0.85
(Probe 2)						
TG 22A	49	0.20	100	1.34	0.0503	0.10-0.80
TR 22A	59	0.25	100	1.50	0.0398	0.15-0.70
TR 22B	87	0.45	200	1.58	0.0129	0.35-0.60
TG 22B	97	0.50	250	1.56	0.0185	0.30-0.65
A p o l l o 17 (Probe 1)						
TG 11A	130	0.70	300	3.90	0.0046	0.55-0.75
TR 11A	140	0.75	300	4.10	0.0122	0.60-0.95
TR 11B	167	0.70	300	4.46	0.0040	0.60-0.80
TG 11B	177	0.75	300	4.00	0.0022	0.65-0.85
TG 12A	185	0.75	300	3.49	0.0039	0.65-0.95
TR 12A	195	0.70	300	4.16	0.0014	0.60-0.75
TR 12B	223	0.70	300	4.15	0.0024	0.65-0.90
TG 12B	233	0.75	300	4.10	0.0025	0.70-0.90
(Probe 2)						
TG 21A	131	0.55	300	2.10	0.0101	0.50-0.70
TR 21A	141	0.60	300	1.99	0.0070	0.55-0.75
TR 21B	168	0.60	300	1.96	0.0042	0.55-0.70
TG 21B	178	0.55	300	2.11	0.0042	0.50-0.70
TG 22A	186	0.55	300	1.74	0.0024	0.50-0.70
TR 22A	196	0.60	300	1.96	0.0032	0.55-0.70
TR 22B	224	0.60	300	2.10	0.0026	0.55-0.70
TG 22B	234	----	---	----	------	$\leq$ 0.70

Thus, for example, at the Apollo 17 probe 1 site (Figure V-C-15) the best fitting curve at the deepest sensor (233 cm) requires an unreasonably large average mean temperature disturbance, which is incompatible with the transient fits at shallower sensors. The restriction of the fit to acceptable values of B (≤ 4.0) still results in residuals well within the precision of the filtered real time data (~ 0.01K).

Refined transient diffusivity deductions for the Apollo 15 and 17 subsurface sensors are presented in Table V-C-2. The parameter values presented in columns 3, 4, and 5 produce the best transient fits (in a least squares sense) for a given sensor. A parameter resolution of 0.05×10^{-4} cm^2/sec in thermal diffusivi y and 50 cm in R was obtained. The diffusivity range presented in column 7 shows the range of κ values which can produce fits (by further variation of B and R) with RMS residuals within a factor of two of the indicated RMS best fit.

Values of the average surface mean temperature disturbance were restricted to values no less than 0.5B* and no greater than 1.2B*, where B* is the B value deduced from the uppermost sensor data at a given probe site. This criterion is based on the assumption that the shallowest sensor, where the measured transient is largest, best reflects the surface disturbance nearest the borestem axis where effects are the largest. For example, the fits at the Apollo 15 probe 1 site require significantly smaller values of B at the lower sensors than at the shallow probe depths, suggesting a decrease in surface disturbance with radial distance from the probe axis.

At the Apollo 15 probe 2 site, the quality and resolution of the theoretical fits are poor. The RMS minimums are relatively large and not sharply defined in the 3 parameter space. At the shallower probe 2 sensors, the transient histories are significantly irregular, suggesting a particularly irregular distribution of mean temperature perturbation at the surface, including regions of negative mean temperature anomaly near the probe axis. (Early probe 2 transients are negative.) Such a surface disturbance results in the poor fits of the idealized model and the downward bias of the diffusivity estimates. Note, however, the large range of κ values which produce comparable RMS fits (within a factor of two) and which are compatible with the probe 1 results.

At the Apollo 17 site, the deeper emplacement of both probes results in a more uniform integrated response to the surface disturbance. Consistent values of the disturbance parameters B and R produce the best RMS fits at all

depths. In all cases, residuals are within the precision of the absolute temperature data. Probe 2 diffusivity estimates are slightly less than at probe 1, a result consistent with the annual wave κ deductions. The slightly lower diffusivity estimates based on the transient fits are probably due to the low conductivity layer near the surface. In view of the assumptions and approximations inherent in the idealized transient fits, the bulk diffusivity results are considered consistent with and supportive of the more reliable annual wave deductions.

3. Regolith Thermal Conductivity from 15-230 cm: Results and Discussion

Analysis of the annual wave and astronaut-induced transient from the long-term data yielded bulk thermal diffusivity results for each of the four probe sites. Conversion to effective thermal conductivity values required the input of bulk density and heat capacity. The specific heat of a number of lunar particulate samples has been measured (Hemingway et al., 1973). Results indicated substantial variation with temperature but almost no variation from sample to sample. A value of 0.67 W sec/gm°K, measured at 250°K was utilized for all probe depth conductivity calculations.

The bulk density of drill core samples was reported by Carrier et al. (1974). The results from the Apollo 15 drill core indicated densities that range from 1.75 to 1.84 g/cm^3 from depths of 40-160 cm. Due to disruption of the soil during drilling, these probably represent minimum estimates of the in situ values. Maximum density measurements on Apollo 15 soils of 1.89 $\pm$ 0.03 g/cm^3 were obtained by Carrier et al. (1974). Thus, a reasonable range of densities to use for converting the Apollo 15 diffusivity estimates to thermal conductivities is 1.75 - 1.90 g/cm^3. Similar results for Apollo 17 soils lead to an estimated range of 1.83 - 2.09 g/cm^3.

Resultant thermal conductivity estimates based on the long-term data are shown in Figure V-C-16 along with the preliminary results based on the initial probe cooldown analysis and the heater activated experiments. Consideration of all the data indicates large scatter between the results of different methods at comparable depths. The final choice of the annual wave deductions as being the most reliable measurement of the undisturbed regolith conductivity was based on considerations of the sampling volume characteristic

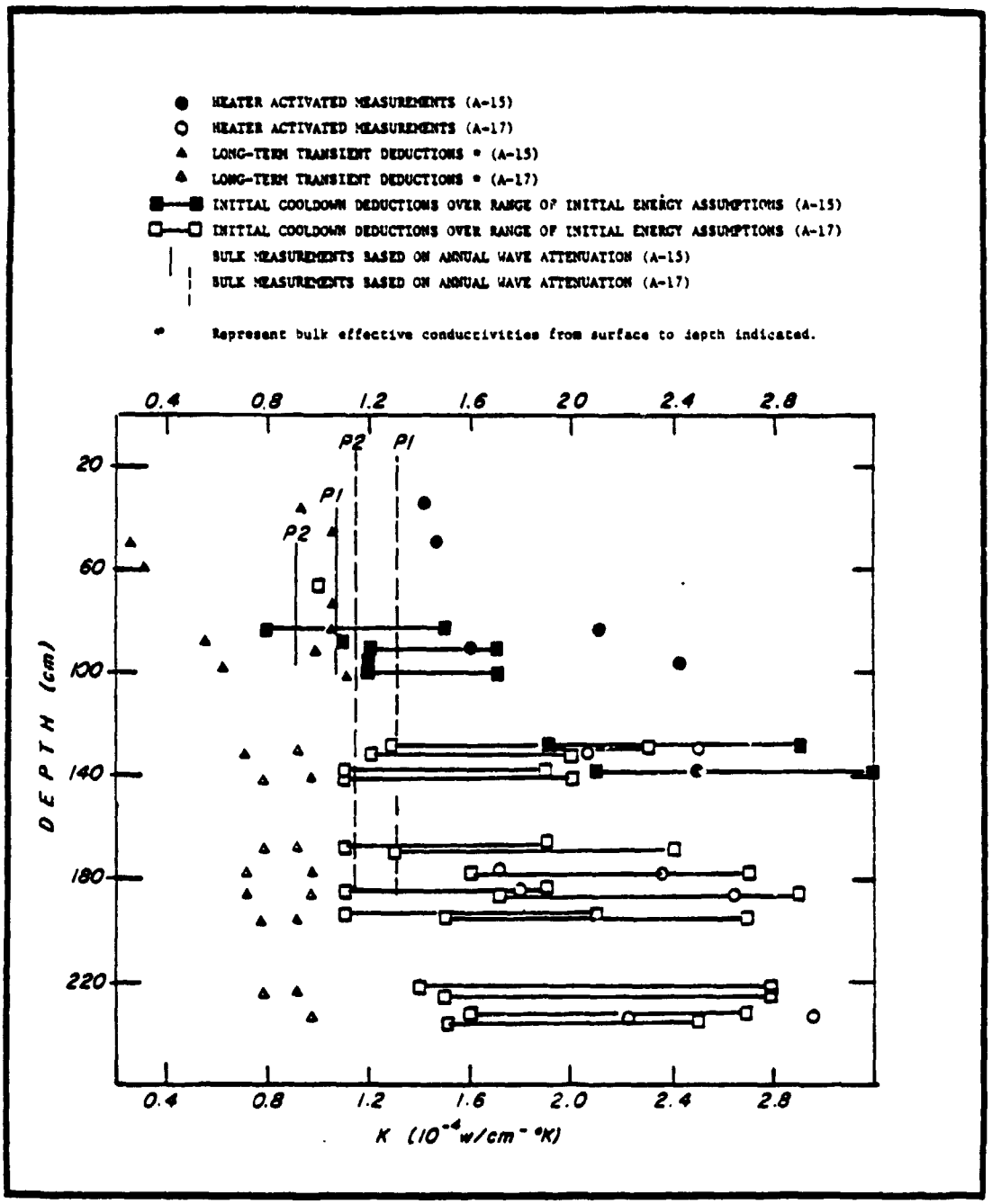

Conductivity deductions based on both short-term experiments and analyses of the long-time data

Figure V-C-16

of the different methods as well as the inherent uncertainties of each. The amount of regolith material influencing the sensor response for each of the transients considered varies directly with the time duration characteristics of the particular transient. In order of increasing time duration, the analyzed transients included;

a. Heater-activated transients (36 hour duration)
b. Initial cooldown equilibration (approximately 45 days)
c. Annual wave propagation (one year period)
d. Astronaut-induced disturbances (approximately three to eight years to reequilibrate).

The short term heater-activated experiments sampled the adjacent regolith only to distances of a few centimeters from each heater location. For this reason, the modeled sensor response, upon which conductivity deductions were based, was particularly sensitive to the designated thermal linkages of the probe and borestem near each gradient sensor. In addition, a significant fraction of the regolith material sample included the contact zone of material disrupted during the drilling process, casting doubt on the representativeness of these measurements.

The conductivity deductions based on the cooldown data were representative of primarily the first 10 cm of regolith adjacent to the borestem. However, the uncertainties of these measurements, in general a factor of about two, were directly proportional to the uncertainties of the initial excess heat estimates. It is to be noted, however, that the assumption of negligible drill heating effects (the minimum initial temperature case), led to conductivity results consistent with the annual wave deductions.

The probe-borestem-regolith numerical model demonstrated that the probe sensor response to transients of long period (one year or more) is controlled entirely by the bulk thermal properties of the regolith. Variations in modelled properties characterizing the thermal linkages of the probe-borestem system and disrupted contact zone had no effect on the probe response to the long period transients. Thus, only uncertainties related to the precision of component identification (for the annual wave deductions) and the magnitude and distribution of the surface forcing function (for the long period astronaut-induced transient) limited the accuracy of the long-term analysis.

The major uncertainty of the deductions based on the astronaut-induced surface disturbance resulted from the necessity to fit the data to a model dependent upon three parameters. The accuracy of the least square fits to the transient data depended upon the magnitude and distribution of the induced mean surface temperature changes as well as the thermal diffusivity of the regolith. In addition, the results were influenced by the low conductivity surface layer (0-10 cm), especially at the shallowest sensors. It was therefore anticipated that the transient deductions would be representative of a lower bound for thermal diffusivity, especially at shallow depths. As shown in Figure V-C-16, at depths greater than 100 cm the results vary little with depth and approach the annual wave deductions.

As discussed in a previous section, fits to the annual wave propagation depend only on one parameter, the thermal diffusivity. Also, the low conductivity surface layer does not affect the results since only the relative attenuation between sensors is considered. For these reasons, we consider the deductions based on the annual wave attenuation to be the most reliable of the in situ conductivity measurements performed to date on the moon.

References

Carrier, W., III, J.K. Mitchell and A. Mahmood (1973) The nature of lunar soil; Jour. Soil Mechan. and Found. Divis., SM10, p. 813-832

Carrier, W.D.,III (1974) Apollo drill core depth relationships. The Moon, V. 10, p. 183-194

Carslaw, H.S., and J.C. Jaeger (1959) Conduction of heat in solids, Oxford at the Clarendon Press, p. 64-69

Hemingway, B.S., R.A. Robie and W.H. Wilson (1973) Specific heats of lunar soils, basalt, and breccias from the Apollo 14, 15 and 16 landing sites, between 90 and 350°K. Proc. Lunar Sci. Conf. 4th, v. 3, p. 2481-2487

Hottel, Hoyt C. and Adel F. Sarofim (1967) Radiative Transfer; McGraw- Hill Book Company, New York; 520 pgs.

Keihm, S.J., K. Peters, M.G. Langseth, Jr., and J.L. Chute, Jr. (1973) Apollo 15 measurement of lunar surface brightness temperatures: Thermal conductivity of the upper 1 1/2 meters of regolith; Earth and Planet. Sci. Lett. v. 19, p. 337-351

Lachenbruch, A.H. (1957) Three dimensional heat conduction permafrost beneath heated buildings; U.S. Geol. Survey Bull. 1052B

Langseth, M.G., S.P. Clark, Jr., J.L. Chute, Jr., S.J. Keihm and A.E. Wechsler (1972) Heat flow experiment. in, Apollo 15 Preliminary Science Report NASA publication SP-289, p. 11-i to 11-23

Langseth, M.G., S.J. Keihm and J.L. Chute (1973) Heat flow experiment. In Apollo 17 preliminary science report; NASA publication SP 330, p. 9-1 to 9-24

Langseth, M.G., S.J. Keihm and K. Peters (1976) The revised lunar heat flow values; Proc. Lunar Sci. Conf. 7th, V. 3, The Moon and Other Bodies Geochim. et Cosmochim. Acta, R.B. Merrill et al., eds, p. 3143-3171

Robie, R.A., B.S. Hemingway and W.H. Wilson (1970) Specific heats of lunar surface materials from 90° to 350°K. Proc. Apollo 11 Lunar Sci. Conf. p. 2361-2367

V-D. STEADY STATE GRADIENTS AND HEAT-FLOW VALUES

Refinement of Subsurface Temperature Profiles

The identification and removal of diurnal, annual and transient variations, and the corrections for shallow sensor radial fluxes allow reliable temperature profiles to be calculated at the Apollo 15 probe 2 site and the upper section of probe 1. Only the probe 1 lower section results have been previously reported for Apollo 15. Figure V-D-1 shows the steady state temperature profiles at the Apollo 15 and 17 sites. Corrections at the Apollo 15 probe 1 lower section and at both Apollo 17 stations due to transient and annual effects were quite small (less than 5%) and the results are largely unchanged from those reported previously (Langseth et al., 1972, 1974).

The temperatures shown at 65 cm at the Apollo 17 stations are thermocouple measurements which are substantially less accurate than the probe sensor results (see Section III-B). With the exception of the Apollo 17 probe 2, 65 cm temperature, all profiles are remarkably linear, suggesting a vertical uniformity of bulk regolith thermal properties at probe depths. The gradients indicated were calculated from a linear least squares fit to the probe sensor results. The anomalously low gradient at Apollo 17 probe 2 represents a lower vertical heat flow along this section (see Section V-C). The gradient increases significantly at shallower depths and may indicate a local disturbance to the heat flow since no comparable change in thermal conductivity is indicated by our analysis.

TABLE V-D-1. Gradients and Heat Flows

	Gradient $^{\circ}K\ m^{-1}$	Diffusivity $10^{-4} cm^2/sec$	Conductivity	Heat Flow $10^{-6} W/cm^2$
Apollo 15, probe 1	1.85	0.87	1.07 ± 9%	1.98 ± 10%
Apollo 15, probe 2	2.52	0.74	0.91 ± 10%	2.29 ± 15%
Apollo 17, probe 1	1.35	1.00	1.31 ± 11%	1.77 ± 12%
Apollo 17, probe 2*	0.79	0.88	1.15 ± 12%	0.91 ± 13%
Apollo 17, probe 2	1.30	0.88	1.15 ± 12%	1.49 ± 16%

* Based on thermometers below 130 cm only.

Table V-D-1 summarizes the gradient, diffusivity and heat-flow values for each probe.

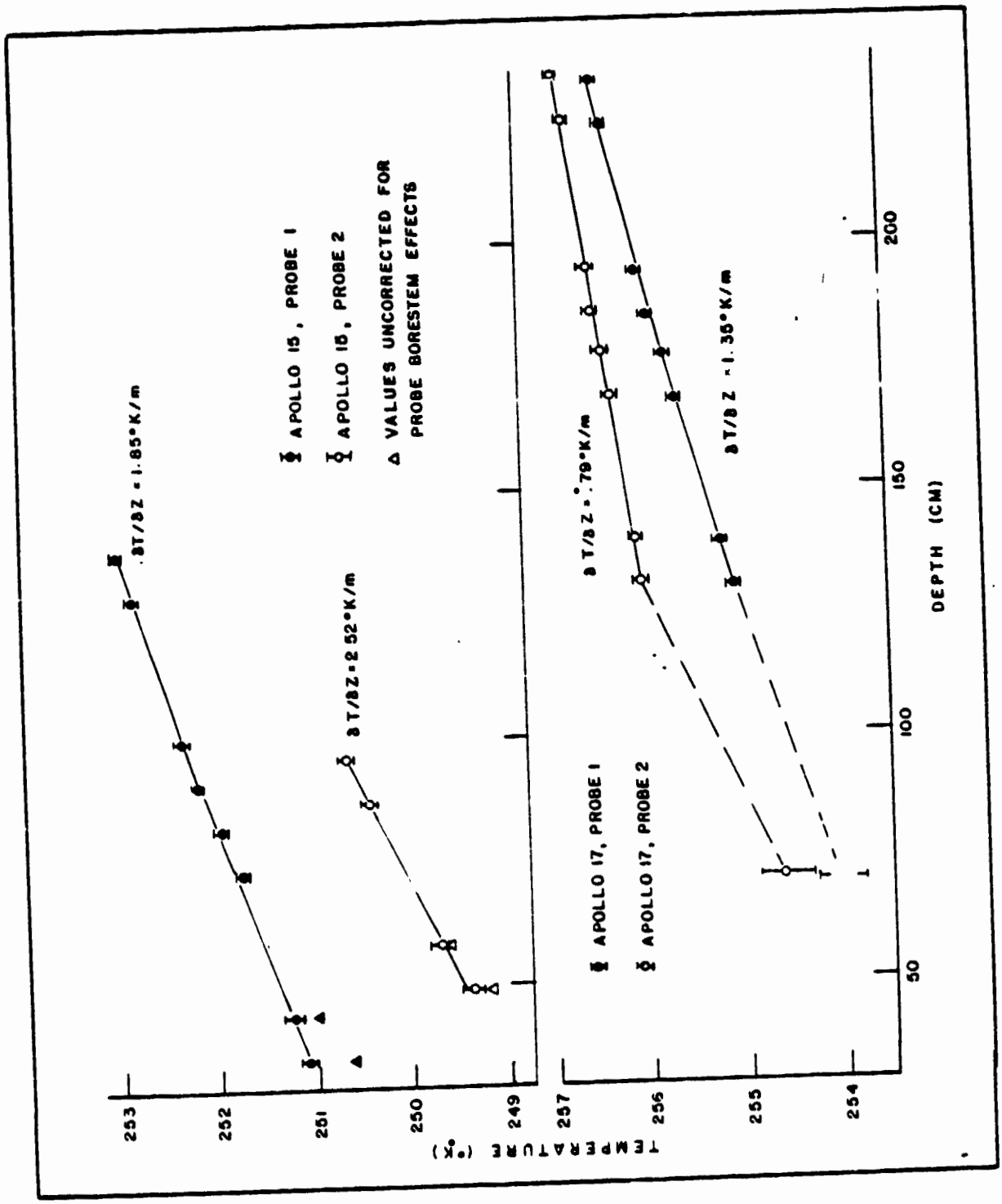

Mean subsurface temperatures at the four probes vs. depth. Note that temperatures of sensors shallower than 65 cm have been corrected upward to account for a steady radiative heat loss to the surface.

Figure V-D-1

Heat-Flow Variability

At the Apollo 15 site the two probes which are separated by ten meters, yield heat flows that differ by about 0.3 x 10^{-6} W cm^2 (14% of the upper value). The gradients differ by 0.67°K/m. If the subsurface temperature gradients are extrapolated linearly to the surface, they yield temperatures that differ by about 2.3°K. It is very likely that the difference in gradient observed results from lateral variations in extrapolated temperature. The extrapolated temperature does not represent the true mean surface temperature but rather the mean temperature at the base of the layer dominated by radiative heat transfer (see Section V-A). Consequently, lateral variations in extrapolated temperatures result from variations in the detailed radiative characteristics of the very near surface layer. These effects are discussed further in Section VI.

At Taurus Littrow we see a similar inverse correlation of extrapolated temperature and gradient if we ignore the thermocouple reading at 65 cm of probe 2. We have no direct evidence that this sensor is giving us a false reading. However, the thermocouples were not as carefully tested as the platinum resistance thermometers and the possibility of a loss of calibration cannot be ruled out. Extrapolating only the probe 2 temperatures (those deeper than 130 cm) to the surface yields a temperature difference between the two locations of 1.7°K, the difference in heat flow is 0.86 x 10^{-6} W/cm^2, 48% of the upper value. The difference in gradient is 0.56 °K/m. The ratio of subsurface gradient difference to extrapolated temperature difference is approximately the same as that observed at Apollo 15. This suggests that the variation in extrapolated temperature between the two probe locations is a primary contributor to the variation in heat flow.

In past reports we have assumed the thermocouple reading at probe 2 (65 cm) is valid. Support for this assumption is that the gradient calculated using the temperature difference between the thermocouple and the lowermost probe 2 thermometer is 1.3°K/m, the same as at probe 1. There are two alternative explanations for the variation in gradient with depth and for the difference between the two locations. The first is to assume that a large volume of high conductivity material lies close to probe 2 in the subsurface. In the Apollo 17 preliminary science report we conjectured that a solid rock may lie adjacent to probe 2 (Langseth et al., 1973). The fact that the long period transients

are apparently not affected by this hypothesized rock detracts from the explanation. An alternative cause of the substantial decrease in gradient below 100 m could be an area of the surface near probe 2 with anomalously high temperature. This hypothesis is supported to some extent by the smaller effect of the astronaut disturbance at probe 2 compared to probe 1 at Taurus Littrow, see Figure V-B-2. At all four probes the astronaut's disruption of the surface resulted in a higher mean surface temperature subsequently. Thus, if an area of anomalously high temperature already existed near the probe 2 location prior to drilling the hole, the relative effect of the astronaut's disturbance would be lessened.

The above discussion clearly illustrates the problems of interpreting only four near surface heat-flow measurements on a surface where sizable and unknown variations can be expected.

The best estimate of the regional heat flow at Hadley Rille is the mean of the two observed values (2.1×10^{-6} W cm^{-2}). At Taurus Littrow we assume that the probe 2 thermocouple reading is valid which indicates a gradient of 1.3°K m^{-1} and a heat flow of 1.49 $\pm$16%. When this value is averaged with the probe 1 value a mean of 1.6×10^{-6} W cm^{-2} is obtained. The value at Taurus Littrow is probably influenced by its position in a valley. The topographic effect of surrounding ridges contributes about 0.2×10^{-6} W/cm^{-2} to the heat flow. The terrain effects will be discussed more fully in Section VI. When the correction is taken into account, our best estimate of regional heat flow at Taurus Littrow becomes 1.4×10^{-6} W cm^{-2}.

References

Langseth, M.G., Jr., S.P. Clark, Jr., J.L. Chute, Jr., S. J. Keihm and A.E. Wechsler (1972) The Apollo 15 lunar heat flow measurement; in, The Moon Volume 4, p. 390-410

Langseth, M.G., Jr., S.J. Keihm and J. L. Chute, Jr. (1974) Heat flow experiment in, Apollo 17 Preliminary Science Report, Section 9, NASA SP-330, U.S. Gov't Printing Office, Wash. D.C., p. 9-1 to 9-24

VI. ANALYSIS OF HEAT-FLOW MEASUREMENTS AND COMPARISONS WITH EARLIER DATA.

*

VI-A. TOPOGRAPHIC EFFECTS

1. Topography

Topographic effects on the moon are complicated by the fact that the mean temperatures of sloping surfaces are a function of the dip angle and azimuth. Variable temperatures over the lunar surface will induce localized gradients in the subsurface and consequently must be taken into account. When correcting oceanic floor geothermal measurements for terrain effects, it is virtually correct to assume that the seafloor surface is isothermal. This simplifies the analysis. In continental regions of rough topography, the surface mean temperature may also be affected by the dip and azimuth of sloping surfaces. For example, in the northern hemisphere the northern slopes of hills will be considerably colder than those on the south facing slopes (see Blackwell et al., in press). Most heat-flow measurements on earth are made at depths great enough so that the effects of mean surface temperature variation are attenuated to a few percent of the regional gradients. However, these effects are important for the lunar heat-flow measurement because they are so shallow.

Figure VI-A-1 illustrates the dependence of mean temperature ten centimeters below the local surface on dip and azimuth angle. The ten centimeter depth is chosen to include the effects of the large mean temperature gradient which results from the large temperature dependence of thermal conductivity within the first few centimeters below the surface. The mean temperature contours shown are based on one dimensional model calculations run over three lunations for dip angles of 0-30° and azimuth angles (measured east of north) of 0-360° at 10° intervals. The contours shown represent the deviation of mean temperature from a flat surface. Note that north facing slopes (azimuth angle 0°) exhibit decreasing mean surface temperatures as the dip angle increases. The opposite effect occurs for the south facing slopes (azimuth angle of 180°).

In the above discussion the radiative exchange between surfaces and shadowing of surfaces by adjacent terrain were ignored. Where slopes are large, greater than

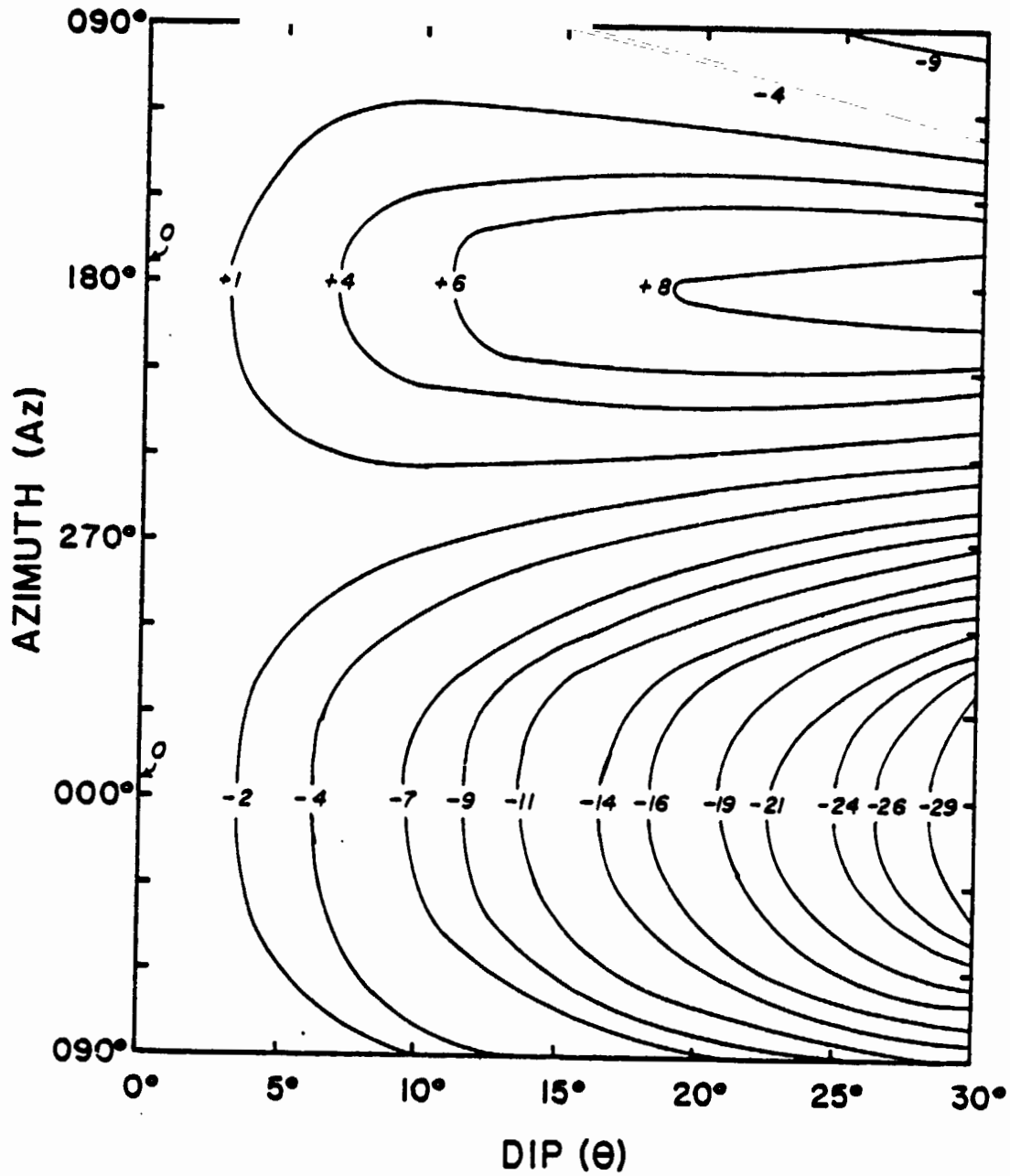

Dependence of mean temperature ten centimeters below the local surface on dip and azimuth angles. The contours represent the deviation (°K) of mean temperature from that of a flat surface.

Figure VI-A-1

10°, the exchange between sloping surfaces and shadowing can be significant and have a pronounced effect on the mean surface temperature. An example of this effect is provided by Hadley Rille. The ALSEP experiments were set up approximately 1.7 km from the eastern rim of Hadley Rille. The rille is about 1.4 km across and 400 m deep. The cross-sectional profile is roughly V-shaped (see Figure VI-A-2). During the morning, the eastern slope which is facing west is in the shadow until the sun rises to nearly 30° above the horizon. However, it is receiving radiation from the western slope which, though partially shadowed during the early morning, once the shadow has passed receives solar radiation at a relatively high incident angle compared to the eastern slope or the surrounding nearly level surface.

The rather complex history of solar insolation and radiative exchange between the sloping walls of the rille were modeled using a two dimensional finite difference model. The geometry of the model is shown in Figure VI-A-2. The computation was carried out in two steps: first, the mean surface temperature was determined by modeling only the upper several centimeters of the regolith and radiative balances at surface nodes during a lunation. Secondly, after the mean surface temperature was calculated (the values are shown in Figure VI-A-2) the effect on subsurface temperatures was found by relaxation techniques on a two dimensional grid of nodes representing the subsurface. The resulting isothermal structure is also shown in the figure. Notable features of the calculation are:

1. The eastern slope actually attains a mean temperature higher than a level surface. As a result, heat flows into the surface here.

2. The western wall of the rille has a temperature 13° lower than a level surface and heat flow through the surface is as a result 3.1 times higher than the observed regional heat flow. The isothermal structure under the western slope is profoundly affected.

3. The disturbance produced by the rille decays rapidly away from the eastern rim and the disturbance at the ALSEP site is -2% of the regional heat flow. Notice that the effect is much larger on the western rim, so that we benefited by the relative location of the experiment to this feature.

At Taurus Littrow, there were two features near the ALSEP site that could produce a prominent terrain effect. The north massif is a ridge of mountains forming a sloping face whose base is only three kilometers from the ALSEP site.

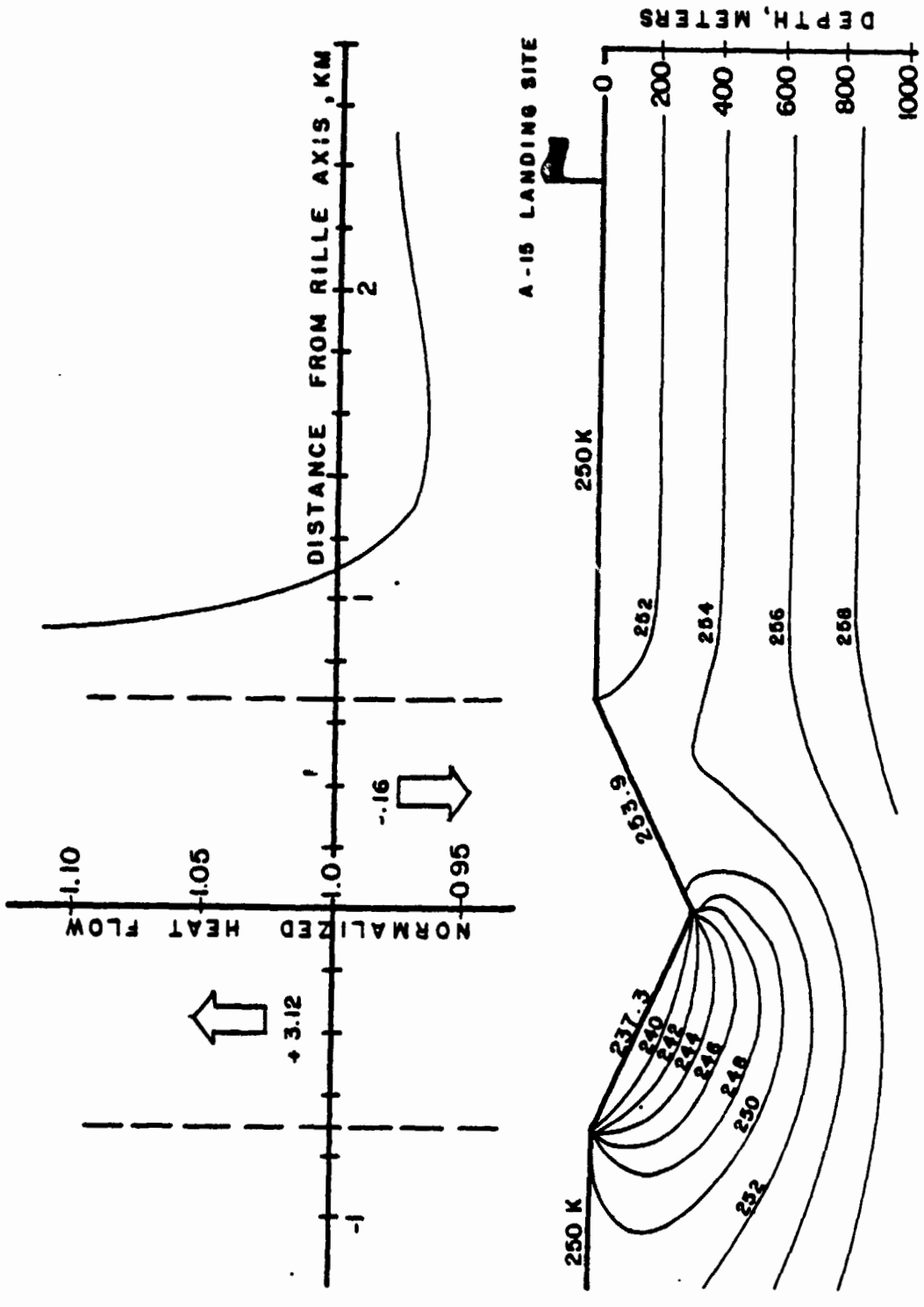

Heat-flow anomaly (above) and subsurface isotherms (°K) for a cross section through Hadley Rille which passes through the Apollo 15 site.

Figure VI-A-2

The ridge is nearly continuous, so that it can be modeled reasonably accurately by a bench 1.67 km high with a plane face sloping 25°. The toe of the bench is 3 km from the ALSEP site. Modeling the feature in this way allows the application of the method of Lachenbruch (1969), to determine that this feature alone results in an 11% increase in the heat flow at the measurement site.

The south massif is about 6 km from the site and its shape is approximated by a truncated cone. The effect on the heat flow of this feature was modeled as a truncated cone, using finite difference techniques in cylindrical coordinates. The choice of a coordinate system transforms the problem into a two dimensional one, that can be more easily formulated and computed. The model showed the effect of the south massif to be surprisingly small. Its presence increased the heat flow only 0.7% at the ALSEP site (see Figure VI-A-3). Similar models of craters showed that terrain features, circular in plan, produce very small effects at distances equal to, or greater, than the radius of the feature.

Application of the Jeffreys or Birch Technique of Terrain Correction:

A good approximation to the terrain effect in complex topography of relatively low relief can be obtained using an approach proposed by Jeffreys (1937) and later developed by Birch (1950). First, the temperature distribution on a fictitious horizontal plane, the reference plane passing through the surface at the station point, is estimated by a simple linear extrapolation of the temperature on the surface to a point on the reference plane using the regional gradient. That is, the temperature on the reference plane ,

$$T(r,\theta,0) = T(r,\theta,h) + \Gamma \cdot h \text{ , where} \qquad \text{(VI-A-1)}$$

r and θ are polar coordinates. The vertical coordinate, z, at the reference plane is 0, h is the elevation of the topography, where positive is higher than the station point and Γ is the regional thermal gradient. The disturbance to the surface gradient at the station point, r = 0, is given by

$$\Delta\Gamma = \int_0^\infty \frac{1}{r} \cdot \frac{d\bar{T}}{dr} \cdot dr \qquad \text{(VI-A-2)}$$

where $\bar{T}$ (r) is the angle averaged temperature around a circle of radius r.

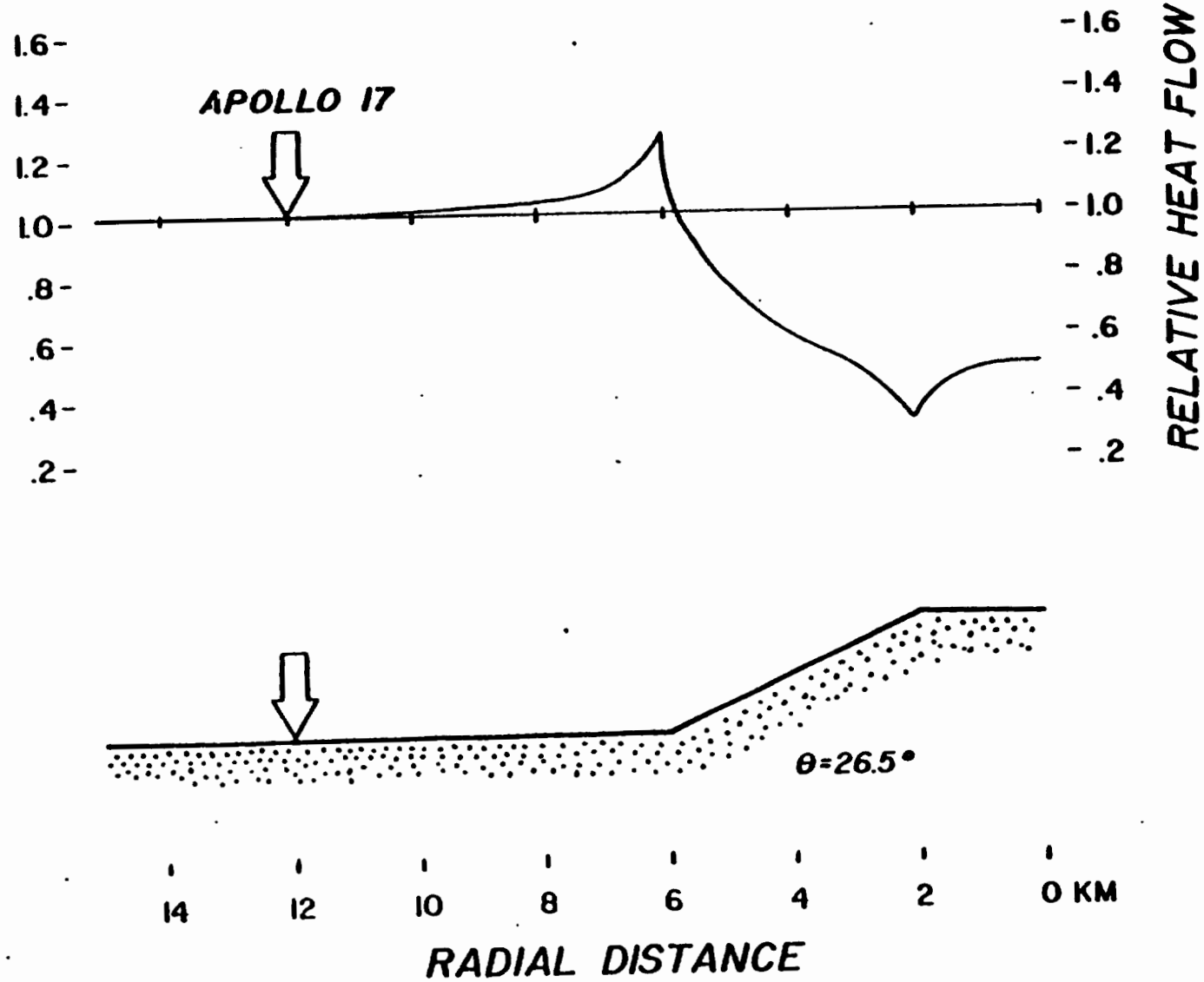

Figure VI-A-3

Heat-flow anomaly (above) for a simple Lachenbruch bench model (shown below). The parameters of the model were chosen to approximate the North Massif at Taurus Littrow.

In practice the effect is assessed by forming a grid over a topographic map. Because the effect of a given area falls off rapidly with distance from r = 0, the area enclosed by the grid lines can be increased rapidly with r without significant loss of accuracy. For each area in the grid, a mean elevation is assigned and a mean temperature is determined. Note that this method can accomodate variable surface temperatures due to the orientation of slopes. The map in Figure VI-A-4 for example, shows the surface temperature distribution at Taurus Littrow using the graph of Figure VI-A-1. Once the temperature distribution on the reference plane has been approximated, using the grid and Equation (VI-A-1), temperatures are averaged around each annulus to determine $\overline{T}$ and then the integral in the equation can be evaluated numerically.

The technique was applied to the topography at Hadley Rille and Taurus Littrow and the correction to be applied to the measurements, given in Table VI-A-1.

TABLE VI-A-1. Terrain Corrections in Percent
For Lunar Heat-Flow Measurements Based on the Jeffreys' Approximation

Site	Topography alone	Surface Temperature	Net
Hadley Rille	-6 ± 3	+ 4.2 to + 8.3	$+ 0.3 \pm 3.7$
Taurus Littrow	-10 ± 4	< 0.1	- 10

Errors resulting from the application of the Jeffreys' method have been investigated for two dimensional topographies by Lachenbruch (1969). His results show that the effects (determined using Jeffreys' method) of positive relief features of moderate slope (less than 30°) on surface gradients at points farther than one relief height from the feature, differ from exact solutions by only 3% or less. For example, the effect due to topography (calculated using Jeffreys' approximation) are essentially the same as that determined using the Lachenbruch bench model discussed earlier. At Hadley Rille there is a pronounced topographic effect of $\sim$ 6% due largely to the

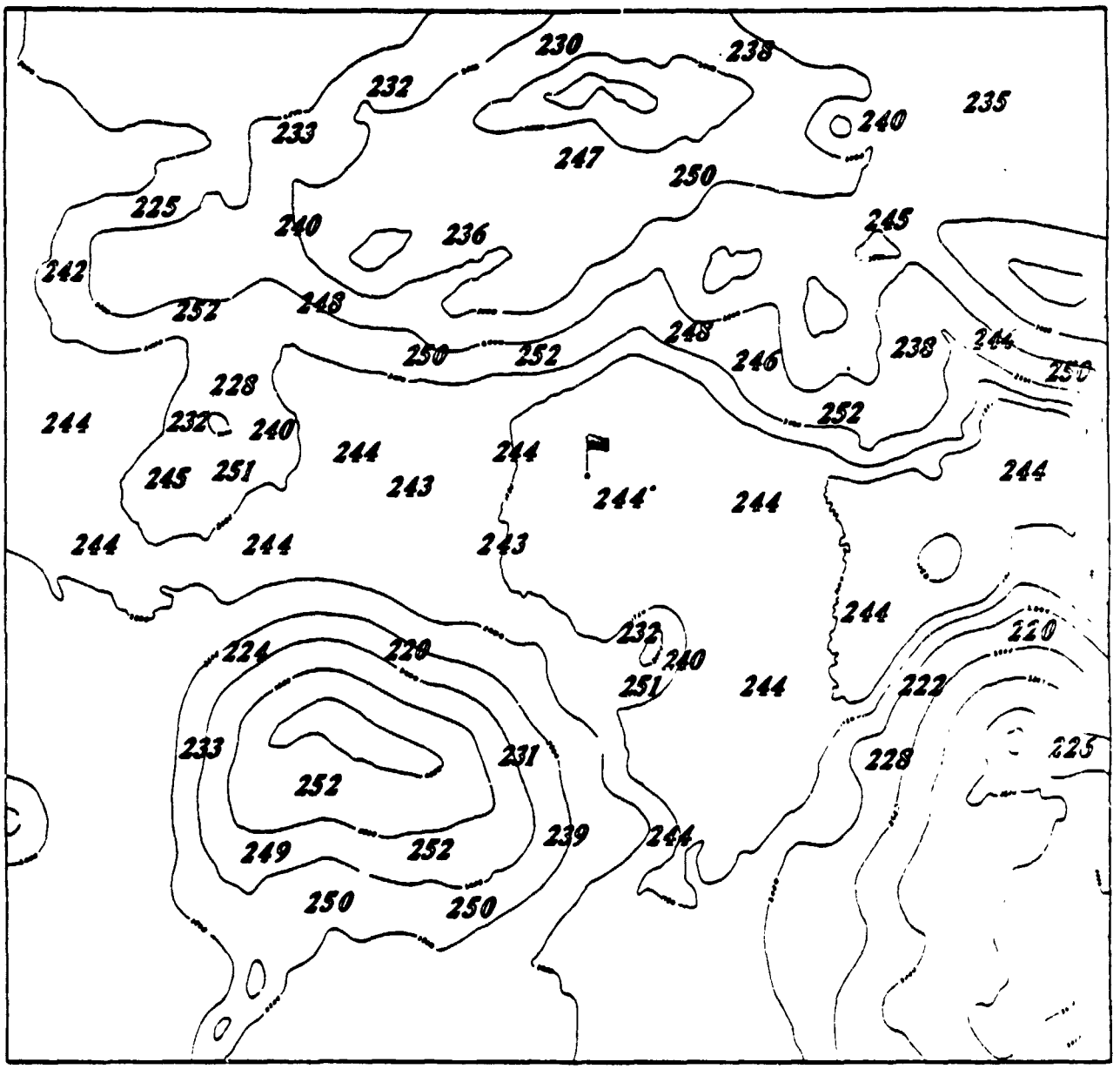

Mean surface temperature (°K) in the region of Taurus Littrow.
The contours represent topography.

Figure VI-A-4

Apennine Front south of the site. However, this front is facing north and consequently, has a surface temperature significantly below that of a level surface. This large area of below average mean surface temperature produces an opposite effect to that of the topography, so that the net effect is not significantly different from zero (see Table VI-A-1). The results given in this table are thought to be the best estimate of the terrain corrections and they have been applied to the raw data to give the best estimates of heat flow. At Hadley Rille, there is no correction so that the value remains 2.1 $\mu w\ cm^{-2}$. A -10% correction is applicable to the Taurus Littrow measurement reducing its value to 1.4 $\mu w\ cm^{-2}$.

Using Random Walks to Estimate Topographic Corrections

We experimented with a novel approach to determine the effect of terrain on surface heat-flow values based on the probability theory. The principle of this method is that the temperature at a point interior to a volume on whose surface the temperature is defined everywhere, can be estimated by averaging the temperatures at points on the surface where random walks launched from the interior point emerge (see for example, Haji-Sheikh, 1965; Haji-Sheik and Sparrow, 1967).

The problems associated with using such an approach aided by a computer are:

1. A large number of walks are required to make a sufficiently accurate estimate at a single point, particularly when the point is close to the surface.

2. Finding a method to determine when a walk had indeed emerged, was a non trivial problem. Associated with this was the problem of finding a convenient way of mathematically representing a complex surface, such as lunar topography, for rapid computer calculations of walk positions relative to the surface.

3. Finding a truly random number generator is important because the slightest bias in azimuth of emerging points could introduce large errors. Test runs using thousands of points were made to determine the distribution of emerging points on a plane surface. The IBM Library Subroutine RANDU was found to be unsuitable for our purposes.

The first problem was largely solved through the use of a very fast machine. To obtain a reasonable accuracy, runs required about 40,000 separate walks from a single point. After initial experiments in which walks were launched from several points along a vertical line near the surface to determine the gradient, we found greater efficiency resulted from using the

random walks to determine the temperature distribution on a reference plane as in the Jeffreys' technique then, using Equation VI-A-2 to calculate the gradient distribution.

The speed of the walks can also be increased by using the so-called floating walk. To perform a floating walk at each step, the length is chosen to be the distance to the nearest point on the surface, although the direction cosines of the walk segment are randomly chosen. Such walks find the surface relatively rapidly. The path was considered to emerge from the volume when the direction of a step made a prescribed, small angle with the direction to the closest point on the surface.

The model used to represent lunar problems was approximately a rectangular paralle'epiped. The upper surface of the box was the topography represented by triangular facets. This is the only means of representing the surface that we tried and it may not be the most efficient. It did lend itself to rather easy mathematical definition.

The floor of the box is a plane horizontal surface placed at a depth, D, about five times the largest relief. The temperature at the bottom was taken as $\Gamma \times D$ where Γ is the regional gradient. The vertical walls were also planar and temperature on the walls was defined using the linear relation

$$T(z) = T(h) + (z + h) \times (\Gamma \times D - T(h)) / (D + h)$$

where h is the elevation at the top of the wall and the depth, z, is zero at the site.

Various tests of the method were made. The single bench was modeled. Random walk determined solutions could be compared with the exact solution of Lachenbruch (1969). Good agreement was not obtained due to the effects of elevated topography outside the perimeter of the model which is not well accounted for by the random walk method. The far topography could be easily and accurately accounted for using the Jeffreys' technique. When the random walk results were added to this the comparison with the exact solution was perfect ($\pm$.3% estimation error) with 18,000 walks .

When the method was applied to the topographies of Hadley Rille and Taurus Littrow the results were in good agreement with the results of the Jeffreys' approximation (see Table VI-A-1).

References

Blackwell, D.D., C.A. Brott and J.L. Steele (in press). The terrain effect on terrestrial heat flow: II. Effect of microclimate on surface temperatures and examples of terrain effects; Jour. Geophys. Res.

Birch, F. (1950) Flow of heat in the Front Range, Colorado; Geol. Soc. Amer. Bull., v. 61, p. 567-630

Haji-Sheik, A. (1965) Application of Monte Carlo Methods to thermal conduction problems. Ph.D. Thesis, University of Minnesota

Haji-Sheik, A. and E.M. Sparrow (1967) The solution of heat conduction problems by probability methods; Jour. Heat Transfer, p. 121-131

Jeffreys, H. (1937) The disturbance of the temperature gradient in the earth's crust by inequalities of height; Month. Notices, Roy. astr. Soc., v. 4, p. 4

Lachenbruch, A.H. (1969) The effect of two-dimensional topography on superficial thermal gradients; Geol. Surv. Bull. 1203E

VI-B. LATERAL MEAN SURFACE TEMPERATURE VARIATIONS

As we noted in Section VI-A, topographic slopes on the moon cause variations in surface temperatures that induce localized gradients in near surface layers. Changes in radiative properties of near surface layers can also cause surface temperature variations on a local scale which should be considered. The most obvious source of an anomalous radiative material are large boulders exposed at the surface, which will in general maintain different mean temperature than the surrounding regolith because (1) their greater thermal inertia results in the retention of more heat during the lunar night, and (2) the conductivity of solid rock materials is less temperature dependent than the soil layers so that only a small mean temperature gradient is induced in the zone where diurnal variations are significant.

At both the Apollo 15 and 17 sites, very large mean temperature gradients were observed in the upper few centimeters of the soil due to the predominance of radiative heat transfer during the lunar day. Temperatures at a few centimeters were 35-40°K higher than the mean surface temperature (Keihm and Langseth, 1973). Since this increase depends on the ratio of radiative transfer to conductive transfer (see, for example, Linsky, 1973) variations in the radiative properties of the upper part of the soil could induce significant lateral variations in mean temperature at a depth of about 10 cm, even if the mean surface temperature is uniform. These subsurface variations will in turn induce localized gradient perturbations.

We have little data related to the possible lateral variations of radiative properties of the regolith and must to a large extent depend on indirect evidence and intuitive arguments.

The effects induced by lateral surface temperature variation on gradients measured at depths of 1-2 m will depend on the proximity of the boundary between regions of contrasting temperature and the magnitude of the contrast. The worst case, as far as geometry is concerned, is a circular area centered over the measurement site, similar to the model discussed for the astronaut disturbance in Section V. In Figure VI-B-1 we show the gradients induced at four

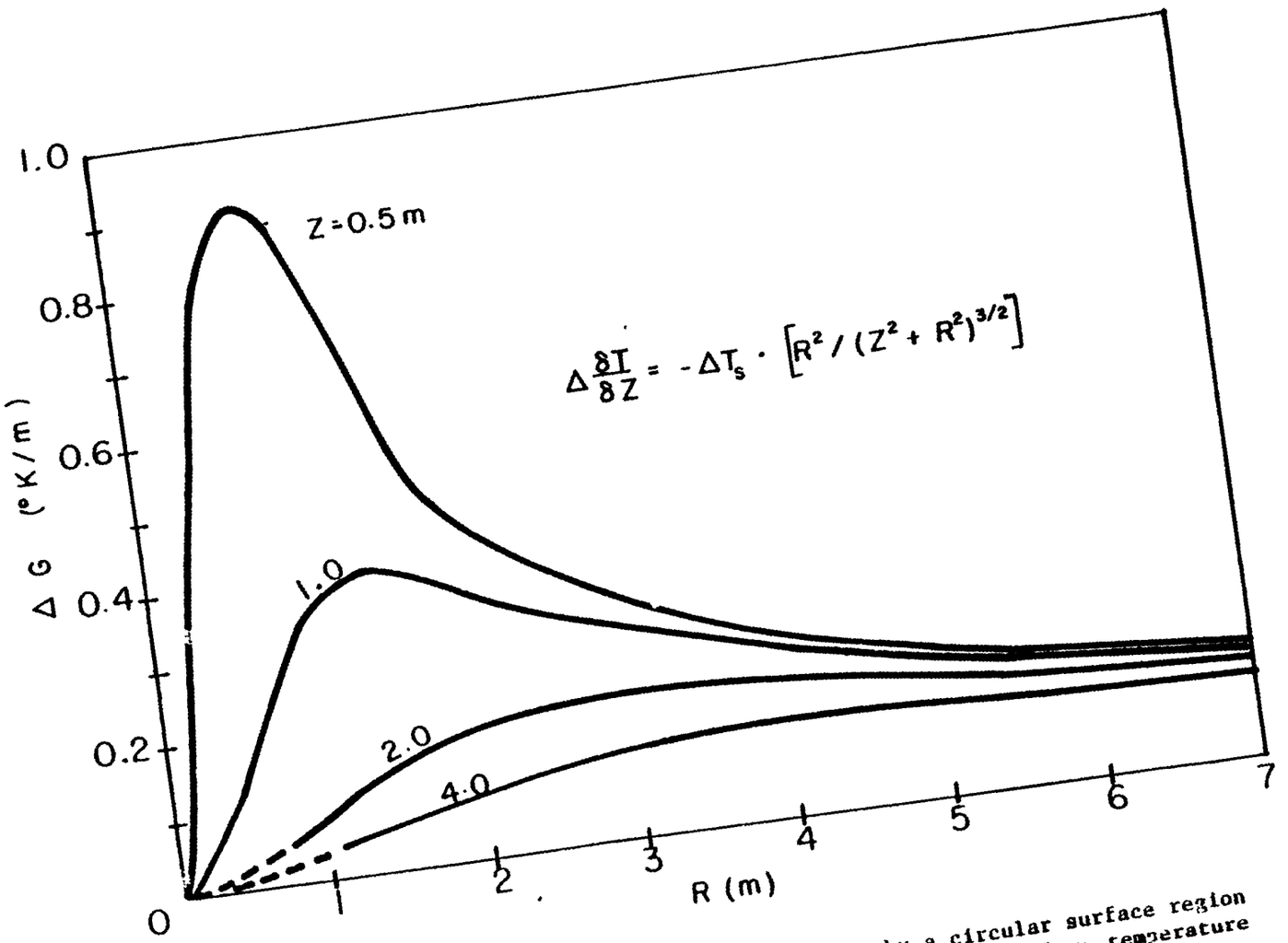

The gradient induced at four different depths, z, by a circular surface region of radius R, centered above the depth points that has an anomalous temperature ΔT_s, 1°K lower than the surroundings.

Figure VI-B-1

different depths by a -1°K temperature anomaly in a circular region as a function of radius of the circle. Notice that at each depth the disturbance goes through a maximum. At the Apollo measurement depths (0.5-2 m) the disturbance is maximum for a boundary that is 1-3 m in radius. As the boundary moves further away, the disturbance decreases rapidly. This illustrates that it is principally local variations on the order of a few meters that create appreciable disturbances.

This mechanism offers an alternative explanation for the 0.6°K/m gradient difference observed between the two probes at the Apollo 17 site. An anomalous temperature boundary a few meters from either of the probes which are separated by 10 m with a contrast of 2-3° is required based on the curves of Figure VI-B-1. The higher temperature would be required above probe 2. Extrapolation of subsurface probe temperatures to the surface shows the surface over probe 2 to be 1 /°K higher if we ignore the thermocouple measurements at 65 cm.

Besides the effects of rocks mentioned earlier, recent craters a few meters of more in diameter may cause lateral variations in radiative properties by disruption and compaction of the soil. In general, the astronauts were able to emplace the probes far from obvious craters and surface boulders. However, the effects on the thermal properties of the near surface soil layer may remain long after the surface expression of the event has become subdued. The inability to exclude local disturbances emphasizes the need for further data which would tend to smooth effects at a scale of meters. Critical information can be obtained by remote sensing of infrared and microwave radiation from the lunar surface, and the response of the surface to the varying insolation function. Such observations can be made by earth-based telescopes but far more valuable results could be obtained from a spacecraft in a low altitude orbit.

References

Keihm, S.J. and M.G. Langseth (1973) Surface brightness temperatures at the Apollo 17 heat-flow site: Thermal conductivity of the upper 15 cm of regolith. Proc. Lunar Sci. Conf. 4th, p. 2503-2513

Linsky, J.L. (1973) The moon as a proposed radiometric standard for microwave and infrared observations of extended sources. Astrophys. J. Suppl., v. 25, p. 163-204

VI-C. SUBSURFACE CONDUCTIVITY CONTRASTS

The disturbance of heat flow by topography can be estimated with good accuracy because it depends on parameters that are observed. There are other possible disturbances due to the subsurface structure of the outer layers of the moon about which we have little direct evidence. One such disturbance is caused by the refraction of heat at sloping interfaces between bodies of different thermal conductivity. Several investigators have examined effects on the lunar surface heat flow of conductivity structures based on geological models of mare basins or ejecta blankets (Conel and Morton, 1975; Mizutani and Osako, 1974). The results of these model computations depend on assigning thermal conductivities to geological units such as mare basin fill, impact ejecta blankets, and the regolith material

The existing experimental data show that the thermal conductivities of lunar rocks and disaggregate soils that compose the outer layers of the moon are mainly controlled by porosity. In Figure VI-C-1 data for lunar rock samples and regolith fines are plotted versus porosity. A clear inverse relation between porosity and conductivity is seen for rock samples (Group I) and disaggregate regolith fines (Group II). The two groups are not described by a single relation between conductivity and porosity. For Group I samples the porosity can hardly increase above 25% or else the rock would fall apart unless it is an extremely vesicular pumice, or similar rock so that there is probably a lower limit to the conductivity (about 1-2 x 10^{-3} W cm^{-1} $°K^{-1}$) that most rock samples can attain. Mainly the porosity of these samples depends on the extent of fracturing of the original glassy or crystalline matrix, and to a lesser extent on the nature and composition of the matrix. Sample measurements show that among the rock samples there is very little differentiation between basalt and breccia samples. The correlation of conductivity with porosity suggests that the conductivity structure of at least the upper 1 km of the moon depends on the history of impacts that have changed rock porosities by fracturing and comminution, and the extent to which the fractures are closed at depth as the compressive load increases.

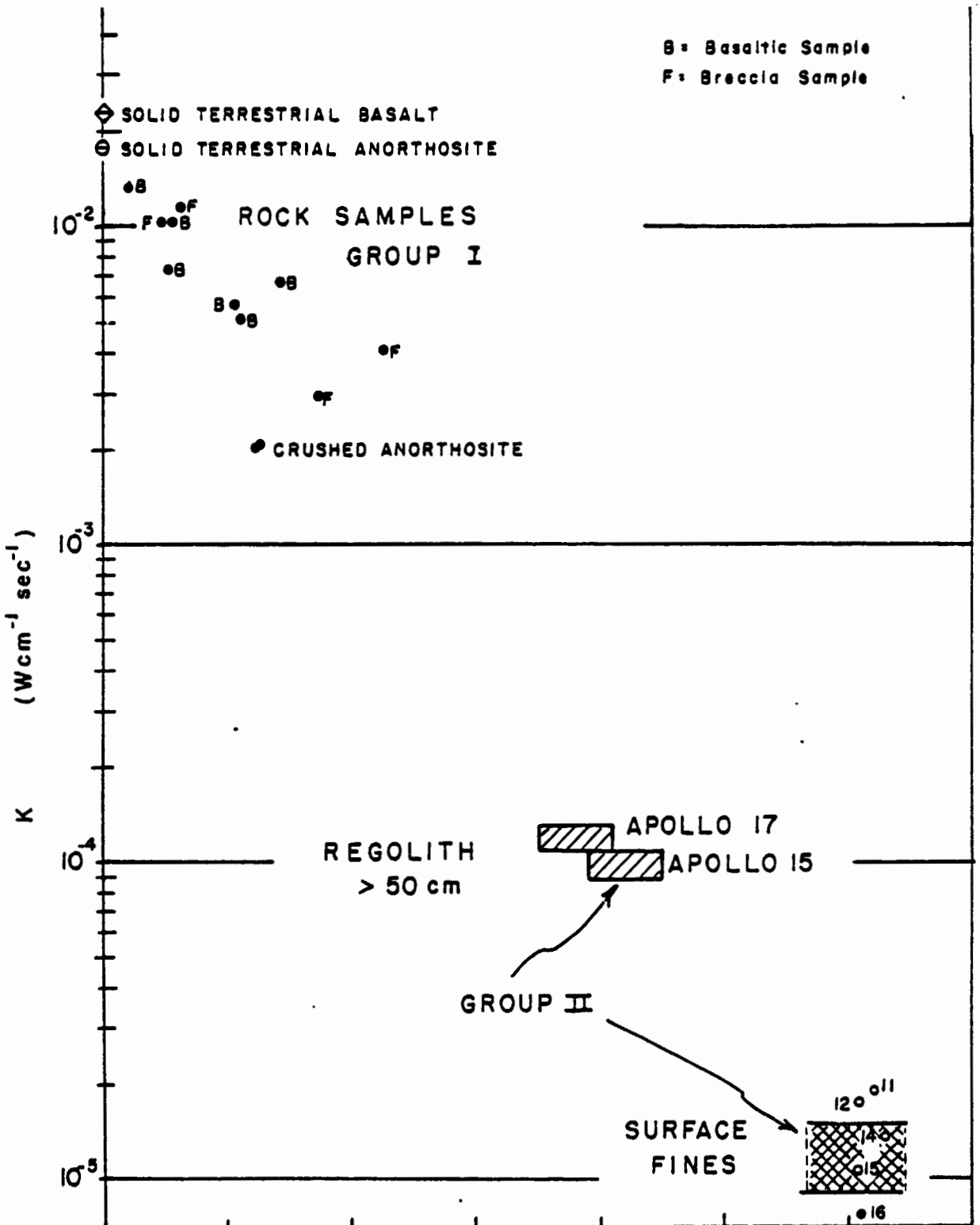

Published conductivity values of lunar materials vs. porosity. For laboratory measurements, values at 300°K are shown as points in the plot. The doubly hatched box is the range of in situ values determined from nighttime cooldown data (Keihm and Langseth, 1973) and the singly hatched boxes are the results reported in this paper. Rock data are summarized in Horai and Winkler (1976) and soil data in Cremers and Hsia (1973)

Figure VI-C-1

In Group II samples the inverse correlation of conductivity with porosity results from the smaller number of intergranular contacts in lower density material. The drive-tube samples show the density of regolith materials increases rapidly downward reaching densities of 1.8 - 2.0 g/cm^3 (Carrier, 1974) below 20 cm. Interpretations of cooldown of the surface during lunar night also indicate a rapid increase in conductivity with depth in the upper 10 cm (Keihm and Langseth, 1973). Values at 10-15 cm are similar to those we have deduced from analysis of long-term variations presented here. The soils at depths greater than 20 cm are near their maximum attainable density and, therefore, near the maximum attainable conductivity for Group II samples. The observed profile of conductivity in the regolith is no doubt determined by the impact history of particles of a few grams and less. The zone of rapid transition from low to higher conductivity corresponds to the depth where the net effects of impacts change from disruptive to compactive processes. Because the porosity profile and consequently the conductivity profile depend on the random impacts that have struck within a given area many times, the conductivity profile in flat regions of the moon should be uniform laterally, except near recent large craters.

The seismic velocity structure of the upper 1 km of the lunar surface has been defined by seismic refraction profiles made at three of the landing sites. These results show the acoustic velocity structure at all sites is very similar to a depth of about 75 m. Cooper et al. (1974) give a comprehensive summary of these results. Figure VI-C-2 shows the P-wave velocity structure reported at Taurus Littrow. Very low velocities of about 100 m/sec characterize the regolith layers. This velocity varied very little between the sites although the thicknesses of the layers at Apollo 14 and 16 sites are greater than at the Apollo 17 site. The velocities of underlying layers range from 250 to 350 m/sec. Only the Apollo 17 seismic experiment defined structure deeper than 100 m. The velocities to 1400 m are low compared to lunar rock samples, indicating that the materials are highly fractured or are rocky layers interbedded with low-velocity materials, even though the traverse gravimeter experiment (Talwani et al., 1973) suggests these layers have high densities (3.3 - 3.5 g/cm^3). The seismic results support the evidence that the extent of fracturing and comminution of near-surface materials determines the seismic velocity structure. These factors, which depend on the impact history of an area, also control the conductivity structure.

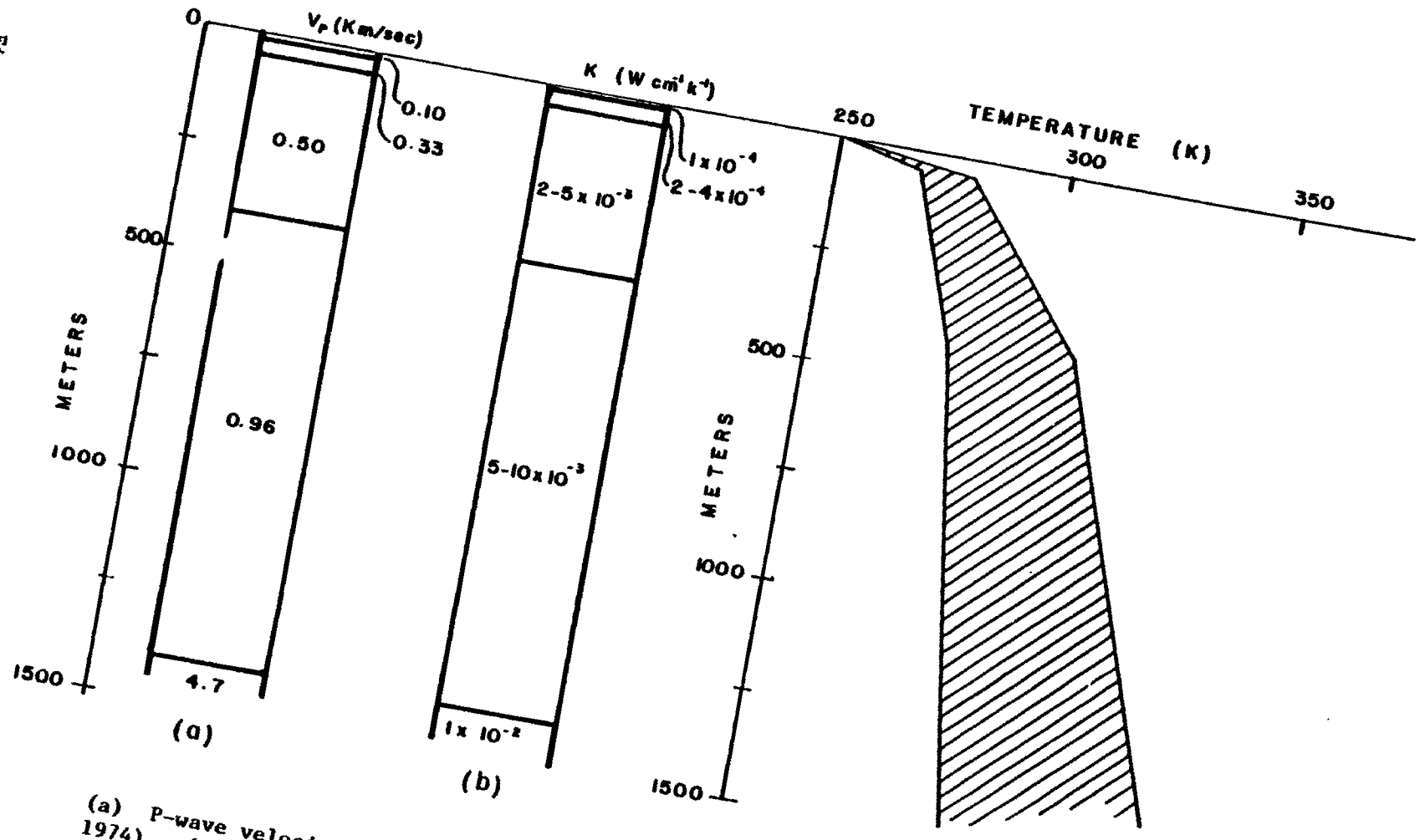

(a) P-wave velocity structure inferred for the Taurus-Littrow site (Cooper et al., 1974). (b) A feasible range of conductivity profiles based upon the porosity-conductivity relationships of Figure VI-C-1 and an interpretation of the seismic layers in terms of porosity. (c) Resultant range of temperature profiles, assuming a vertical heat flow of 1.6 $\mu W/cm^2$

By assuming that the velocity contrast at 30 m in Figure VI-C-2a corresponds to the interface between primarily disaggregate materials (Group II) and fractured but essentially intact rocky layers (Group I) we have estimated ranges of bulk conductivity, shown in Figure VI-C-2b and c, are shown bracketing temperature profiles corresponding to a uniform vertical heat flow of 1.6 $\mu W/cm^2$.

The laboratory and in situ measurements of the physical properties of lunar surface materials, though still very few, indicate that the conductivity structure of the upper 1 km of the moon is laterally uniform at a regional scale in level areas. Consequently, large-scale near-surface conductivity contrasts that are steeply sloping are unlikely to occur even at the margins of major geological provinces. At depths below 1 km the lower porosity will result in conductivity contrasts between rock types such as anorthosite and basalt. However, these contrasts are small and their refractive effects on surface heat flow will be muted by the overlying more uniform blanket of lower porosity material. Suggestions that the heat flow at Apollo 15 and 17 may be anomalously high by a factor of two or more because they are made at the edge of filled circular basins are not supported by existing data.

Although evidence suggests that at a regional scale the physical properties' structure of the upper 1 km is uniform over level regions of the moon, large physical properties contrast can occur at the scale of several meters. The large boulders scattered over the surface at all landing sites clearly attest to this. One cannot exclude a finite probability that measurements made to depths of 2 m are disturbed by refraction effects of such local heterogeneities. The change in heat flow with depth observed at probe 2 at Taurus Littrow no doubt results from such a local effect. although it is not necessarily due to conductivity contrasts.

References

Carrier, W.D., III (1974) Apollo drill core depth relationships, The Moon , v. 10, p. 183-194

Conel, J.E. and J.B. Morton (1975) Interpretation of heat-flow data. The Moon, v. 14, p. 263-289

Cooper, M.G., R.L. Kovach and J.S. Watkins (1974) Lunar near-surface structure Rev. Geophys. Space Phys., v. 12, p. 291-308

Cremers, C.J. and H.S. Hsia (1973) Thermal conductivity and diffusivity of Apollo 15 fines at low density. Proc. Lunar Sci. Conf. 4th, p. 2459-2464

Horai, K. and J.L. Winkler, Jr. (1976) Thermal diffusivity of four Apollo 17 rock samples. Proc. Lunar Sci. Conf. 7th.p. 3183-3204

Keihm, S.J., and M.G. Langseth (1973) Surface brightness temperatures at the Apollo 17 heat-flow site: Thermal conductivity of the upper 15 cm of regolith; Proc. Lunar Sci. Conf. 4th, p. 2503-2513

Mizutani, H. and M. Osako (1974) Elastic wave velocities and thermal diffusivities of Apollo 17 rocks and their geophysical implications; Proc. Lunar Sci. Conf. 5th, p. 2891-2901

Talwani, M., G. Thompson, B. Dent, H.G. Kahle and S. Buck (1973) Traverse gravimeter experiment; in, Apollo 17 Preliminary Science Report, NASA Publ. SP-330, p. 13-1 to 13-13

*.

VI-D. COMPARISON WITH MICROWAVE OBSERVATIONS

It has long been realized that the opacity of the lunar surficial material to electromagnetic waves decreases with increasing wavelength. Thus, whereas observations of the moon's infrared emission indicated surface temperature variations, observations at longer wavelengths (in the millimeter and microwave spectral region) yielded information related to the subsurface temperature profile. The primary difficulty in interpreting the microwave results lay within the problem of the interdependence of the thermal and electrical properties and their possible variation with depth and temperature. Additionally, most of the observations have been subject to large errors in absolute calibration resulting in large scatter among all of the data.

In the absence of more definitive information of the physical properties of the surficial material, the standard procedure for interpreting microwave observations has been the following: Assuming a locally plane parallel semi-infinite medium, the electromagnetic energy flux (expressed in terms of brightness temperature), leaving the surface at angle θ_e relative to the local normal, is expressed in the form

$$T_b(\lambda,\ t,\theta_e) = [1-R(p,\theta_e)]\sec\theta_i \int_0^\infty \kappa_\lambda(z,T)\ x\ T(z,t) e^{-\int_0^z \kappa_\lambda(z'T)\sec\vartheta_i\, dz'} dz, \qquad \text{(VI-D-1)}$$

where $T_b(\lambda,t,\theta_e)$ is the equivalent brightness temperature expressed as a function of the wavelength λ, time of lunation t, and the emerging angle θ_e; $R(p,\theta_e)$ is the intensity reflection coefficient dependent on the state of polarization p, and θ_e; θ_i is the angle at which the observed radiation impinges on the surface from below and is related to θ_e by Snell's law; $\kappa_\lambda(z,T)$ is the power attenuation coefficient expressed as a function of depth z and temperature T.

Equation (VI-D-1) is a generalization of the equation given by Piddington and Minnett, 1949. The Rayleigh-Jeans approximation is assumed valid for the lunar situation at microwave frequencies. Equation VI-D-1 also assumes that the attenuation coefficient κ_λ, is purely absorptive with no scattering component and does not take into account the possibility of ray-path bending due to possible inhomogeneities in the regolith material. Additionally, Equation VI-D-1 yields

the equivalent brightness temperature that would be observed by an antenna beam sufficiently narrow so that the surface area included in the beam is small enough to be considered planar. In actuality, the observations are made with antenna beam widths which necessarily average the radiation over a large portion of the lunar disk including a range of emergent angles.

At longer wavelengths, the entire disk contributes to the observed radiation. Krotikov (1963) has derived a formula to convert disk center brightness temperature to disk average temperatures assuming homogeneous regolith properties. The conversion formula is primarily a function of the real part of the dielectric constant. For wavelengths less than 3 cm, many of the observations have been made for the disk center; i.e., the antenna beam width are smaller than the disk. Because the intensity contribution away from the disk center varies according to a cosine law, the predominant contribution for such observations comes from the area near disk center. Thus, these observations can be compared directly with little loss of information to theoretical models governed by Equation VI-D-1 with $\theta_e = \theta_i = 0$

Because of the averaging character of the observations and the inherent accuracy limitations of the remote measurements, Equation VI-D-1 has been used mainly in the simplified form in which the lunar regolith properties are assumed homogeneous in depth and independent of temperature. The assumption of homogeneity allows the temperature profile T(z,t) to be expressed as a Fourier time series in terms of the harmonic amplitudes of the surface temperature variation and the thermal attenuation coefficient for each of n harmonics, $\beta_n = [n\omega\rho c/2\kappa]^{1/2}$, where ω is the lunation frequency and ρ, c, and κ are respectively the density, specific heat, and thermal conductivity of the material (Carslaw and Jaeger, 1959, p. 63-70). Equation VI-D-1 can then be solved for the Fourier components of the lunation brightness temperature variation (Muhleman, 1972). The resultant brightness temperature amplitude components are related to the surface temperature components through the empirical parameter $\delta_n = \beta_n/\kappa_\lambda$, the ratio of the thermal to electrical attenuation coefficient for the nth harmonic:

$$T_{bn}(\lambda) = [1 - R(p)]\, T_n / [1 + 2\delta_n + 2\delta_n^2]^{1/2} \qquad \text{(VI-D-2)}$$

where $T_{bn}(\lambda)$ is the nth component of the observable brightness temperature at disk center and T_n is the nth component of the surface temperature diurnal variation at disk center.

The microwave observations have been analyzed in terms of a mean temperature and the amplitude and phase shift of the fundamental frequency. The standard procedure has been to derive the fundamental parameter, $\delta_1 = (\omega\rho c/2k)^{1/2}/\kappa_\lambda$, from the observations of T_{bo}/T_{b1}, which is the ratio of the mean to the amplitude of the first harmonic:

$$T_{bo}/T_{b1} = (T_o/T_1)(1 + 2\delta_1 + 2\delta_1^2)^{1/2} \qquad \text{(VI-D-3)}$$

The ratio T_{bo}/T_{b1} can be determined directly from the observations with inaccuracies due to calibration errors minimized. The only sources of data for the mean to first harmonic ratio of surface temperature prior to the lunar missions were the infrared observations during lunar night. Daytime surface temperature variations are controlled mainly by the solar insolation, surface topography and the radiative properties of the surface. Troitsky, 1965, adopted a value of $\delta_1 = 2.0\lambda$ based on measurements between 0.1 and 3.2 cm and a value of $T_o/T_1 = 1.5$. Corrections for moonwide averaging effects were applied.

The interpretation of the empirical parameter δ_1, in terms of electrical properties of the surficial material cannot be done unambiguously without an independent determination of the thermal properties. Prior to the more definitive measurements of the thermal properties from the Apollo missions, infrared observations of eclipse and lunation cooling curves were the primary source of thermal property information. The controlling parameter for the cooling curves is $\gamma = (\kappa\rho c)^{-1/2}$ (see, for example, Jaeger ,1953).

It was found that the eclipse data controlled by properties of the upper few centimeters at most, required a value of γ much higher than the lunation cooldown data which, because of its longer duration, reflected thermal properties from deeper layers down to about 20 cm. Values in the range γ = 250-350 ($cm^2 K\ W^{-1}\ sec^{-1/2}$) characterized the eclipse measurements and γ = 100-200 characterized the lunation nighttime curve. Selection of an appropriate thermal parameter γ, based on the infrared observations, then permitted an independent determination of the thermal absorption length once values for ρ and c were estimated from other information

$$\ell_T = \frac{1}{\beta_1} = \frac{1}{(\omega/2)^{1/2}\rho c\gamma}. \qquad \text{(VI-D-4)}$$

The telescopic observations reveal that almost no variation in the microwave brightness temperature of the lunar disk can be detected at wavelengths beyond about 5 cm. If one, therefore, assumes that the electrical attenuation coefficient is independent of depth for the effective emitting layers corresponding to $\lambda > 5$ cm, and that the thermal conductivity k, is uniform in depth and independent of temperature for these same layers, the disk center brightness temperature as a function of wavelength can be written from Equation VI-D-1 as

$$T_b(\lambda) = [1 - R(p)] \times \kappa_\lambda \int_0^\infty (T_o + q \cdot z/k) e^{-\kappa_\lambda z} \, dz \qquad \text{(VI-D-5)}$$

where q is the heat flow from the interior and q/k the uniform temperature gradient. The integral is elementary and yields

$$T_b(\lambda) = [1 - R(p)](T_o + (q/k)/\kappa_\lambda). \qquad \text{(VI-D-6)}$$

If we now assume that the reflection coefficient (or equivalently, the real part of the dielectric constant for the lunar situation) is independent of wavelength, we can write the spectral gradient directly by differentiating (VI-D-6)

$$\delta T_b/\delta\lambda = [1 - R(p)](q/k)(\delta \ell_\lambda/\delta\lambda) \qquad \text{(VI-D-7)}$$

(since $\kappa_\lambda = 1/\ell_\lambda$).

For the conditions known to exist in the lunar regolith, and if we neglect scattering, it can be shown (Muhleman, 1972) that the electromagnetic absorption length may be written in the form

$$\ell_\lambda = \lambda/(2\pi\varepsilon^{1/2}\tan\Delta) = c_1\lambda, \qquad \text{(VI-D-8)}$$

where ε = the real part of the relative dielectric constant and $\tan\Delta = 2\sigma/\varepsilon\nu$ is the loss tangent expressed in terms of the dielectric constant ε, and the electrical conductivity σ at frequency ν.

The form of Equation (VI-D-8), together with the assumption that $\tan\Delta$ be independent of wavelength (i.e., σ proportional to ν), has actually already been

utilized in the assumption that δ_1 is directly proportional to the wavelength.

Incorporating Equation (VI-D-8) into (VI-D-7) yields the heat flow directly:

$$q = k\,(\delta T_b/\delta\lambda)\; c_1^{-1}\,[1 - R\,(p)]^{-1} \qquad \text{(VI-D-9)}$$

where $c_1 = 1/(2\Pi\varepsilon^{1/2}$ tau $\Delta)$ is assumed wavelength independent. The spectral gradient, $\delta T_b/\delta\lambda$, can be computed directly from the observations at different wavelengths. Then, by using values of k and c_1 deduced by methods described previously and an R(p) value based on radar studies, an expected value of the heat flow can be calculated.

It is to be noted that independent deductions of the constant c_1 and the thermal conductivity k could only be made from remote observations of the infrared and short centimeter emissions which yield information characterizing only the upper $\sim$ 20 cm of the lunar regolith. Thus prior to the lunar landing missions, extrapolation of near surface properties to the greater depths was required for heat flow determinations to be made. For example, Baldwin(1961) estimated an upper limit of $q = 1.0 \times 10^{-6}$ W cm^2 based on a homogeneous thermal model proposed by Jaeger (1953), a derived lower limit of the electrical absorption length ℓ_λ, and a brightness temperature measurement at 168 cm. Russian investigators, using a new calibration technique called the 'artificial moon' method, made a series of high precision observations at wavelengths between 0.4 and 70 cm in 1961 through 1964 at the Radiophysics Research Institute (NIRFI) in the Soviet Union. Tikhonova and Troitsky (1969), postulating two layer models with a high density, high conductivity rock layer overlain by a less dense, less conductive regolith, and using thermal and electrical material properties deduced from the infrared and short centimeter ($0.1 < \lambda < 3.2$ cm) observations, estimated a lunar heat flow in the range $2.7 - 4.6 \times 10^{-6}$ W/cm^2 based on NIRFI observations. Additionally, they suggested that a regolith layer thickness between 3 and 13 m best fit observations of a decreasing spectral gradient for $\lambda > 30$ cm.

Observations made with the Arecibo radio telescope in 1969 suggest the possibility that at wavelengths between 69.8 and 406.5 cm the spectral gradient may be negative, i.e., the observed brightness temperature decreases with wavelength. However, the calibration difficulties involved in the detection of lunar thermal emissions at these long wavelengths make any strong reliance on these data extremely dubious. This point will be examined in more detail. Nevertheless, Salibury and Fernald (1971) assuming a power absorption length of

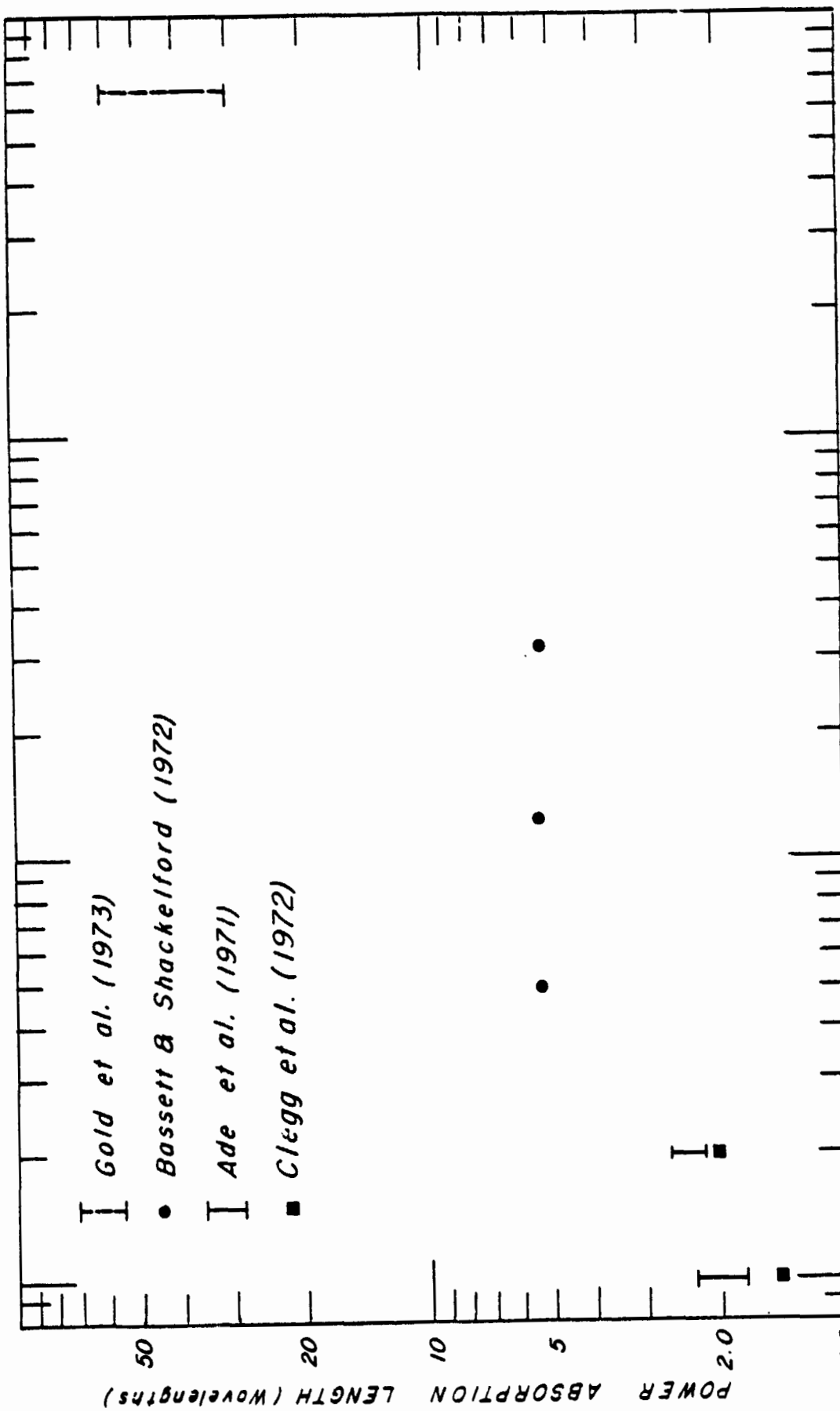

Figure VI-D-1

Wavelength dependence of the electrical absorption length in wavelengths from measurements on lunar powder samples. The data of Ade et al. (1971) and Clegg et al. (1972 correspond to densities of 1.25 and 1.18 g/cm^3; that of Bassett and Shackelford to a density of 1.80 g/cm^3 and Gold et al. (1973) to a density of 2.0 g/cm^3.

$\ell_\lambda = 40\ \lambda$, and accepting the observed negative spectral gradient as real, estimated a thermal temperature gradient of - 1/3 Km for depths corresponding to the observation wavelength emissions. They interpreted this result in terms of heat escaping the moon not by thermal conduction, but by the transpiration of volatiles from the lunar interior through the porous surface material. We postulate that, if the negative spectral gradient is real, it is not produced by a negative thermal gradient, but by the processes of scattering from debris layers tens of meters below the surface. Only the near linear portion of the brightness temperature spectrum ($5 < \lambda < 25$ cm) can be utilized in the determination of the lunar heat flow. Observations at longer wavelengths are most valuable in the interpretation of the structure of the deeper surface layers.

Electrical Absorption Length

In Figure VI-D-1, data are shown for the parameter ℓ_λ/λ for a number of different wavelengths between 0.1 and 68 cm. The data of Ade et al. (1971) correspond to a density of $\rho = 1.25$. The data of Clegg et al. (1972) are for a density of $\rho = 1.18$. The values at $\lambda = 0.5$, 1.25, and 3.2 cm were calculated from Equation VI-D-8 using the data of Bassett and Shackelford (1972) for the dielectric constant at $\rho = 1.8$ and a reported value of $\tan \Delta = 0.015$. The span of absorption lengths at 68 cm were taken from the data of Gold et al. (1973) at a density of 2.0 g/cm^3. The particular densities chosen correspond to the estimated densities at the depths of the primary emitting layers for a given wavelength. It can be seen from Figure VI-D-1 that the validity of Equation VI-D-8 assuming a nearly constant value of ε over the relevant wavelength range, requires a wavelength dependence of the loss tangent with a variation of $\tan \Delta = 0.040$ at $\lambda = 0.1$ cm to $\tan \Delta = 0.002$ at $\lambda = 68$ cm. Such a decrease in $\tan \Delta$ with wavelength is not expected based on measurements of dry dielectric materials which are characterized by a nearly frequency independent loss tangent for frequencies above 10^3 Hz (Strangway, 1969). Gold et al. (1973) have pointed out that even very slight atmosphere contamination may significantly increase the losses for a given sample measurement. Such contamination could be responsible for the low absorption lengths measured at the millimeter and short centimeter wavelengths. Clegg et al. (1972) postulate that scattering processes may be responsible for the absorption behavior at the millimeter wavelengths. Linsky (1973) points out that, at millimeter wavelengths, one may be seeing the low frequency tail of far infrared resonances and thus a frequency dependence of the

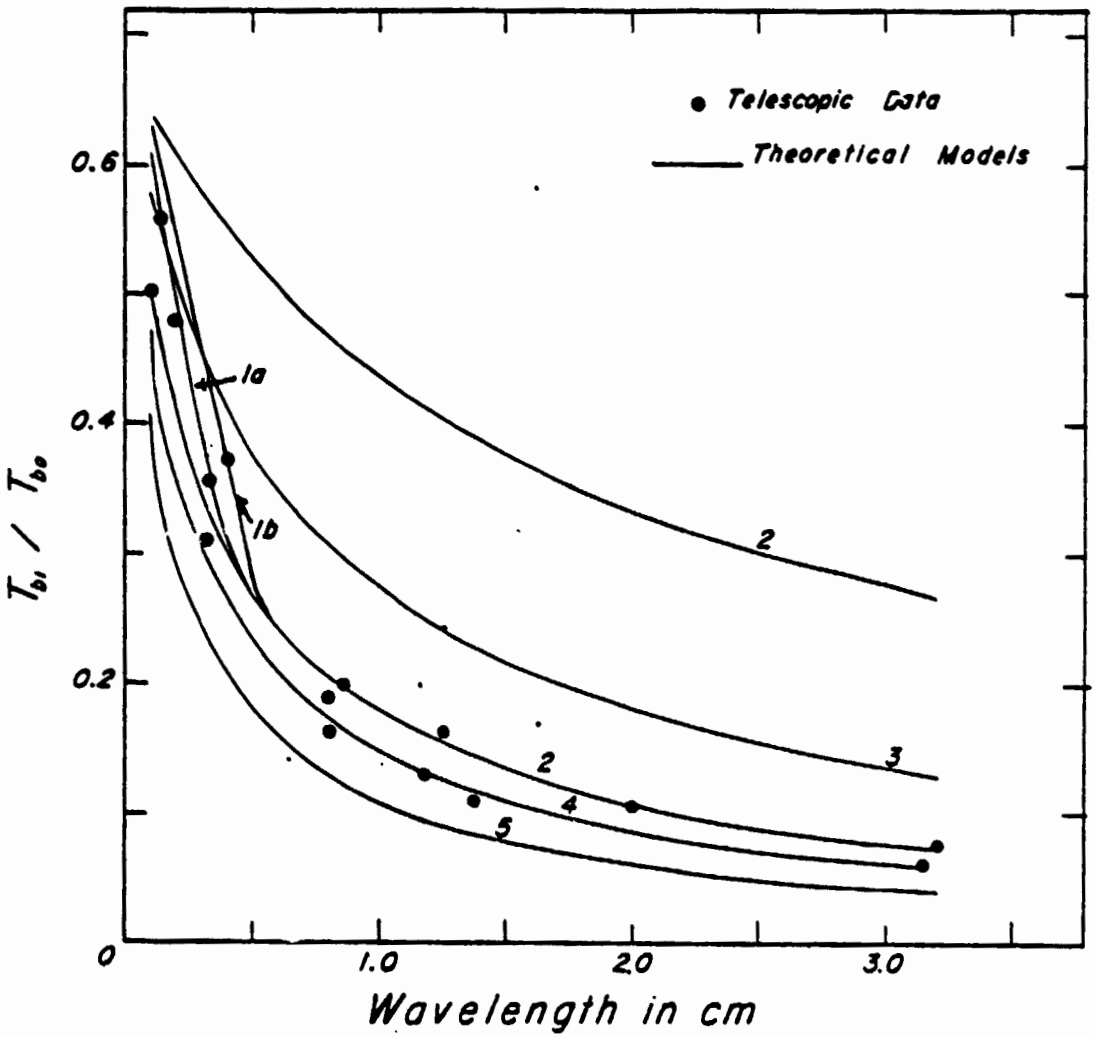

Ratio of the amplitude of variation to the mean brightness temperature over a lunation vs wavelength. The curves 1-7 are results of theoretical calculations based on Apollo 15 thermal properties and 7 different dielectric property profiles. 1) data of Bassett and Shackelford (1972). 2) $\ell_\lambda = \lambda$, 3) $\ell_\lambda = 3\lambda$, 4) $\ell_\lambda = 8\lambda$. 5) $\ell_\lambda = 12\lambda$. Curves 1a used the results of Ade et al., 1971 and 1b the results of Clegg et al. (1972) for $\lambda = 0.1 - 0.2$.

Figure VI-D-2

absorption length. It will be shown that the absorption behavior shown in Figure VI-D-1 fits the remote observations quite well. Relatively low absorption lengths are required to fit the 0.1 - 3.2 cm observations and significantly higher absorption lengths, near those measured by Gold and coworkers, are required to fit the 5-25 cm wavelength emission observations.

Compatibility of the Measured Physical Properties and the 0.1 to 3.2 cm Remote Observations

Millimeter and centimeter microwave emissions originate in the upper few centimeters of the lunar surface material where the thermal and electrical properties vary significantly with depth and there are large temperature fluctuations during the lunation cycle. Therefore constant property models cannot be used and Equation (VI-D-1) must be solved numerically, using physical property relationships derived from the available data. To obtain the temperature profile T(z), as a function of time of lunation, the heat conduction equation was solved, using the density and thermal conductivity profiles deduced for the Apollo 15 heat flow site. The functional relationship between ℓ_λ and density was taken from a linear fit to the calculated values of ℓ_λ/λ vs density based on the data of Bassett and Shackelford (1972). From these data we derive

$$\ell_\lambda/\lambda = 8.0 - 1.5\rho \qquad (\rho \text{ in g/cm}^3).$$

The curves shown in Figure VI-D-2 of the ratio of the fundamental amplitude to the mean T_{b1}/T_{bo}, as a function of wavelength result from the numerical solution of Equation (VI-D-1) with $\Theta_i = \Theta_e = 0$. The observational data points are taken from the review paper of Hagfors (1970). The comparison with disk center observations is quite good, considering the scatter in the data. The fit for the short millimeter wavelengths can be improved by incorporating the data of Ade et al. (1971) or Clegg et al. (1972), for $\lambda = 0.1 - 0.2$ cm into the numerical solution of Equation (VI-D-1) (see curves 2,3 in Figure VI-D-2). Curves 4-7 result from electrical property models in which ℓ_λ/λ does not vary with depth (density) and are shown to illustrate sensitivity to the T_{b1}/T_{bo} ratio of the electrical absorption length.

Shown in Figure VI-D-3 are the curves using the same ℓ_λ/λ functions of density but incorporating the thermal conductivity and density profile derived for the Apollo 17 heat flow site. It can be seen that the agreement is still good, although the higher T_{b1}/T_{bo} values obtained at the longer wavelengths

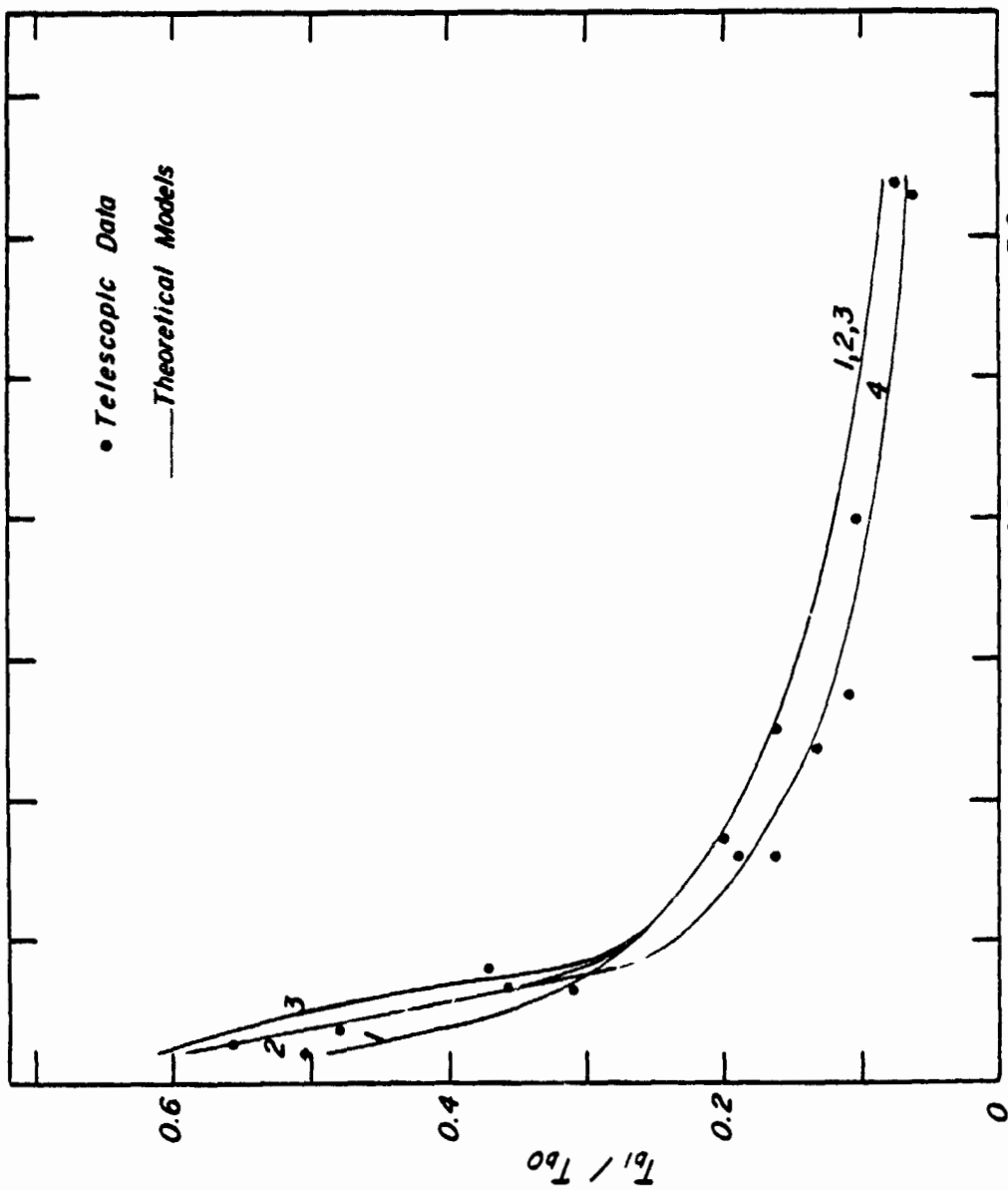

Figure VI-D-3

The same data as shown in Figure VI-D-2 are compared with theoretical models based on the deduced Apollo 17 thermal properties profile translated to 0° latitude. Solid curves 1-4 utilize the same electrical properties as models 1, 1a and b and 4 of Figure VI-D-2.

imply that slightly longer absorption lengths are required to best fit the observational data. In fact, model 4 fits the observations best using the $\ell_\lambda/\lambda = 8.0$ for $0.5 \leq \lambda \leq 3.2$, a value only slightly higher than the values of ℓ_λ/λ obtained from Bassett and Shackelford's data. The fact that the thermal properties derived from in situ data and the electrical absorption lengths measured for returned lunar samples produce good agreement with the 0.1 to 3.2 cm microwave data lends strong support to the representativeness of these physical property determinations for a large portion of the lunar surface to depths of 10-20 cm.

The 5-500 cm Emission Spectrum. Heat Flow Deductions and the Mean Depth of The Lunar Regolith

Diurnal variations in microwave emission for $\lambda > 5$ cm are very difficult to detect. This indicates that the primary emitting layers for wavelengths greater than 5 cm lie below the depths at which substantial diurnal variations and mean temperature changes due to the temperature dependence of the thermal conductivity are felt. The subsequent increase in brightness temperature with wavelength up to $\lambda \approx 30$-50 cm is thus due to the steady state thermal gradient in the lunar regolith.

Table VI-D-1 shows the observations upon which our deductions will be based. The data up to 70 cm wavelength is based on the artifical moon technique. The observations at 69.8 cm and three longer wavelengths were made at Arecibo by Salisbury and Fernald (1971). The stated accuracy of the Arecibo data is highly questionable. Problems of absolute calibration and substantial sky background have discouraged most radio astronomers from attempting measurements of the lunar thermal emission at wavelengths beyond 70 cm. The Arecibo data are included only as tangible evidence for the possibility of a negative spectral gradient existing at meter wavelengths.

The primary inferences drawn here depend only on the reliability of the Soviet data. The Soviet measurements represent the only observations made at a number of different wavelengths in the microwave band using a consistent calibration method. The Soviet data agree quite well, in absolute temperature levels, with models based on in situ thermal property determinations and measured subsurface temperature levels, expecially when the large scatter among other observations is considered. It must be pointed out, however that the importance of observed brightness temperature measurements to inferences of global heat flow and physical

TABLE VI-D-1. Lunar Disk Average Brightness Temperature Observations at Wavelengths Between 3 and 500 cm

Wavelength (cm)	Brightness/Temperature (K)	Error estimate (K)
3.2	213	± 4
9.6	218	± 5
11.0	219	± 6
14.2	221	± 5
20.8	225	± 5
25.0	226	± 6
30.2	227	± 7
35.0	236	± 8
36.0	237	± 6
40.0	224	±10
50.0	229	± 6
58.0	224	---
70.16	225	± 7
69.8	256.9	± 7
152.7	241.9	± 5
269.1	228.2	±10
406.5	214.8	±14

structure of the upper crust lies in the change of brightness temperature with wavelength. The spectral gradient between 5 and 20 cm wavelengths, upon which any inferences regarding global heat flow must be based, cannot be considered definitively accurate from a statistical viewpoint because of the short range of wavelengths relative to the absolute temperature uncertainties (see Table VI-D-1). In this regard, conclusions drawn of lunar global heat flow must be considered tentative until additional, more refined measurements can be made.

Inferences drawn regarding the average depth of the lunar regolith layer depend on the turnover in the spectral gradient between 30 and 70 cm wavelength suggested by the Russian data. The sharpness or precise location of the spectral peak is not as important to the implication of regolith thickness as the accuracy of the 5-20 cm spectral gradient is to the estimates of global heat flow. Because of the scatter in the four longest Russian observations, a more precise positioning of the spectral peak cannot be made, and only a range of feasible regolith thickness can be estimated.

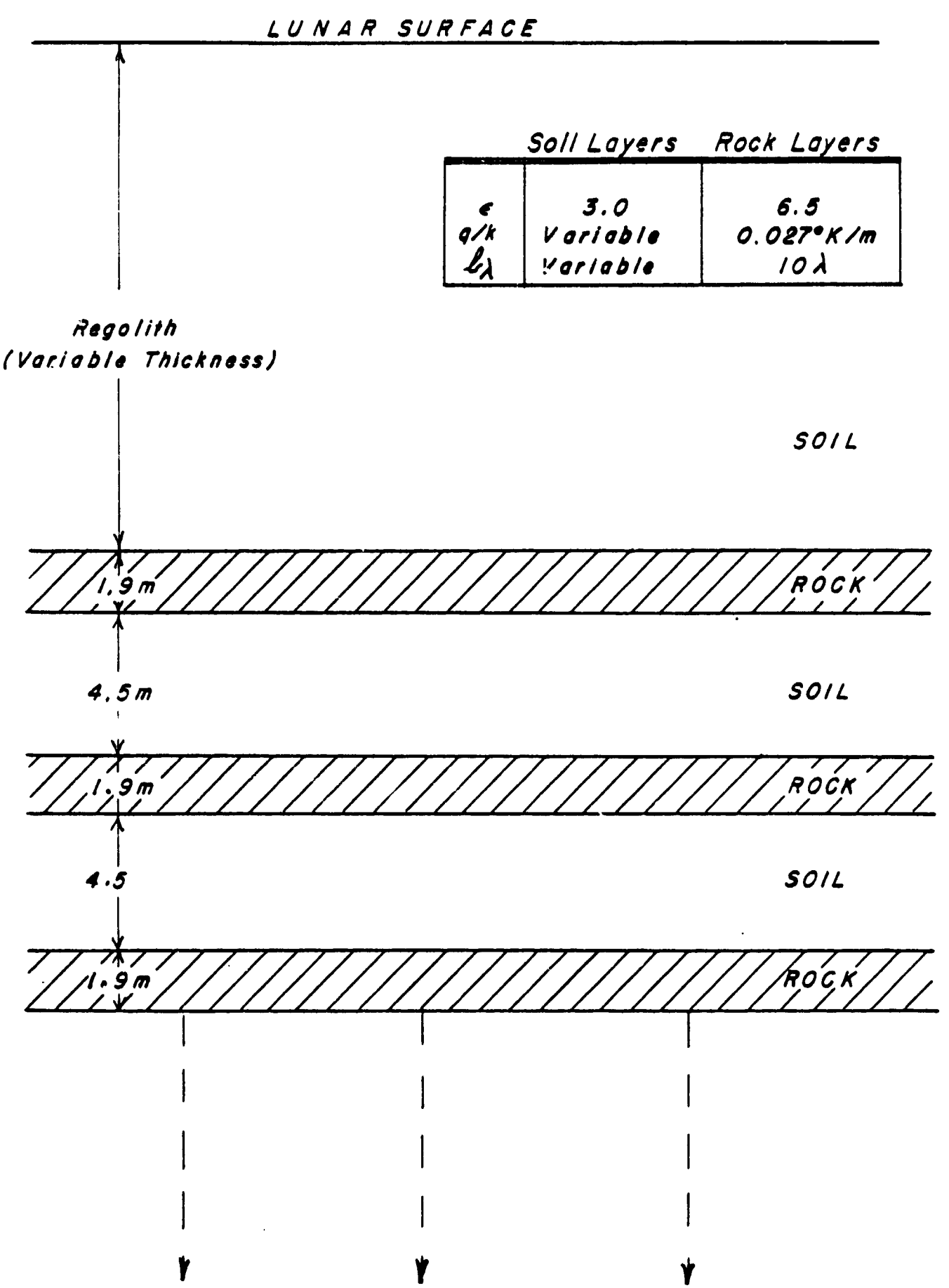

A schematic drawing of the multilayered models of the upper lunar crust. The designated physical properties are based on lunar in situ experiments and measurements on returned lunar samples.

Figure VI-D-4

Two features of the Russian data stand out. The near linear increase in brightness temperature with wavelength between 5 and 20 cm (see expanded scale of Figure VI-D-5) is consistent with a homogeneous regolith over the depth range from which the 5-20 cm waves originate. If regolith homogeneity were maintained to depths on the order of 100 m, a continuation of a linear emission spectrum to meter wavelengths would be expected. The observations, however, indicate a flattening of the emission curve beyond 20 cm followed by a possible decrease in brightness temperature at longer wavelengths. One explanation for a flattening of the emission curve is the possibility of increasing limb darkening effects at longer wavelengths. If the regolith density increased significantly over depths relevant to the 5-30 cm regolith material reaches a state of near maximum compaction within the upper 10-30 cm of the surface, lending support to the assumption of uniformity with depth for all but the very near surface material of the regolith (cf. Carrier et al. (1973)). Also, the thermal conductivity measurements at depths in the range 91-233 cm at the Apollo 15 and 17 sites showed only a slight trend toward higher conductivities at greater depths (Langseth et al., 1973). Most of the variation was more likely due to the presence of centimeter size rock fragments at different locations along the heat flow probes. Such small fragments would only negligibly affect the propagation of the longer wavelength emissions.

It should be pointed out that the seismic data (Kovach and Watkins, 1973) indicate that no widespread solid rock layers exist within 20-200 m of the lunar surface. However, the multilayered models are utilized only to demonstrate the feasibility of reflective scattering processes contributing to the observed negative spectral gradient for $\lambda > 30 - 70$ cm. The actual scattering is most likely due to a random distribution of large rocks and boulders within the rubble layers. The simplified models can, however, provide information related to the extent of the scattering and the average depth of layers with significant amounts of boulder size rocks.

The solution for the surface intensity observed for a two-layer model of regolith material overlying bedrock is presented in the paper of Tikhonova and Troitsky (1969). The general problem of N emitting layers is more complicated but can be solved using basically the same ray-tracing approach as was illustrated by Tikhonova and Troitsky.

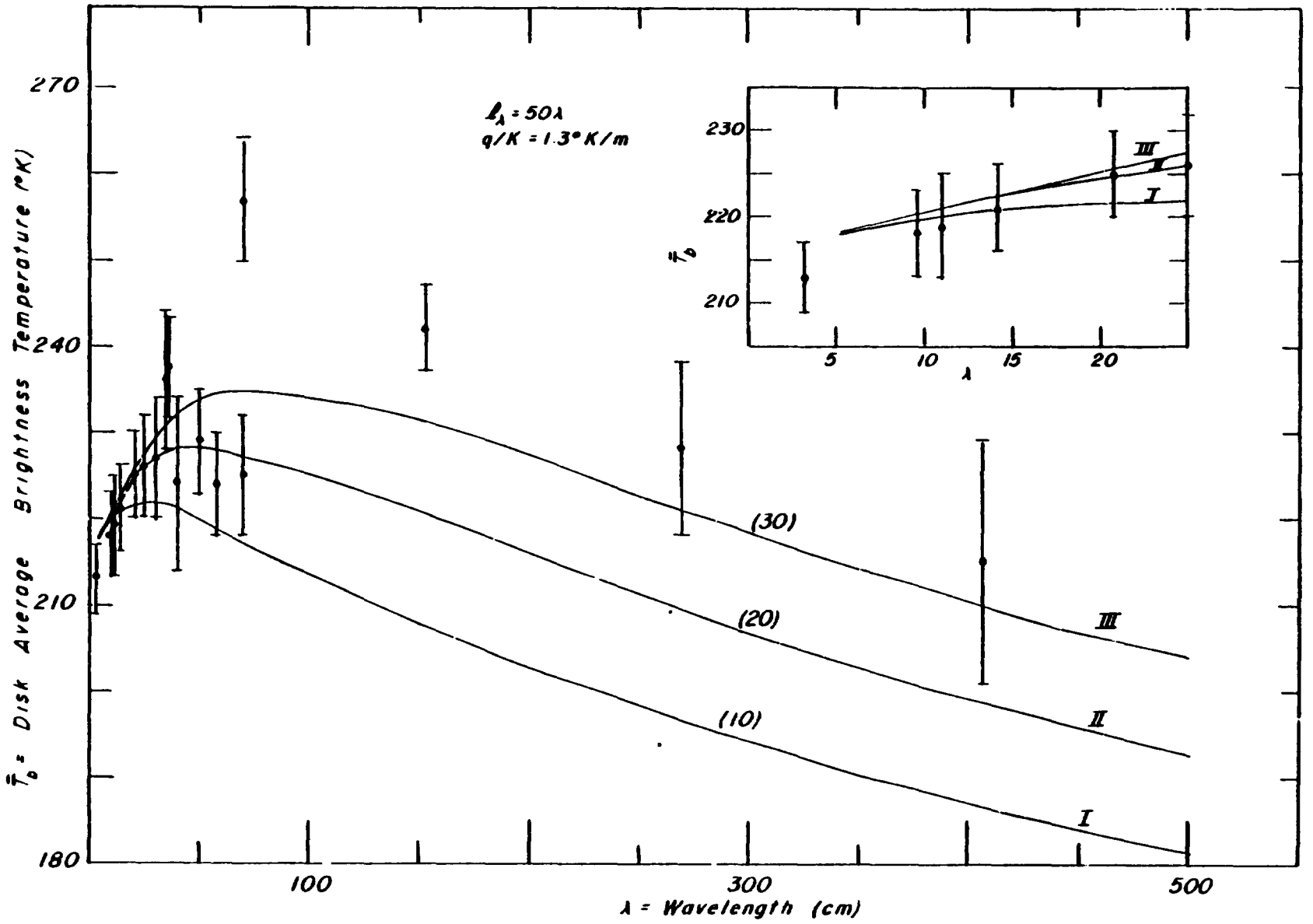

Figure VI-D-5

Wavelength dependence of the steady-state disk average lunar brightness temperature. Data points are taken from earth-based observations. The theoretical curves shown are based on multilayer models of the moon's upper crustal structure. The regolith thermal gradient utilized, 1.3 K/m is based on a mean heat flow of $3 \times 10^{-2} w/m^2$ and a mean thermal conductivity of 2.3×10^{-2} watt $m^{-1}K^{-1}$ measured at depths below 1 m at the heat flow sites.

The general method of solution is to replace the continuous distribution of sources in a given layer with two discrete sources, one located at the top of the layer radiating upward and one at the bottom of the layer radiating downward. Multiple reflections are taken into account. The next step is to calculate the power attenuation of each source as its energy propagates to adjacent layers above and below. These layer-to-layer transmission factors may then be used to calculate the contribution to the observable intensity emergent at the surface from each of the discrete sources. The total observable intensity is simply the sum of the intensities due to each of the sources. The multilayer solution for a given emergence angle θ_e will depend on the absorption coefficient κ_λ, real dielectric constant ε (through the reflection coefficient appropriate to each boundary) and the temperature distribution within each layer.

As discussed previously, the earth based observations for wavelengths greater than 5 cm necessarily average the emission over the whole disk. Thus, for a valid comparison of theory and observation, theoretical disk average brightness temperatures must be computed.

$$\bar{T}_b(\lambda) = \frac{1}{\pi} \int_{-\pi/2}^{\pi/2} \int_{-\pi/2}^{\pi/2} T_b(\phi,\psi,\lambda) \times \cos\psi \cos^2\phi \, d\psi \, d\phi, \quad \text{(VI-D-10)}$$

where $\bar{T}_b(\lambda)$ is the disk average theoretical brightness temperature observable from the earth and $T_b(\phi,\psi,\lambda)$ is the theoretical brightness temperature observable at lunar latitude ϕ and longitude ψ (relative to the subearth point) at an angle $\theta_e = \cos^{-1}(\cos\phi\cos\psi)$ relative to local normal.

For each particular multilayer model, solutions for $T_b(\phi,\psi,\lambda)$ were carried out for 81 different sets of lunar coordinates at 10° intervals in ϕ and ψ. Regolith and subsurface physical properties and layering configurations were considered invariant with ϕ and ψ. Temperature profiles at different lunar coordinates were adjusted for latitude.

In all of the theoretical models considered, the physical properties and spacing of the rock layers below the regolith were the same. The general geometry and physical properties which remained unchanged from model to model are shown in Figure VI-D-4. Values of $\varepsilon = 6.5$, $\ell_\lambda = 10\lambda$ and $q/k = 0.027$K/m were chosen for the rock layers based on the measurements of Gold et al. (1973) for ε and ℓ_λ; Horai and Simmons (1972) for k; and a mean heat flow of 3×10^{-6}W/cm^2 based on the Apollo 15 and 17 measurements (Langseth et al., 1973) A value of

$\varepsilon = 3.0$ was chosen for all the soil layers including the regolith based on the data of Gold et al. (1973) at a density of $\rho = 2.0$ g/cm^3 and the bistatic radar measurements of Tyler (1968). The particular spacing used for the rock soil alternating layers was chosen to produce the negative spectral gradient of $\sim$ -10 K/m observed at Arecibo for wavelengths beyond 70 cm. The particular physical parameters chosen for the subregolith reflecting layers are not critical in that a different set of parameters can be made to produce the - 10 K/m spectral gradient simply by varying the thicknesses of the reflecting layers. The spacings and physical properties of the subregolith layers have negligible effect on the 5-20 cm spectral gradient and location of the emission peak. Only the regolith properties and thickness substantially affect the emissions at wavelengths where the spectral gradient is positive.

In all models, the local temperature profile was considered to take the form

$$T(z,\phi) = T_o(\phi) + \int_o^z \frac{q}{k}\, dz \qquad \text{(VI-D-11)}$$

If each layer is homogeneous, the temperature in any layer n, can be written

$$T_n(z,\phi) = T_o(\phi) + \sum_{i=1}^{n-1} \frac{q}{k_i} a_i + \frac{q}{k_n}(z - d_{n-1}) \qquad \text{(VI-D-12)}$$

where $T_o(\phi)$ = the adjusted mean surface temperature at latitude ϕ ,

a_i = the thickness of layer i,

d_i = the depth to the lower boundary of layer i from the surface.

k_i = the thermal conductivity of layer i, and

q = the steady state heat flow.

Mean surface temperature variation with latitude ϕ was calculated using the thermal model established for the Apollo 15 heat flow site(Keithm et al., 1973) and the solar insolation function appropriate to a given latitude. 'Adjusted' mean surface temperatures $T_o(\phi)$ were calculated by adding the mean temperature difference observed in the upper few centimeters at Hadley Rille ($\sim$ 40K) to the surface mean calculated from the Hadley Rille thermal model applied at various latitudes. The large mean temperature gradient is confined to the upper few centimeters of surface material and has negligible effects on calculations of lunar emission for $\lambda > 5$ cm. Thus, the approximation of a constant regolith

Figure VI-D-6

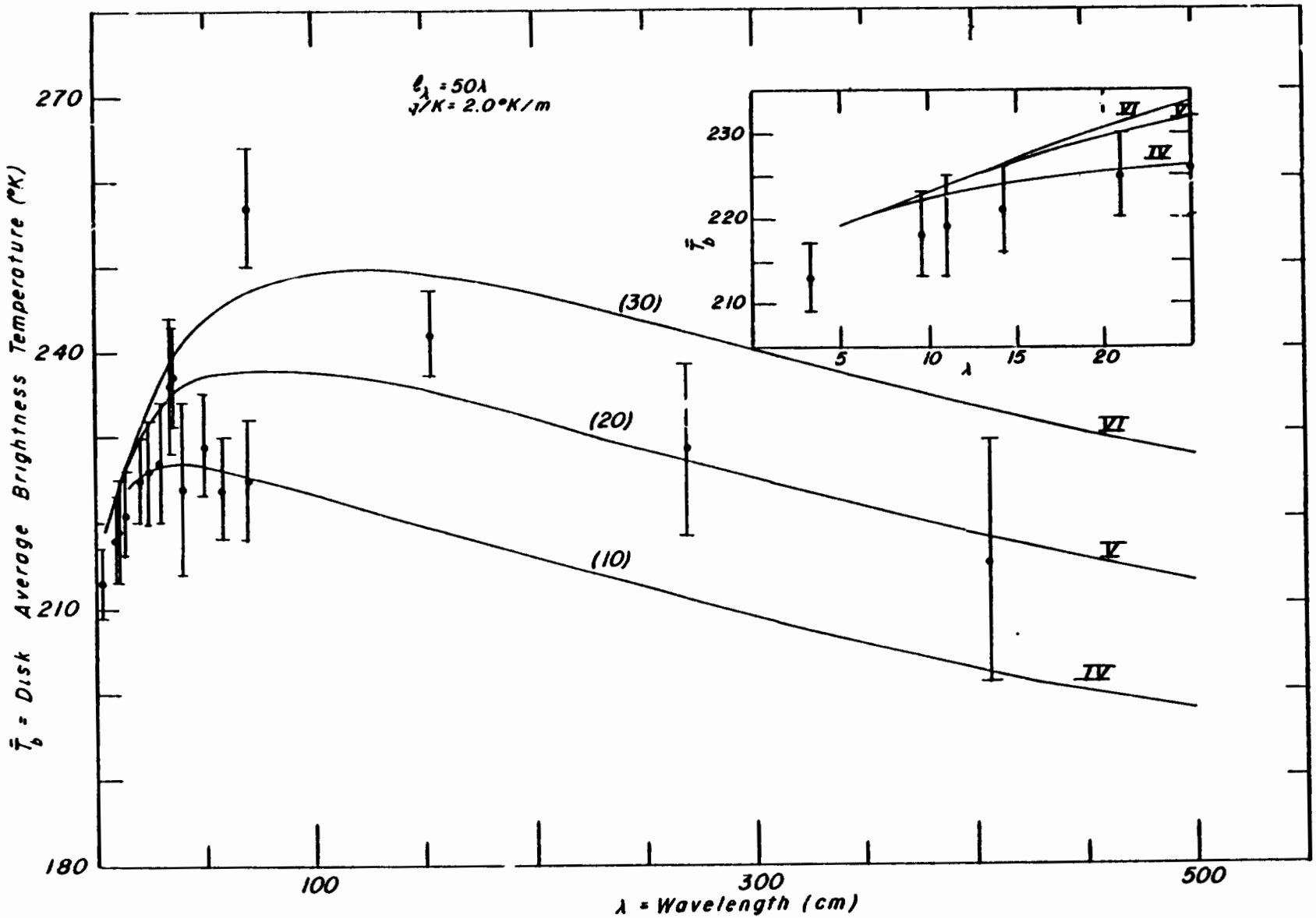

The same data and models as shown in Figure VI-D-5, with the exception that the models incorporate a regolith thermal gradient of 2.0 K/m, ∿ 50% higher than the mean gradient measured at meter depths at the Apollo 15 and 17 heat flow sites.

thermal gradient is still valid. However, the total mean temperature difference must be added to the actual mean surface temperatures to avoid a constant error $\sim$ 40 K in the subsurface temperature profiles

Theoretical results are shown in Figures VI-D-5 to VI-D-8 with the Russian and Arecibo data plotted for comparison. The inset of each figure repeats the 5-25 cm spectra on expanded scale to show more clearly the data relevant to global heat-flow determinations. The curves of Figure VI-D-5 are produced using the following regolith parameters:

$$q/k = 1.3 \text{ K/m} \quad ; \quad \ell_\lambda = 50\lambda \quad \text{[models of Figure VI-D-5]}$$

These values are based on the average gradient measured at the Apollo 15 and 17 heat flow sites (Langseth et al., 1973) and the absorption length measurements on Apollo 15 and 16 samples (Gold et al., 1973). The three models shown are distinguished by varying regolith thicknesses. For a fixed absorption length and thermal gradient, the regolith thickness controls the level and wavelength at which the emission maximum is reached. At wavelengths beyond the wavelength of maximum brightness temperature, the effective emitting layers lie substantially within the rubble or reflecting layers. Thus, energy loss through multiple reflections limits the observable longer wavelength intensities despite the fact that the effective emitting material is at higher temperatures. It can be seen from Figure VI-D-5 that a regolith thickness of $\sim$ 20 m produces a disk average brightness temperature maximum between 40 and 50 cm wavelength, compatible with the observations.

In the same vein, it can be seen from the inset of Figure VI-D-5 that the regolith thickness also controls the range over which the spectral gradient remains linear. At wavelengths for which the effective emitting layers lie substantially above the reflecting layers, the spectral gradient remains nearly constant in accordance with Equations (VI-D-7) and (VI-D-8). In this respect, the models of Figure VI-D-5 indicate that a regolith thickness of 20-30 cm is required to maintain a near linear emission spectrum out to 20 cm wavelength.

The linear portion of the spectrum must be used to estimate global heat flows and regolith properties. The magnitude of the near linear spectral gradient is controlled by the thermal gradient q/k, and the electrical absorption length ℓ_λ. All of the models shown in Figure VI-D-5 produce spectral gradients that are less than that observed by the Russians over the 5-20 cm wavelength band.

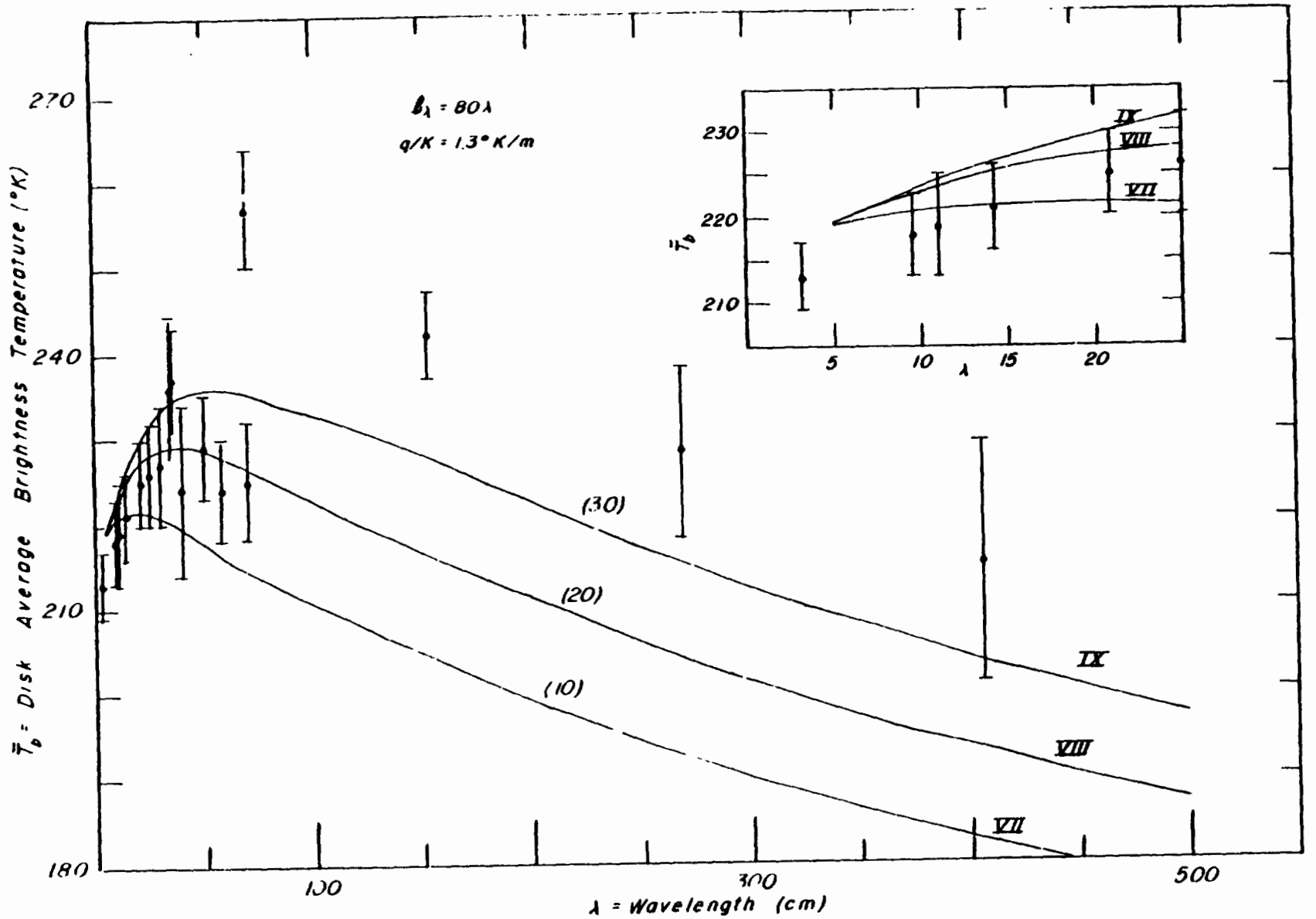

The same data models as shown in Figure VI-D-5, with the exception that the models incorporate a regolith electrical absorption length of $\ell_\lambda = 80\ \lambda$, a value near the upper bound of the measurements of Gold et al. (1973).

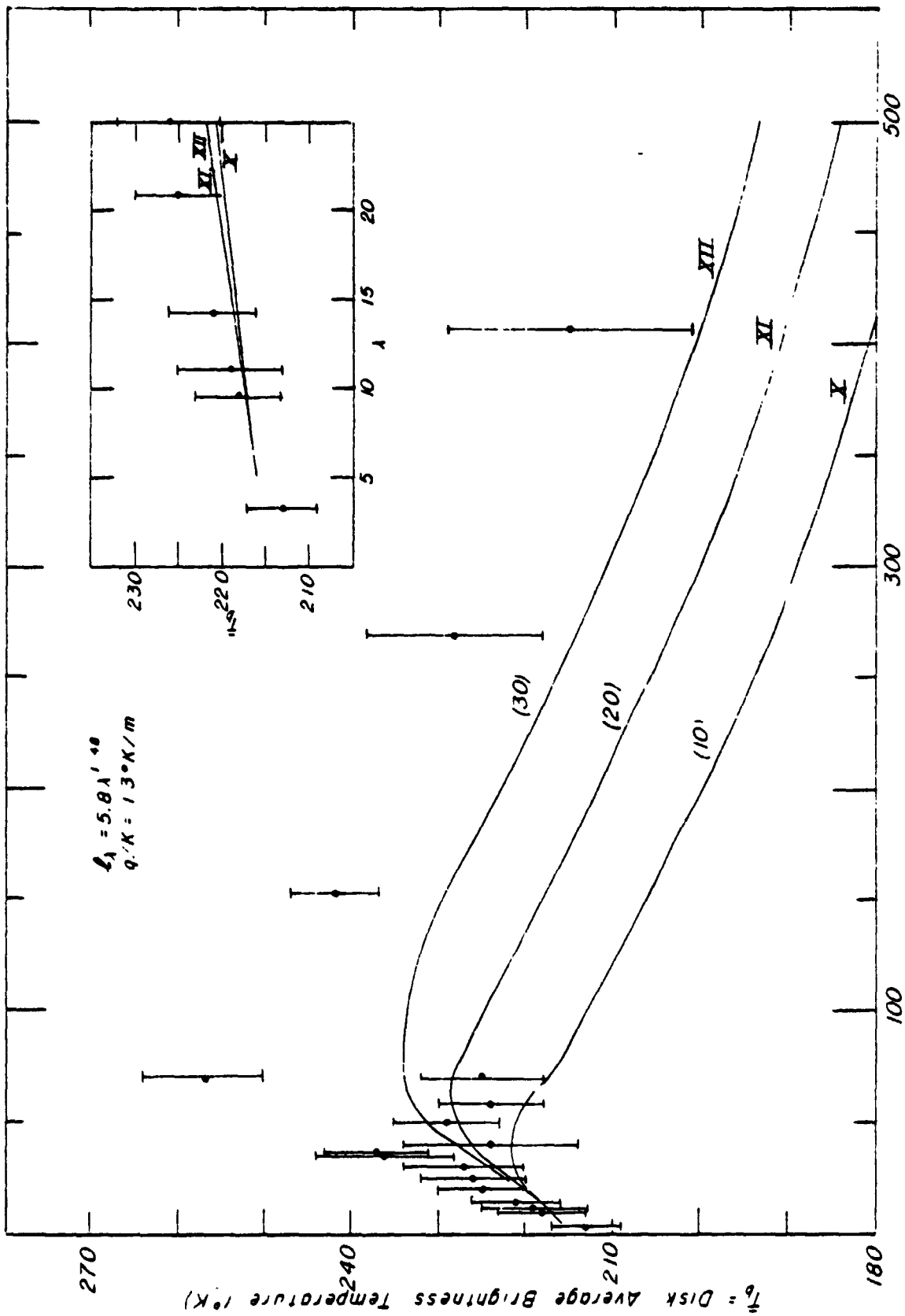

The same data and models as shown in Figure VI-D-5, with the exception that the models utilize a power fit to the regolith absorption lengt! from the data of Figure VI-D-1

Figure [illegible]-6

Equation VI-D-7, used as an approximation to the disk average spectral gradient, indicates that a larger spectral gradient requires either a larger thermal gradient or longer absorption lengths.

The emission curves of Figure VI-D-6 are produced using a thermal gradient of 2.0 K/m, larger by a factor of one half than the mean value measured at the heat flow sites. The 5-20 cm spectral gradient now matches the Russian data quite well if a 20-30 m regolith thickness is used, although the absolute brightness temperatures lie near the upper error estimate of the observations. The absolute brightness temperatures are dependent on the global distribution of mean surface temperature assumed in the models. Errors of 5-6 K could result from extrapolation of the Apollo 15 and 17 observations. The most serious discrepancies of models V and VI lie in the spectral range 20-70 cm where the high brightness temperatures reached exceed the Russian observations by 15-25 K.

A method for increasing the 5-20 cm spectral gradient without significantly increasing longer wavelength brightness temperatures is illustrated by the models of Figure VI-D-7. In these models, an electrical absorption length of $\ell_\lambda = 80\lambda$ is assumed. This value is near the maximum measured by Gold et al. (1973) at a 68 cm wavelength on lunar samples. Model IX produces good agreement with the Russian spectral gradient for $5 < \lambda \leq 20$ cm although a mean regolith thickness of at least 30 m is now required to maintain the linearity of the spectrum out to 20 cm wavelength. This is due to the fact that, because of the longer absorption lengths, the effective emitting layers begin to lie within the reflecting rubble layers at shorter wavelengths. Such a regolith thickness is two to three times greater than that inferred from active seismic data (Kovach and Watkins, 1973).

It is to be noted that all of the models shown in Figures VI-D-5, 6 and 7 apply electrical absorption length data at 68 cm wavelength to the entire spectral band from 5 to 500 cm. It is quite possible that the absorption constant ℓ_λ/λ, varies substantially over this large wavelength band as suggested by the data of Figure VI-D-1. To examine the feasibility of a systematic increase in ℓ_λ/λ with wavelength, we have fit a power curve to the data of Figure VI-D-1 to obtain $\ell_\lambda/\lambda = 5.8\lambda^{1.48}$. The resultant theoretical curves are shown in Figure VI-D-8. Note that the 5-20 cm spectral gradient is much less than the observations. A thermal gradient of $\sim$ 3.0 K/m would be required to match the data, indicating either a global heat flow more than twice that measured at the Hadley Rille and Taurus Littrow sites or a mean regolith conductivity less than half the mean value measured at the heat-flow sites. If the interpolative formula for

ℓ_λ/λ does apply to the average regolith material, however, a mean regolith thickness of 10-15 m would be sufficient to match the wavelength at which the observational maximum occurs (30-70 cm). Such a regolith thickness is in good agreement with the seismic data.

One point is quite clear from all of the models. If the Russian data are accepted at face value, the regolith thermal gradient measured at the two lunar heat flow sites lies at the lower end of the range of likely moonwide average values. Higher gradients could be explained without increasing the heat flow if over much of the nearside of the moon, regolith conductivities were 30-50% lower than those measured at the heat-flow sites. Slightly less compact regolith material than that found at the mare heat flow sites would be characterized by lower thermal conductivities and longer absorption lengths, effectively increasing the spectral gradient between 5 and 20 cm wavelength.

References

Ade, P.A., J.A. Bastin, A.C. Marston, S.J. Pandya and E. Puplett (1971) Far infrared properties of lunar rock. In, Proc. Lunar Sci. Conf. 2nd, v. 3, p. 2203-2211.

Baldwin, F.E. (1961) Thermal radiation from the moon and the heat flow through the lunar surface. Mon. Not. Roy. astron. Soc., v. 122, p. 513-622.

Bassett, H.L., and R.G. Shackelford (1972) Dielectric properties of Apollo 14 lunar samples at microwave and millimeter wavelengths. In, Proc. Lunar Sci. Conf., 3rd, v. 3, p. 3157-3160.

Carrier, W.D., III, J.K. Mitchell and A. Mahmood (1973) The relative density of lunar soil. In, Lunar Science IV , eds. J.W. Chamberlain and C. Watkins, Lunar Sci. Inst., Houston, p. 118-120.

Carslaw, H.S. and J.C. Jaeger (1959) Conduction of Heat in Solids, Oxford University Press, London

Clegg, P.E., S.J. Pandya, S.A. Foster and J.A. Bastin (1972) Far infrar[illegible] properties of lunar rock. In, Proc. Lunar Sci. Conf. 3rd, v. 3, p. 3035-3045

Gold, T., E. Bilson and M. Yerbury (1973) Grain size analysis and high frequency electrical properties of Apollo 15 and 16 samples. In, Lunar Science IV, eds. J.W. Chamberlain and C. Watkins; Lunar Sci. Inst., Houston, p. 293-295

Hagfors, T. (1970) Remote probing of the moon by infrared and microwave emissions and by radar. Radio Science, v. 5, p. 189-227

Horai, K. and G. Simmons (1972) Thermal property measurements on lunar material returned by 11 and 12 missions. In, Thermal Characteristics of the Moon ed , J.W. Lucas; Progress in Astronautics and Aeronautics, v. 28, p. 243-267, M.I.T. Press, Cambridge, Mass.

Jaeger, J.C. (1953) The surface temperature of the moon. Austral. J. Phys. v. 6, p. 10-21

Keihm, S.J., K. Peters, M.G. Langseth, Jr., and J.L. Chute, Jr., (1973) Apollo 15 measurement of lunar surface brightness temperatures: Thermal conductivity of the upper 1 1/2 meters of regolith. Earth Planetary Sci. Lett., v. 19, p. 337-351

Kovach, R.L. and J.S. Watkins (1973) The velocity structure of the lunar crust. The Moon, v. 7, p. 63-75

Krotikov, V.D. (1963) A contribution on total lunar electromagnetic radiation from the moon. Radiofizika, v. 6, p. 889

Langseth, M.G., Jr., J.L. Chute, Jr. and S.J. Keihm (1973) Direct measurements of heat flow from the moon. In, Lunar Science IV, eds. J.W. Chamberlain and C. Watkins; p. 455-456, Lunar Sci. Inst., Houston

Linsky, J.L. (1973) The moon as an absolute calibration source for astronomical microwave and infrared observations. Preprint.

Muhleman, D.O. (1972) Microwave emissions from the moon. In, Thermal Characteristics of the Moon, ed. J.W. Lucas, Progress in Astronautics and Aeronautics, v. 28, p. 51-81, M.I.T. Press, Cambridge, Mass.

Piddington, J.H. and H.C. Minnett (1949) Microwave thermal radiation from the moon. Austral. J. Sci. Res., v. 2A, p. 63-77

Salisbury, W.W. and D.L. Fernald (1971) Subsurface temperature of the moon. J. Astronautical Sci., v. 18, p. 236-243

Strangway, D.W. (1969) Moon: electrical properties of the uppermost layers. Science, v. 165, p. 1012-1013

Tikhonova, T.V. and V.S. Troitsky (1969) Effect of heat from within the moon on its radio emission for the case of lunar properties which vary with depth. Soviet Astronomy - AJ, v. 13, p. 120-128

Troitsky, V.S. (1965) Investigation of the surface of the moon and planets by the thermal radiation. Radio Sci., v. 69D, p. 1585-1611

Tyler, G.L. (1968) Oblique-scattering radar reflectivity of the lunar surface: Preliminary results from Explorer 35. J. Geophys. Res., v. 73, p. 7609-7620.

*

VII. SIGNIFICANCE OF THE HEAT-FLOW RESULTS

A. HEAT-FLOW AND SURFACE THORIUM ABUNDANCES

The heat flows reported in Section V-D indicate that the measurement at Hadley Rille is significantly higher than that observed at Taurus Littrow. There is no reason to prefer one measurement relative to the other as representative of the global heat-flow based on an assessment of local disturbances (see Section VI). The orbiting gamma-ray experiment flown on Apollo 15 and 16 (Metzger et al., 1974; Bielefeld et al., 1976) showed the western mare plains of the moon's nearside to have relatively high abundances of thorium at the surface. Over the eastern margin of Imbrium, the surface abundance of thorium is over two times higher than over Taurus Littrow which suggests that the higher heat flow at Hadley Rille may be related to the higher thorium abundances. These high relative abundances are probably confined to a near surface layer. If the abundance detected by the gamma-ray experiment represented abundances uniformly distributed in a 60 km thick crust, then the very high surface concentrations such as those observed over the Archimedes and Fra Mauro regions cannot be representative of average lunar crustal abundances as they would lead to unreasonably high heat flows and near melting temperatures at the base of the crust. In Figure VII-A-1, the dashed line shows the heat flow at the surface of a 60 km crust as a function of thorium abundance assuming a K/U ratio of 3200 and a Th/U ratio of 3.7 higher than the earth's average heat flux! Furthermore, the temperature at the base of a 60 km crust would be nearly 1200°C which would place material there very close to the solidus. Consequently, the high thorium concentrations observed by the gamma-ray experiment over Oceanus Procellanum must be a surficial enrichment in thorium rich materials.

Interpretations of geothermal measurements on earth have revealed a persistent correlation of heat flow with the surface abundance of heat producing isotopes. The correlations are most striking in regions that are tectonically older (Mesozoic or older; see, for example, Birch et al., 1968 and Lachenbruch 1970). The correlation within a large geographic region is linear and described by the relation $q = q^* + D\,A(o)$; where q^* is the intercept and $A(o)$ the heat production. When a line is best fitted to the heat flow and heat production data, it extrapolates the zero heat production axis to yield a positive heat-flow value, q^*, interpreted as the heat flow into the base of the crust.

Two models have been proposed to explain the observed linear relationship. The first proposed by Birch et al. (1968) has the heat producing isotopes concentrated uniformly in a surface layer of finite thickness D. This thickness is given by the slope of the linear fit to the data. For the eastern United States the average thickness determined is 8 to 10 km. The second alternative model was proposed by Lachenbruch (1970). It assumes that the abundance of heat producing isotopes decreases exponentially with depth in the crust with the logarithimic decrement D. Lachenbruch (1970) has also pointed out that a linear decrease of isotopes would satisfy the relation. Lachenbruch further shows that, of the three models, only the exponentially decreasing source with depth remains valid under differential erosion, which is a highly likely circumstance on earth.

It may be overly optimistic to apply the relation to two points for the moon; nonetheless, this is done in Figure VII-A-1 and is shown by the solid line. The value of q* is seen to be 0.9μW cm^{-2} and slope D is 19 km. The value of 0.9 μW cm^{-2} for the heat flow into the base of the crust is within the range of values calculated by another analysis given in Section VII-B. There is already evidence that the value D cannot be applied to the lunar crust in a manner that fits well for the earth's crust. Firstly, Metzger et al. (1974) have noted the very strong inverse correlation between surface thorium abundance and elevation of the lunar surface. The very lowest abundances are observed over the highest farside regions. Unless there are enormous lateral variations in the crustal abundance of radioisotopes, this correlation suggests that the heat production increases with depth, at least to depths of a few kilometers. This is exactly opposite to what is observed on earth. Secondly, the surface abundance of thorium seems to correlate most strongly with the extent of mare forming volcanism on the surface and inversely with the age of the mare volcanism.

It seems a reasonable conjecture that the surface thorium abundance correlated with intrusive type volcanism in the lunar crust as well. It has been suggested by several investigators that the upward extent of magma flooding or injection was controlled by internal stress (essentially hydrostatic) and equipotential surfaces at the time of injection. This model would fit the observed inverse correlation of elevation and surface abundance of thorium. Lower elevations simply have more volcanic intrusives than the higher areas which extended above the reach of magmas at the time of their emplacement.

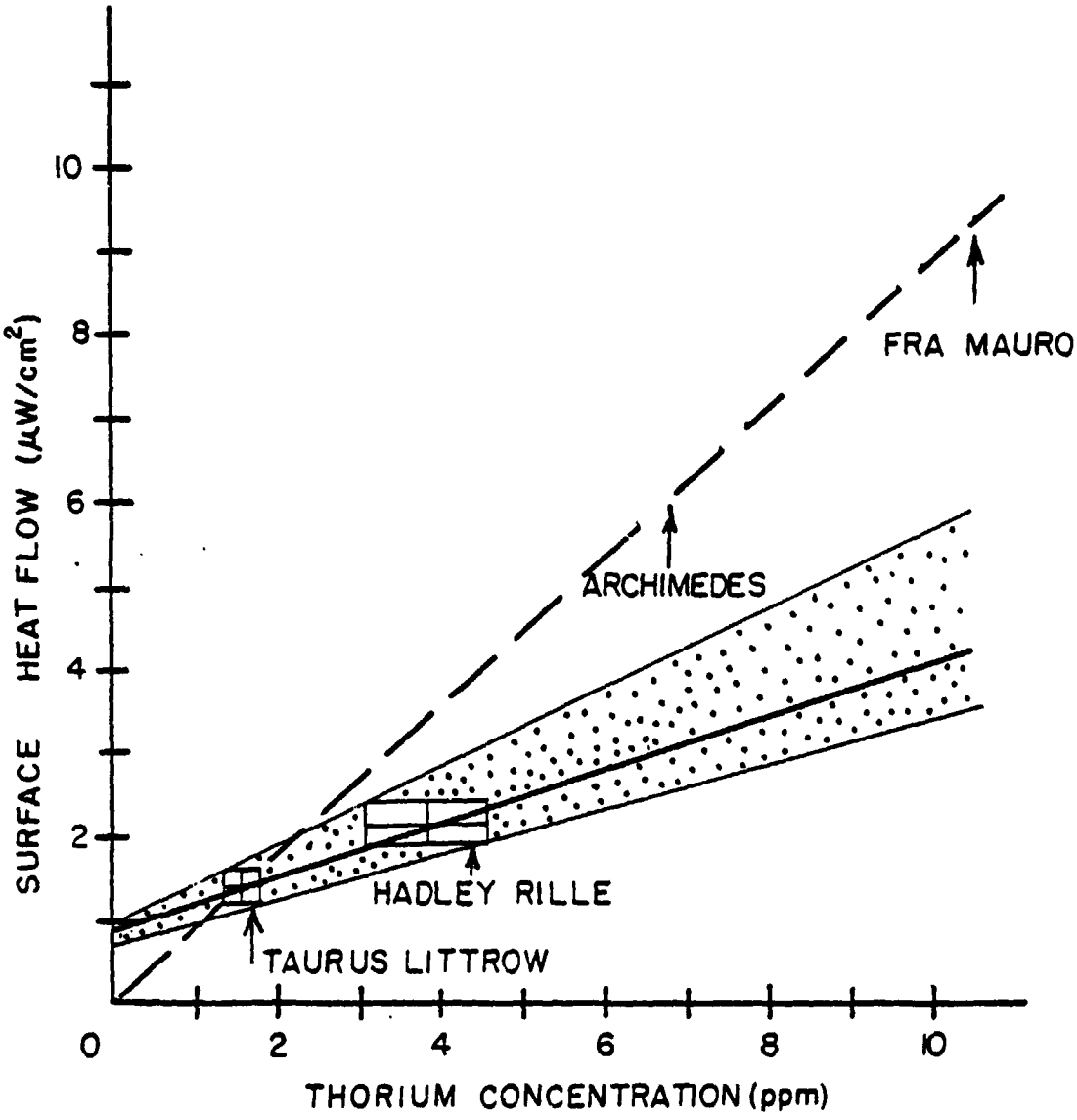

Heat flow vs thorium abundance; the dashed line shows the expected heat-flow vs. thorium concentration if thorium is uniformly distributed through a 60 km crust. The surface thorium abundance in the regions Archimedes and Fra Mauro defined by Metzger et al. (1974) are indicated by arrows for reference. The stippled zone and line connect the observed heat-flow values (squares).

Figure VII-A-1

The foregoing discussion is highly speculative; yet it is set down here to show the enormous and profound results that could be gained from the global mapping of thorium abundance, elevation and heat flow on the moon. They would provide data relevant to the chemical stratigraphy of the crust on a broad scale, the lateral heterogeneity of the crust, the extent both laterally and vertically of volcanism subsequent to lunar crust formation. Such measurements have been proposed as part of a polar orbiter mission which was until recently an active candidate mission in the foreseable future. Unfortunately, due to the costs of other activities by NASA, among them the Space Shuttle, such a scientifically valuable mission has been posponed indefinitely.

References

Bielefeld, M.J., R.C. Reedy, A.E. Metzger, J.I. Trombka and J.R. Arnold (1976) Surface chemistry of selected lunar regions; Proc. Lunar Sci. Conf. 7th, p. 2661-2676

Birch, F., R.F. Roy and E.R. Decker (1968) Heat flow and thermal history in New York and New England, in Studies of Appalachian Geology: Northern and Maritime, ed. W. White and E-an Zen, Chapter 33, Interscience, N.Y.

Lachenbruch, Arthur H. (1970) Crustal temperature and heat production: Implications of the linear heat-flow relation; Jour. Geophys. Res., v. 75, n. 17, p. 3291-3300

Metzger, A.E., J.I. Trombka, R.C. Reedy and J.R. Arnold (1974) Element concentrations from lunar orbital gamma-ray measurement; Proc.Lunar Sci. Conf. 5th , 1067-1078

VII-B. TEMPERATURES IN THE UPPER 300 KM OF THE MOON

The contents of this section are largely extracted from a paper given at the Lunar Science Conference no. VIII.

An abundance of the geophysical and geochemical data from Apollo is relevant to the present thermal regime of the lunar interior with varying degrees of significance. The seismic data strongly imply the absence of any widespread melting in the outer 800-1000 km and a high Q upper mantle that extends to 300-500 km (Nakamura et al., 1976; Dainty et al., 1976). The observed anisostasy of the circular mare mascons leads to rigidity requirements for the crust and upper mantle that have been interpreted in terms of viscosity and lithospheric thickness (e.g. Arkani-Hamed, 1973). The magnetics data, on the other hand, suggest that temperatures within a few hundred degrees of solidus may occur at depths as shallow as 200-300 km (Kuckes, 1974; Sonett and Duba, 1975; Dyal et al., 1976). However, quantitative interpretation of the seismic and electrical properties, as well as the gravity data, in terms of temperature, are subject to the uncertainties of modelling assumptions, composition, and laboratory measurements relating elastic, viscous and electrical properties to temperature.

Data relevant to the total abundance and radial distribution of heat sources are provided by the Apollo 15 and 17 heat-flow measurements and the gamma-ray mapping of surface thorium abundances over the Apollo 15 and 16 groundtracks. These observations are not subject to prior modeling or compositional assumptions but do suffer the uncertainties of extrapolating measurements of limited areal coverage to global averages. We thus have available observations relevant on essentially a global scale (seismic, gravity and magnetics data) which are subject to interpretational uncertainties, and measurements of limited areal coverage (crustal thorium abundance and heat flow) which may or may not be globally representative. It can be quite arbitrary which observations are considered 'constraints' on the models and which observations are to be tested by the model results. However, since the thermal models themselves require bulk and radial distribution of heat sources as inputs, the inferred crustal thorium enrichment and measured heat flow will be

referred to as constraints in the present work. It should be kept in mind, however, that this choice is only one of convenience. None of the observations can be considered definitive. The essential question is: Can a model of the present day thermal regime of the lunar interior be constructed which is consistent with all of the relevant observations?

The one constraint which we do assume is that the moon is presently thermally at steady state, in the sense that the heat generated internally is balanced by the surface loss to space. Evidence in this regard is based on theoretical as well as observational considerations. The absence of surface features related to thermal expansion or contraction implies that the mean lunar temperature has not changed considerably since the time of mare emplacement. Present day high temperatures suggested by the magnetics data at 200-300 km and the subsolidus requirement imposed by the seismic data to 1 00 km imply that radial temperature gradients in the interior are small. This, in turn, implies either that significant heat sources are absent from the deep interior or that heat now generated is efficiently transferred to the outer layers by a process of solid state convection. In either case, a near steady-state thermal regime would result. From a theoretical standpoint, the measured surface heat flow implies bulk heat source abundances one to two orders of magnitude larger than that required for the occurrence of convective transport, assuming a realistic temperature dependence of the material rheology. With the initiation of a solid state convective process, the time required to reach steady state would be greatly reduced, to a small fraction of the lunar age.

In this section, we examine the coupling of global heat flow, crustal heat source enrichment, thermal conductivity and crust and upper mantle temperatures for the outer layers of a steady-state moon where conductive heat transfer dominates. By utilizing a range of heat source distributions that would result from the formation of the crust by differentiation of the upper mantle and a thermal conductivity profile based on experimental data, comparisons can be made with model dependent constraints imposed by other geophysical and geochemical data.

Observations Relevant to Total Heat Source Abundance and Radial Distribution

Heat flow -- For a moon near steady-state, the global heat flux can be interpreted directly in terms of the total internal heat generation. In situ measurements carried out at the Hadley Rille (Apollo 15) and Taurus Littrow (Apollo 17) sites yielded regional heat flows of 2.1 and 1.4 $\mu W/cm^2$ respectively.

Earth based microwave observations of the lunar thermal emission (Troitsky, 1965), interpreted using laboratory measurements of regolith samples' electrical absorption length (Gold et al., 1973), lead to subsurface thermal gradients near the center of the lunar disk consistent with the in situ gradient measurements of 1.3 - 1.75 °K/m (Keihm and Langseth, 1975) Combined with evidence for large scale homogeneity of the upper few meters of regolith, the microwave data support the global heat flow estimate. Based on these results, we have examined the implications constraining the range of average surface heat flow to values between 1.4 and 2.1 $\mu W/cm^2$. This constraint restricts the total heat source abundance of the lunar interior to values between 2.4 and 3.6 x 10^{-8} $\mu W/cm^3$

With the total internal heat production constrained by the range of measured heat flow, the present day radial distribution of heat sources can be estimated from geochemical and geologic evidence relevant to the total amount of differentiation which has taken place. Thermal history calculations have long pointed to a need for very high, possibly liquidus, temperatures in the outer layers of the moon early in its history to explain the episodes of mare volcanism and differentiation of the lunar crust (e.g. Toksöz et al., 1972). Recent geochemical modeling studies (Walker et al.,1975; Hubbard and Minear, 1975) suggest that the early high temperature layer was on the order of 200-500 km thick. A thermal analysis, based on the lack of extensional or compressional features on the surface of the moon, suggests that the early high temperature layer was limited to a thickness between 100 and 300 km (Solomon and Chaiken, 1976). These results imply that the lunar crust was differentiated from a substantial outer layer (the magma ocean), which would have a profound effect on the radial distribution of heat sources. A direct constraint on the amount of heat source differentiation which has taken place is provided by estimates of the mean abundance of heat generating isotopes concentrated in the lunar crust.

The orbital gamma-ray determinations of the surface thorium abundances along the Apollo 15 and 16 groundtracks provide the most relevant data. These data have been shown to be consistent with the measured abundances of returned lunar samples from the Apollo sites (Metzger et al.,1974). Bielefeld et al. (1976) recently updated the surface thorium data. Abundances in regions of high albedo (nonmare areas) are shown in Figure VII-B-1 as a histogram of values within 5° x 5° areas.

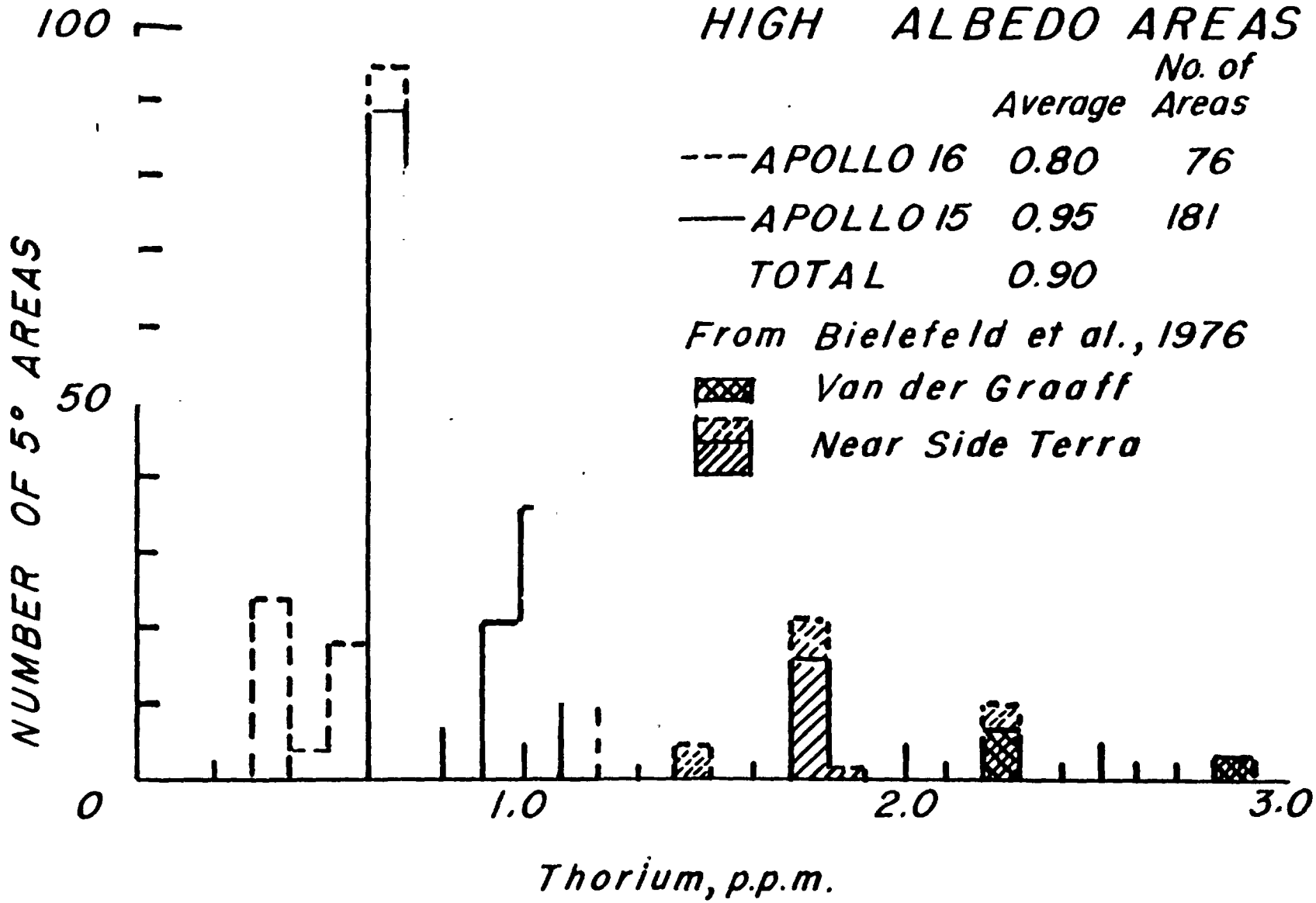

Figure VII-B-1

Histogram of the surface thorium abundance distribution over 5° x 5° areas of the Apollo 15 and 16 ground tracks from the analysis of Bielefeld et al. (1976) of the gamma-ray data. Only high albedo (nonmare) areas are included in the compilation

Measurements from mare have been excluded since observations from these areas are probably not representative of crustal abundances because the basalts that fill the mare basins are products of partial melting in the mantle or deep crust of the moon. Uranium and thorium would be preferentially concentrated into the liquidus fraction of a partially molten mantle. The most commonly found value, 0.6 to 0.7 ppm, is observed over the farside highlands; the second peak at 1.0 corresponds to limb highland areas. These values are highly biased toward Apollo 15 observations because of the larger area covered. How to relate the surface distribution to the average crustal abundance is far from clear. A strong inverse correlation has been observed between surface thorium abundance and surface elevation (Trombka et al., 1974). This could be interpreted as indicating that the crust is stratified relative to thorium in which case the values from the elevated farside regions would not be representative. On the other hand, it would be surprising if stratification in the highland crust could have survived the large scale mixing that would have accompanied the intense bombardment by large bodies, unless the increase of thorium with depth was emplaced subsequent to 4 b.y.b.p. by widescale intrusions into the lower part of the crust. Subsequent intrusion would not explain the relatively high values observed in the nearside terrae; therefore, the possibility of significant lateral heterogeneity of the crust cannot be dismissed. Until we have a more credible model of the crustal composition and stratification, an area weighted average of the surface abundances in nonmare regions offers the most unbiased estimate of the thorium abundance. As shown in Figure VII-B-1, this is 0.9 ppm for all regions (see also Taylor, 1977). Because of the uncertainties discussed above, we examine the consequences of constraining the average crustal thorium abundance to values between the peaks of the frequency distribution ($\sim$0.63 - 1.0 ppm). The lower limit admits the possibility that the enrichment in incompatible elements may decrease with depth as it does in continental crust on earth and the upper limit reflects the uncertainties associated with the nearside data. It will be shown in a later section that the inferred range of crustal thorium abundance, combined with the heat-flow constraint, has important implications for the amount of differentiation which has taken place and present day temperatures in the lunar lithosphere.

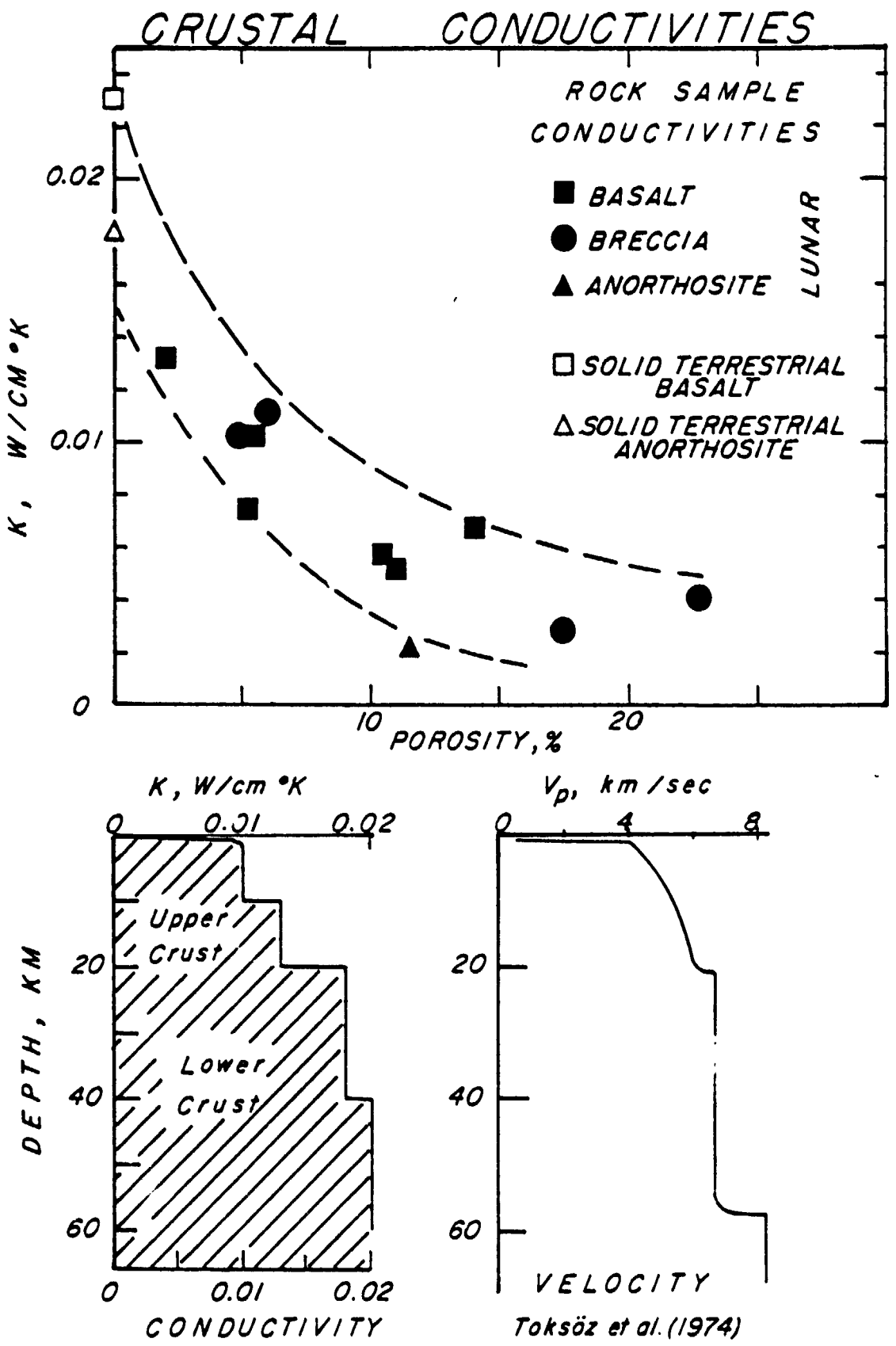

Top: Thermal conductivity versus porosity from laboratory measurements of returned lunar samples as summarized in Horai and Winkler (1976). Bottom: Inferred crustal thermal conductivity profile (left) based on a correlation of porosity and the seismic profile (right) of Toksöz et al. (1974)

Figure VII-B-2

The orbital data and sample data have established with a fair degree of certainty the isotopic ratios of potassium to thorium and thorium to uranium. We have used a K/U of 2500 and a Th/U of 3.7 to calculate heat production in terms of the thorium abundance. Because potassium is so volatile, the K/U ratio inferred for surface rocks may not be representative of the lunar interior. However, since present day radioactive heat generation is dominated by the uranium and thorium isotopes, interior K/U ratios even as high as terrestrial values would not significantly affect the model results.

Description of Steady-State Models

Thermal conductivity profile: — For a given heat flow and radial heat source distribution, temperatures in the conducting lunar lithosphere depend only on the thermal conductivity and its variation with depth and temperature. Realistic models of lithospheric temperatures must take into account the insulating properties of the lunar crust (relative to an olivine-pyroxene upper mantle). Simplified models which assume a mean conductivity for the lithosphere appropriate to an olivine-pyroxene mantle (0.04 W/cm °K is a commonly used value) will lead to temperature estimates for the upper mantle hundreds of degrees lower than when the insulating properties of the crust are taken into account.

Laboratory measurements of lunar crustal rock samples show that porosity is the most important factor controlling the thermal conductivity (Figure VII-B-2, top). Mainly, the porosity depends on the extent of fracture of the original glassy or crystalline matrix, and to a lesser extent on the nature and composition of the matrix. This suggests that a measure of the extent of fracture and crack closure with depth, such as the crustal p-wave velocity profile, can provide a good estimate of the thermal conductivity variation in the crust. A semiquantitative correlation is shown at the bottom of Figure VII-B-2. The large increase in V_p from just below the unconsolidated regolith to a depth of 20 km is believed to result from the closing of fractures as the compressive load increases. A porosity of about 5%, corresponding to a conductivity of 0.01 W/cm°K, is believed to be an upper limit for a compressive load greater than 1 km. Conductivities in the range of 0.018 - 0.020 W/cm°K at depths of 20-60 km are based on the assumption that cracks and fractures are almost totally closed in the lower crust, as suggested by the p-wave data. Comparable crustal conductivities were obtained by Mizutani and Newbigging (1973) using a similar analysis. Crustal conductivity models $\pm$ 30% removed from our nominal profile

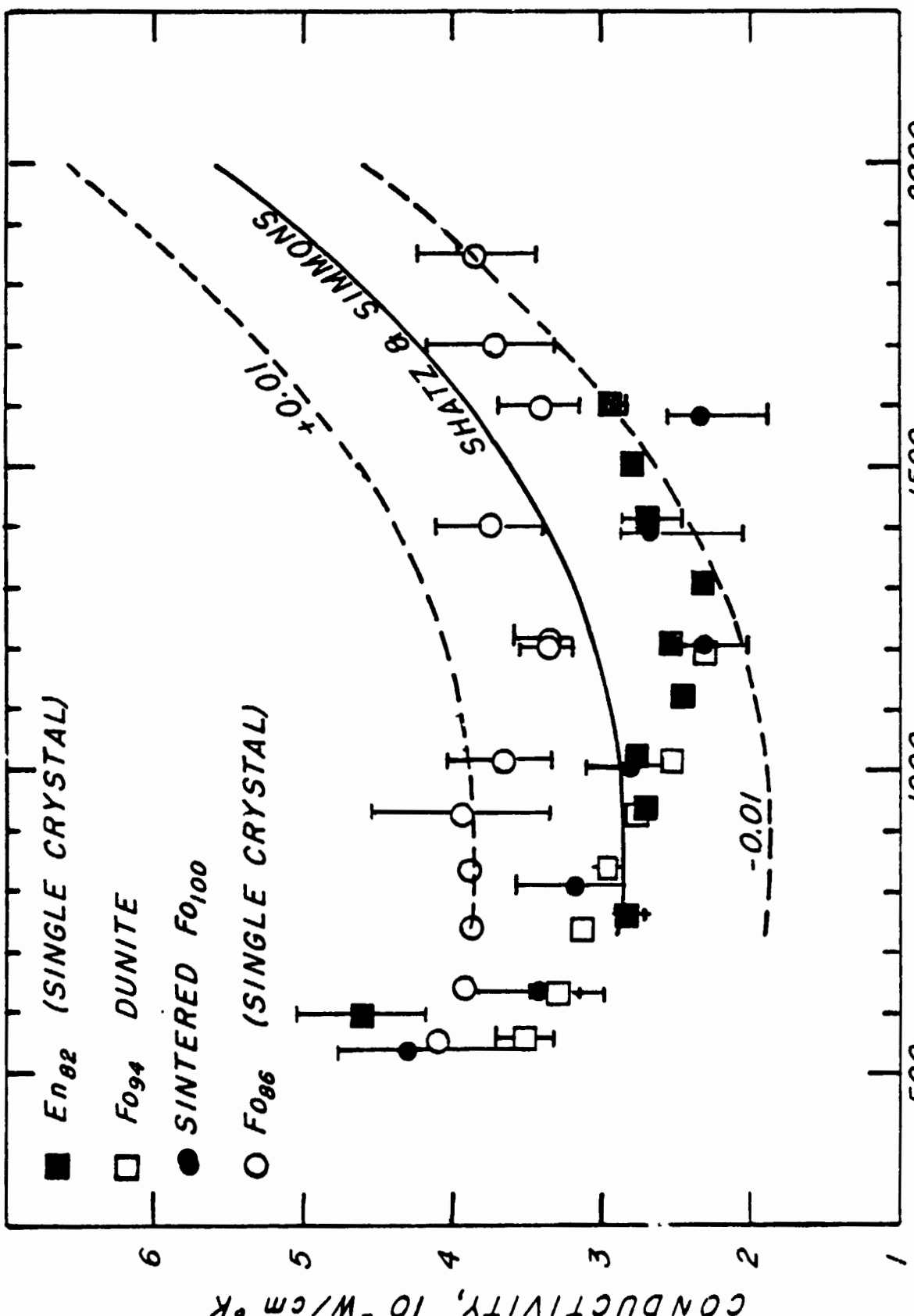

Laboratory measurements of thermal conductivity versus temperature for lunar mantle simulant materials (from Schatz and Simmons, 1973). The solid curve is a theoretical curve for a mantle of FO_{90} which has been used as the nominal mantle conductivity. The dashed curves, which nearly bracket the data have been used in the models to examine the effects of the mantle conductivity uncertainty

Figure VII-B-3

were also examined to determine the resultant uncertainties in the derived temperatures.

Below the crust, the most important variations in thermal conductivity are probably due to temperature. Seismic and geochemical models suggest an olivine-pyroxene composition for the upper mantle with possibly a slight increase in Fe/Fe + Mg ratio with depth. The data shown in Figure VII-B-3 are from the laboratory measurements of Schatz and Simmons (1973) on lunar mantle simulant materials. The samples show a slight decrease in conductivity to temperatures of about 1200°K, followed by a conductivity increase as radiative effects become important at higher temperatures. For our nominal mantle conductivity model, we have adopted a theoretical conductivity versus temperature relation proposed by Schatz and Simmons for a mantle of FO_{90} (solid curve of Figure VII-V-3). We have also examined mantle conductivity models $\pm$ 0.01 W/cm °K removed from the nominal curve, thus bracketing nearly all of the experimental data in the temperature range of interest.

Heat sources distribution: -- A wide range of radial heat source distributions were examined by employing two parameter models of the early lunar differentiation. A given model was characterized by the depth, d, to which heat source differentiation took place and the fraction, α, of the initially uniform distribution of heat sources which were redistributed into the crust. For example, a model with d = 500 km and α = 1.0 has all heat sources originally distributed uniformly in the upper 500 km concentrated in the present day crust. For a given model, the total heat source abundance is determined by the assumed heat flow.

For all models presented, an average crustal thickness of 60 km, based on the seismic velocity structure (Latham et al., 1972; Toksöz et al., 1974), is assumed. The effects of different average crustal thicknesses are essentially equivalent to variations in the constraint of present day crustal thorium abundance. The abundance range we have assumed, 0.63 - 1.0 ppm, probably encompasses the range of uncertainty of average crustal thickness.

Each steady-state model was characterized by a choice of thermal conductivity, heat flow and differentiation depth and efficiency. Lithospheric temperature solutions for the radially symmetric heat conduction equation in spherical coordinates were obtained iteratively, assuming constant thermal conductivity over 10 km intervals. For all calculations, a fixed outer boundary temperature of 310°K was assumed. This is based on the porosity-conductivity relationship shown in Figure VII-B-2, and the p-wave velocity structure inferred for the

1 km at the Taurus Littrow site (Cooper et al., 1974). A flux boundary condition was calculated at the base of the lithosphere using the assumed global heat flow and radial heat source distribution. Models designated compatible were those with heat flow in the range of 1.4 - 2.1 $\mu W/cm^2$ and differentiation processes which resulted in present day crustal thorium abundances between 0.63 and 1.0 ppm.

Formulation of the Model: -- Using the surface heat flow, F_{surf} the average volumetric heat production of the moon is calculated by the simple steady state relation for a sphere

$$\bar{H} = 3\ F_{surf} / R_1$$

where $\bar{H}$ is the average volumetric heat production and R_1 is the radius of the moon taken as 1740 km. Petrological and chemical differentiation in the outer layers of the moon are assumed to produce three layers; the crust, depleted mantle and the primitive interior. The radial distance from the center of the moon to the upper boundary of each layer r_i , i = 1,3 could be varied in the model. The volumetric heat production in each layer was calculated using the following simple relations:

For lunar crust: $$H_1 = \bar{H}\ (1 + \alpha)(r_2^3 - r_3^3)/\ (r_1^3 - r_2^3)$$

For depleted mantle $$H_2 = \bar{H}\ (1 - \alpha)$$

For the lunar interior $$H_3 = \bar{H}$$

Alpha is the fraction of heat producing isotopes depleted from the mantle.

The thermal conductivity K_i was defined within 10 km intervals based on the model shown in Figure VII-B-2. The initial conductivity in the mantle is given an assumed value which is uniform throughout. With the assumptions of thermal steady state, and spherical symmetry, the temperature at the base of any 10 km interval T_i can be computed from the temperature T_{i-1} at the top of the i - 1 layer by:

$$T_i = T_{i-1} + R_{i-1} F_{i-1}(R_{i-1} - R_i)/K_{i-1} R_i + H_K(3R_{i-1}^2\ R_i - 2R_{i-1}^3 - R_i^3)/6\ K_{i-1}\ R_i .$$

where F_{i-1} = the heat flow at the top of layer $i-1$.

R_i equals the radial distance to the top of layer i, and

$$H_K = H_1 \text{ for } R_i > r_2 ,$$
$$H_2 \text{ for } r_2 \geq R_i > r_3 , \text{ and}$$
$$H_3 \text{ for } R_i \leq r_3 .$$

The flux into the base of layer i can be computed from the flux at the surface of the layer by

$$F_i = F_{i-1} \cdot R_{i-1}^2 / R_i^2 - H_K (R_{i-1}^3 - R_i^3) / 3 R_i^2$$

Using these formulae, the calculation is made layer by layer starting from the surface.

The temperature dependence of conductivity in the mantle is assumed to have the form proposed by Schatz and Simmons (1973).

$$K(T) = A - B\bar{T} + D\bar{T}^3$$

This dependence is included in the model by recalculating K_i for each mantle layer letting $\bar{T} = (T_{i-1} + T_i)/2$ and repeating the computation of temperatures until the sum of differences in temperatures of all of the layers was less than a degree on subsequent runs.

Results and Discussion

For the nominal crustal and mantle thermal conductivity functions, the relationships between heat flow, differentiation depth, crustal thorium abundance and 300 km temperatures are shown in Figures VII-B-4 a, b, and c. The 300 km temperatures are shown as dashed contour lines. The solid contours illustrate the relationship between crustal thorium enrichment and heat flow and differentiation thickness. The stippled region shows the range of temperatures at the base of a 300 km lithosphere which are compatible with the heat flow and crustal thorium observations as well as the subsolidus requirement (less than 1600°K). Figures VII-B-4 a and c differ only in the assumed heat source differentiation efficiency, α. Note that for highly efficient

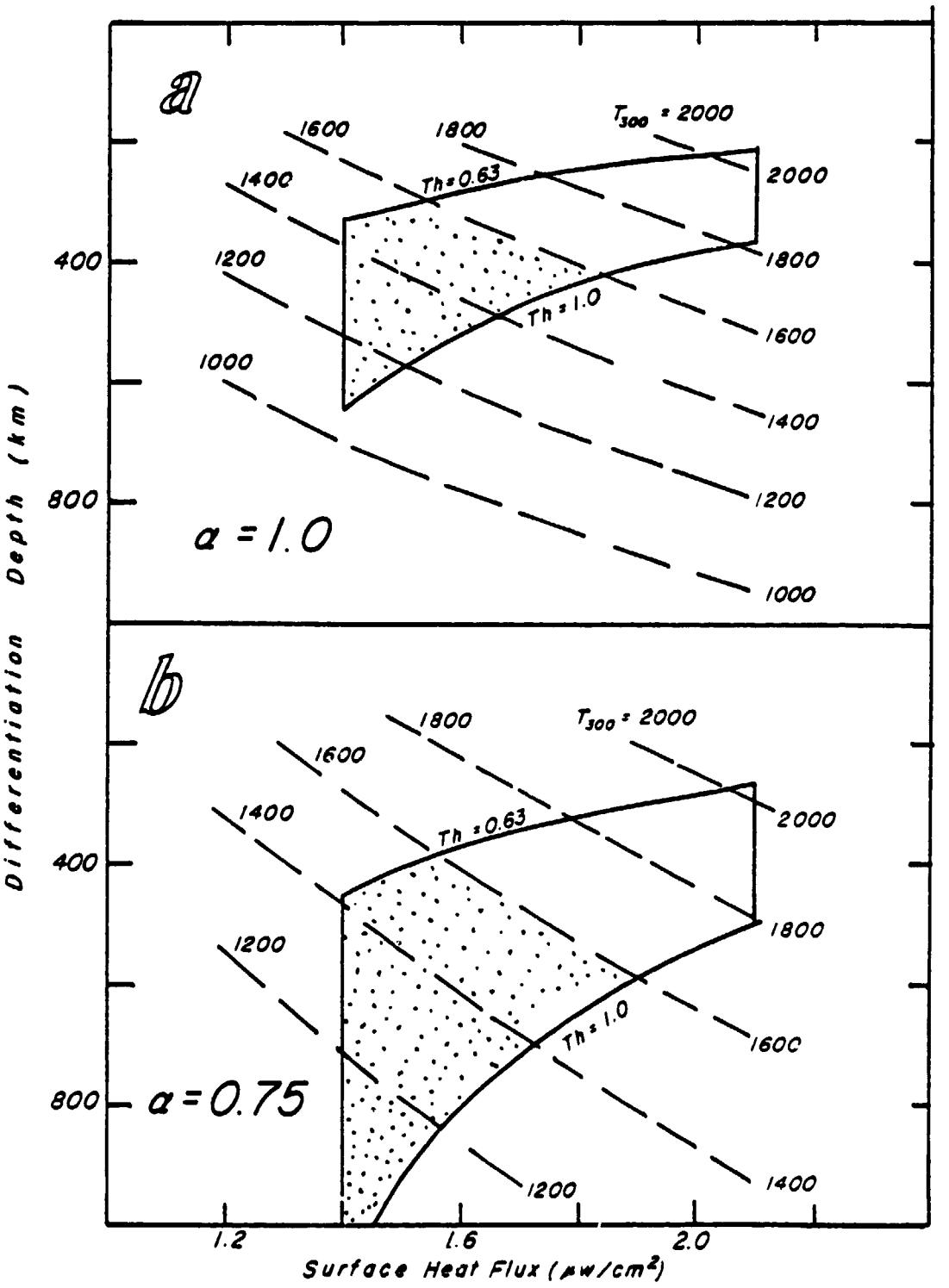

Figure VII-B-4 a & b

heat source differentiation (α greater than 0.75; Figures VII-B-4a and b), 'magma ocean' depths of 300-800 km are implied, compatible with the geochemical requirements. If early outer layer melting was restricted to depths of 100-300 km, as suggested by the thermal expansion constraint of Solomon and Chaiken (1976), the present day average crustal thorium abundance must be near the lower limit (0.63 ppm) inferred from the gamma-ray data, implying that the heat source enrichment may decrease significantly in the lower crust. Much deeper differentiation layers can be compatible with the heat flow and crustal thorium constraints (Figure VII-B-4c); however, much less efficient upward migration of heat sources must be invoked.

For a wide range of compatible heat flow and differentiation models, temperatures in the range of 1100 - 1600°K result at the 300 km depth. The requirement of a subsolidus upper mantle restricts the acceptable heat flows to values less than 1.9 $\mu W/cm^2$. Observations of the magnetic field in orbit and on the lunar surface yield determinations of the electromagnetic response of the whole moon to transient variations in the ambient magnetic field. The response has been examined in the time frequency domain by several authors (e.g. Sonett and Duba, 1975; Dyal et al., 1976) by comparison with electrical conductivity models. All of these analyses require a rapid increase in electrical conductivity with depth in the outer 100 - 200 km, and values on the order of $3 : 10^{-4}$ - 5×10^{-3} mhos/m are reached at 300 km. Uncertainties remain in the analysis of the magnetic data which stem from asymmetries in the enveloping electric field produced by the solar wind and the effects of higher modes of induced response. A recent analysis by Dyal et al. (1976) of the transient response when the moon was shielded from the solar wind in the earth's magnetic tail, yielded results in general agreement with those of other workers.

Correlation of inferred electrical conductivity and temperature is based on the strong temperature dependence demonstrated in the laboratory by common silicate rocks. Consideration of all data shows a relatively large scatter and led to a large uncertainty in early interpretations of mantle conductivities in terms of temperature. More recently, however, the role of oxygen fugacity has been more fully recognized and the measurements of Duba et al. (1974, 1976) on olivine and orthopyroxene samples under simulated lunar conditions have considerably narrowed the uncertainties in the temperature deductions. Mantle temperatures based on the electrical conductivity models of three different

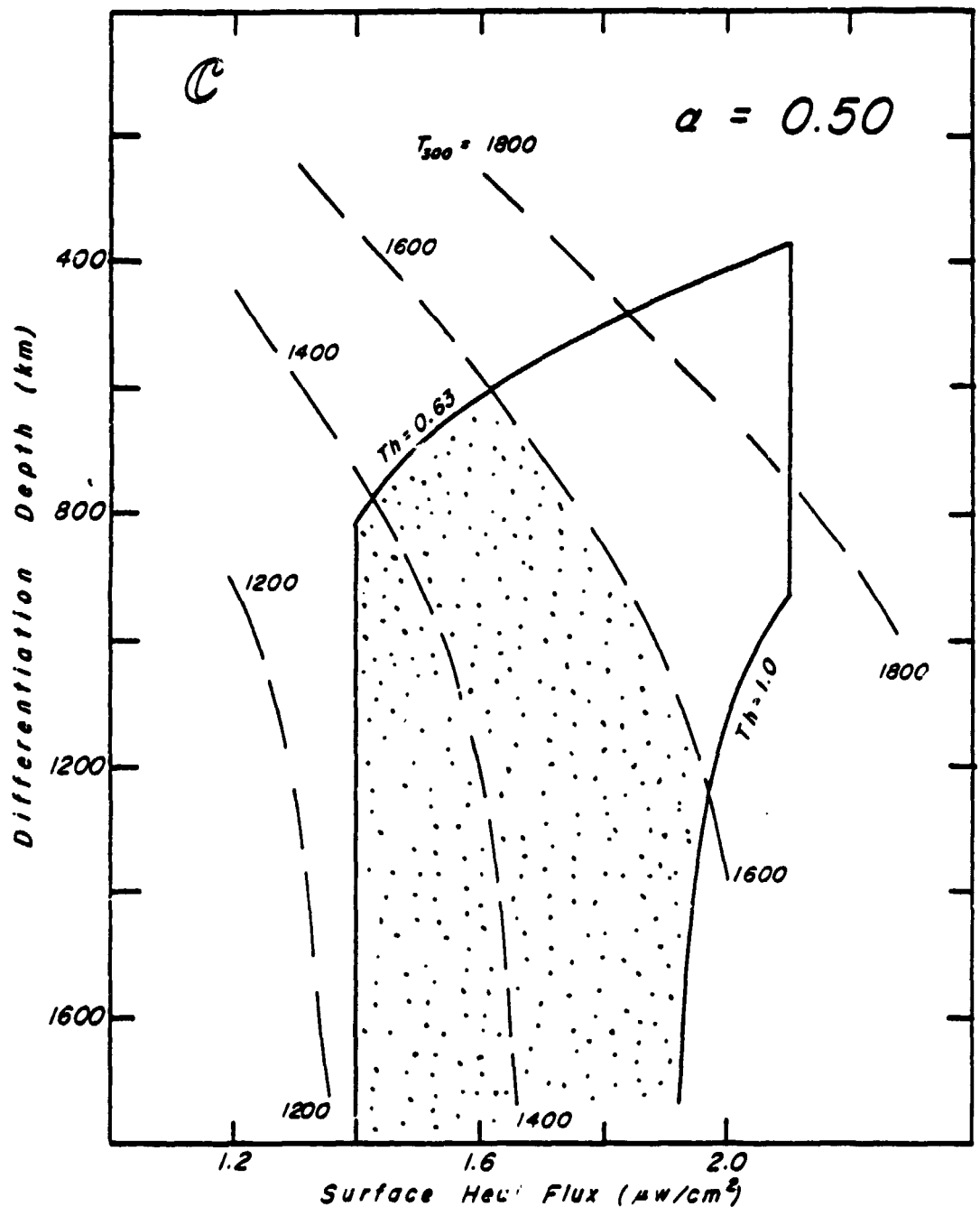

Three hundred kilometer temperature contours plotted versus average surface flux (F_s) and differentiation depth. The stippled area describes the range of 300 km temperatures and differentiation thicknesses which satisfy the heat flow and crustal thorium abundance data and the subsolidus requirement. The three sets of contours are distinguished by the assumed differentiation efficiency, α: (a) α = 1.0; (b) α = 0.75; (c) α = 0.50.

Figure VII-B-4 c

investigators are shown in Figure VII-B-5 along with a range of selenotherms produced by models compatible with the heat flow and crustal thorium abundance constraints. Note that all three electrical models require temperatures within 200°K of the solidus (Hodges and Kushiro, 1974) at depths greater than 200 km. The representative selenotherms based on the present work are consistent with these results, although temperatures as low as 1100°K at 300 km can also be compatible with the heat flow and crustal thorium abundance constraints. The approach towards solidus temperatures at about 300 km is also supported by the seismic model of Nakamura et al. (1976). A large negative shear wave velocity gradient above 300 km suggests large temperature gradients in this region. The decrease in shear wave Q from 4000 to 1500 at about 300 km may indicate a softening of the material as the solidus is approached, causing the lower mantle to behave more plastically to stress. It has been argued previously that high seismic Q values precluded temperatures within a few hundred degrees of solidus in the upper mantle. Especially relevant to this point are the high p-wave Q values of ∿ 5000 to depths of approximately 500 km inferred from the analysis of seismic surface events (Dainty et al., 1976). These results conflict somewhat with the seismic models of Nakamura et al. (1976), which require a lower s-wave Q below 300 km. Based partly on the higher seismic Q values of Dainty et al., lower temperatures and significant temperature gradients were expected to depths of at least 500 km. However, the laboratory measurements of Tittman et al. (1976, 1977) indicate that waterless lunar materials can exhibit very high Q values even at elevated temperatures. Recent measurements up to 2.5 kbar and 800°K (Tittman, personal communication) suggest that these effects may remain significant at pressures and temperatures characteristic of the lunar upper mantle. Seismic property measurements up to 15 kbar and 1200°K could be crucial in resolving the high temperature, high seismic Q requirements of the lunar crust and upper mantle.

A second objection to high upper mantle temperatures has been the rigidity requirements imposed by the anisostasy of the circular mare mascons. Kuckes (1977) has suggested that the load of the mascons could be supported by flexure of a relatively thin elastic lithosphere over a viscous mantle. He finds that the moon's elastic lithosphere must flex as a plate about 60 km thick to support the mascons. On earth, the oceanic lithosphere flexural thickness has been shown to be about 24 km (Watts and Cochran, 1974). Temperatures of about 750°K are reached at this depth in the oceanic lithosphere greater than 50 m.y. old

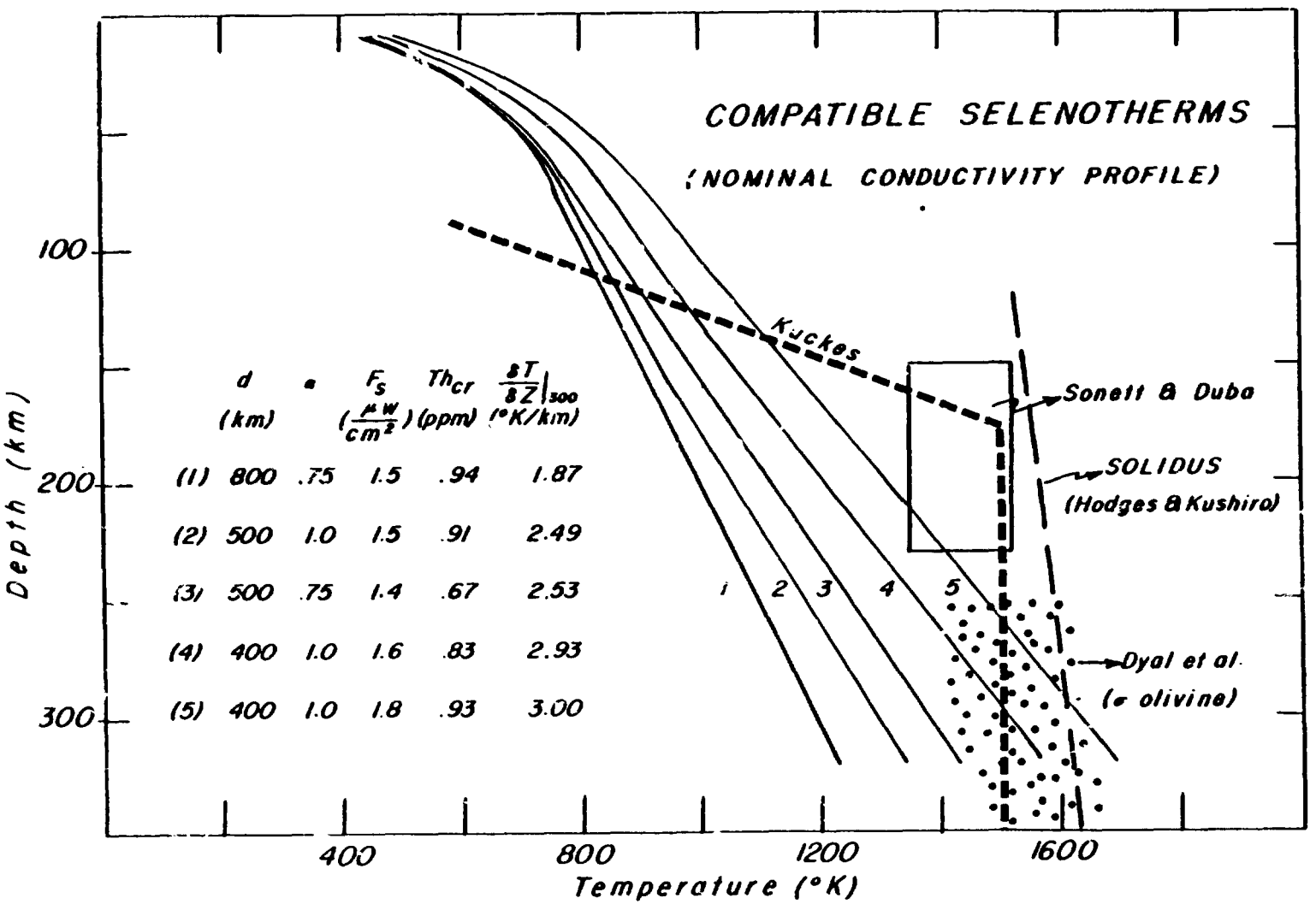

Representative selenotherms calculated for steady-state models. Model parameters for each selenotherm are shown in the accompanying table. The dotted curve, and rectangular and stippled regions are upper mantle temperature estimates from the magnetometer data (Kuckes, 1974; Sonett and Duba, 1975; Dyal et al., 1976). The solidus of Hodges and Kushiro (1974) is shown for reference

Figure VII-B-5

(see, for example, Langseth and Von Herzen, 1970). Thus, comparable temperatures might be expected at 60 km in the mc , that is at the base of the lunar crust. It is seen from Figure VII-B-5 that the compatible selenotherms require crustal base temperatures between 700 and 850°K.

Because of the temperature dependence of the thermal conductivity below the crust, thermal gradients are limited to values between about 1.8 and 3.2°K/km for compatible models. These gradients are not large enough to account for the measured shear wave gradient of - 0.0013 km/sec/km (Nakamura et al., 1976), without invoking an additional effect, such as an increase in the Fe/Fe + Mg ratio with depth. Experimental data by Chung (1971) gives $\delta V_s/\delta T = -3.2 \times 10^{-4}$ km/sec/°K; $\delta V_s/\delta p = 3.7 \times 10^{-3}$ km/sec/kbar; and $\delta V_s/\delta$% (Fe/Fe + Mg) = - 0.015 km/sec/ % (Fe/Fe + Mg) for forsterite samples. Combining these values with the observed shear wave gradient of - 0.0013 km/sec/km yields a thermal gradient of 4.6 °K/km if no compositional changes are significant. Thus, if the actual gradient is about 2.5 °K/km, an increase in the Fe/ (Fe + Mg) ratio of $\sim$ 0.03% km may be implied for the upper mantle.

The discussion to this point has been based on results obtained using the nominal thermal conductivity profile described earlier under the 'Description of Steady-State Models'. The effects of the conductivity uncertainty are best illustrated by assuming extreme cases of uniformly higher and lower crustal and mantle conductivity profiles and examining the effects on the thermal regime still subject to the heat flow and crustal thorium abundance constraints. The selenotherms shown in Figure VII-B-6 are for variations in crustal conductivity of $\pm$ 30% from nominal and variations in mantle conductivity of $\pm$ 0.01 W/cm °K, which nearly brackets the laboratory data for olivine and pyroxene samples. The model parameters are d = 500, α = 1.0, F_s = 1.5 and Th_{crust} = 0.91 ppm for all five cases. Variations in crustal base and 300 km mantle temperatures of $\pm$ 150°K result. The effects of the crustal and mantle conductivity uncertainties are approximately additive so that errors of up to $\pm$ 300°K at 300 km could result if both the mantle and crustal conductivities were uniformly in error by the amount of their stated uncertainties.

Conclusions

By utilizing the steady-state criterion and a thermal conductivity model for the crust and upper mantle based on experimental data, the relationship between global heat flow, crustal heat source enrichment and lithospheric temperatures can be quantitatively evaluated. If the measured ranges of crustal

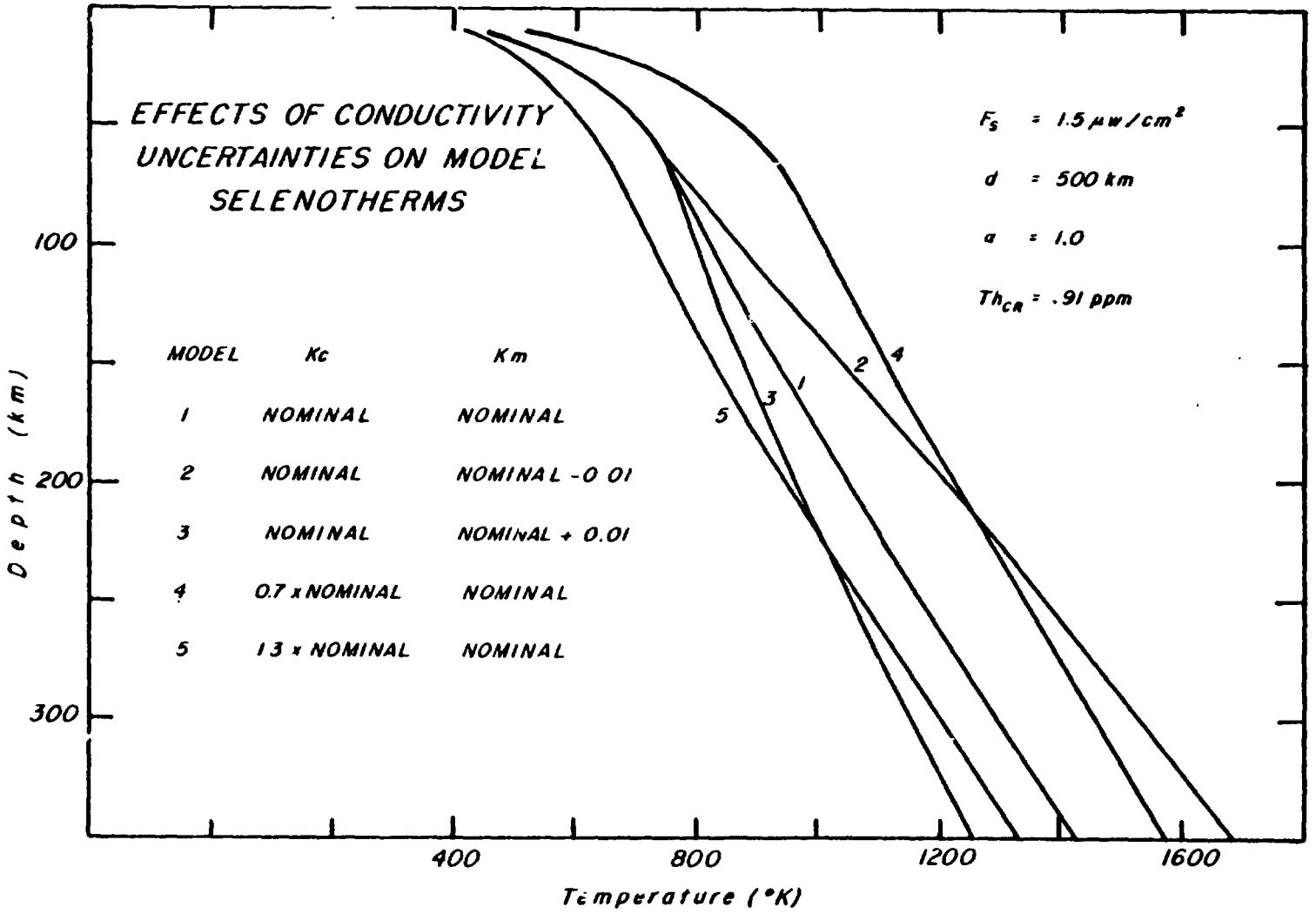

Figure VII-B-6

Variations in model selenotherms which result from changes in crustal and mantle conductivities by their stated uncertainty. The models differ only in the assumed conductivity profile. Other model parameters are shown at the upper right.

thorium enrichment and heat flow are globally representative, the features of a lunar thermal lithosphere that extends to at least 300 km can be summarized as follows:

1) At 300 km, temperatures are in the range 1100 - 1600°K. Magnetic models of the upper mantle electrical conductivity and the requirement of a subsolidus outer regime favor temperatures in the range of 1300 - 1500 °K and a global heat flow of 1.4 - 1.8 $\mu W/cm^2$. Three hundred kilometer temperatures significantly lower than 1200°K require a global heat flow less than 1.4 $\mu W/cm^2$ or a crustal heat source enrichment greater by a factor of two than that inferred from the gamma-ray data.

2) Models of heat source differentiation require an outer layer extending to depths of 300 - 600 km if 100% of the heat sources in the differentiated zone have migrated upward into the crust. If 75% have migrated upward, the layer could be as much as 800 km thick. The 100% differentiation model compares favorably with the 'magma ocean' model thicknesses of 200-500 km derived from broad geochemical constraints and 100 - 300 km based on Solomon and Chaiken's (1976) analyses of constraints on the allowable thermal expansion and contraction of the moon compatible with the absence of related surface features. Alternate models of deeper heat source differentiation can be compatible with the heat flow and crustal thorium constraints only if a significant fraction of the heat sources remain in the deep interior.

3) Upper mantle gradients in the range of 1.8 - 3.2 °K/km are required at 200 - 300 km depths. These values are not high enough to account for the observed seismic shear wave gradient and suggest that an additional effect, such as a small increase in iron abundance with depth, is required. The mantle gradients imply significant heat generation below 300 km. Heat fluxes in the range of 0.7 - 1.3 $\mu W/cm^2$ at 300 km indicate that 1/3 to 1/2 of the measured surface heat flow is derived from deep interior heat sources. An efficient solid state convection process is required to maintain subsolidus temperatures to depths of 800 - 1000 km.

The primary uncertainty for the steady state models is the thermal conductivity and its variation with depth and temperature in the outer, nonconvecting layers of the moon. A realistic range of possible conductivity error leads to uncertainties of 100 - 200°K in the derived upper mantle temperatures for a given model. The range of compatible heat source differentiation models is not strongly

affected by the conductivity uncertainty. Neither is the general conclusion from this analysis that the measured heat flow and inferred crustal thorium abundances are consistent with the high upper mantle temperatures interpreted from the magnetics and seismic data, a differentiated outer moon supported by broad geochemical constraints and a convecting subsolidus lunar interior.

References

Arkani-Hamed, J. (1973) On the formation of the lunar mascons. Proc. Lunar Sci. Conf., 3rd, p. 2673-2684

Bielefeld, M.J., R.C. Reedy, A.E. Metzger, J.I. Trombka and J.R. Arnold (1976) Surface chemistry of selected lunar regions. Proc. Lunar Sci. Conf. 7th. p. 2661-2676

Chung, D.H. (1971) Elasticity and equations of state of olivines in the Mg_2SiO_4 - Fe_2SiO_4 system. Geophys. J.R. astr. Soc., v. 25, p. 511-538

Cooper, M.R., R.L. Kovach and J.S. Watkins (1974) Lunar near-surface structure Rev. Geophys. Space Phys. v. 12, p. 291-308

Dainty, A.M., M.N. Toksöz and S. Stein (1976) Seismic investigation of the lunar interior. Proc. Lunar Sci. Conf. 7th, p. 3057-3075

Duba, A., H.C. Heard and R.N. Schock (1974) Electrical conductivity of olivine at high pressure and under controlled oxygen fugacity. J. Geophys. Res., v. 79, p. 1667-1673

Duba, A., H.C. Heard and R.N. Schock (1976) Electrical conductivity of orthopyroxene to 1400°C and the resulting selenotherm. Proc. Lunar Sci. Conf. 7th, p. 3173-3181

Dyal, P., C.W. Parkin and W.D. Daily (1976) Structure of the lunar interior from magnetic field measurements. Proc. Lunar Sci. Conf. 7th, p. 3077-3095

Gold, T., E. Bilson and M. Yerbury (1973) Grain size analysis and high frequency electrical properties of Apollo 15 and 16 samples (abstract) in, Lunar Science IV, p. 293-295. The Lunar Science Institute, Houston, Texas.

Hodges, F.N. and I. Kushiro (1974) Apollo 17 petrology and experimental determination of differentiation sequences in model moon composition. Proc. Lunar Sci. Conf. 5th, p. 505-520

Horai, K. and J.L. Winkler, Jr. (1976) Thermal diffusivity of four Apollo 17 rock samples. Proc. Lunar Sci. Conf. 7th, p. 3183-3204

Hubbard, N.J. and J.W. Minear (1975) A physical and chemical model of early lunar history. Proc. Lunar Sci. Conf. 6th, 1057 - 1085

Keihm, S.J. and M.G. Langseth (1975) Lunar microwave brightness temperature observations reevaluated in the light of Apollo program findings. Icarus, v. 24, p. 211-230.

Kuckes, A.F. (1974) Lunar magnetometry and mantle convection, Nature, v. 252 p. 670-672

Kuckes, A.F. (1977) Lunar gravity and flexure of a thin elastic lithosphere, in Lunar Science VIII, p. 564-565, The Lunar Science Institute, Houston, Texas

Langseth, M.G. and R.P. Von Herzen (1970) Heat flow through the floor of the world oceans. in, The Sea Volume IV, Part I, ed., A.E. Maxwell, p. 299-352, Wiley-Interscience, New York

Latham, G.V., M.Ewing, F. Press, G. Sutton, H.J. Dorman, Y. Nakamura, N. Toksöz D. Lammlein, and F. Duennebier (1972) Passive seismic experiment. In, Apollo 15 Preliminary Science Report, NASA publication SP-289, p. 8-1 to 8-25.

Metzger, A.E., J.I. Trombka, R.C. Reedy, and J.R. Arnold (1974) Element concentrations from lunar orbital gamma-ray measurement. Proc. Lunar Sci. Conf. 5th, p. 1067-1078

Mizutani, H. and D.F. Newbigging (1973) Elastic-wave velocities of Apollo 14, 15 and 16 rocks and thermal conductivity profile of the lunar crust. (abstract) in, Lunar Science IV, p. 528-530, The Lunar Science Institute, Houston, Texas

Nakamura, Y., G.V. Latham, H.J. Dorman and F.K. Duennebier (1976) Seismic structure of the moon: A summary of current status. Proc. Lunar Sci. Conf. 7th, p. 3113-3121

Schatz, F.J. and G. Simmons (1973) Thermal conductivity of earth materials at high temperatures. J. Geophys. Res., v. 77, n. 35, p. 6966-6983

Solomon, S.C. and J. Chaiken (1976) Thermal expansion and thermal stress in the moon and terrestrial planets; Clues to early thermal history. Proc. Lunar Sci. Conf. 7th, p. 3229-3243

Sonett, C.P. and A. Duba (1975) Lunar temperature and global heat flux from laboratory electrical conductivity and lunar magnetometer data, Nature, v. 258, p. 118-121

Taylor, S.R. (1976) Geochemical constraints on the composition of the moon. Proc. Lunar Sci. Conf. 7th, p. 3461-3477

Tittman, B.R., L. Ahlberg and J. Curnow (1976) Internal friction and velocity measurements. Proc. Lunar Sci. Conf. 7th, p. 3123-3132

Tittman, B.R., L.Ahlberg and H. Nadler (1977) Quality factor Q under confining pressure. In, Lunar Science VIII, p. 937-939. The Lunar Science Institute Houston, Texas

Toksöz, M.N., A.M. Dainty, S.C. Solomon and K.R. Anderson (1974) Structure of the moon. Rev. Geophys. Space Phys., v. 12, p. 539-567

Toksöz, M.N., S.C. Solomon, J.W. Minear and D.H. Johnston (1972) Thermal evolution of the moon. The Moon v. 4, p. 190-213

Troitsky, V.S. (1965) Investigation of the surface of the moon and planets by the thermal radiation. Radio Sci. v. 69D, p. 1585-1611

Trombka, J.I., J.R. Arnold, I. Adler, A.E. Metzger and R.V. Reedy (1974) Lunar elemental analysis obtained from the Apollo gamma-ray and x-ray remote sensing experiment. Preprint of a paper presented at the Soviet American Conference on the Geochemistry of the Moon and Planets, June 4-8, 1974

Walker, D., J. Longhi and J.F. Hays (1975) Differentiation of a very thick magma body and implications for the source regions of mare gasalts. Proc. Lunar Sci. Conf. 6th, p. 1103-1120

Watts, A.G. and J.R. Cochran (1974) Gravity anomalies and flexure of the lithosphere along the Hawaiian-Emperor Seamount Chain. Geophys. J.R. astr. Soc., v. 38, p. 119-141.

VII-C. IMPLICATIONS FOR THE MOON'S BULK CHEMISTRY

As we have stated in other sections of this report, there is strong evidence that at present the moon is close to thermal steady state. Solomon and Chaiken (1976) have drawn attention to the lack of compressional or extensional surface tectonic features on the moon, indicating radially averaged internal temperatures have been nearly constant since the time of the last mare flooding, about 3.2 b.y.b.p. The extremely low level of mean surface seismic activity (Latham et al., 1973) indicates that thermally induced stress levels are very small at present. Thermal history models of the moon containing radioisotopes at concentrations sufficient to explain the surface heat flow and which fit other well established constraints (see, for example, Toksöz and Johnston, 1974; Toksöz et al., 1976; and, Toksöz et al., 1977) indicate that most of the radioactive heat sources have been concentrated in the outer 100 km where their generated heat would equilibrate with the surface flux in 10^9 years or less, or the deep interior is convecting so that the heat transfer is enhanced and steady state conditions are more rapidly approached.

For a moon at steady state, the heat generation in the interior is related to the average surface heat flow by

$$H_v = \frac{3F}{r}$$

where F is the mean heat flow and r is the lunar radius. If the thorium to uranium ratio is assumed to be 3.7 and the potassium to uranium ratio for the whole moon is 2000, then the volumetric heat production in W/cm^3 is related to the uranium abundance [U] in gm/gm by

$$H_v = 6.73 \times 10^{-7}[U]$$

From these two simple relations we can estimate the global heat flux and the uranium concentration in ppb. In Section VII-B we showed that for a moon at steady state heat flow values in the range of 1.4 to 1.8 $\mu W\ cm^2$ are consistent with other data relevant to interior temperatures in the moon.

If an analysis similar to that described in Langseth et al. (1976) is carried out, a similar range of values is found. The analysis used the two measured values of heat flow, a mean heat production in the crust, $\bar{H}_c$ and determinations of crustal thickness along the Apollo 15 and 16 tracks to calculate a mean heat flow for these areas. Isostatic adjustment of the crust is assumed so that lunar elevations can be converted into crustal thicknesses if a density contrast $\Delta\rho$, between the crust and mantle is assumed. If we start from the seismically determined crustal thickness of 60 km over eastern Procellanum and use the mean densities assumed by Solomon (1975), a crustal density of 2.8 and a mantle density of 3.4, $\Delta\rho = 0.06$ and the isostatic assumption, then the thickness T over highland areas and nonmascon mare plains is given by:

$$T = 73 + 5.7\ h$$

where h is the elevation relative to the mean lunar radius of 1738 km. In areas of mascons the surface mass concentration of 10^6 gm/cm is assumed to be uncompensated and,

$$T = 56 + 5.7\ h.$$

In nonmascon areas that are not enriched in surface thorium, the heat flow within an area was calculated by the relation

$$F = F_M + T \cdot \bar{H}_c$$

where F_M is the flux from the mantle (the value at Taurus Littrow). Values determined in Section VII-B can be used here. In areas where the surface thorium is enriched

$$F = F_M + T \cdot \bar{H}_c + F_{add}$$

where

$$F_{add} = D' \cdot (H_o - \bar{H}_c)$$

H_o is the surface heat production calculated from the surface thorium abundance and D' is the slope of the line in Figure VII-A-1.

Once the values in each area are determined by this model, the average heat flow is calculated by

$$\bar{F} = \sum_{n=o}^{N} F_n \cdot A_n \Big/ \sum_{n=o}^{N} A_n$$

where F_n and A_n are the heat flow and area of each area of available data. Using the areas defined by Metzger et al., (1974) or Bielefeld et al. (1976) the values at Hadley Rille of 2.1 $\mu W/cm^2$ and Taurus Littrow of 1.4 $\mu W/cm^{-3}$ can be used to calculate a mean value. For values of H_c between 0.9×10^{-13} W cm^{-3} to 1.55×10^{-13} W cm^{-3} mean heat flows of 1.4 to 1.8 $\mu W/cm^{-2}$ are obtained.

This range of global heat flows would correspond to average maximum contents of 36 to 46 ppb for the case of a moon at steady state. More detailed calculations of the thermal evolution of the moon from initial conditions and including possibilities of convection lead to heat flows of about 1.7 $\mu W\ cm^{-2}$ if a uranium content of 35 ppb uranium is assumed (Toksöz et al., 1977). However, the computations by Toksöz et al. lead to substantially lower temperatures in the lunar interior at present than our steady state models with internal convection implies. The model of Toksöz et al. indicates that temperatures of 1500°K are reached at about 800 km compared with 300 km deduced from the steady state model. The Toksöz et al. model also concludes that solid state convection is confined to a relatively small region of the lunar interior deeper than 1000 km. These models assume crustal conductivities that are equal to those of the mantle. This assumption would greatly decrease gradients in the crust and enhance the heat flux from the mantle to the surface during lunar history. The thermal conductivity is not known with sufficient certainty to settle on a 'best' model at this time.

An important implication of uranium abundances of 36 ppb is that they are very similar to abundances now implied for the earth's mantle.

Recently, estimates of the earth's average heat flow have increased to account for the contribution from the seafloor spreading process. Williams and Von Herzen (1974) have given a new estimate of the global heat flow from the earth of 8.4 $\mu W/cm^2$, which is 30% higher than the previous estimate of 6.3 $\mu W/cm^2$, based on an average of all heat flow observations. For an earth at steady state, a uranium abundance of 32 ppb is required to produce a flux of 8.4 $\mu W/cm^2$ if we assume the usually accepted K/U and Th/U ratios. If all of the heat sources are concentrated in the mantle then the abundance of uranium in the mantle is 42 ppb.

References

Bielefeld, M.J., R.C. Reedy, A.E. Metzger, J.I. Trombka and J.R. Arnold (1976) Surface chemistry of selected lunar regions; Proc. Lunar Sci. Conf. 7th, p. 2661-2676

Langseth, M., S. Keihm and K. Peters (1976) The revised lunar heat flow values Proc. Lunar Sci. Conf. 7th, V. 3, The Moon and Other Bodies Geochm. et Cosm. Acta, R.B. Merrill et al., eds, p. 3143-3171

Latham, G., J. Dorman, F. Dunnebier, M. Ewing, D. Lammlein and Y. Nakamura (1973) Moonquakes, meteoroids and the state of the lunar interior; Proc. Lunar Sci. Conf. 4th, v. 3, p. 2515-2527

Metzger, A.E., J.I. Trombka, R.C. Reedy and J.R. Arnold (1974) Element concentrations from lunar orbital gamma-ray measurement. Proc. Lunar Sci. Conf. 5th, v. 2, p. 1067-1078

Solomon, S.C. (1975) Mare volcanism and lunar crust structure. Proc. Lunar Sci. Conf. 6th, v. 1, p. 1021-1042

Solomon, S.C., and J. Chaiken (1976) Thermal expansion and thermal stress in the moon and terrestrial planets: clues to early thermal history. Proc. Lunar Sci. Conf. 7th, V. 3, p. 3229-3243

Toksöz, M.S., A.T. Hsui and D.H. Johnston (1976) Evolution of the moon revisited in, Lunar Science VII, p. 367 (abstract), The Lunar Science Institute Houston

Toksöz, M. Nafi, A.T. Shui and D.H. Johnston (1977) Thermal evolutions of the terrestrial planets; in, The Moon, Special Volume in Honor of Professor H. Alfvén,

Toksöz, M.N. and D.H. Johnston (1974) The evolution of the moon. Icarus, v. 21 p. 389-414

Williams, D.L. and R.P. Von Herzen (1974) Heat loss from the earth: new estimate. Geology, v. 2, p. 305-368

VIII. RECOMMENDATIONS & FUTURE MEASUREMENTS OF LUNAR HEAT FLOW

The present status of our knowledge about the heat flow from the interior of the lunar surface consists of direct measurements of heat flow through the lunar surface layers at two widely separated locations in the northern part of the nearside, numerous measurements of the microwave brightness temperature versus wavelength using earth-based radio telescopes, and a large library of new data on the thermal and electrical properties of lunar surface materials that resulted from the lunar sample program.

Indirect observations that set limits on heat flow at depths of a few hundred kilometers come from the study of seismic wave propagation in the moon and the whole moon's interaction with the time variable magnetic field of the solar wind as measured by surface and orbiting magnetometers. These observations indicate gradients of seismic velocity, attenuation coefficients, and electrical conductivity in the lunar interior which can be related through experimental data to temperatures and radial temperature gradients in the lunar mantle (Nakamura et al.,1976; Sonett and Duba, 1975).

The two direct surface measurements of heat flow made during the Apollo program were made in similar physiographic settings; i.e., on the edge of two of the moon's major mascon basins (Langseth et al., 1974). How representative these values are of the true global heat flow from the moon is not known because the variability of flux over the surface is not known.

The gamma-ray results taken from orbit indicate larger variations of thorium over the surface (Bielefeld et al., 1976) as well as variations in critical isotopic ratios. Far infrared emission spectra also give evidence for compositional variations over the lunar nearside. The orbiting x-ray and gamma-ray results show similar variations over the belts covered by the Apollo 15 and 16 Command Modules. If these compositional variations continue to considerable depth in the moon, they would result in variations in surface heat flow.

Near-surface measurements of heat flow are also subject to near-surface disturbances. One of the principal disturbances for which we have little data to estimate the effect is the refraction of heat flow at sloping interfaces between bodies of different thermal properties. If, for example, dense rock rises close to the surface beneath the mountainous rings of the circular mare basins, they could have a considerably higher conductivity than the

overlying regolith, and consequently, a pronounced effect on the distribution of heat flow near such structures (see also, Conel and Morton, 1975; Mitzutani and Osako, 1974). Consequently, it is extremely important to obtain further data that may determine the variability of heat flow over the lunar surface.

Microwave Spectra of the Moon:

One class of observation that bears directly on the variability of heat flow over the lunar surface is that of the microwave spectra between the wavelengths of 3 and 100 cm. The dielectric properties of the moon's surface are such that it is semitransparent to these wavelengths and, thus, the intensity of any given wavelength is determined by the integrated temperature profile to depths roughly equal to absorption length of the given wavelength. Consequently, microwave spectra can be interpreted in terms of the vertical temperature gradient if the dielectric properties, in particular the loss tangent is known. The first effort to determine the heat flow from the moon using microwave spectra was made by Bat in (1961) based on a very long wavelength observations (178 cm). At about the same time, similar observations were being made by Soviet astronomers. One of their publications (Troitsky and Tikhonova, 1970) inferred heat flows 2.9 to 4.0 x 10^{-6} cm^{-2}.

Recent improvements in radio astronomy have greatly improved the resolution of modern telescopes. Conceivably, earth-based telescopes could map the lunar nearside in the wavelength range from 3-20 cm at sufficiently good resolutions to detect regional variations in the brightness temperature gradient. Measurements of this type are currently being carried out by scientists of the Jet Propulsion Laboratory.

Observations of the variation of the microwave brightness temperature spectra with solar phase angle provide a direct measurement of the ratio between the thermal and electrical absorption lengths, the microwave data contain information on the variability of the subsurface properties over the surface. However, an independent estimate of either the thermal diffusivity or the electrical absorption length is required to convert microwave brightness temperature gradients to temperature gradients or heat flow. These estimates must be based on laboratory measurements of Apollo samples and in situ measurements of thermal parameters. The uniformity of conductivity values deduced from the heat-flow experiment are particularly significant in this regard.

Microwave Measurements from Orbit

It has long been recognized that passive microwave observations from a lunar orbiter would map heat flow over the entire lunar surface if, as in the case of earth-bound observations, the thermal or dielectric properties can be independently estimated. Such measurements were considered by the 1965 Falmouth meeting described earlier. More recently, NASA has been considering a Lunar Polar Orbiter mission as a follow-up to the Apollo Program. If this mission carried passive microwave radiometers, it could map the brightness temperature gradient and the parameter, δ, which is the ratio of microwave to thermal extinction length over the lunar surface. Such an instrument could map the variability of heat flow at the scale of 100 km or less.

An instrument to be flown on a polar orbiter has been proposed by a group at the California Institute of Technology. Work is now in progress on the problem of interpreting these types of data. Maps of global heat flow over the entire lunar surface, when combined with simultaneous measurements of the surface composition by gamma-ray spectrometry and other techniques, promises a synoptic view of the moon's surface and bulk chemistry which would rival our knowledge of the earth.

Future In Situ Measurements of Lunar Heat Flow

Remote observations relevant to lunar heat flow will always suffer from the problem of making a unique interpretation from the data because of uncertainty in estimates of certain crucial in situ physical properties. Thus, additional in situ measurements of the thermal properties of the lunar surface layer and the heat flow through the lunar surface would be extremely valuable because it would allow a refined interpretation of the microwave results. Especially important is an improvement in the absolute value of the heat flow.

Based on our present knowledge of the lunar surface layer and its thermal regime, accurate surface heat-flow measurements could be made from a soft landing station of moderate size and cost.

Recommendations for the Design of Future Instruments to Measure the Lunar Surface Heat Flow

The mechanical and thermal properties of the lunar surface layer were

reviewed in Section III-A. Those properties that most strongly influence future heat-flow instrument designs are reviewed here.

1) The regolith is covered nearly everywhere by a thin 2-15 cm layer of relatively low density, fine grained rock and glassy powder that has extremely low thermal conductivities on the order of 2 - 8 x 10^{-5} watt/cm °K. This layer has two important effects on the time-varying thermal structure of the regolith. Firstly, radiative transfer is important and a steady state temperature difference of several tens of degrees will be established across this layer. Secondly, the very low thermal conductivity will greatly reduce the periodic variations of temperature due to diurnal fluctuations of the solar flux at the surface; see Section V-A where the depth dependency of the amplitude and phase of diurnal variations is shown. The effect on the mean temperature of the radiative transfer in the uppermost layer based on data at the Apollo 15 and 17 sites are also shown.

2) Below the low density surface layer, the regolith fines are densely packed, approaching the maximum possible density (Carrier, 1974). The conductivity at these depths is 4-7 times greater than the near surface material. Conductivities of 1 to 1.5 x 10^{-4} watts $cm°K^{-1}$ were deduced from the attenuation of the annual wave with depth (Langseth et al., 1976). The regolith exhibits some stratification at the millimeter and centimeter scale in the lunar regolith, based on the grain size distribution and composition. Consequantly, some variability of the thermal conductivity can be expected. Despite the density of subsurface material radiative heat transfer may still be important and any thermal experiments such as those needed to measure the thermal conductivity should produce temperature differences less than three degrees.

3) Almost any disruption of the lunar surface will result in a change in the surface radiative and thermal properties and, therefore, the mean surface temperature. This change will produce a transient disturbance that propagates slowly downward from the surface. See Section V-C which shows examples of the disturbance induced at various depths by a 1°C change in surface temperature over a one meter radius circle. To avoid disturbance of any measurements by these effects, the measurement period should either be constrained to a short period after installation; or a very long period of one year or more so that transients can be observed and eliminated from the data.

4) The measured heat-flow values at Hadley Rille and Taurus Littrow of 1.4 and 2.1 watt/cm^2 induce vertical temperature gradients on the order of a degree per meter in the subsurface to depths of about 2-3 meters.

5) Heat flow may vary laterally over the lunar surface at the scale of a few meters due principally to variations in the radiative properties of the very near surface layer and the lateral heterogeneity of subsurface thermal properties. Thus, within any given region numerous measurements should be made to measure and average out this variability.

6) The regolith layer is relatively easy to penetrate with a tool of small cross sectional area and a sharp hard tip as was amply demonstrated by numerous core tubes driven into the soil and penetrator tests carried out on the lunar surface by the astronauts.

The characteristics described above apply over a very large proportion of the lunar surface. There are some isolated regions, however, where hard rock and higher thermal conductivities lie only a few centimeters below the surface. The IR hot spots (see e.g. Shorthill, 1972) identified from earth-based telescopes and lunar orbit (Mendell and Low, (1975) are one such area . It is also possible that on slopes greater than 10° the regolith may be considerably thinner than over more level areas.

Conceptual Design for a Lunar Station Heat Flow Experiment

The thermal and mechanical properties of the lunar soil layer described above are such that an accurate measurement of the mean temperature gradient (related to the steady outward flow of heat) could be obtained by a probe inserted only one meter into the lunar surface. The gradient measurement would be made in the lower 70 cm.

Figure VIII-1 shows a conceptual design for such an experiment. The main component is the long needle probe that makes the temperature and conductivity measurements. This probe could be made of titanium alloy tubing with a sharpened carbide steel tip. If a relatively high conductivity material such as titanium is used, the needle probe must have a large length to diameter ratio. In the design, we recommend a ratio of 200, which is more than adequate.

The temperature profile would be measured by a single small temperature element near the tip of the needle (the prime temperature element). Use of a single element would reduce the stringent requirements on the accuracy of an array of elements such as those used in the Apollo instrument. Thus, a

sensor such as a thermistor could be used.

The temperature profile would be measured by driving the probe, which is initially retracted inside the housing, slowly into the soil. A motor driven lead screw and vibrating head at the top of the needle probe accomplish this. The probe makes ten or more predetermined stops on the way down. A wait at each stop is made long enough to allow calculation of the equilibration temperature of the adjacent regolith material. For a probe 0.5 cm in diameter, made of titanium alloy, the equilibration time is about a half hour.

Additional sensors along the probe (K-sensors) would be used in conjunction with a single filament wire running the length of the probe to measure the thermal conductivity. The technique for conductivity measurement is the well known needle probe technique used in seafloor geothermal studies. The absolute accuracy of these sensors is not important. A resolution of about 0.003 K is required for the measurement and stability over a six hour period. The conductivity measurements require about six hours. Measurements at all locations would be made simultaneously.

Measuring the gradient with the 'moving sensor' technique can only be used below depths of about 30 cm, because of the sizable variations introduced by the diurnal wave in the near surface regolith and heat transfer along the probe from the housing on the surface.

The instrument should also include surface temperature thermometers. Lunar surface thermometers are hard to design. The primary temperature element sees thermal radiation, and during the lunar day reflected solar radiation, from the lunar surface over a field of view of 2π steradians. Over the other 2π steradians, the sensor sees the interior of blackened copper cavity, which is kept at as low a temperature as possible. The average interior temperature of the cavity is measured by additional thermometers. The cavity is kept relatively cold by shielding it from direct sunlight and giving it the largest possible view of outer space.

The greatest uncertainty arises from the solar albedo which will be a factor only when the sun is up. Thermometers with an accuracy of a few tenths of a degree would be adequate to give temperatures with far greater accuracy than heretofore. The surface temperature observation is required to determine the forcing temperature function at the surface.

Surface temperature observations at a single point should be taken during one lunar day. This would allow determination of the variation of

surface temperature over a complete lunation cycle. From these data, the mean surface temperature and an estimate of the parameter $(K \rho c)^{1/2}$ of the upper 10-15 cm of material can be determined.

Penetration of the regolith would be accomplished during either the lunar day or lunar night, depending on when the most power was available. The subsurface measurements could be accomplished in approximately ten earth days. Temperature profiles measured by the heat-flow probe would have to be corrected for transient disturbance caused by the diurnal and annual variation propagating downward from the surface. The instrument would obtain sufficient data to make these corrections quite accurately.

This approach could be used on any planet with an extremely tenuous atmosphere and penetrable surface layer.

Other Possible Techniques to Measure In Situ Heat Flow:

The method of heat-flow measurement described above could only be carried on a soft landing spacecraft. Another type of mission that has been considered, is the so-called penetrator mission. By this concept, small probes would be launched from an orbiting spacecraft and bury themselves in the lunar surface layer. The body of the probes and internal instruments would have to be of rugged design to withstand impact and penetration. There is a major technical problem to using the penetrator technique on an atmosphereless planet. A rather accurate orientation and guidance technique is required to assure vertical penetration, or the vehicle will be destroyed by shearing forces on penetration.

Such a penetrating probe would provide good penetration at most areas on the moon; deep enough so that undisturbed gradients, due to heat flux from the interior could be measured, after the initial heating during penetration has dissipated. The dissipation would require at least two to three lunations. A serious problem is the heat generated by any dissipating circuits or power sources in the penetrometer. Because of the extremely low conductivity of the regolith material, very high temperatures would result from very low power levels. At the present time, the penetrator mission does not appear to offer an attractive possibility for accurate lunar heat-flow measurements.

References

Baldwin, F.E. (1961) Thermal radiation from the moon and the heat flow through the lunar surface. Mon. Not. Roy. astron. Soc., v. 122, p. 513-622

Bielefeld, M.J., R.C. Reedy, A.E. Metzger, J.I. Trombka and J.R. Arnold (1976) Surface chemistry of selected lunar regions; Proc. Lunar Sci. Conf. 7th, p. 2661-2676

Carried, W. David, III (1974) Apollo drill core depth relationships; The Moon, v. 10, p. 183-194

Conel, J.E. and J.B. Morton (1975) Interpretation of heat-flow data. The Moon, v. 14, p. 263-289

Langseth, M.G., Jr., S.J. Keihm and J.L. Chute, Jr. (1974) Heat Flow Experiment; in, Apollo 17 Preliminary Science Report, Section, NASA SP-330, U.S. Gov't Print. Off., Wash. D.C., p. 9-1 to 9-24

Langseth, M., S. Keihm and K. Peters (1976) The revised lunar heat flow values. Proc. Lunar Sci. Conf. 7th, v. 3, The Moon and Other Bodies; Geochim. et Cosmogr. Acta, R.B. Merrill et al., eds., p. 3143-3171

Mendell, W.W. and F.J. Low (1975) Infrared orbital mapping of lunar features; Procl Lunar Sci. Conf. 6th, p. 2711-2719

Mizutani, H. and M. Osaka (1974) Elastic wave velocities and thermal diffusivities of Apollo 17 rocks and their geophysical implications: Proc. Lunar Sci. Conf. 5th, v. 3, p. 2891-2901

Nakamura, Y., G.V. Latham, H.J. Dorman and F.K. Duennebier (1976) Seismic structure of the moon: A summary of current status. Proc. Lunar Sci. Conf. 7th, p. 3133-3121

Shorthill, Richard W. (1972) The infrared moon: A review: in, Thermal Characteristics of the Moon; J.W. Lucas, ed., Progress in Astronautics and Aeronautics: v. 28, p. 3-49

Sonett, C.P. and A. Duba (1975) Lunar temperature and global heat flux from laboratory electrical conductivity and lunar magnetometer data Nature, v. 258, p. 118-121

Troitsky, V.S. and R.V. Tickhonova (1970) Thermal radiation from the moon and the physical properties of its upper mantle; Radiofizika, v. 13, n. 9, p. 1273-1311

APPENDIX A. EARLY EXPERIMENTAL CONCEPTS

The text of this section is largely extracted from a 1966 report* by Arthur D. Little of a study of various concepts for measuring the temperature gradient in the regolith and the thermal conductivity.

To guide the design of a probe to determine lunar heat flow, we (ADL) established a list of "desirable characteristics." The relative ranking of many alternative concepts and selection of the probe design was guided by these characteristics. The desirable characteristics are first outlined in general terms and then a number of specific designs and their advantages and disadvantages are discussed.

DESIRABLE PROBE CHARACTERISTICS

Fail Safe

An ideal probe is "fail safe." That is, it is highly desirable that the probe should be capable of yielding useful data even if one component fails. For example, there is an increased possibility of failure of a probe with moving parts, however, by appropriate design such a probe would not become completely useless.

In situ Calibration

Both absolute and differential temperatures are to be measured. The heat flow experiment requires very high accuracy in the differential measurements. It is advantageous to determine, at least intermittently, whether the differential temperature signals are real or spurious. A simple check is to force the differential sensors to read the same temperature; a zero

---

*Design Definition of Heat Flow Probe - Summary Report by Arthur D. Little, Inc. 68399

signal indicates that any transmitted signal is, in fact, due to a temperature difference. In the absence of an in situ calibration the sensor has to maintain the original calibration during launch, traverse to the moon and observation period.

Thermal Conductivity Measurements

Thermal conductivity of the lunar material has to be measured in the region where the temperature gradient is to be determined. Depending upon the local conductivity two techniques are to be used. For low-conductivity materials, an integral heater-temperature sensor is necessary. For high-conductivity materials, the heater and temperature sensor must be separated axially. To determine axial inhomogeneities in the lunar material, thermal conductivity is to be measured at different axial locations. Thus, in any probe design at least one heater and two temperature sensors have to be provided. One of the temperature sensors can be the same as that used to measure the temperature gradient.

Maximum Interval for Temperature Difference Measurement

It is desirable to measure the axial temperature difference over the total probe length. Additional measurements over a portion of this length or multiple probes are desirable if weight limitations are not exceeded.

Simplicity

The design of the probe should simplify the experiment. Certain sensors require simple electronics; others do not require motion of any part relative to another. Simplicity will increase reliability, require less development work, and thus shorten development time and cost.

Emplacement

The probe has to be designed to be compatible with astronaut human factors, emplacement tools, and packaging requirements. Both emplacement

at the required depth and radial positioning within the hole have to be accomplished by an astronaut.

Low Axial Conductivity

To measure small temperature differences accurately in the lunar material, the probe must not behave as a thermal short in the axial direction. The axial thermal resistance of the probe wall, insulation, lead wires, etc., must be large.

Weight

The probe weight should be as small as possible.

Resistance to Vibration and Shock

Each probe must be designed to meet ALSEP environment specifications without decreasing the operational effectiveness of the probe.

Conceptual Probe Designs:

THE STATIC PROBE

The static probe is the simplest type. Temperature sensors are placed at or near the probe ends and held apart by a lightweight, strong, thermally resistive structural member. A schematic diagram of this type of probe is shown in Figure 1. Two additional temperature sensors would be needed about 8-12 cm from the end heater-sensor units to measure temperature when operating the thermal-conductivity experiment for high-conductivity lunar materials.

Additional temperature sensors can be incorporated within the probe to measure the gradients between different locations, or two probes can be connected in tandem to determine temperature differences over an additional distance in the drill hole.

The principal disadvantage of the static probe is the dependence on the absolute sensor stability. There is no way to calibrate the probe in situ to test that measured temperature differences are real and not spurious.

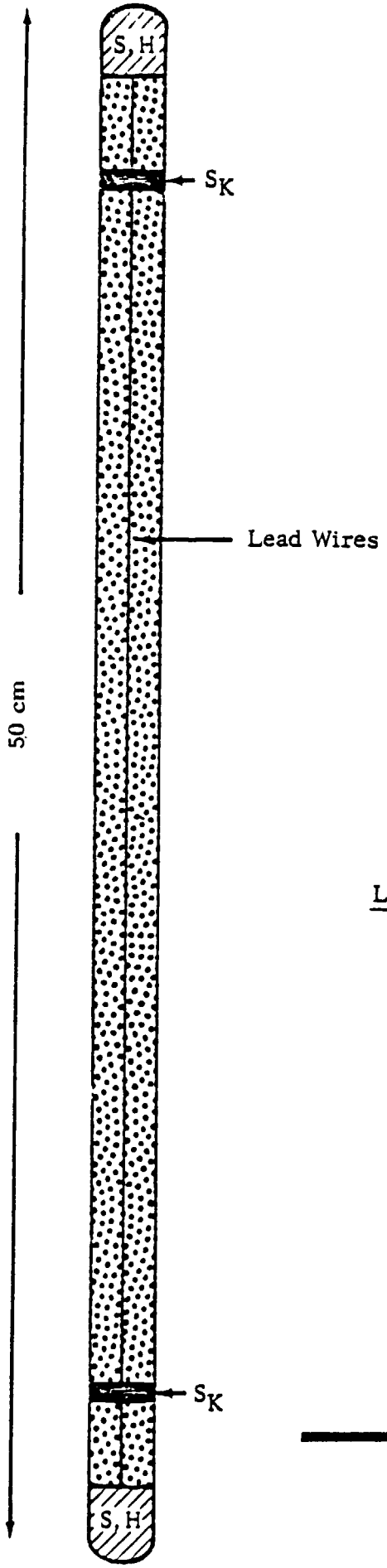

LEGEND:

▨	Isothermal Section
⊡	Insulation Section
S	Sensor
H	Heater
S_K	Thermal Conductivity Sensor

SCHEMATIC DIAGRAM OF STATIC PROBE

Appendix A-Figure 1

This type of probe can only be used when the long-term stability of the two end sensors can be ensured. However the thermal conductivity sensors on the probe wall do not need long-term stability since they are only used to measure a temperature rise during a short time interval.

DYNAMIC PROBES

In a dynamic probe at least one moving part is incorporated within the probe. The dyanmic probe concepts can be subdivided according to the required movement: long, short, or very short. Long-movement devices require relative movement of one part over the entire probe length, e.g., to be accomplished by a motor at the lunar surface. Short-movement devices require movement over a few centimeters, e.g., by a solenoid mounted on the probe. Very-short-movement devices limit motion to a fraction of a centimeter, e.g., a magnetic-latched reed switch. Lead wire bending should be kept to a minimum to prevent generation of spurious signals. It is convenient to simplify dynamic probe designs we have considered into two general groups. In one type, the temperature sensors are thermally short circuited to obtain a zero reading. In the other type, a single sensor is moved vertically up and down inside the probe to sense the temperature at various stations, and to indicate any offsets of temperature sensors.

Thermal Switch Probes

The thermal switch probe concept is illustrated in Figure 2. The two end sensors have been extended by "isothermal" bars to points near the center of the probe. The open circle area indicates a thermal switch zone. To avoid long recovery times, the two ends of the isothermal extensions should not be thermally shorted; therefore, a third "sampling" sensor must be incorporated. Such a sensor must be light-weight (low thermal capacity), insulated from the probe walls, and mounted so as to sample first one end and then the other end

of the extension bars. This sensor could be differentially compared to a second sensor located in either the top or bottom isothermal section. If the top were chosen, then when the thermal switch is closed the sampling sensor is thermally shorted to the top section and no signal should be received from the sampling sensor. An automatic zero-offset calibration is thereby achieved.

When the sampling sensor is shorted to the lower section, the probe temperature difference should be obtained. This difference may be compared to the value read by the fixed sensors and thus the offset of the latter may be checked. The thermal mass of the sampling sensor is sufficiently small so that no significant variation in the temperature of the upper and lower sensors occurs during switching.

The fixed sensors are redundant if the sampling sensor operates satisfactorily. However, if the sampling sensor fails to operate, the fixed sensors would provide a back-up so the experiment need not be aborted.

The thermal switch can be of several types; we considered two types:

The sampling sensor can be centered so that an enclosed reed switch is magnetically latched to contacts on either the upper or lower extension bars (see Figure 2a).

The extension bar of the upper sensor can be made into an annulus with an insulated bar extending through its entire length (see Figure 2b). Near the end of this insulated bar is a high-thermal-conductivity section. The lower bar has a pocket for receiving the rod and the sampling sensor is provided with an annulus to allow passage of the rod. The insulated rod can be driven by a solenoid on the top of the probe. When the sampling sensor is bridged by the high-conductivity section of the rod to the upper isothermal arm, it is thermally shorted to measure the upper sensor temperature.

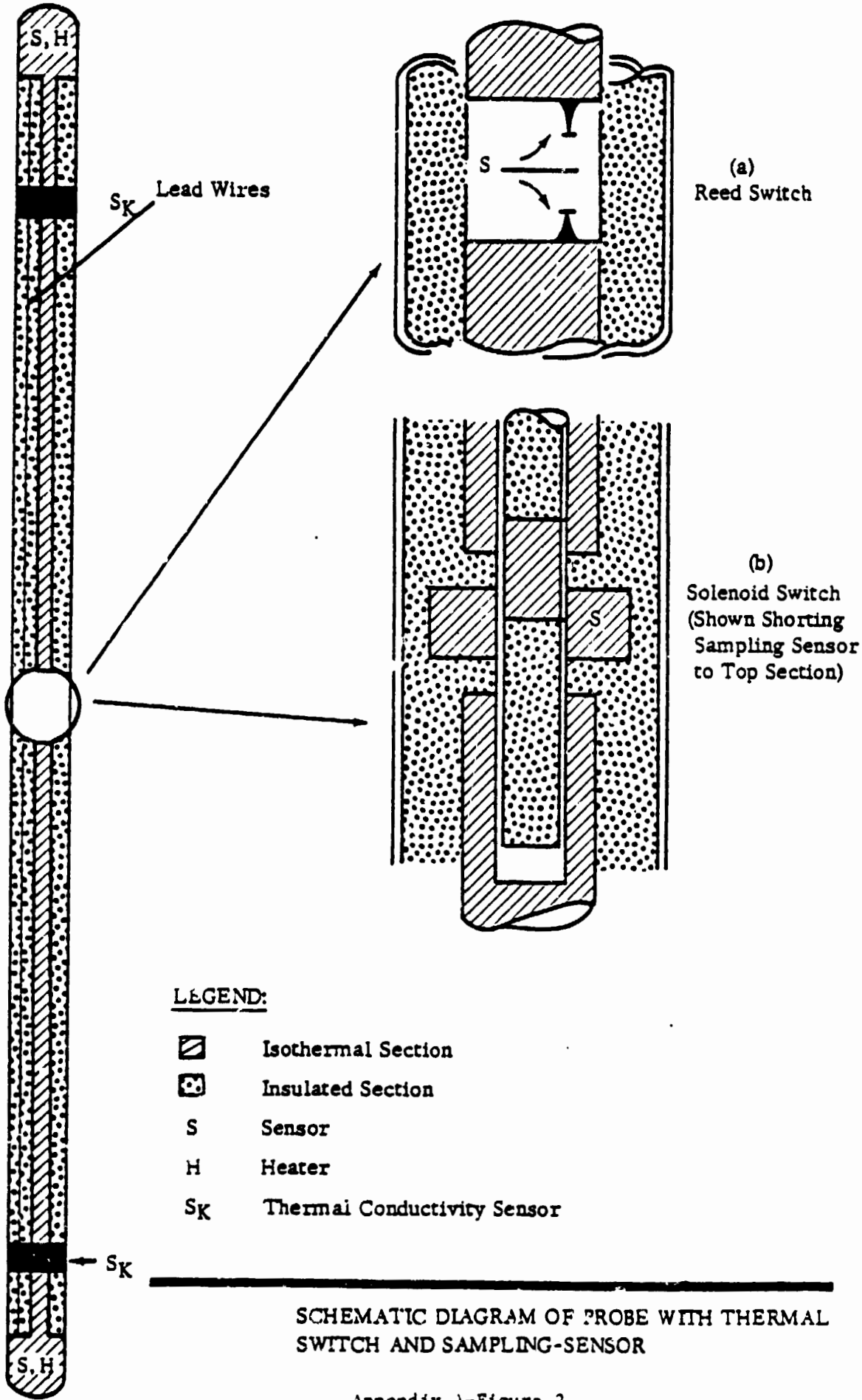

SCHEMATIC DIAGRAM OF PROBE WITH THERMAL SWITCH AND SAMPLING-SENSOR

Appendix A-Figure 2

Downward movement of the rod causes the high-conductivity section to move through the sampling sensor and thermally short to the lower extension bar. One disadvantage of the solenoid switch is the necessity of holding the sampling sensor in position rigidly. This can be done by axial springs.

Alternatively, the sensor could be eliminated and incorporated into the high-conductivity section of the solenoid-actuated rod. Shorting can be accomplished as before. The short travel of the solenoid will reduce bending effects on the leads.

These concepts satisfy the requirement of providing a zero-offset calibration for the temperature gradient sensors. Probes incorporating these concepts require considerable development work, would be heavier and have a lower axial thermal resistance.

Moving Sensor

This concept would use a single movable sensor that is raised and lowered inside the probe sheath. To utilize this method, techniques must be available to move a sensor over distances of 50 cm without introducing effects caused by the continual bending of lead wires. Figure 3 shows the moving sensor concept. Two fixed sensors are placed in the top and bottom isothermal sections. The center of the probe is enclosed by a thin-walled tube inside of which another thin-walled tube moves vertically. A small sensor is attached to the lower end of this tube. This sensor is an absolute temperature-measuring device with a low heat capacity so that it rapidly reaches the upper or lower sensor temperatures without significantly affecting the sensor temperature at those locations. To calibrate, the sensor is lowered to the bottom station of the probe. It is then raised to the top station and another reading taken. The difference in temperature should agree with that read out on the fixed sensors.

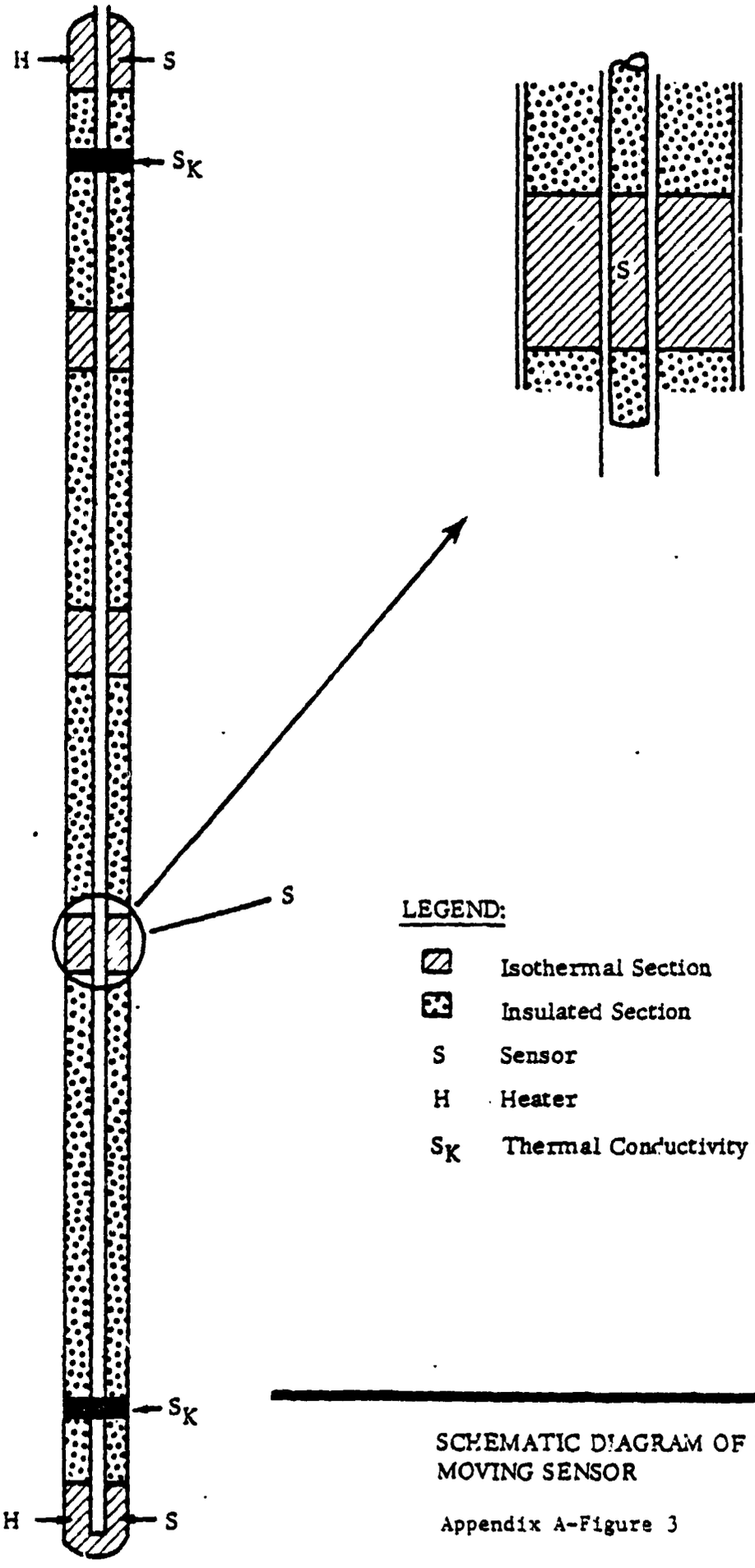

LEGEND:

▨	Isothermal Section
⊠	Insulated Section
S	Sensor
H	Heater
S_K	Thermal Conductivity Sensor

SCHEMATIC DIAGRAM OF PROBE WITH MOVING SENSOR

Appendix A-Figure 3

As an alternate feature, other heat stations can be added at intervals along the probe. Between calibrations, the moving sensor can be located at any of these stations to yield additional temperature data. In addition, the tubes can extend to much higher levels and the moving probe can be used to monitor amplitudes and phases of the "AC" thermal wave propagation downward from the lunar surface. The thermal conductivity can be determined at the top and bottom locations with two heaters. If the moving sensor fails, the moving probe degenerates to a static probe. If the fixed sensors fail, the device can still operate to produce data.

The moving sensor probe may be used without fixed sensors at the probe ends but the reliability of providing the motion over long periods of time is such as to make it desirable to have the probe degenerate to a static probe if failure of the moving parts occurs.

TEMPERATURE SENSORS

Platinum Resistance Bridge Sensors

For the static probe only the platinum resistance bridge is a suitable sensor capable of meeting the stringent stability requirements. Figure 4 shows the sensor design selected for the measurements of temperature gradient.

The sensor design has been developed specifically for use in the probe. The physical configuration of the sensors, in the form of a hollow cylinder, allows them to be mounted in the probe with minimum difficulty and to sense temperature with a time constant not limited by the sensor time response; it also allows interconnecting leads for other probes or sensors to pass unhindered.

Each cylinder contains two platinum resistance sensors of nominal 500-ohm resistance. Each resistance element is bifilar wound of 0.0015-inch platinum wire on an inner platinum cylinder. Each element consists

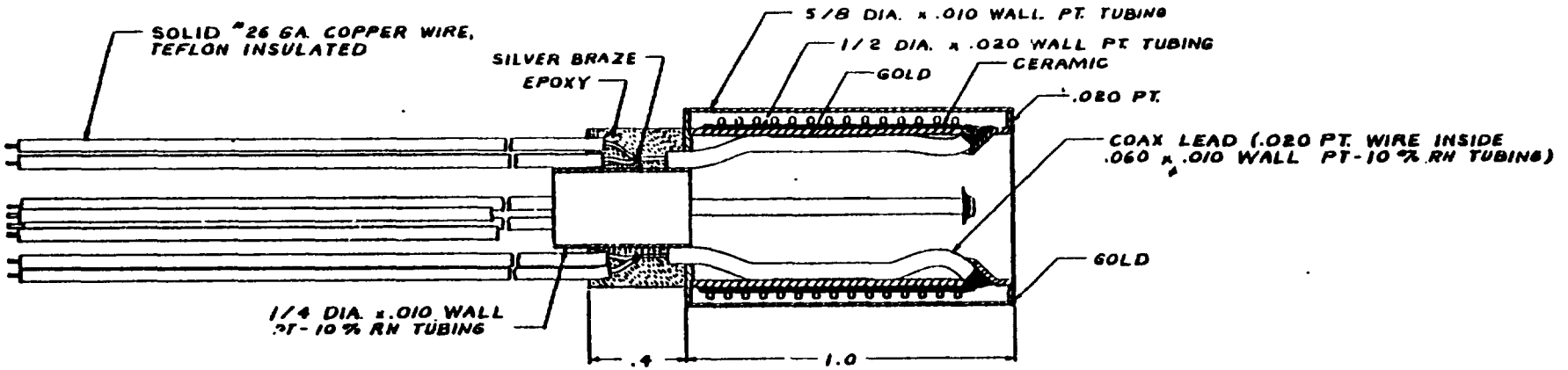

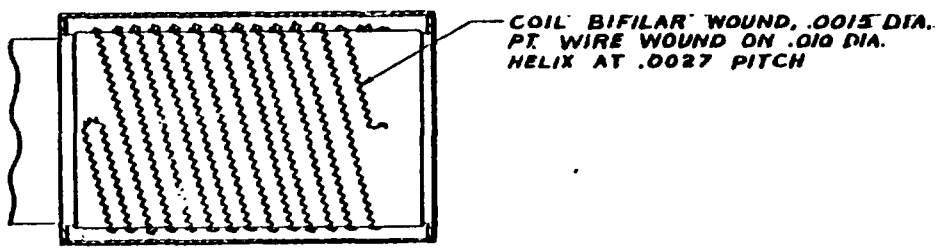

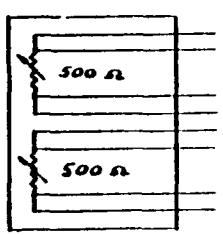

SCHEMATIC DIAGRAM

QUANTITY PER ASSY	PART NO	ITEM NO	DESCRIPTION
			LIST OF MATERIAL

UNLESS OTHERWISE SPECIFIED REMOVE ALL BURRS AND SHARP EDGES MACHINE SURFACE FINISH 125 TOLERANCES DECIMALS X ± .1, XX ± .03, XXX ± .010 FRACTIONS ± 1/32 ANGLES ± 2° METRIC 0.38 to 1.50 ± 0.08, 1.50 to 3.00 ± 0.13, 3.01 to 9.00 ± 0.25 DO NOT SCALE PRINT

ROSEMOUNT ENGINEERING COMPANY MINNEAPOLIS, MINN

TITLE: SPECIFICATION DRAWING SENSOR, TEMPERATURE, PLATINUM RESISTANCE TYPE

DR BY	DATE	CODE IDENT NO	SIZE	DRAWING & PART NO	REV
JERGENS	6-10-66	04274	C	137CR-1	
CHK'D					
APPD Peat	6 10 66	SCALE 4/1	WT	SHEET 1 OF 1	

SCHEMATIC DIAGRAM OF PLATINUM RESISTANCE TEMPERATURE SENSOR

Appendix A-Figure 4

of a long coil, 0.010-inch in diameter, laid on a ceramic substrate in such a way that only the bottom portion of each turn of the coil is embedded in the ceramic. This particular mounting technique ensures that the wire is pure after annealing and will remain pure. The design of the coil provides resistance to dimensional changes of the substrate and induced strain changes of resistance, and assures a rugged mounting of the sensing element.

It is this mounting technique to which we may attribute the outstanding sensor performance. The stability of the sensors in a bridge configuration was 2 millidegrees or better after meeting the LEM environment shock, and random and sine vibration requirements as well as thermal cycling between 195°F and 355°F (See Figure 5).

The element is protected by an outer gas-tight platinum case, and the sensor cavity is filled with helium. The sensor pinch-offs are designed to minimize both leakage resistance and gas loss. The epoxy sealing technique allows a gas-tight seal with low electrical and gas leakage.

The smaller temperature sensor is preferable for the thermal-conductivity measurements. It must be installed on the surface of the probe. T' present design consists of platinum wire wrapped on a ring-shaped platinum sleeve and embedded in a ceramic cement. Because this sensor has to measure the temperature rise during a short time interval, no long-term stability is required.

Later testing of these sensors indicated that their stability was nearly as good as the more elaborate sensor described above. The temperature histories of these "ring" sensors on the lunar surface indicate that they have held their calibration within a few thousandths of a °K.

Alternative Temperature Sensors

We also evaluated several different movable probe-type temperature sensors.

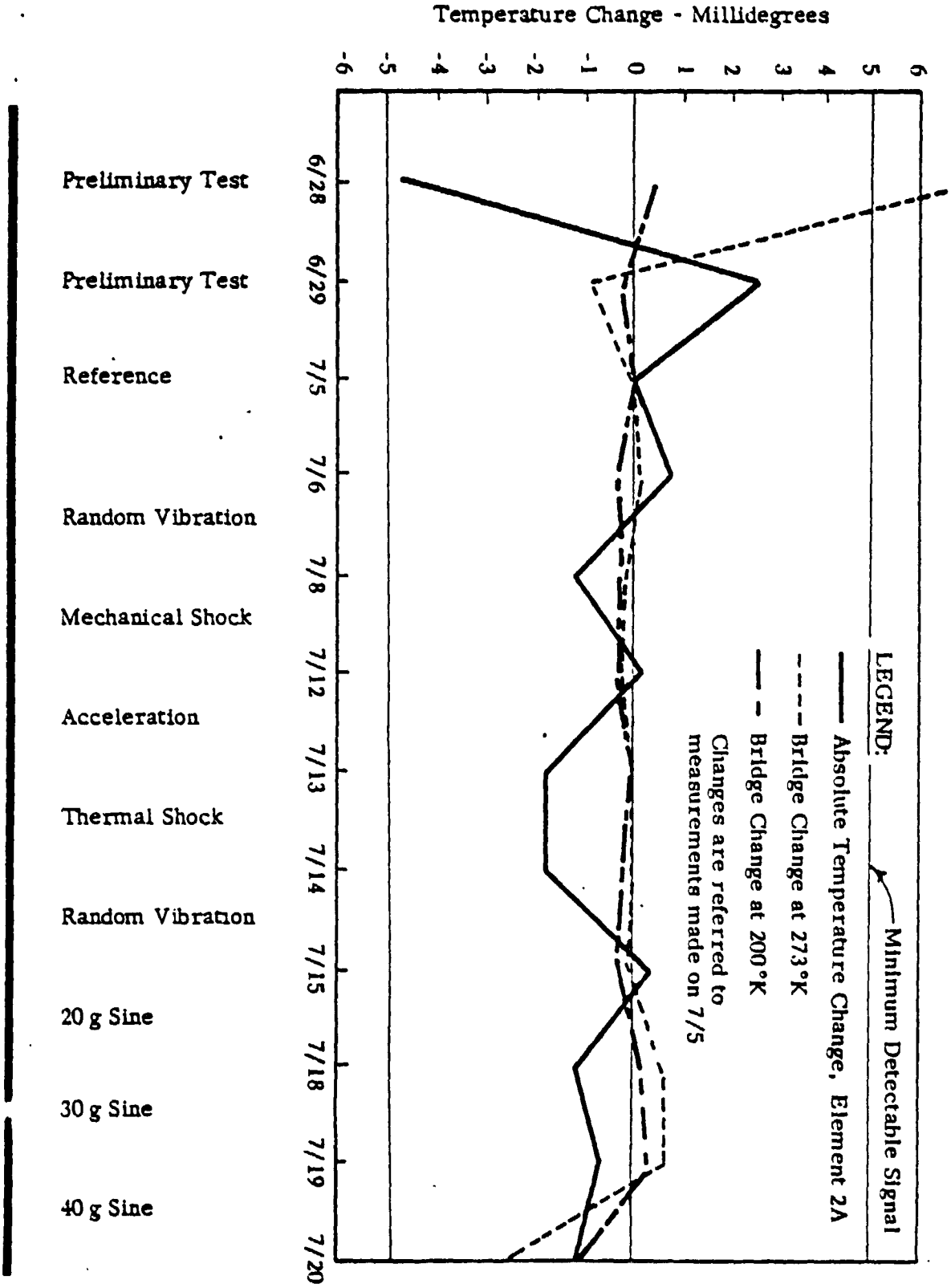

Appendix A-Figure 5

Because this concept permits zero-offset calibration, long-term stability of the temperature sensors can be relaxed. The sensors considered include the following:

- resistance thermometers (platinum, nickel, carbon)
- thermocouples and thermopiles (iron-constantan, chromel-constantan, copper-constantan, gold-cobalt-copper
- solid-state devices (thermistors, doped silicon, germanium, gallium-arsenide)
- mechanical resonators (quartz crystals)
- property variation sensors (gas thermometers, nuclear magnetic resonance).

When we applied selection criteria such as documented performance data in the specified mechanical and lunar environment, compatibility with electronics, development status, and availability from reputable suppliers to meet delivery schedules, none of the temperature sensors could approach the over-all suitability of the platinum resistance temperature sensors. The silicon carbide semi-conducting sensors and quartz crystal oscillators were the most promising of those considered although they did not meet several of the selection criteria. When installed in the probe cable, thermocouples can be used to measure the temperature changes within the borehole.

The Preferred Probe Design:

Because of its simplicity and the demonstrated stability of the platinum resistance thermometer the static probe design seems the best approach at this time. The design of a static probe has been further advanced and is described in more detail below.

Two separate static probes are connected by a flexible cable so that one is directly above the other when installed in the borehole. This configuration can provide the desired data with greater reliability than a single static probe.

The two probes, of identical construction, are connected with a flexible cable which permits the whole assembly to be bent into a "U" shape. In this manner the probes and cables can be packaged to meet the requirements of the ALSEP scientific equipment bay.

The probes consist of epoxy-fiberglass tubular structures which support and house temperature sensors and their associated electrical wiring. The probe structure is designed to hold the components in a fixed relationship and to protect the sensors, heaters, and internal leads from the imposed mechanical and lunar environments. The structural materials have been chosen to provide a minimum axial thermal conductivity consistent with minimum weight requirements. The probe structure consists of two concentric thin-walled filament fiberglass-epoxy tubes, spaced by five annular braces which are bonded in place.

Thermal Conductivity Measurement

Design Criteria

A method for determining lunar material thermal conductivity in the borehole is a required part of the heat flow experiment. The criteria which we have used in evaluating various design possibilities are:

(1) K_{moon} Measurement

Range: 4×10^{-3} to 2×10^{-5} watt/cm°K*

Accuracy: greater than 20%

(2) Power Available

100 mw (for 1 month)

1 watt (for less than 14 days)

(3) Time Available

1 month or less if possible

---

* This range recognizes the possibility that an experiment might be surrounded by a solid rock in the regolith.

(4) Temperature Measurement Cabability

Range: 0-2°K differential (possibly two fourfold-amplification stages)

Accuracy: $\pm$ 0.001°K

Maximum Environment Temperature Allowed: $\sim$ 400°K

(5) Temperature Read-Out Intervals

10 min (for single point read-out: 1 min)

(6) Design

The device must be a compatible part of the heat flow probe, and should meet all operational requirements for the static probe. Because the probe will not be in physical contact with the lunar borehole, heat transfer between the probe and the lunar material will be by radiation only. If necessary for obtaining a conductivity measurement, solid contactors could be added to portions of the probe.

(7) Multiple Determinations

If possible, to indicate either homogeneity or stratification.

Experiment Concepts:

Thermal Conductivity (k) and/or thermal diffusivity ($\frac{k}{\rho c}$) may be determined by placing a controlled heat source within a medium and measuring temperature at a point in the system. A heater-temperature sensor arrangement which appears most suitable for the present application is shown in Figure 6. Since the possible range of lunar material thermal conductivity values extends over two orders of magnitude, two modes of operation are required.

In the "Low K" mode the heater is turned on and its temperature is measured as a function of time. A typical power level of 1-5 milliwatts produces about a 2°K dynamic range requirement for the temperature sensor. The steady-state

temperature level is related to both the lunar material thermal conductivity and the resistance across the radiation gap between the heater and the moon. If the radiation resistance can be estimated with sufficient accuracy, then the thermal conductivity may be computed.

Should the lunar material be highly conductive, then the radiation gap resistance becomes large -- relative to the effective lunar resistance. A small error in predicting the radiative flux can be amplified by as much as twenty times in the thermal conductivity estimate. Although the gap resistance could be reduced by the use of solid contactors, the uncertainty in estimating contact conductance becomes very great due to the strong dependence of the conductance on the unknown structure of the borehole surface.

Therefore, if the Low K mode temperature level indicates a high lunar conductivity (which, however, cannot be resolved within a $\pm$ 10 per cent accuracy), a second type of thermal conductivity experiment is carried out. In Hi-K mode, the heater power is suddenly raised to a continuous level of about one watt. Temperature sensing is initiated at a location on the probe about 8-10 cm away from the center of the heater (again for a 2°K dynamic range). For the ideal case of a perfectly insulating probe, the temperature monitored in the moon at a specified distance away from the heat source will be determined by only the rate of propagation of the thermal wave through the lunar material. The time derivative of this temperature-time curve will have a maximum value which is inversely proportional to the density-heat capacity product (ρc) of the moon and a peak width or position on the time axis which is related to thermal diffusivity. If these two quantities can be measured with sufficient accuracy, thermal conductivity can also be determined.

In a practical system, several real effects decrease the sensitivity of the measurement. The probe section between the heater and the Hi-K mode sensor must be designed to prevent the effects of thermal shorting down the probe from masking the signal in the moon. In addition, the thermal mass of the Hi-K mode sensor must be small, so that thermal inertia in the sensing device does not alter the transient response of the data signal. Both of these real effects have been considered and it appears feasible to use the Hi-K mode in the conductivity range of 4×10^{-3} to about 4×10^{-4} watts/cm°K. For lower thermal conductivities, the shorting effect of even a well designed probe becomes significant. The time required for the measurement in this case becomes appreciably longer than several hours and the large amount of energy transferred to the moon requires an excessively long time to dissipate (several weeks). For these reasons, use of the Hi-K mode is suitable only for measurements at the high end of the possible conductivity range. However, this is the range where Low-K mode measuring capability is poorest. Used together, the two methods complement each other and can meet the experimental requirements.

The time required for making the thermal conductivity measurement is less than a month for both methods. For low conductivity, measuring times can become long, since an approach to a steady-state temperature level is required. The time scale is longest for the lowest thermal conductivity to be determined — about 10-20 days. In the Hi-K mode, the time scale of the experiment is greatly reduced, both because of the higher thermal conductivity and because transient, rather than steady-state, data are obtained. However, for a lunar material thermal conductivity of about 4×10^{-4} watt/cm°K a heating period of about 6 hours at a 1 watt source level is estimated. The time required for the gradient resulting from the heating to decay to five percent of the undis-

turbed lunar gradient ranges from about 20 days for the case just mentioned down to about two days for a material of high thermal conductivity.

Design of Thermal Conductivity Apparatus

The components required for measurement of lunar material thermal conductivity by the methods described are:

Lo-K mode: A heater which is integral with a stable, sensitive temperature sensor and is radiatively coupled to the moon.

Hi-K Mode: A heater located about 8-10 cm away from a sensitive temperature sensor. The sensor should be lightweight (∿1 gm), but long-term stability is not required. The heat flow down the probe section should produce a temperature rise at the corresponding point in the moon -- the probe wall should not act as a thermal short.

The design is indicated in Figure 6. One such conductivity instrument is located at each probe end. The heater is mounted directly on one of the main platinum temperature sensors. The sensor has been assumed to have a dynamic range of 2°K and a sensitivity of 1:2000. The heater winding forms a cylindrical heat source of about 2 cm diameter and 2.5 cm in length. Initial estimates, which will require further refinement in terms of either a detailed digital or analog simulation of the actual system, indicate that the power dissipation in the heater will be about 1-5 milliwatts for the Lo-K mode operation (low conductivity range) and about 1 watt for the Hi-K mode (high conductivity range). On the basis of a 29 volt (maximum) power supply, the heater winding should have an electrical resistance of about 840 Ω.

The Hi-K mode sensor, located about 10 cm away from the center of the heater, can have the same range and sensitivity as the main bridge sensor.

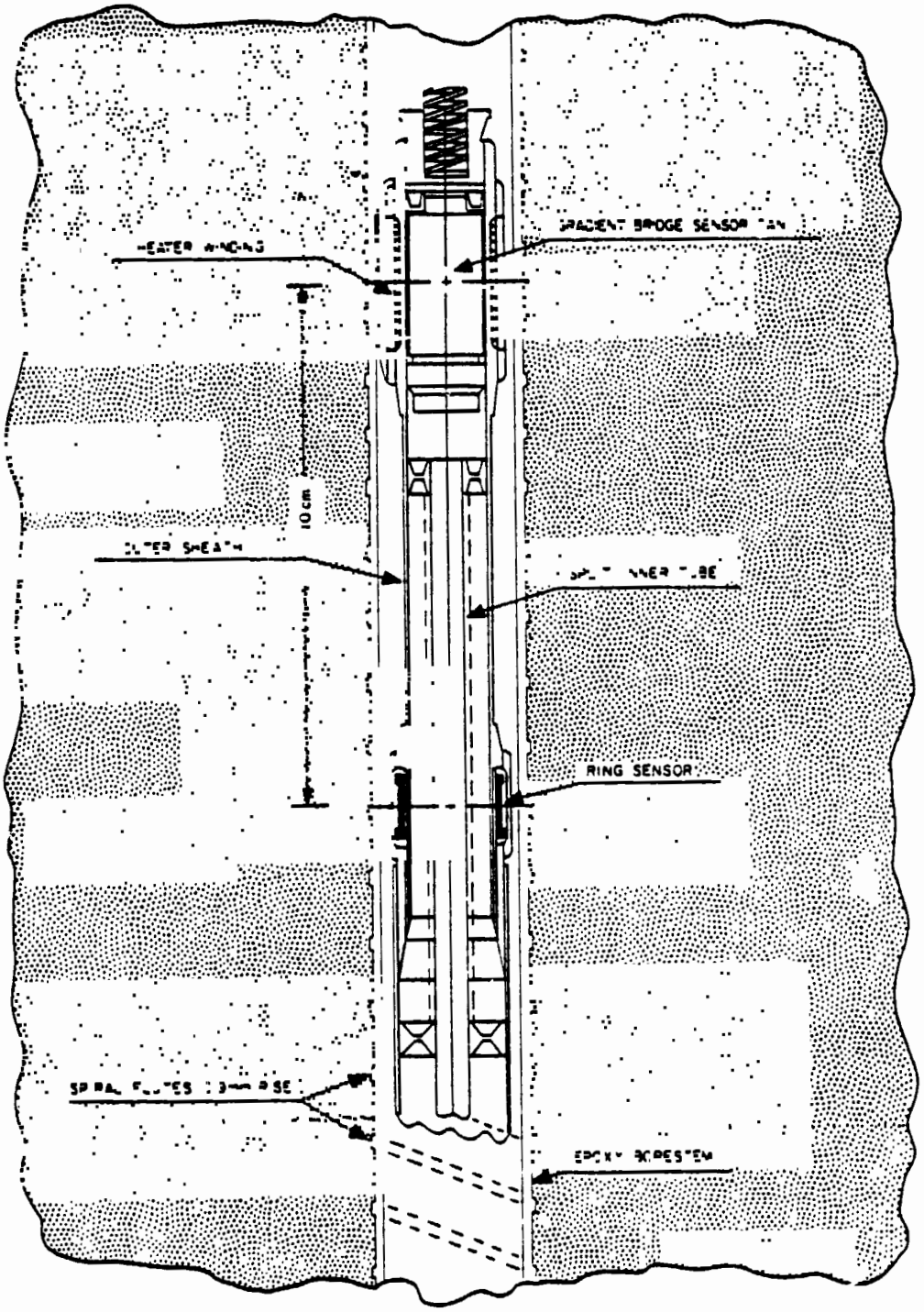

Appendix A-Figure 6

The smaller sensor will also be a platinum bridge designed to have a total weight of about two grams, with stability required only for periods of several hours (as opposed to the larger main sensors which must be stable for a year). The sensor will be mounted in a conducting band (width about 0.5 cm) which encircles the body of the probe.

The two small sensors on each probe (one toward each end) will each form half of a platinum bridge. Only one heater will be run at a time and the farther sensor will act as a reference. The wires connecting the bridge will be run along the inside of the probe body wall to prevent equilibration with the main cable bundle. Power and signal leads to the bridge will be introduced at the midlength point where thermal shorting from the heater down the main cable bundle will be at a minimum.

The inner tube which holds the cables may also act as a thermal short. To reduce this effect, the surfaces of the cable sheath and the inside of the probe body are silvered in the region between the heater and the remote sensor to prevent radiative transfer to the probe body from the cables. (These surfaces are black in regions outside of the Hi-K mode experiment zone). The outside of the probe body is black to permit heat loss from the probe wall to the hole wall, thereby greatly reducing the thermal shorting down the probe.

Final Design, Calibration and Data Interpretation

Although initial probe design has been based on valid, but approximate, models which can be treated analytically, a detailed model including all the interrelated effects of heat transfer between and within probe components as well as between the probe and various types of possible lunar materials is required for probe calibration and accurate interpretation of data.

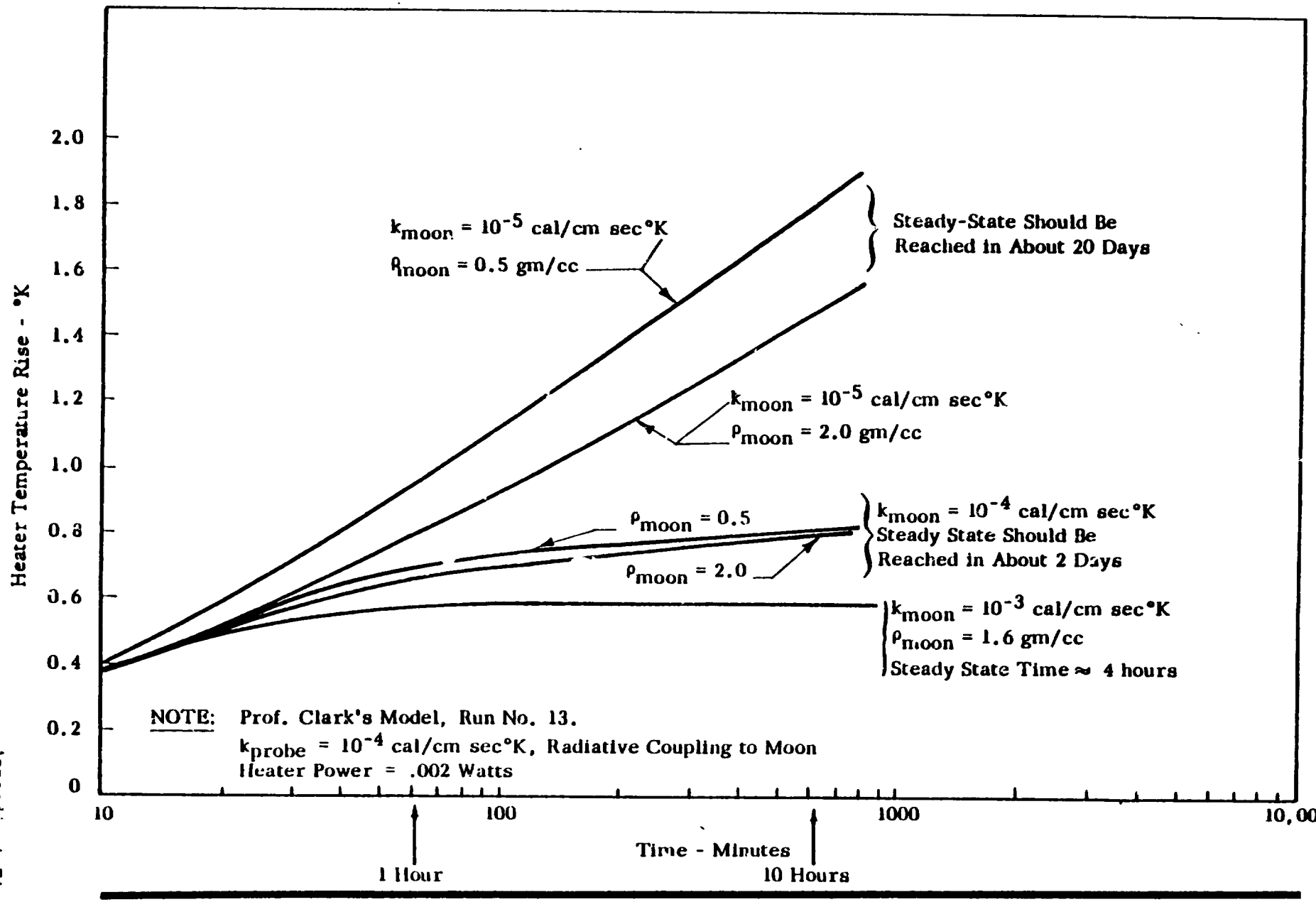

COMPUTED HEATER TEMPERATURES FOR MODE A CONDUCTIVITY EXPERIMENT

Appendix A-Figure

Such a model can be either a digital computer program for the actual system or an electrical analog simulation. The latter method has much to offer in terms of ease of formulation, low cost and inherent flexibility, but results are limited in accuracy by the use of components of $\pm$ 1 percent precision. Since the temperature sensors are designed for a 1:2000 resolution, the electrical analog is not sufficiently accurate for measurements requiring full resolution over the entire dynamic range of the sensor. In the Hi-K mode conductivity experiment, full temperature resolution is required so that accurate values of the temperature derivative can be obtained. However, errors in evaluating the temperature derivative can be avoided in the electrical analog by direct measurement of current (proportional to the derivative of voltage). The electrical analog therefore appears to be suitable at least for final design purposes and for calibration. A digital model may also be used, and although model formulation probably would require a major programming effort, the computer simulation would be more accurate and more suitable for final interpretation of results.

A digital computer program, written and run by Professor Sydney Clark (coinvestigator, Yale University) has yielded temperature-time curves for various system designs over the anticipated range of lunar parameters. Although the results have been utilized to demonstrate the effect of various design parameters for different lunar materials the model is approximate since the probe has been treated as a solid cylindrical rod.

Figure 7 presents curves computed by the Clark program for an effective probe conductivity of 10^{-4} cal/cm sec°K. This is equivalent to a probe thermal resistance of about 800°K/watt cm which is quite close to the anticipated thermal resistance for the actual probe. (The probe body is the main conduction path

since the cables and center rod are weakly coupled to the wall in this region.) In the Lo-K mode operation (low thermal conductivity range), steady-state heater temperature level is used to find thermal conductivity. Although the program was only run for 14 hours (real time), it is evident that steady state has been reached for the 'rock' material and is being approached quite closely for the 'vesicular' material. At steady-state, lunar density should not affect the temperature level. The difference due to density for the 'powder' material appears large, but is a manifestation of strong transient effects which would disappear after about twenty days (estimate of steady-state time based on computation for similar spherical source). The steady-state temperature level for this case would be about 3°K. A large separation in steady-state level due to variation in thermal conductivity occurs in the range of $10^{-5} < k_{moon} < 10^{-4}$ cal/cm sec°K. However, resolution by the Lo-K mode becomes poor in the high conductivity range. The initial temperature, indicated at ten minutes, is due primarily to the temperature drop across the radiation gap between the heater and the moon. Small errors in predicting the radiation resistance can vary the steady-state level in this 'rock' material range so much that a $\pm$ 10 percent estimate of lunar conductivity cannot be made. Although increasing heater power would increase the temperature amplitude of the results, the relative error would remain the same.

Consequently, Hi-K mode operations should be used if data from the Lo-K mode indicate a high thermal conductivity. The Clark model was used to estimate temperature at the probe surface for various distances between heater and sensor locations. Figure 8 shows the time derivative of computed temperatures at a point 8.075 cm away from the center of the heater. The original temperature curves at this point are similar in shape to those in Figure 7. For a one watt heater output, the peak amplitudes of the derivative curves range from about 0.010

to 0.035°K/min (related to density values for lunar material from 0.5 to 2.0 cm/cc. Since a one minute time interval is small compared to the time scale of the peak, temperature differences should be taken on the basis of time increments of several minutes to reduce error due to the $\pm$ 0.001°K uncertainty in temperature determination (i.e., the temperature-time curves should be smoothed before their derivatives are taken).

The time at which the maximum occurs (or some other characteristic time, such as that elapsed between the half-amplitude and full-amplitude points (can be used to compute thermal diffusivity. Therefore, thermal conductivity is related to a ratio between the time scale of the peak and the peak amplitude.

In Figure 8, the thermal diffusivity for the lower peak is $3 \times 10^{-3} cm^2/sec$ and for the higher, $10^{-3} cm^2/sec$. The separation between peaks is in about the same ratio. The Clark model indicates that thermal shorting through the probe is not serious. Less resolution would be obtained for a real probe because of two effects: (1) the concentrated thermal mass of the sensor, and (2) the temperature averaging due to the finite width of the sensor ring. With a sensor weight of 1-2 grams and a width of 0.5 - 0.8 cm, adequately resolvable data should be obtained. However, data interpretation using a fairly exact computer (or analog) model would be necessary to compensate for these effects.

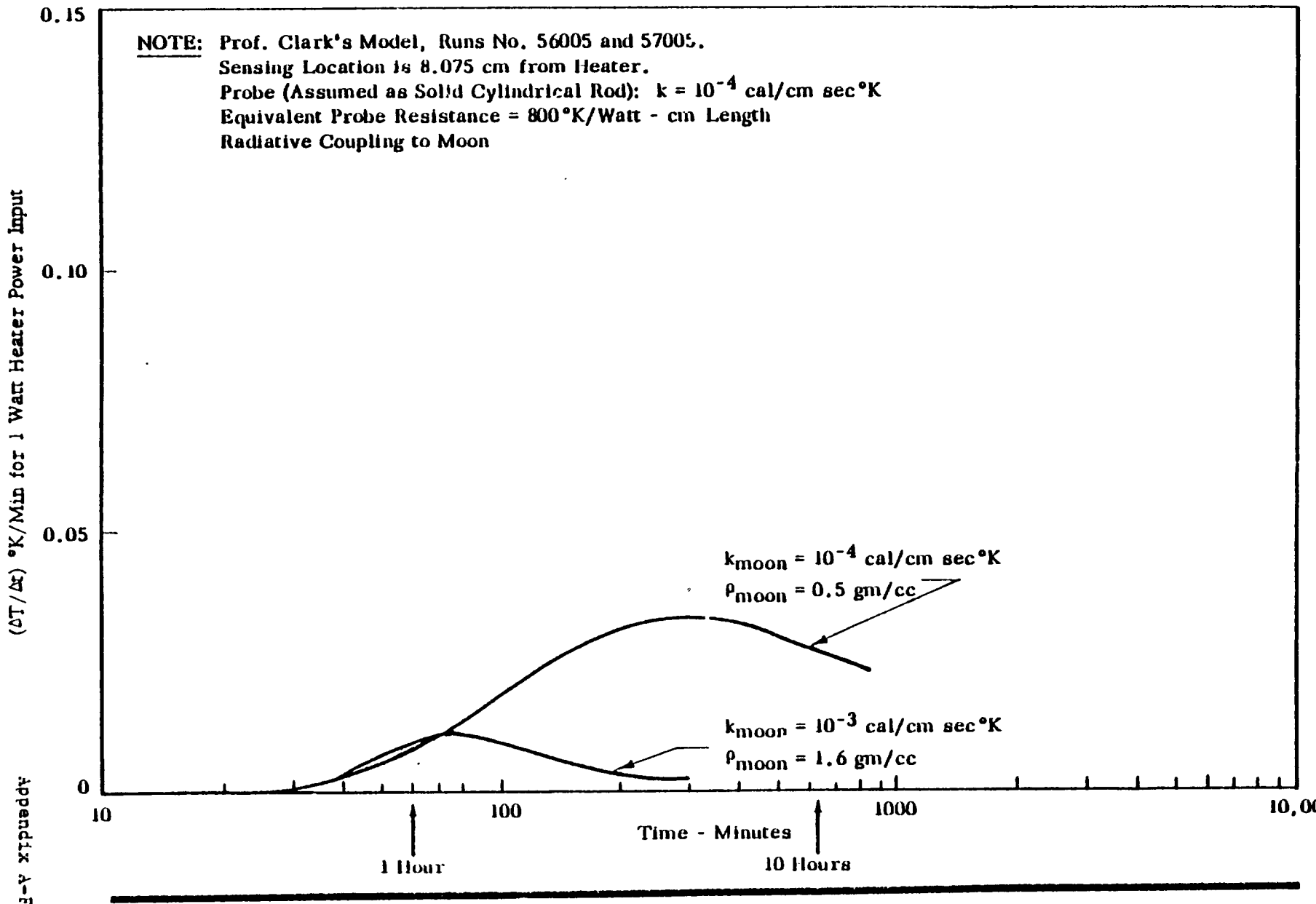

COMPUTED TEMPERATURE DERIVATIVES FOR MODE B CONDUCTIVITY EXPERIMENT

Appendix A-Figure 3

APPENDIX B. THE DEVELOPMENT OF THE LUNAR SURFACE DRILL

What follows is a brief history of the development of the Apollo Lunar Surface Drill (ALSD). This tool went through several stages of development and was the main preoccupation of the Lunar Heat-Flow Experiment. The basic design for the heat-flow probes was decided by the end of 1966 and, compared to the drill development and testing, went smoothly. With the static probe design which was preferred it was clear that a hole in which it would be placed had to be predrilled. Based on the range of conductivities that were thought likely to characterize the lunar regolith, it was determined that the meter long probe sections should be buried between two and three meters below the surface. At these depths the surface variations of temperature would be barely detectable.

Two problems loomed large and were difficult to define:

1. Would solid rock be encountered; and if so, how much should the ALSD be designed to penetrate to guarantee a three meter hole?

2. Would the hole collapse after the drill was extracted?

Results from Surveyor Missions indicated that rocks larger than a few centimeters were prevalent. What the distribution of solid rock fragments in the subsurface was, was a matter of conjecture. If they were as numerous as they are on the surface, then there was a finite chance that a rock 20 cm or less would be encountered when drilling a three meter hole. Thus, we specified that the ALSD should be capable of penetrating at least a 20 cm section of solid rock with a hardness similar to terrestrial basalts.

The soil mechanics tests carried out on the Surveyor Mission indicated that the lunar soil was not very cohesive; consequently, there was some likelyhood that the hole would collapse after the drill was extracted. The probe design selected, with two tandem probe sections flexibly connected would be extremely hard to insert into an open bare-walled hole in any case. Consequently, we concluded that some means to sleeve the hole would be required.

Hard Rock Drilling

From the start of the drill development, the working design put forward by Martin Marietta (the prime contractor for the ALSD) was an open faced bit of rather narrow kerf. The outside diameter of the hole would be about one inch and the ID of the drill was 0.8 inches. Such a design would, of course, obtain a core sample of the material through which it drilled.

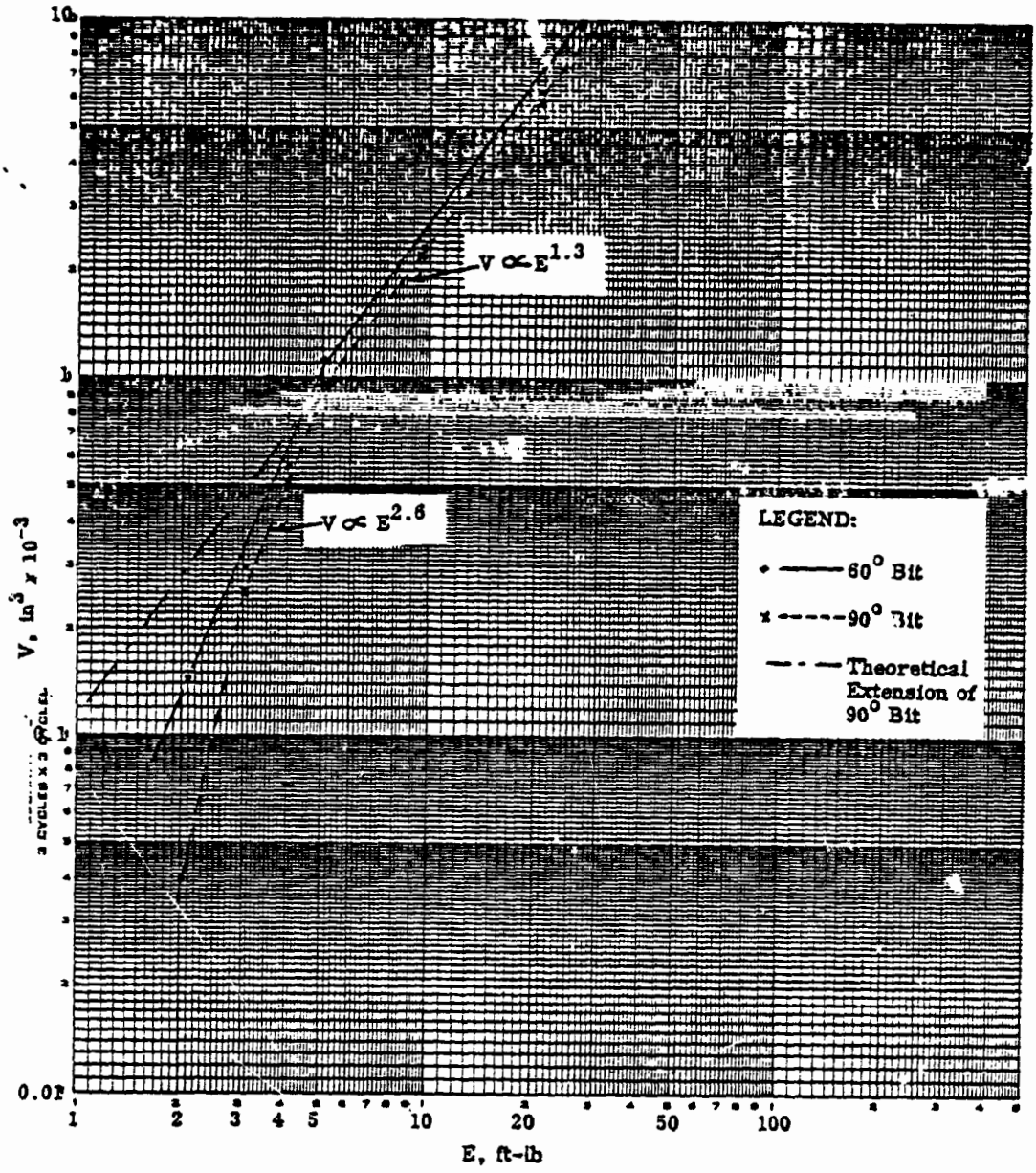

Volume-Energy Relation for 60° and 90° Wedge Bits in Drop Tests on NASA Standard Basalt Sample.

Appendix B-Figure 1

For the bit to be able to cut through solid crystalline rock, using relatively low power and a small downward force (an astronaut on the lunar surface could apply a downward force of only approximately 30 lbs), a rotary-percussive action was used. If properly designed, this allowed the bit to actually chisel the rock face and not grind it away as rotary diamond drills do. The optimum design for a bit face was achieved after considerable testing. An excerpt from the Martin Marietta final report follows, describing the developments and testing of a core bit and conclusions.

" Core Bit Optimization

The objective of these tests was to develop a core bit with a cutting tip geometry and material which would drill reliably (minimum degradation) and efficiently (maximum penetration rate with minimum power consumption) when powered by a light-weight, low energy power head. These characteristics were required for all lunar material simulants such as dense basalt, vesicular basalt, scoria, pumice, and conglomerates.

Optimization of the core bit was primarily accomplished using the dense basalt as a standard because of its tougher drillability characteristics and its homogeneity, which was conducive to the performance of repeatable tests. Subsequent tests indicated that the vesicular basalts, although easier to drill, can often result in greater degradation of the core bit than the dense basalt. This factor had to be taken under consideration during design finalization.

Dense Basalt 'Standard' Characteristics - The NASA furnished dense basalt standard, which represented the maximum drilling energy requirement of the lunar matetial simulants, was subjected to a series of tests (15) to determine its characteristics. The uniaxial, ultimate, compressive strangth of the sample was measured at 21,732 psi (average) and the average shore hardness was 41.6 with a standard deviation of $\pm$23. Drop tests were conducted in accordance with standard procedures using 60° and 90° wedge bits in the energy range of 2 to 20 foot pounds as shown in Figure 1 . . Using the data for the 90° bit, it was calculated that the ALSD operating at a percussive blow rate of 2250 bpm . would require a bit delivered energy of 27.6 inch-pounds per blow to maintain a 2 inch/minute penetration rate. Assuming a power head output energy of 30 inch-pounds, a cuttings scavenging loss of 20% and a 10% energy loss per extension tube, the following empirical ALSD penetration rates were calculated:

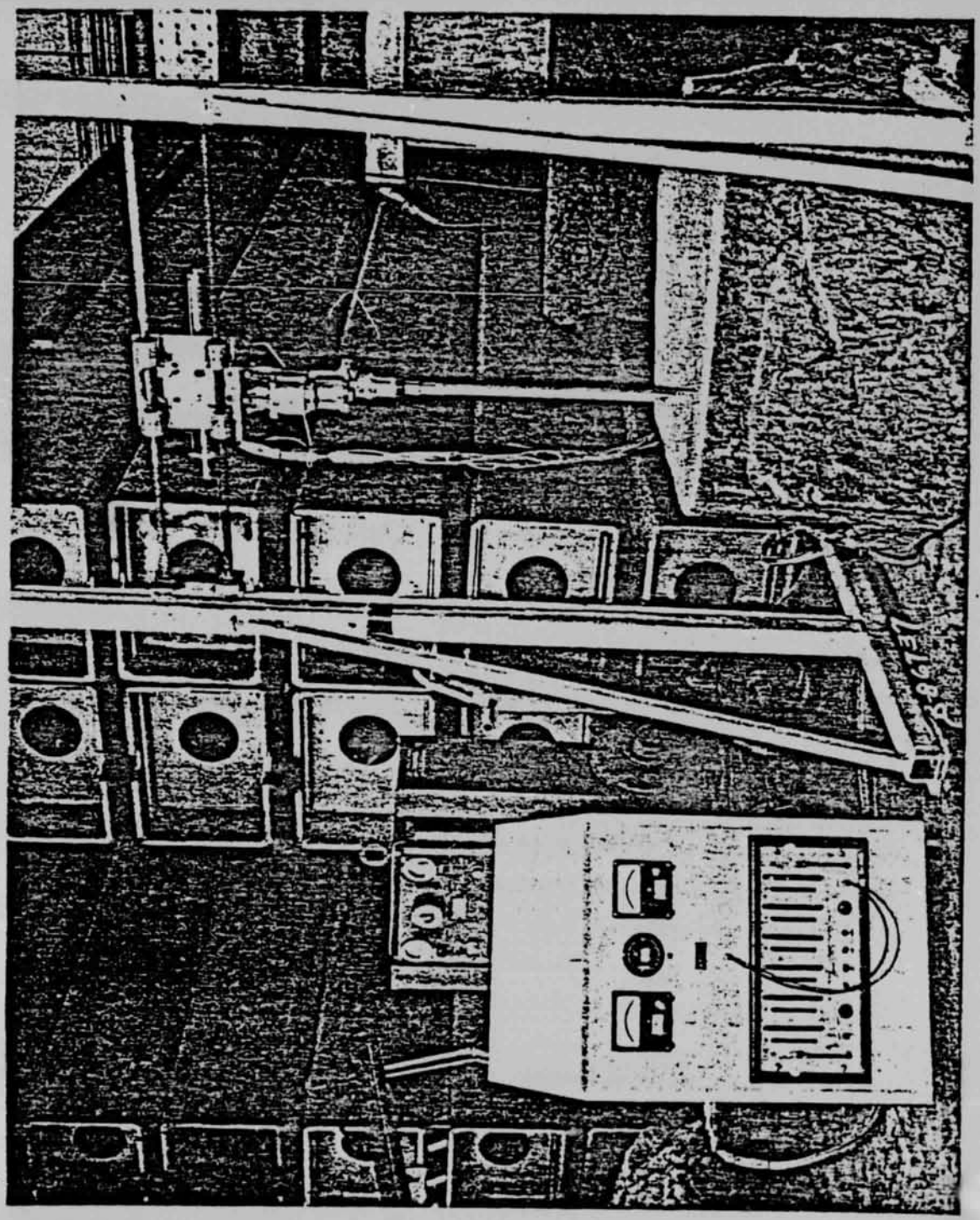

Core Bit and Extension Tube Optimization Tests

Appendix B-Figure 2

Number of Extension with Bit	Penetration Rate (In./Min.)
1	1.26
2	1.09
3	0.93
4	0.81

These predictions did not take into account the benefit derived from optimization of blow indexing, which, at the time of initial power head design, was believed by most researchers to be of little or no benefit.

Core Bit Test Summary - Throughout the performance of this program, approximately 100 development bits were tested. In general, the bits were designed and fabricated in groups of 6 to 15 each, tested, and the results of the tests and redesign recommendations forwarded to the core bit contractor for incorporation in subsequent test groups. Major design variations included tip geometry and tip material (tungsten carbide) chemistry. Minor variations in tip brazing techniques and core bit body geometry were also studied prior to selection of the final design.

Most of the optimization tests (16-21) were conducted using the equipment illustrated in Figure 2 . . With this arrangement it was possible to accurately control the axial bit force and power head input voltage while monitoring rpm, penetration rate and power consumption of the system.

Typical bit configurations tested included those illustrated in Figure 3, where 3, 4, and 5 tips per bit of a single geometry and tungsten carbide chemistry were tested to investigate the effects of index variations. The advantage of indexing was clearly demonstrated during these particular tests.

Tests clearly demonstrated that the 3 and 5 carbide tip bits outperformed the 4-tip version due to improved indexing. At this point in the ALSD development program, a decision was made to replace the original 4-tip design bits with the 5-tip configuration. Although the 3-tip design indicated slightly superior performance, the bit tended to 'chatter' excessively during operation and it was anticipated that rapid degradation of the tips would occur.

Another factor demonstrated during the performance of the core bit test program was the importance of optimum axial bit force to obtain maximum penetration rate at a minimum power consumption. Data clearly illustrate the significance of optimum axial bit force in dense basalt. Bit force is not as critical in softer rocks such as scoria or vesicular basalt, because

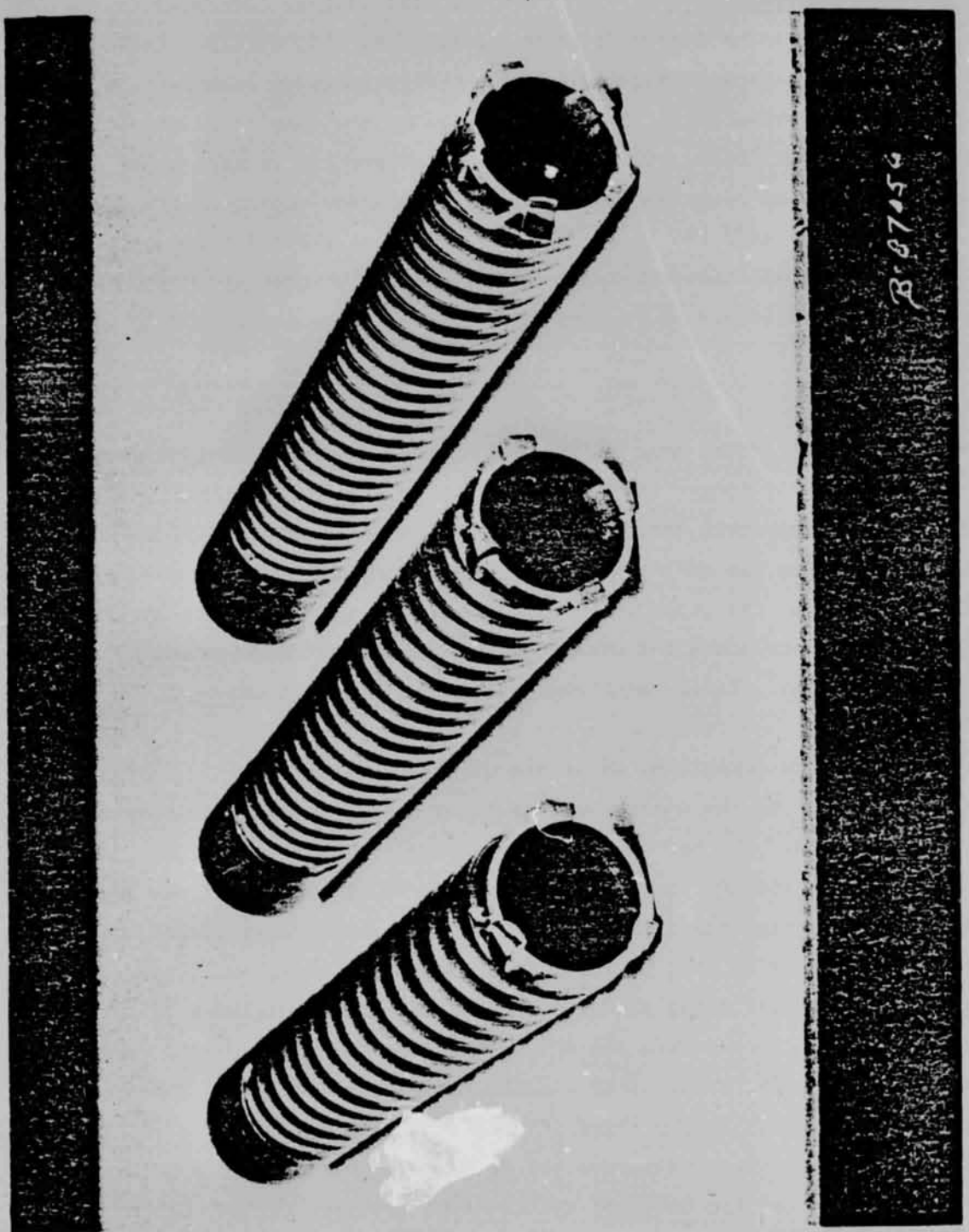

Typical Core Bit Test Specimens

Appendix B-Figure 3

of the lower energy threshold required for predictable fracturing.

Final Core Bit Selection - The core bit test program indicated that a compromise design was mandatory in order to meet the ALSD drilling requirements in all lunar simulant materials. The harder tungsten carbides (91.3 RA) possess good wear characteristics in dense basalt, but tend to fracture if operated under light loads. Tip geometries which perform at high penetration rates and low power consumption tend to degrade rapidly. The final basic configuration selected is detailed in MMC drawing PS600100023-11. A minor modification was incorporated, as shown on MMC Drawing 467A8050000-011, to ensure that a uniformly round material (89.3 RA) consists of 87% WC and 13% cobalt. ".

Drill Stem

To drill a three meter hole additional tubing would be needed to produce a drill stem somewhat longer than three meters. The wall thickness of the tubing had to be less than the fit's kerf width of 0.1 inches (2.54 mm). To remove cuttings from the hole while drilling, spiral fluting was required on the exterior wall of the tubing. To fit in the stowage bay on the LEM it would be necessary to break the drillstem down into lengths no greater than 22 inches (55.88 cm). These requirements called for a high strength. A titanium alloy was then found to be the best suited to all of these requirements and it had the additional advantage of light weight.

A critical part of the design was the joint to connect and disconnect the drill stem sections. The Martin Marrietta design was a threaded type joint that could be made in a single turn. When mated, the flute continuity was preserved and the stem walls remained flush. A special lubricating coating was applied to the joint surfaces so that they would not seize up during drilling.

Having this type of joint produced some serious human engineering problems for the astronaut. To uncouple the drill string as it was retracted, a special treadle was designed. This treadle was restrained by the astronaut's foot as he drilled. It incorporated a hole to guide the stem and a built-in clamping arrangement that restrained the drill stem at the treadle while the astronaut disconnected the corehead and the stem sections filled with core material.

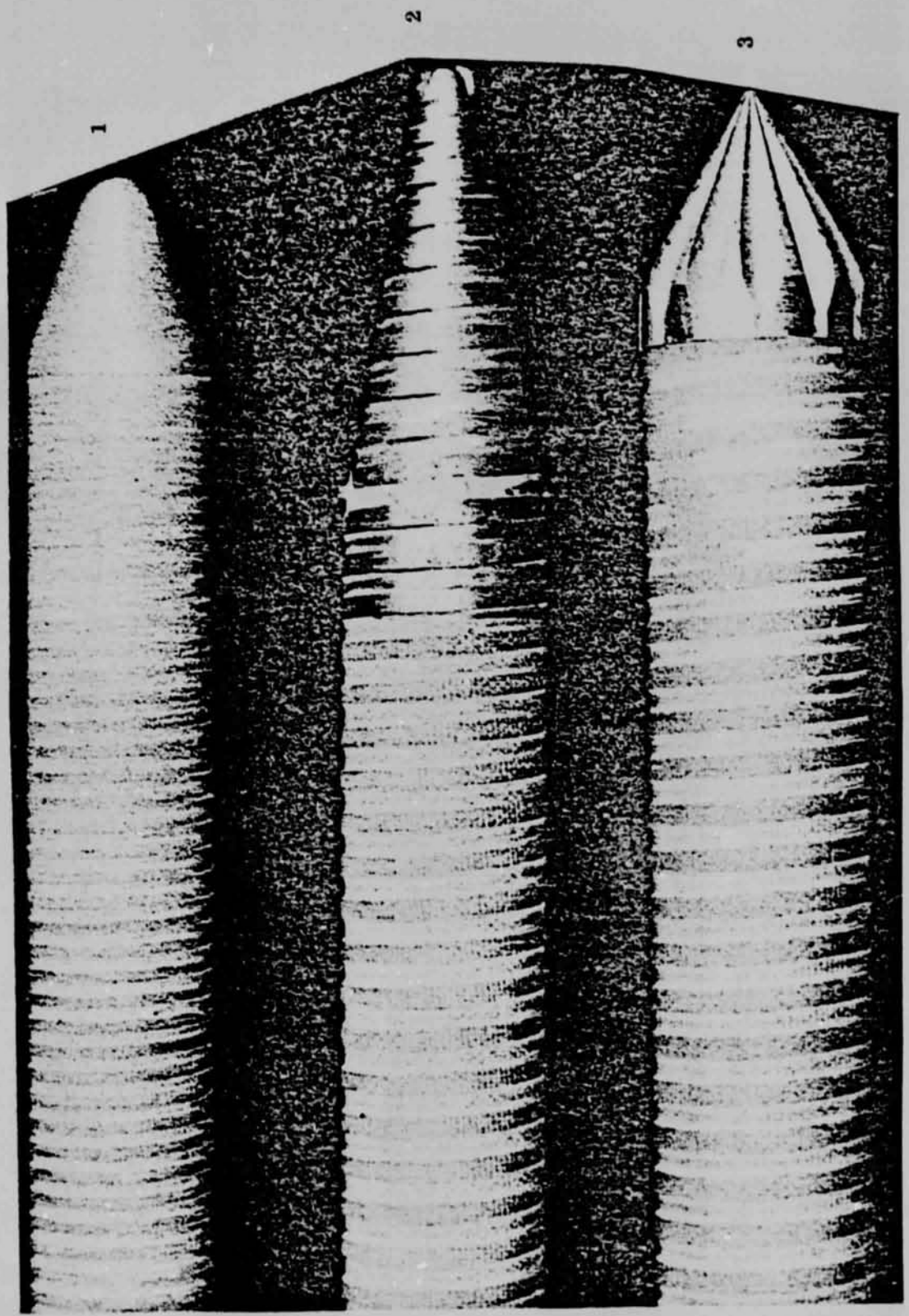

Hole Casing Tip Configurations

Appendix B-Figure 4

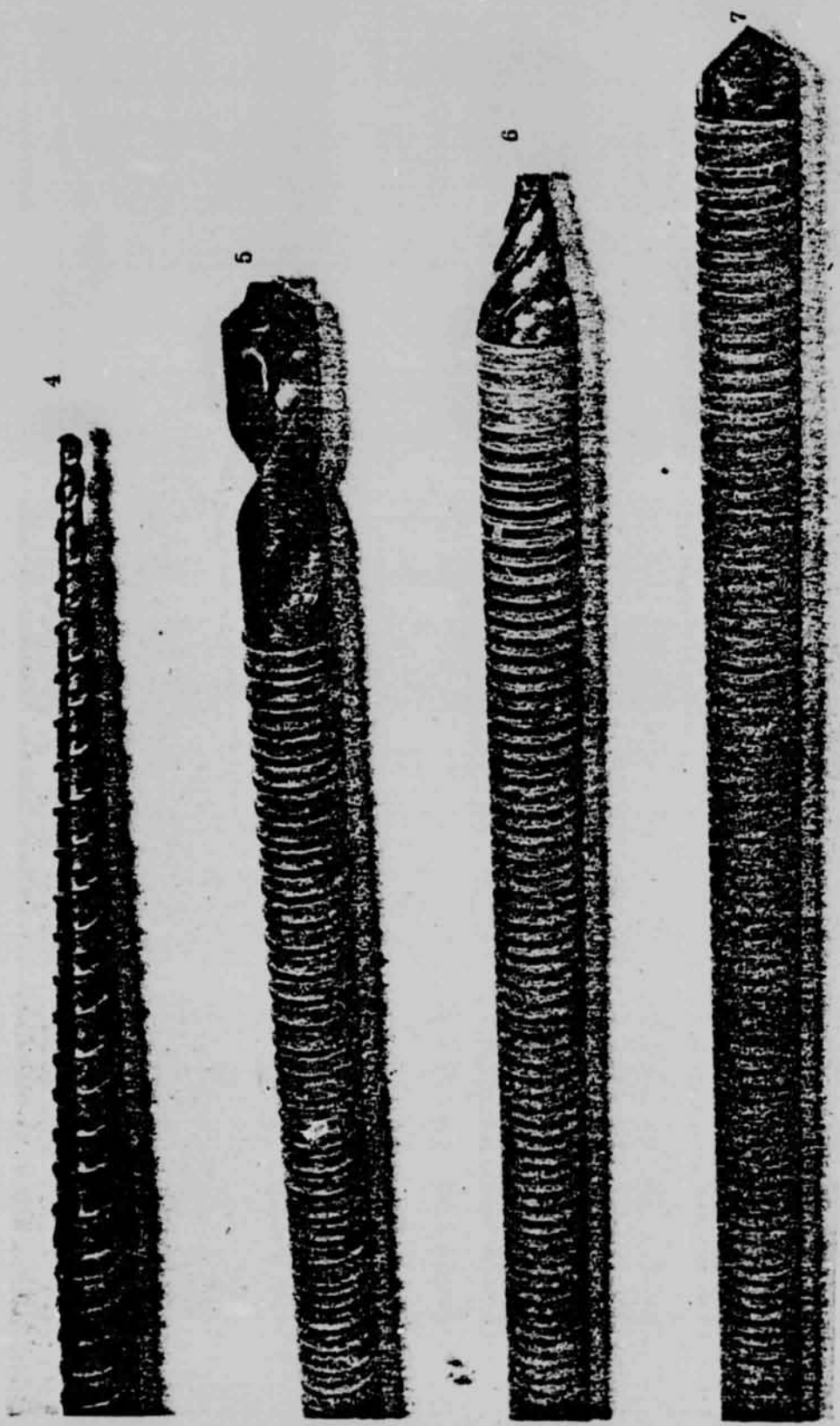

Appendix B-Figure 5. Hole Casing Tip Configurations

Powerhead

To provide the rotary and percussive motions to the drillstem, a battery operated powerhead was developed by Black and Decker Manufacturing Company for the ALSD. The powerhead consisted of an electric motor of about a half horsepower which provided torque to the drillstem coupling and recocked a spring driven hammer, which fell on an anvil coupled to the top of the drillstem during each revolution. The unit was housed in a pressure-tight case so that it could maintain nitrogen gas at atmospheric pressure to help maintain the internal parts at low temperature.

Saving the Hole

Originally, the drill system was designed without any provision to insure that the hole stayed intact so that the heat-flow probes could be inserted. Consultations with scientists working with the surveyor results indicated that cohesion of the regolith was too low to support a bare-walled hole and we were advised to provide some type of sleeving.

The first attempts to provide such sleeving used thin walled fiberglass tubes that joined together by force fitting matching tapers cut into the ends of the tubes. The bottom tube was fitted with a conical head. The sleeving was designed to be powerdrilled into place after the hole had been completed. Some typical designs that were tried are shown in Figures 4 and 5.

Regolith Model for Testing the ALSD

Early in the development program it was clear that a full scale test bed of the lunar regolith would be needed to evaluate the drill performance.

The first such test bed was constructed at the Martin Marietta plant in Baltimore, Md. Lamont-Doherty Geological Observatory undertook the design of the three meter deep regolith model. The basic ingredient of the model was powdered basalt. Using particle-size distributions determined from Surveyor photographs, the appropriate size fractions were calculated in terms of standard sieve and screen sizes. The components were then produced by a local (Haverstraw, New York) trap rock company and stored in 55 gallon(208.18 liter) drums. Large blocks of basalt, to be placed at known spots in the model, were ordered from Oregon since the flood basalts there had been used as a standard in earlier tests.

A large rectangular steel tank was made at Martin Marietta to contain the model. A diagram of the model is shown in Figure 6. The unsorted part of the model was made by remixing the components according to the Surveyor recipe in a standard cement mixture. Layers of roughly a foot were poured into the tank, large chunks (10 cm or greater) were thrown in by hand. Each layer was tamped down which made the fabrication of the model dusty and unpleasant work. The completed model was used extensively to test the ALSD.

Tests in this regolith model showed that the drill was capable of penetrating three meters including 50 cm of vesicular basalt within the prescribed time and power available from the silver cell battery pack. However, the design for installing the casing was far less successful. The casing would frequently break, or large torques (enough to stall the motor) would build up before the casing sleeves had penetrated the full depth of the drilled hole.

Field Tests

We were also desirous of carrying out tests under field conditions where we would be drilling into an unknown subsurface. Finding an area that would be a reasonable analog to the lunar surface was challenging. It would be important that the soil contain virtually no moisture to depths on the order of three meters. We looked at some areas around Flagstaff, Arizona which had been selected by the Lunar Geology group at Flagstaff as lunar analogs. There were ash flows and lava flows but the water content of the soil was just too high.

We decided instead to try Death Valley, hoping that the extremely dry conditions would result in bone dry soil layers.

We found three very interesting targets.

1. Small pedestals of calcareous lacustrine deposits were abundant in the Shoshone Valley. Since the diameter of these pedestals was no more than 10 to 15 meters and the heights were about five meters, there was a good chance that these very fine grained sediments were quite dry. Of course, the composition of these sediments was not lunar-like.

2. Large fans of loosely compacted conglomerates, which had formed at the mouth of small ravines cut into the hills bordering the Shoshone Valley and Death Valley.

3. Alluvial and fluvial deposits of silts and sand in arroyos. Vertical banks had been cut into these deposits by the most recent streams, so that a vertical section of what was drilled could be seen.

ORIGINAL PAGE IS
OF POOR QUALITY

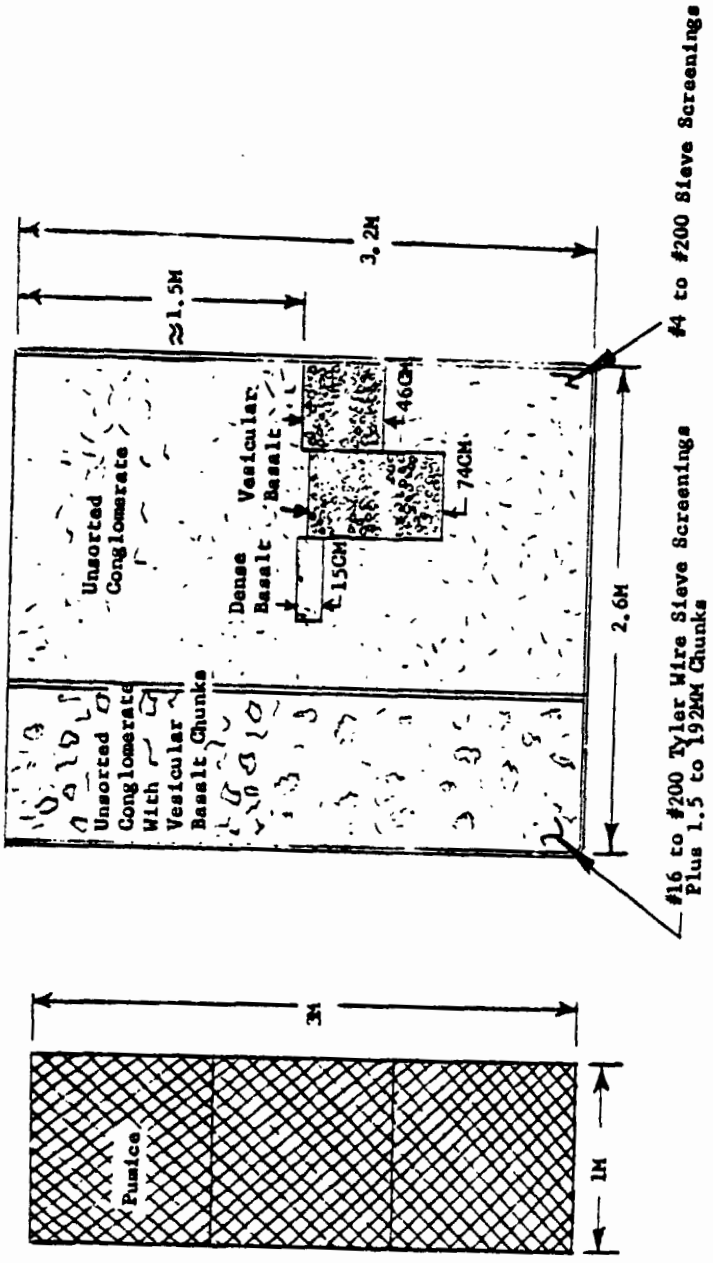

3-Meter Conglomerate and Pumice Model Construction

Appendix B-Figure 6

Drilling was attempted in the lacustrine deposits. At about 2.5 meters the drill experienced stalling torques. This was because of significant moisture at those depths. We found it extremely difficult to remove the drill, it could not be moved by hand, so we jury-rigged a large lever to force the stem out of the ground. Once the drillstem was removed, the hole stayed intact so that no casing was needed.

In the fanglomerates drilling was more difficult because the drill would occasionally encounter a cobble 10 cm across, but the holes could be drilled and the stem removed without problems. The holes made were not preserved. We then tried reentering with the fiberglass sleeving and encountered the same problems we had earlier in the model at Baltimore.

The main result of these field tests was that the drill was capable of penetrating the full three meters in a variety of soil types that in most cases presented more difficult drilling conditions than on the moon.

The methods for casing the hole were not yet reliable and design improvements were needed.

The Boron Reinforced Borestem and the Solid Faced Bit

The principal investigator's group saw a possible means of overcoming the problem of the hole collapsing.

One means of accomplishing this would be by using a drillstem that does not have to be retracted from the lunar subsurface. Such a drillstem must have a low thermal conductance, so as not to degrade the heat-flow experiment performance, yet have an axial modulus high enough to effectively transmit the percussive energy of the powerhead to the bit. To utilize a low conductance drillstem that can be left in the lunar subsurface it is, of course, necessary to develop either a solid-face bit that does not allow material to enter the drillstem, or, if a coring bit is used, to develop a core retrieving system that can remove material from inside the stem.

The approach that seemed most feasible was to replace the titanium drillstem with a stem made of composite material. An epoxy resin was chosen for the matrix of the stem tube because of its low thermal conductivity. The epoxy is strengthened by glass fibers wound circumferentially in the tube walls. The axial stiffness is increased by an order of magnitude by including filaments of crystalline boron (Young's modulus 60 x 10^6 psi), aligned with the tube axis.

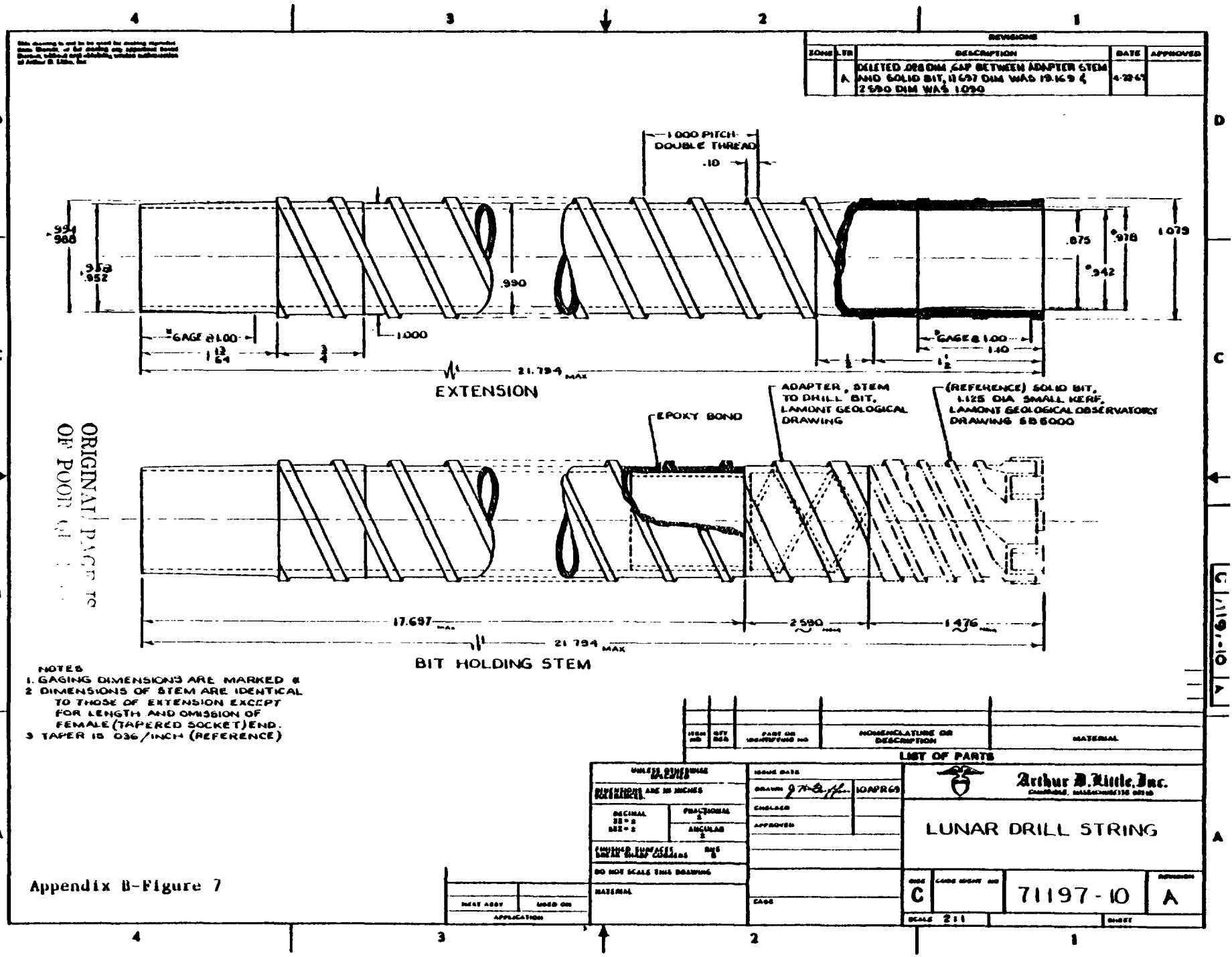

ORIGINAL PAGE IS OF POOR QUALITY

Appendix B-Figure 7

We hoped to develop a solid-face bit by a modification of the existing ALSD coring bit designed by Martin Marietta and Chicago-Latrobe, thus benefiting from the experience and testing that went into that bit development. Our approach, which proved successful, was to insert a central cutter inside the annulus of cutters of the core bit. When drilling solid rock, the core bit leaves a small cylinder of material standing above the cutting face, this cylinder is broken up by the carbide central cutter.

An alternative to the solid-face bit is to remove the core material of the subsurface core samples, a system that could retrieve the sample would be worth the extra astronaut effort required. To this end, we began development of a 'core retrieval system.' We decided to utilize a system similar to that used in standard drilling techniques. The basic feature of the system is a thin-walled core liner that is locked in the bottom section of the drillstem. These core liners would be inserted and locked in place. After drilling into the lunar subsurface the length of the core liner, it is unlocked and removed by the astronaut. For emplacement and retrieval of the liners a special tool would have to be designed. This liner serves as a core sample container on the return flight.

The AVCO Space Systems Division, under a subcontract from Lamont-Doherty Geological Observatory, was initially chosen to perform the design and development of the composite drillstem. The work was done under the guidance of Lamont-Doherty. The subcontract with AVCO consisted of two tasks:

Task I: To conduct a design and manufacturing feasibility study.

Task II: Fabrication of prototype sets of drillstem.

Phase II was completed under a separate subcontract with Arthur D. Little, Inc. This work was also done under the supervision and direction of Lamont-Doherty Geological Observatory.

The development solid-face bits were purchased by Lamont-Doherty from Chicago-Latrobe, Inc., based on Lamont-Doherty Geological Observatory drawings.

Program Developments and Test Results

The boron filament reinforced fiberglass drillstem:

The boron drillstem developed under this program is shown in Figure 7. The tubular body of the drillstem has a sandwich construction (the details of which are shown in Figure 8. Innermost are two layers of epoxy fiberglass

ORIGINAL PAGE IS
OF POOR QUALITY

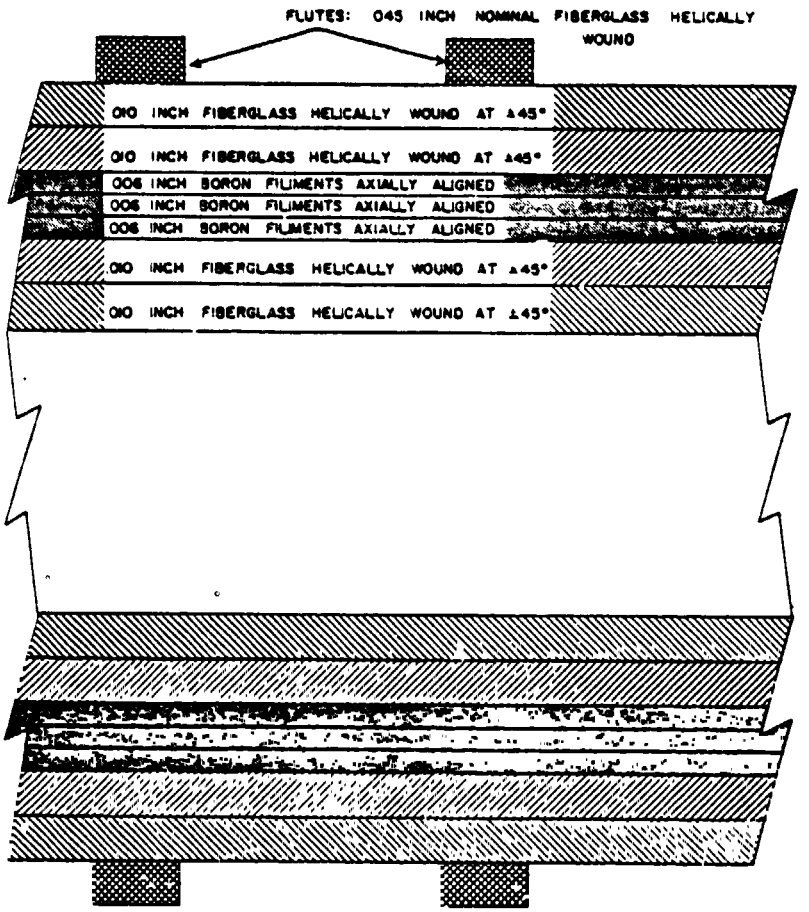

AS NOTED	Lamont Geological Observatory of Columbia University Palisades, New York
NONE	BORON FILIMENT DRILL STEM STRUCTURE
UNLESS OTHERWISE SPECIFIED DIMENSIONS ARE IN INCHES AND INCLUDE PLATING	
S KAGHAN / R S PERRY	

Appendix B-Figure 8

with the glass filaments helically wound at ± 45° to the stem axis. Three layers of boron filaments are wrapped over these layers that are aligned with the long axis of the tube. Two additional layers of fiberglass are wound over the boron at angles ± 45° to the stem axis. This configuration gives a nominal outer diameter of 0.990" with an inner diameter of 0.875".

The flutes to transport drill cuttings to the surface are helically wound around the stem body as shown in Figure 7. The flutes are also made of fiberglass and form a double helix with a one inch pitch. The outer surface of the flutes are impregnated with silica powder to increase abrasion resistance. Each flute is 0.10" to 0.15" across and stands about 0.45" above the stem body. As can be seen in Figure 7 , the diameter of the stem body is increased at the female joint, whereas the flute diameter is constant, and as a result the flute depth over the joint area is very small; i.e., about 0.01".

Conductivity measurements on the boron stem were made at Arthur D. Little, Inc. by request of the Lamont-Doherty Geological Observatory. These results give a value of conductivity equal to 0.0096 watts/cm°C at 27°K and 0.018 watts/cm°C at -73°K.

Designing a workable taper joint for the boron filament drillstem proved to be the most difficult task in the development of the boron drillstem. The initial taper joint design was a simple taper of 0.012 inches/inch for a length of 1" machined into the outer glass layers of the male and female pieces. The inner part of the tube containing the boron filaments was ground to form a flat shoulder that butted when the joint was made up. This type of joint failed during testing due to lack of adequate hoop strength; also the boron filaments sheared off at the shoulders.

These tests led to a basic revision of taper joint design. The steel reinforcing rings were removed, and the female taper was reinforced by overlaying it with short lengths of boron filaments. In addition, circumferentially wound fiberglass was applied around the female taper joint to increase hoop strength. The taper angle was increased from 0.012 inches/inch to 0.018 inches/inch to decrease radial stresses in both the male and female sections of the taper. This joint configuration has proven successful, and is the basis for the final design.

Many tests of the taper joints were made in the course of development. For the final taper joint design we ran an endurance test that lasted for 22

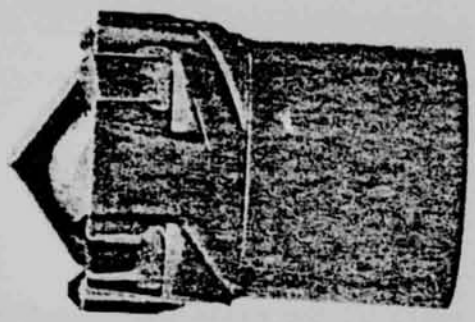

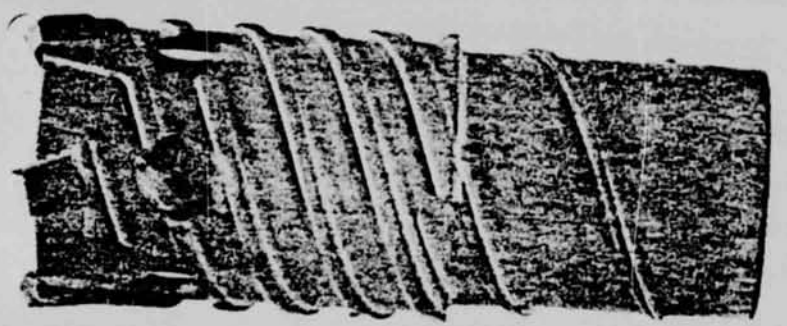

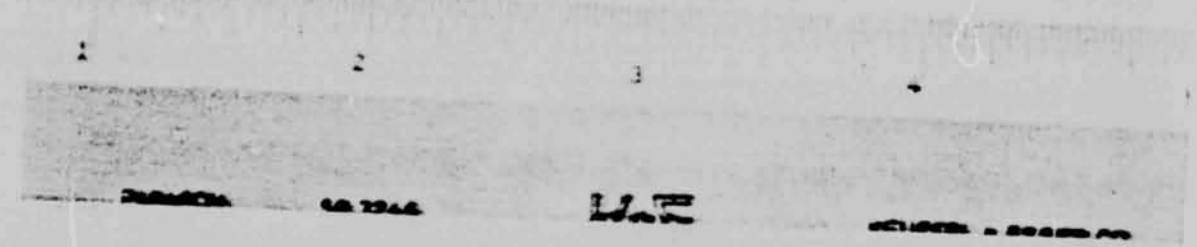

Appendix B-Figure 9 Prototype of solid faced drill bit. Note the core cutter protuding beyond the kerf cutter at left.

Appendix B-Figure 10 Solid faced drill bit, final design. Three of the six elliptical exit ports for core cuttings are visible.

minutes of drilling in dense basalt with no apparent joint degradation.

The Solid-Faced Bit

1.. Experience gained in developing the ALSD coring bit provided information on bit design parameters. Point pressure exerted on the rock by the carbide kerf cutters must be kept above a finite threshold value to obtain chipping at the rock face. If point pressures are below the threshold, the rock is pulverized rather than chipped and the drilling rates will be much lower than those obtained with the ALSD bit.

2. The design basis of the solid-face bit was the ALSD coring bit. In the first solid bit design, a single tungsten carbide blade was placed inside the bit shell to remove the core. On the first prototype this blade protruded beyond the kerf cutters (see Figure 9).

Drilling rates obtained with this bit were extremely low because of low point pressures. A second test was made with this bit to determine the efficiency of the core cutter. An ALSD coring bit was used to drill a hole in dense basalt, leaving the central core undisturbed. This hole was redrilled with the solid-face bit as a test of core cutter efficiency. The central core was removed at a high rate. This test showed that it is relatively easy to break up the central core once it is standing about half an inch above the cutting face. The reason for this is that the free cylindrical surfaces lead to fracturing of the column both in shear and spallation. This discovery lead to a final, highly efficient solid-face bit design.

The second prototype solid-face bit also used the ALSD coring bit. However, the blade was recessed about 3/8 of an inch behind the kerf cutters of the core bit. Six elliptical holes were machined into the body of the bit at the base of the core cutter to serve as exit points for the core cuttings. (see Figure 10).

Tests of this bit were successful, giving rates of 4 inches/minute in vesicular basalt and 1 inch/minute in dense basalt. This bit configuration has been chosen for the flight hardware with only minor modification.

A Core Retrieval System

The core retrieval system was designed to collect a subsurface core sample without the necessity of removing the drillstem from the borehole. This system was never used as part of the ALSD. This is accomplished by locking a

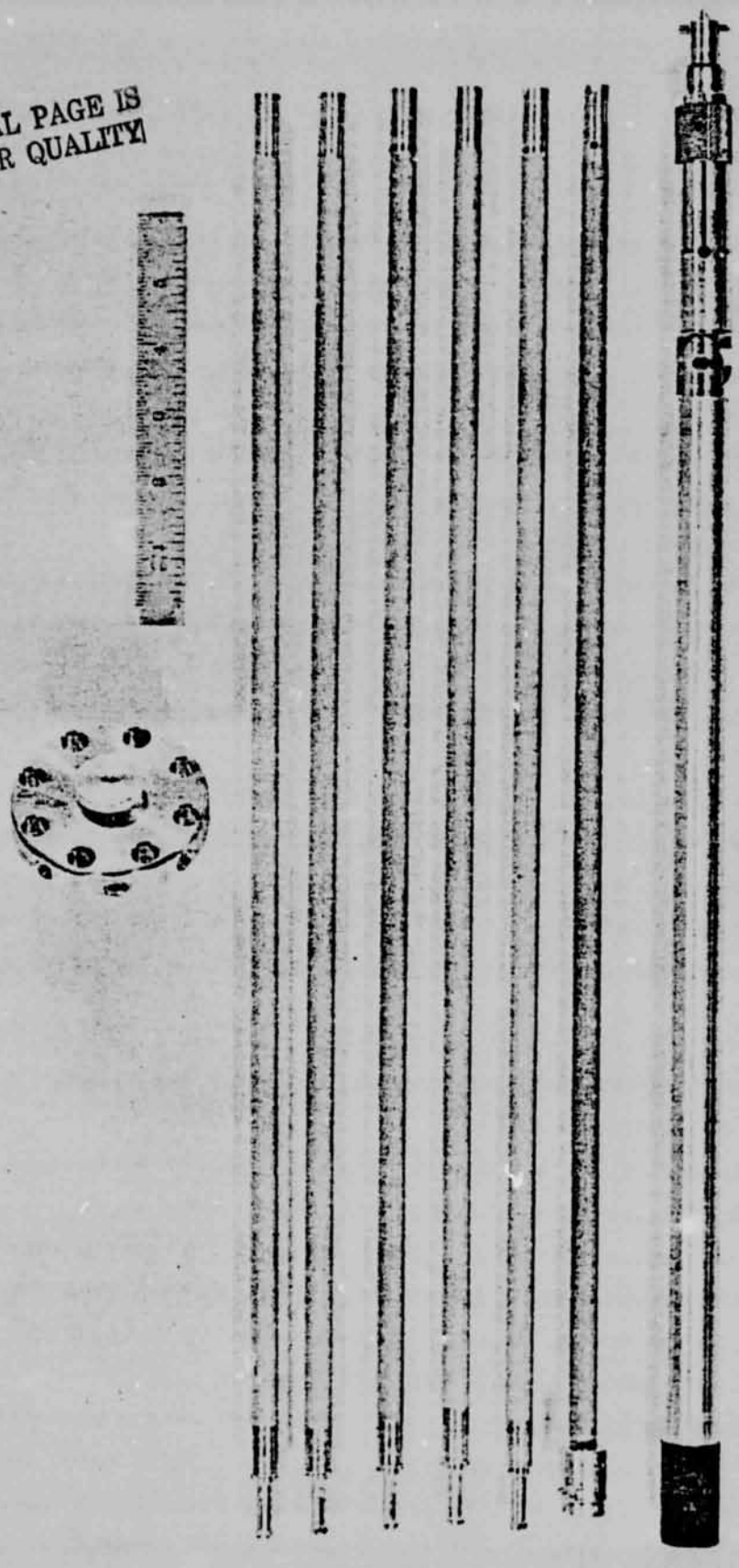

Appendix B-Figure 11 A set of coring equipment. From left to right; torque limiting handle for emplacement retrieval tool, five extension sections for emplacement retrieval tool, interface adapter section, and the core lock - core liner assembly.

core liner tube into the lower end of the drillstem, drilling to a depth approximately equal to the length of the core liner tube and then removing the tube.

The core liner was designed to function as both a core liner and a sample return container. Strict design requirements are placed on it as a result of this dual function. The core tube must interface with the drillstem, core lock and sample return container and meet the aseptic requirements for returning lunar samples.

The prototype core liner is fabricated from thin-wall, high strength aluminum alloy tubing. Testing of early designs showed that the tubes were deficient in two areas:

1. The presence of rock particles which became lodged between the core tube outer surface and the inside of the drillstem made removal of the core assembly difficult; and,

2. core material was frequently lost during removal of the liner from the stem.

Core liner jamming was eliminated by installing a felt-flocked paper seal at the bottom of the core liner (see Figure 11). This seal effectively limits the entry of rock and rock dust particles into the core liner-drillstem interface and cleans that interface during core liner insertion. Loss of cored material was minimized by using a core liner fitted with a core catcher.

Core Lock

A core lock was required to hold the coring assembly in place during the drilling operation.

Our initial core lock design utilized phosphor bronze spring fingers, which were forced against the drillstem wall at an acute angle. A screw driven cam actuated the spring fingers. Upward force on the coring assembly caused the spring fingers to slightly penetrate the drillstring wall thereby preventing movement of the coring assembly. Tests showed that these fingers were not nearly strong enough to hold the core liner in place.

A second development core lock used a ball detent mechanism. Two 0.250" diameter steel balls were contained in the core lock body. Detent holes were made in the drillstem wall to accomodate the steel balls. A screw driven cam forced the balls outward into the detent holes. Reversal of the cam motion allowed the balls to retract during core retrieval. Tests in dry rock powders

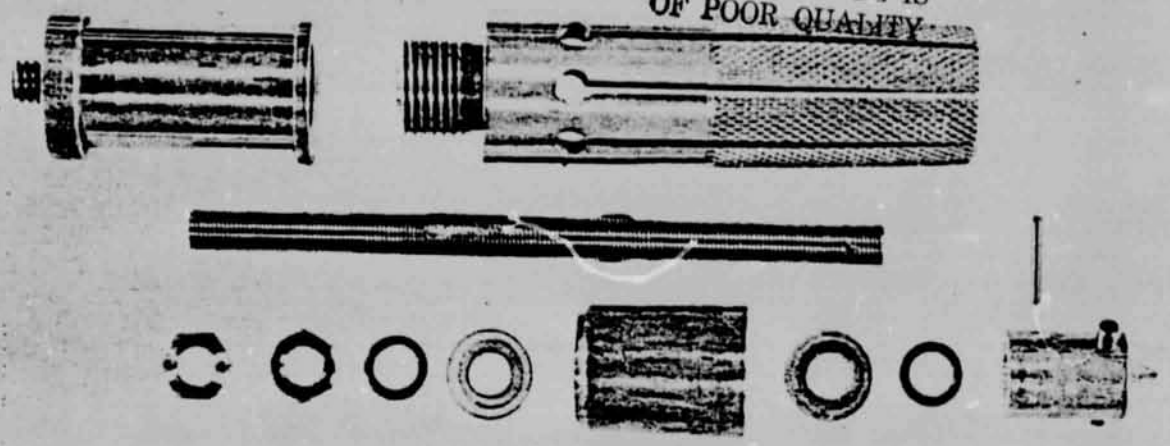

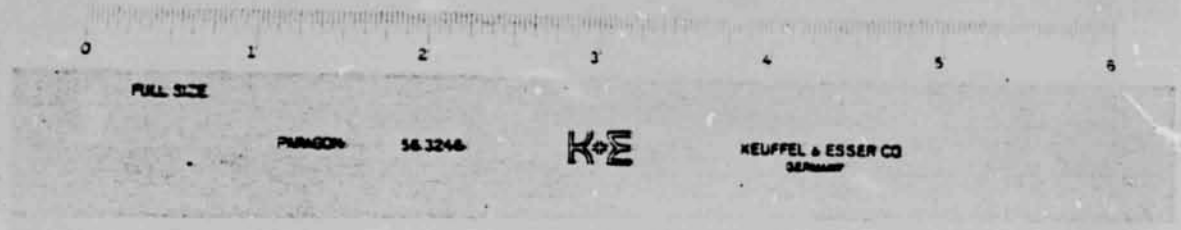

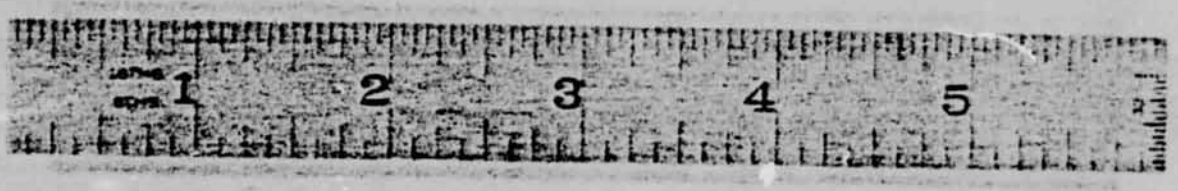

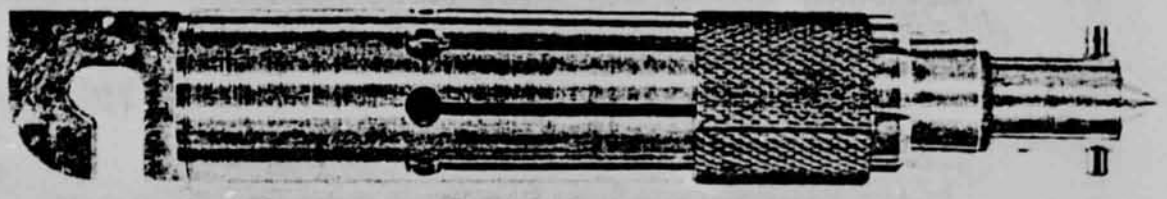

Appendix B-Figure 12 Parts of a Prototype core lock of a design similar to the final design.

Appendix B-Figure 13 The final design core lock with half of knuckle joint attached. Note the separate knurled sleeve.

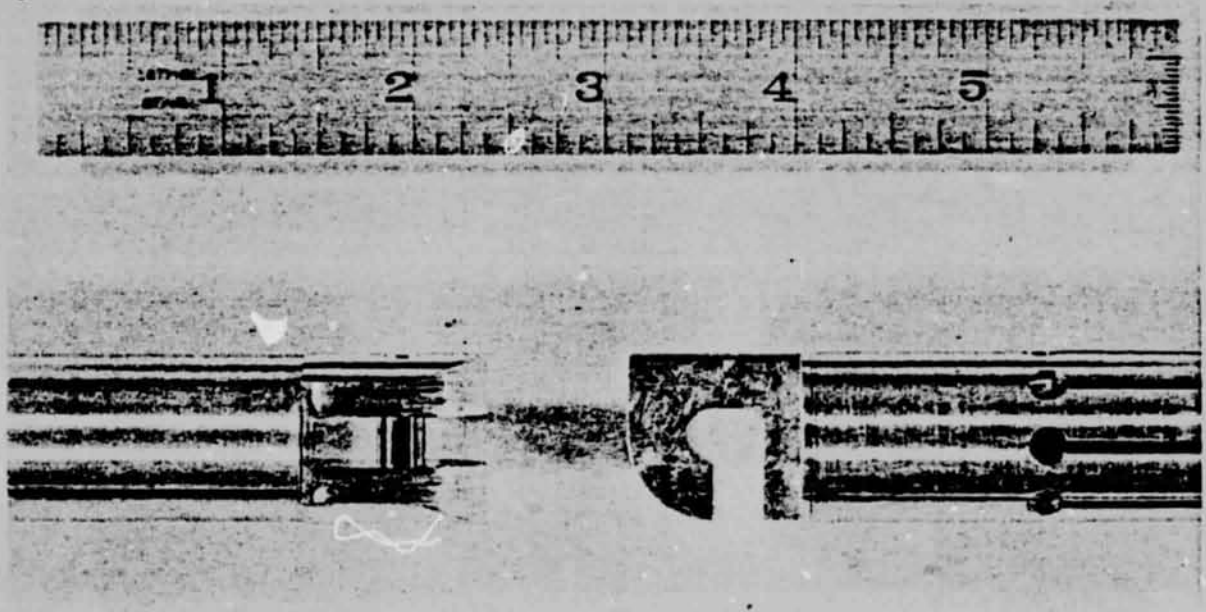

Appendix B-Figure 14 The knuckle joint, core liner tube on left and core lock on right.

revealed that the core liner exerted such a strong upward force during drilling that the steel balls actually tore the fiberglass stem upward from the detent holes.

A third and final core lock design utilized an expandable cylinder with a knurled surface to engage the interior surface of the stem. In the final design, the core lock utilizes only one taper plug and is articulated at only one end. The final core lock design is shown in Figures 12 and 13.

The core lock and core liner are joined with a knuckle type joint mated by rotating one of the pieces through a 90° arc, picture in Figure 14.

Emplacement-Retrieval Tool

Emplacement, retrieval and core lock actuation are performed with a special tool. This tool must be designed to transmit tension, compression and bidirectional torque to the core lock capstan. The prototype unit consists of a torque limiting handle, five extension sections, and one adapter section. The handle is connected to the adapter section directly or with one to five extension sections interposed. The interstem joints are not separable once they have been connected except with a special tool. Ordinarily, there is no need to separate the sections on the lunar surface.

The handle limits the torque applied to the core lock to a preset amount.

Summary of Development Tests of the Core Retrieval System

Development tests were carried out at the Lamont-Doherty Geological Observatory test facility using a Black and Decker model 723 rotary hammer run at a reduced voltage to simulate the ALSD powerhead. A fifty-five gallon drum, filled with material from the model Martin Marietta Corporation was used to simulate the lunar surface. Hard rock drilling was done in either a 17 inch thick block of vesicular basalt or an 8 inch thick block of dense basalt.

The results of these tests showed the amount of fine material obtained by the corer was dependent on drilling rate, with optimum results giving about 75% recovery if a rate of 1 cm/sec was maintained.

In the end, the core retrieval system was not incorporated into the ALSD system. It was deemed to be too complicated for reliable astronaut operation. On hindsight, this judgement was probably correct.

The boron filament reinforced fiberglass drillstem and the solid-faced bit were used successfully as part of the ALSD system. This type of stem was used to emplace the heat-flow probes.

The experience at Apollo 15 showed that the larger diameter and loss of continuity of fluting at the taper joints between the sections did not allow cuttings to pass up the hole and jammed the drill's operation soon after the first joint had entered the lunar surface. For subsequent flights the taper joint was replaced by a titanium joint section that was bonded by Epoxy into ends of the stems. These redesigned stems worked very well at Apollo 16 and 17 (see also Section IV).

APPENDIX C. DESCRIPTION OF THE LUNAR HEAT FLOW EXPERIMENT INSTRUMENTATION

The material that appears in this section is only slightly modified from a paper prepared by Bruce D. Smith of the Bendix Corporation.

EXPERIMENT THEORY

The heat-flow instrument performs measurements to determine the mean vertical temperature gradient dT/dz and the effective thermal conductivity k of the material across which the measured gradient is developed. Conducted heat flow F diffuses down a temperature gradient in accord with the relationship between these two quantities in one dimension,

$$F=-k(dT/dz) \qquad (1)$$

Table 1 lists ranges of predicted density of heat-flow rates and soil thermal conductivities (Langseth et al., 1968; Langseth et al., 1970; Langseth, 1968) with the corresponding limits of average temperature gradients.

To meaningfully extract the average gradient from the composite temperatures that may exist at practical lunar measuring depths, the temperature-measuring instrument must have a wider range than the gradients in Table 1 indicate, readings must be recorded frequently for more than a year, and absolute measurement accuracy must equal the relative accuracy requirement for the lowest mean temperature gradient expected.

Two different approaches are used in measuring lunar subsurface thermal conductivity by means of the heat-flow instrument. In the first approach, the thermal response of *in situ* lunar material to known heat sources is tested. In the second, vertical strings of temperature sensors record the characteristics of the periodic propagations into the surface to determine diffusivity; with this diffusivity information and good estimates of soil mass density and

TABLE 1. Predicted Experiment Ranges

Temperature Gradient dT/dz, °K/meter	Heat Flow J, watts/cm^{-2}	Thermal Conductivity κ watts/cm °K
0.24	1.0×10^{-6}	4.2×10^{-4}
31	6.3×10^{-6}	2.1×10^{-6}

*

SYMBOLS

$A_{1...6}$ platinum bridge constants determined by calibration
$B_{1...6}$ platinum bridge constants determined by calibration
C constant
dT/dz mean vertical temperature gradient
G system gain
I_E bridge excitation current
J heat flow
k thermal conductivity
$\bar{m}$ mean value
n point of constant input ratio
$N_{1...4}$ digital numbers
$N'_{1...4}$ $N - 4096$
R_0 resistance at 0°C
$R_{1...4}$ Wheatstone bridge arm resistances
R_{100} resistance at 100°C
R_B total bridge resistance
R_I idealized output ratio
R_T resistance at T°C
T temperature in degrees Centigrade
T_R reference-bridge temperature
TC thermocouple
u digit resolution (2.4412 millivolts)
v^+, V^+ positive voltage
v^-, V^- negative voltage
v_e sensed reference-bridge excitation voltage
v_o reference-bridge output voltage
v_{off} error offset voltage referred to amplifier input
V_E bridge excitation voltage
V'_E sensed bridge excitation voltage
V_L potential difference across 20-ohm resistance for current I_E.
V_O bridge output voltage
V_T potential difference across 2-ohm resistance for current I_E
V_X voltage at connection point X
V_Y voltage at connection point Y
$X_{1...4}$ calibration constants for reference bridge
z vertical distance
Z attenuation ratio V'_E/V_E
α_s solar absorptance
β Van Dusen calibration constant
δ Callendar calibration constant
ΔT temperature difference in degrees Centigrade
e system error offset
e_0 output-sense-line offset
e_1 excitation-sense-line offset
e_{IR} infrared emittance
σ standard deviation

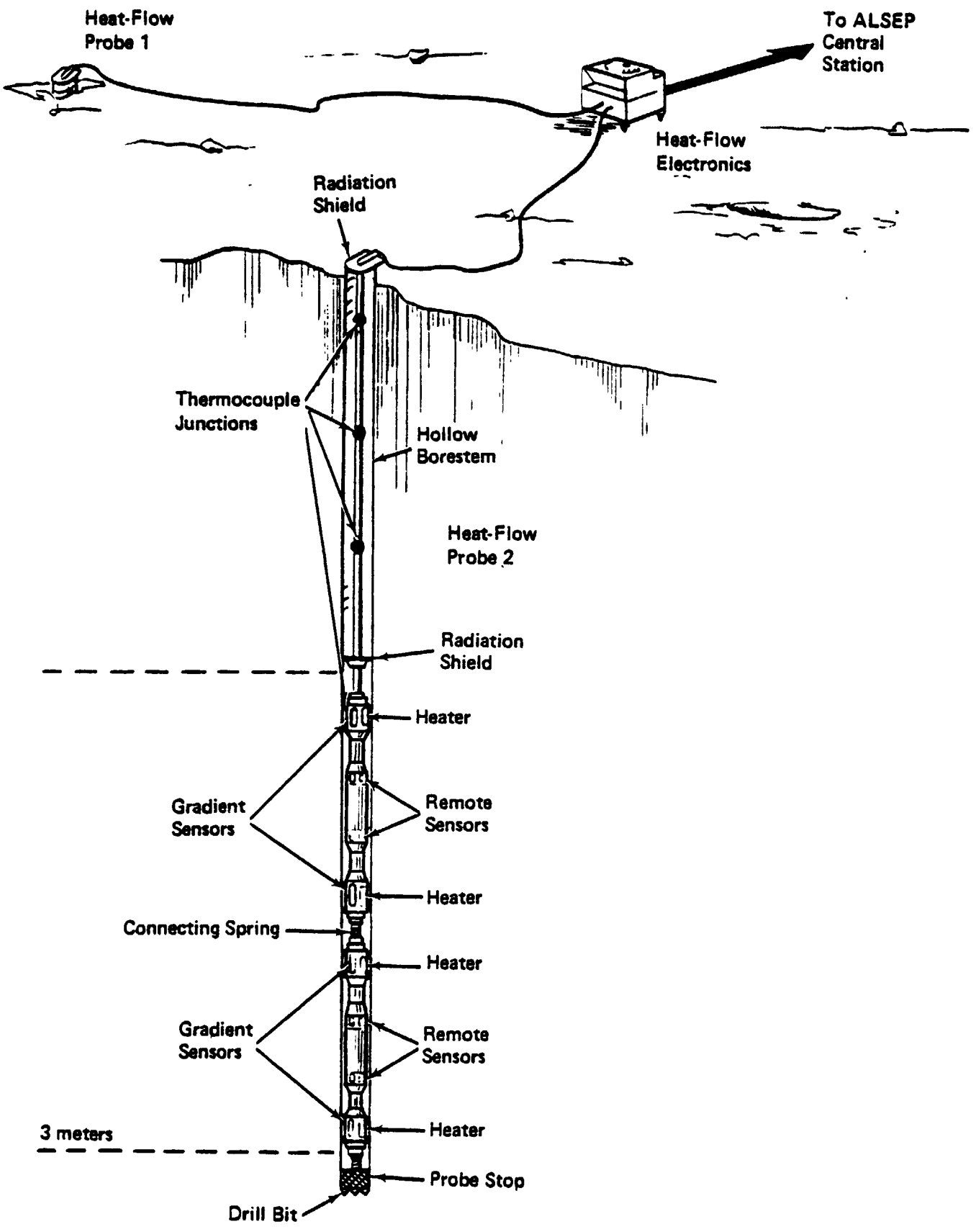

Appendix C-Figure 1

specific heat, thermal conductivity can be calculated.

EXPERIMENT DESCRIPTION

The optimum configuration in the lunar surface for the Lunar Heat Flow Experiment is depicted in Figure 1. Two hollow fiberglass borestems, 2.5 centimeters in diameter, are drilled into the lunar surface to a depth of 3 meters at a distance of 10 meters from one another. Four sets of temperature sensors, spaced along a probe consisting of two flexibly joined rigid sections, occupy the bottom meter of each hole. The flexible joint permits the probe to be folded for transportation to the moon. The sensors, which are primarily radiatively coupled to the borestem and lunar soil, are connected electrically by 8-meter woven cables to a package of electronics on the surface. Each cable carries four precisely located thermocouple junctions in the borestems above the probes. The electronics unit is connected by a flat ribbon cable, 9 meters long, to the Apollo Lunar Surface Experiments Package (ALSEP) Central Station, which formats all the data from and controls the operation of all the scientific-station instruments on command from earth.

The heat-flow instrument returns data giving average-temperature, differential-temperature, and low- and high-thermal-conductivity information from four locations on each probe, with the thermocouples supplying readings for temperature determinations in the upper part of the boreholes. Instrument performance requirements for these measurements are summarized in Table II. In the normal operating mode, the heat-flow instrument gathers ambient and high and low-sensitivity differential temperature data from the "gradient" sensors situated at the ends of each half-probe section and samples the thermocouple outputs during the 7.25 minute measurement sequence. Various subsequences can be selected (e.g. measurements on one probe only), but most of them would not normally be used. Low-conductivity experiments are performed on command, with each heater activated in turn to 0.002 watt for about 40 hours. The normal measurement sequence is

TABLE 2. Heat-Flow-Instrument Performance Requirements

Measurement	Requirement			
	Range	Resolution	Accuracy*	Minimum Stability
Temperature Difference across 0.5 meter probe section in lowest meter of hole	± 2°K (high sensitivity) ± 20°K (low sensitivity)	0.0005°K (high sensitivity) 0.005°K (low sensitivity)	±0.003°K	0.003°K/year
Ambient temperature probe in lowest meter of hole	200 - 250°K	0.02 - 0.08°K	±0.1 °K	0.05°K/year
Temperature of thermocouples in upper 2 meters of hole	90 - 350°K	0.17°K	±0.5°K	0.5°K/year
Thermal conductivity of material surrounding probes	$2\text{-}400 \times 10^{-5}$ W/cm °K	± 20%	± 20%	----

* Maximum probable error

unchanged. The high conductivity mode of operation requires the selection of measurements on the remote sensors in any half-probe section, the type of data returned alternating between high-sensitivity differential and absolute temperature measurements. Either of the adjacent heaters at the ends of the probe half may be activated by command. Each heater should be on for about six hours, but this depends on the conductivity experienced.

PROBE AND SENSOR CONSTRUCTION

The platinum resistance sensors used in the heat-flow instrument probe contribute significantly to the quality of the measurements obtained. The approach to sensor construction is not new: Siemens (1871) described a platinum resistance thermometer, with wire wound on a clay cylinder enclosed in a wrought-iron tube, at a meeting of the Royal Society of London in 1871. Whereas present commercial thermometers have stabilities of 10 to 100 millidegrees Kelvin per year with normal use (Klaven et al., 1970) the lunar gradient measurements require stabilities of the order of 1 millidegree Kelvin. These have been achieved in standards laboratories for some time, but with sensors susceptible to quite low levels of shock and vibration, and with substantial precision equipment required to obtain accurate readings.

Two types of platinum resistance thermometers are used in the heat-flow instrument, the so-called 'gradient' sensor and the 'ring' or 'remote' sensor. The gradient sensor, the construction of which is detailed in Figure 2, incorporates a unique method of supporting the resistance wire to reduce instability normally induced by mechanical or thermal stress. Pure annealed 0.04 millimeter diameter platinum wire is mounted, coiled in a 0.3 millimeter diameter helix extended to 0.07 millimeter pitch, on a glass-insulated platinum mandrel. The base of each loop is arranged so that only 10 percent of the turn is embedded in the substrate. The mandrel and glass have the same expansion coefficients as the coil, and the assembly is annealed at 673°K for 15 hours before sealing. The platinum coil is isolated from contamination by an

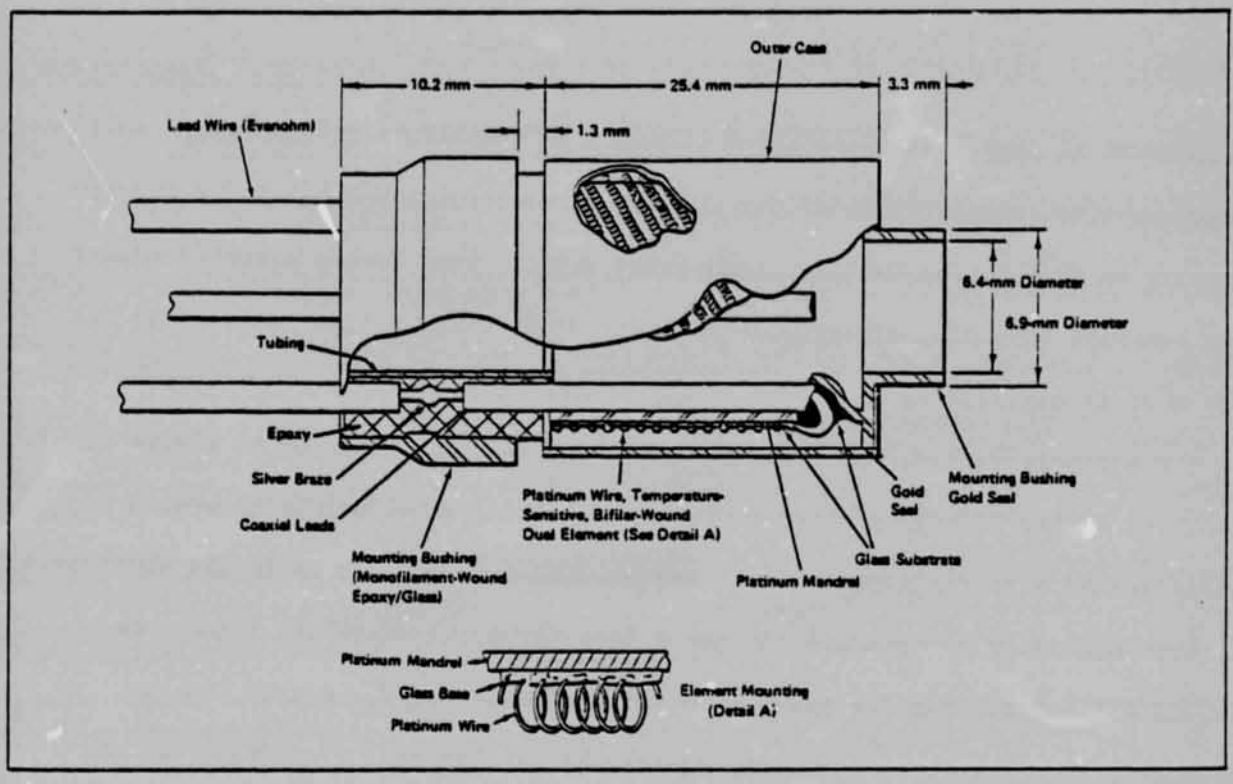

Figure 2 Gradient-Sensor Construction

Appendix C-Figure 2

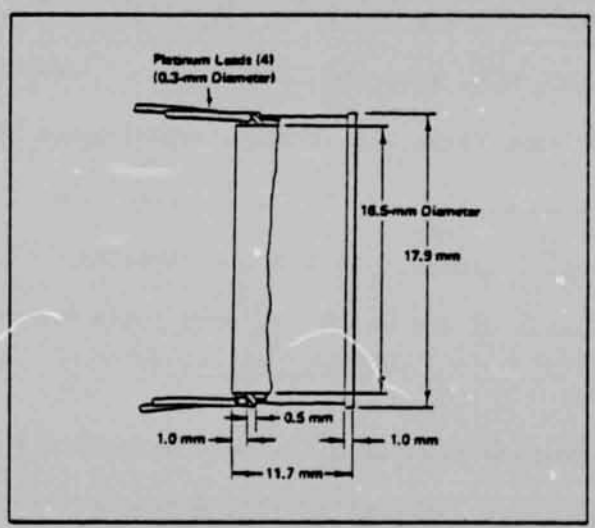

Figure 3 Ring- or Remote-Sensor Construction

Appendix C-Figure 3

atmosphere of pure helium contained within a gold-sealed platinum outer case. Platinum-wire coaxial leads extend through ceramic-insulated tubes for silver brazing to Evanohm and Manganin connecting wires. Each sensor assembly houses two separate elements, effectively bifilar wound, with nominal resistances of 500 ohms at 273.16°K (0°C).

The remote sensor, the construction of which is illustrated in Figure 3, consists of two 500-ohm-nominal-resistance platinum wires set in a ceramic glaze around a thin platinum ring. Because its intended use is in the short-term high-conductivity experiments, it has a less stringent stability requirement (0.002°K/6 hours) than the gradient sensor. Unexpectedly, however, it has demonstrated a long-term stability comparable to that of the gradient sensor.

The sensors are mounted as shown in Figure 4, which illustrates the configuration common to the ends of all half-probe sections. The gradient assembly is epoxied at the mounting bushing at the sensor-lead exit end to the inside of the probe end-sheath. The small tube on the opposite end (also shown in Figure 2) is supported by a snugly fitting fiberglass bushing, which permits strain-free differential expansion with good mounting support. Associated with each gradient sensor is a 1000-ohm Karma wire heater, wound concentrically with the gradient sensor on the thin section of the end sheath. The ring-sensor platinum band is partially cemented internally to a filler sheath, which, in turn, is attached to the outer sheath of the probe. A tube joins the two end pieces to form a probe half-section.

The structural components providing the span between the sensors are manufactured from low-conductivity thin-walled filament-wound epoxy fiberglass. All cabling is carried through the probe body inside the split inner sheath, which is shielded with multilayer insulation to reduce radiative coupling between the wiring and probe wall, particularly during conductivity experiments with a heater on. The areas around the sensors are partially enclosed with guards for

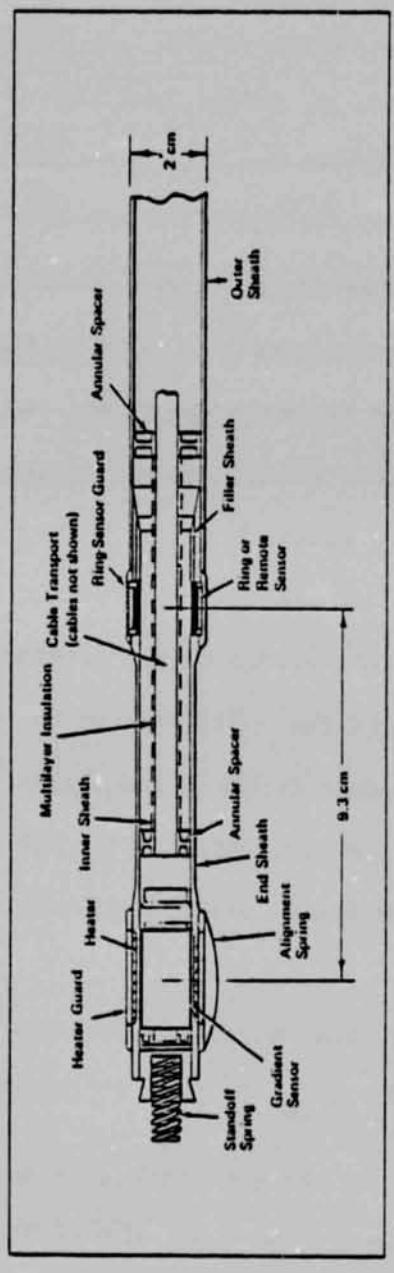

Figure 4 Half-Probe End Section

Appendix C-Figure 4

protection during handling.

A probe assembly is 1.09 meters long when unfolded at the closely coiled extension spring that joins the two half-sections. The complete unit is coated with a matt-black thermal control paint. An assembled probe, with its 8-meter 35 conductor connecting cable, weighs less than 0.5 kilogram.

Gradient and ring sensors are each interconnected within a probe half with AWG 23 Evanohm wire to form bridges, the opposite arms of which are physically situated in the same sensor assembly at a common temperature. A schematic of this resistance-bridge arrangement is shown in Figure 5 (left), where T_1 is the temperature of one sensor assembly and T_2 the temperature of the other. The gradient-sensor assemblies, which form one bridge, are separated by 47 centimeters; the remote-sensor assemblies, which form the other, are located 29 centimeters apart and 9 centimeters from the heater windings.

Six wires connect each bridge to the electronics unit. Those from a lower half-probe are conveyed in the upper section through the hollow sensor assemblies. Evanohm wire is used because it has a remarkably small temperature coefficient of resistance (0.00002/°C), with closely controllable resistivity and a thermal conductivity that is low for an electrical conductor.

SENSOR CHARACTERISTICS

In Callendar's empirical parabolic equation (Callendar, 1887 and 1871)

$$T = 100[(R_T-R_0)/(R_{100}-R_0)] + \delta\,[(T/100)-1]\,(T/100) \qquad (2)$$

the constant δ defines the characteristics of an individual platinum resistance thermometer over the temperature range 0°C to 630°C, where T is temperature in degrees Centigrade, R_T is resistance at temperature T, R_0 is resistance at 0°C, and R_{100} is resistance at 100°C. The Callendar constant is determined by calibration at three fixed points: the triple point of water (0.0100°C), the steam point (100°C), and the boiling point of sulfur (444.600°C). For use

ORIGINAL PAGE IS
OF POOR QUALITY

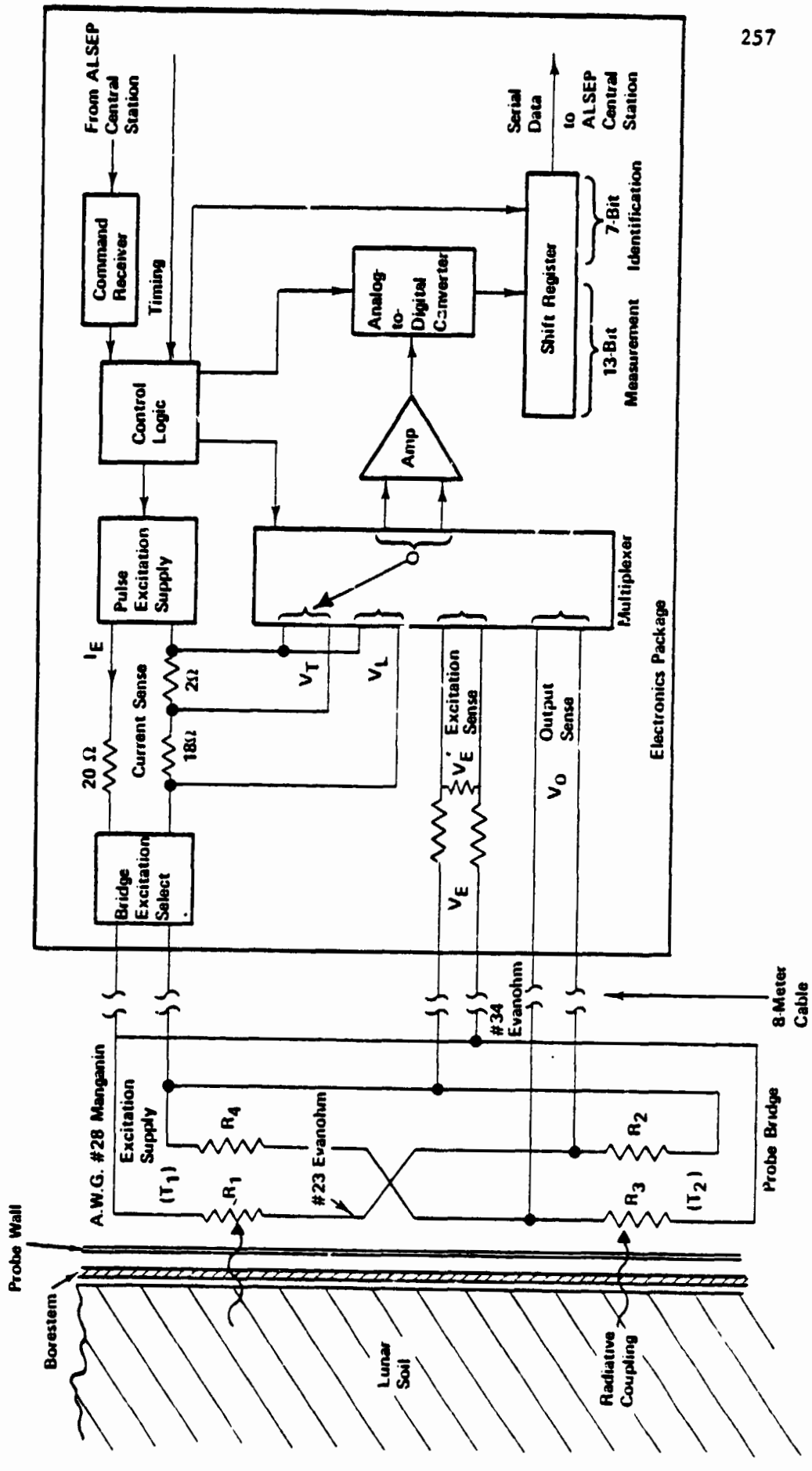

Appendix C-Figure 5

between 0°C and -183°C, a correction term devised by Van Dusen is added to the Callendar equation to give (Robertson and Walch, 1962)

$$T = 100\,[(R_T - R_0)/(R_{100} - R_0)] + \delta\,[(T/100) - 1]\,(T/100) + \beta\,[(T/100) - 1]\,(T/100)^3 \qquad (3)$$

where the constant β for an individual thermometer is found by calibrating at the boiling point of oxygen (-182.97°C). The resistance of one platinum element at temperature T relative to its resistance at 0°C is therefore:

$$R_T/R_0 = 1 + (1/100)\,[(R_{100}/R_0) - 1]\,\{T - \delta\,[(T/100) - 1]\,(T/100) - \beta\,[(T/100) - 1]\,(T/100)^3\} \qquad (4)$$

Referring to Figure 5, the bridge voltage ratio is defined

$$V_O/V_E = (R_1R_4 - R_2R_3)/[(R_1 + R_3)(R_2 + R_4)] \qquad (5)$$

where R_1, R_2, R_3, and R_4 are Wheatstone bridge arm resistances, V_E is the excitation voltage across the bridge, and V_O is the output voltage. By combining equations (4) and (5) and eliminating small terms, the following simplified expression is obtained,

$$(V_O/V_E)R_B = A_1 + A_2T + A_3T^2 + A_4\Delta T + A_5\Delta T(\Delta T + 2T) + A_6[\Delta T(4T^3 - 300T^2) + \Delta T^2(6T^2 - 300T) + \Delta T^3(4T - 100) + \Delta T^4] \qquad (6)$$

where R_B is total bridge resistance, T is the temperature of one sensor assembly expressed in degrees Centigrade, ΔT is the temperature differential between sensor assemblies in degrees Centigrade, and A_1, A_2, A_3, A_4, A_5, and A_6 are constants. Similarly, bridge resistance R_B can be related to temperature T and temperature differential ΔT by the simplified expression

$$R_B = B_1 + B_2T + B_3T^2 + B_4\Delta T + B_5\Delta T(\Delta T + 2T) + B_6\,(T - 100)T^3 \qquad (7)$$

where B_1, B_2, B_3, B_4, B_5, and B_6 are constants. Equations (6) and (7) are transcendental in T and ΔT. To find absolute and differential temperatures, an iterative simultaneous solution of both calibration equations is required

The reduction of voltage differences and bridge resistances to temperatures and temperature differences was accomplished differently at the Johnson Space Craft Center and at L-DGO. The calibration data consisting of bridge resistance and voltage ratio versus bridge average temperature and temperature difference were fitted to two dimensional functions of the following form by least squares.

$$\Delta T = \sum_{\substack{\ell=o \\ k=o}}^{3.3} A(\ell,k) \cdot R_B^{\ell} \cdot (V_o/V_e)^k \qquad k \neq \ell \qquad (8)$$

$A(\ell,k)$ are 16 coefficients derived by least squares.

$$T = \sum_{\substack{\ell=o \\ k=o}}^{3.3} B(\ell,\mu) \cdot R_B^{\ell} \cdot (V_o/V_e)^k \qquad k \neq \ell \qquad (9)$$

where $B(\ell,k)$ represent 16 coefficients.

THE ELECTRONIC MEASUREMENT SYSTEM

System Operation

It can be seen from equations (6) and (7) that the electrical measurements required to solve for T and ΔT are total bridge resistance R_B (measured as a single element), excitation voltage V_E, and differential output voltage V_O. The system by which these measurements are made is represented in the simplified block diagram in Figure 5, which incorporates the essential features of the bridge measurement method, although it includes only one of the eight probe bridges and omits thermocouple circuits, power supplies, and the bulk of the logic and control circuits.

Each of the bridges is selected through reed relays for excitation by direct current. The bridges produce a differential output-to-input voltage ratio V_O/V_E of approximately $\pm 5.8 \times 10^{-3}$ for a dynamic range of $\pm 2^{\circ}K$. With 8

volts applied to the bridge excitation cables, the data-chain maximum input requirement is set at ±34 millivolts. The gradient-bridge low-sensitivity range of ±20°K requires 0.8 volt excitation for a similar output maximum. Measurements for total bridge resistance are made at the 8-volt supply level. Excitation voltage V_E is reduced to the maximum level of output voltage by an attenuator in the excitation sense circuit. The series elements of the attenuator include cable resistance that does fluctuate slightly with the large surface-temperature variations, but the proportion of cable resistance in the temperature-matched attenuator is small, and very high attenuation-ratio stability is achieved. The output impedance is arranged to be the same as the bridge differential output impedance. At the low-sensitivity excitation level of 0.8 volt, the attenuator output V'_E is one-tenth the maximum bridge unbalance voltage V_O at ±20°K temperature extremes. To effectively normalize these readings and at the same time avoid attenuator switching or gain changes, excitation current I_E is sensed. This current is combined with the total bridge resistance value, determined from readings at 8 volts excitation made within a short time of the current measurement, to calculate the low-level excitation supply voltage. Low sensitivity current is found from the potential difference V_L developed across a precision 18+2 ohm resistance in the supply line; high-sensitivity current is found from the potential difference V_T across the 2-ohm resistor only. The latter value is used with the attenuated bridge-excitation-voltage measurement to determine total bridge resistance R_B. Differential output voltages are read directly.

These various measurements are presented sequentially through a low-level field-effect-transistor (FET) multiplexer to the input of the common signal amplifier, which has a gain of 288 and full-scale output of ±10 volts. The amplified signal is converted to a 13-bit digital number and clocked into a shift register along with a 7-bit mode-identification and binary-measurement

TABLE 3. Sources of Error in Experiment Data

Platinum-bridge error sources
* initial calibration accuracy
* element stability with age
* dissimilar metal EMF's at sense-wire connections
Measurement-system error sources
* initial calibration of electronics
* system noise
* spurious EMF's in multiplexer
* excitation voltage
stability
sense-attenuation stability
bridge heating
* amplifier
common mode rejection
gain and offset stability
linearity
settling time
* analog-to-digital converter
linearity
reference-voltage stability
quantizing magnitude
Data-processing error sources
* truncation errors
* iterative solution accuracy of bridge equations

code. The resulting 20-bit number is serially shifted into the ALSEP Central Station for insertion as two 10-bit words into the ALSEP data stream for transmission to earth. On earth, the binary numbers are converted back to the sensor temperatures from which they originated by applying the calibration factors for each bridge of thermocouple and each measuring channel. The sources of error to which the reconverted temperature values may be subject are outlined in Table III.

THE RATIO MEASUREMENT TECHNIQUE

Errors due to long-term system gain and offset instability are circumvented by using a ratio technique, which eliminates system gain and offset as factors in the reconstitution of the original bridge ratio, depending for its success only on gain and offset stability during the brief measurement period. All measurements are made twice, at two different levels. To utilize the full system range and obtain maximum resolution, it is convenient for each bridge input and output measurement to be made at reversed polarity, with equal bipolar excitation levels. The bridge is pulsed twice in 2.4 seconds for 2.6 milliseconds at a maximum duty cycle (0.2×10^{-3}), which limits self-heating to an acceptable 0.1 microwatt; two measurements are made during each excitation pulse. The sequence outlined in Figure 6 for a high-sensitivity differential measurement is typical of all measurements. Power is applied to the bridge from the excitation-pulse supply at bipolar 4-volt levels, giving a positive 8-volt total excitation. After 1 millisecond to allow the system to settle, the attenuator output V'_E+ corresponding to excitation level V_E+ is converted to a digital number N_1. Output voltage V_0^+ is then selected for measurement, and, after a 2.3-millisecond positive pulse duration, V_0^+ conversion to N_2 is executed. The entire process is repeated 2.4 seconds from the start of the sequence, with the pulse-excitation supply output reversed to -8 volts; during application of this negative pulse, V'_E- and V_0- are converted to digital

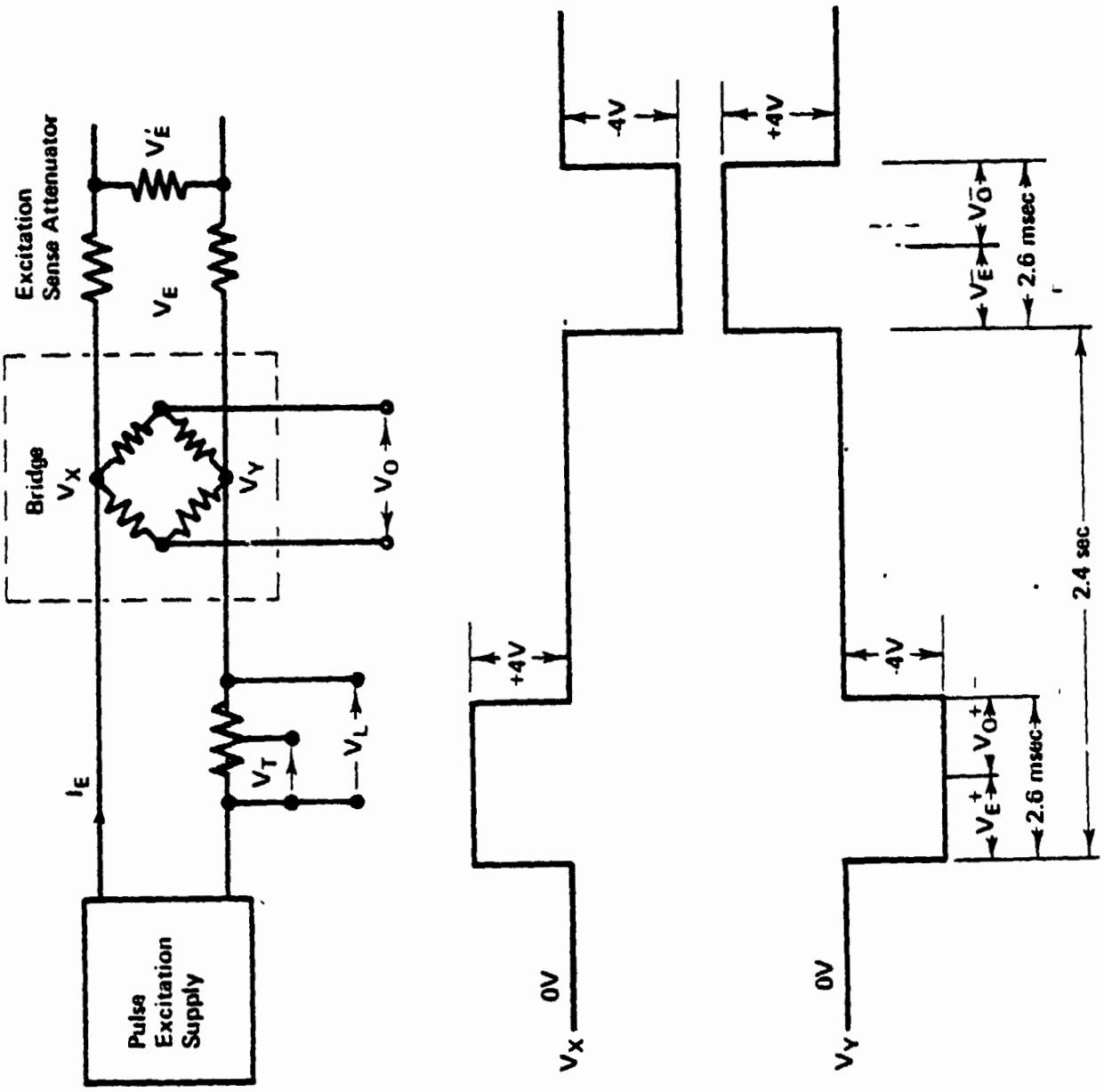

Appendix C-Figure 6

numbers N_3 and N_4, respectively.

If G represents amplifier and analog-to-digital-converter gain,

$$(N_2-N_4)/(N_1-N_3) = [(V_0^+ + \varepsilon_0 + \varepsilon)G - (V_0^- + \varepsilon_0 + \varepsilon)G]/[(V_E'^+ + \varepsilon_1 + \varepsilon)G - (V_0^- + \varepsilon_1 + \varepsilon)G] = (V_0^+ - V_0^-)/(V_E'^+ - V_E'^-)$$
$$= (V_0^+ / V_E'^+)[1-(V_0^-/V_0^+)]/[1 - (V_E'^- / V_E^+)] \tag{8}$$

where ε is the amplifier and analog-to-digital-converter offset, ε_0 is the output-sense-line offset, and ε_1 is the excitation-sense-line offset. Since the temperature of a bridge in the lunar regolith will not change during the 2.4-second measurement period,

$$V_0^+ / V_E'^+ = V_0^- / V_E'^- = C \tag{9}$$

where C is a constant regardless of the excitation magnitudes of V_E^+ and V_E^-. Rearranging equation (9) to read

$$V_0^- / V_0^+ = V_E'^- / V_E'^+ \tag{10}$$

and combining equations (8) and (10) results in

$$(N_2 - N_4)/(N_1 - N_3) = V_0^+ / V_E'^+ \tag{11}$$

where $V_0^+/V_E'^+$ is the ratio between measured bridge signals, independent of gain and offset. The required bridge ratio V_0/V_E is obtained by applying the excitation-sense measurement attenuation factor Z, the accuracy and stability of which clearly affect the result. Since $Z = V_E'/V_E$,

$$V_O / V_E = V_O / ZV'_E$$

OTHER DESIGN FEATURES

The use of excitation-polarity reversal, with one data converter for all measurements, eliminates some major sources of error and obviates need for separate periodic calibrations on the moon and additional circuitry with which to perform them. Nevertheless, numerous sources of error remain. It is therefore pertinent to summarize here the more significant features of the principal components of the data chain, which account for demonstrated measurement accuracies of better than 0.02-percent-full-scale probable error over a temperature range of $0^{\circ}C$ to $60^{\circ}C$.

The pulsed-power supply produces 4.000-volt±1-millivolt bipolar pulses, which are stable to within 0.002 percent during bridge excitation and output measurements. The supply operates from positive and negative reference levels, derived from constant-current-driven low-temperature-coefficient zener diodes, which are switched by the control logic for positive and negative bridge excitation outputs from two series-connected operational amplifiers, each having a push/pull output stage to supply the 20-milliampere bridge current.

The multiplexer for the heat-flow instrument is a double-tiered N-channel field-effect-transistor (FET) commutator, with 32 differential input pairs. It is divided into four sections, one for each probe set of gradient sensors and one each for the remote sensors and the thermocouples. Each FET section is powered only when necessary to restrict the effects of a single-channel failure. Field-effect-transistor temperature-dependent offset voltages and mismatched differential impedances, which act with circuit impedances and amplifier bias currents to introduce variable offset voltages for each channel and different offsets between channels, are cancelled by the ratio measurement

technique previously described.

The most basic design trade-offs in analog-to-digital converter design are speed and accuracy. Neither is of great consequence in this application, where extreme linearity, stability, and sensitivity are the only critical requirements. Digital conversion of the amplified sensor signals is achieved by 13-bit successive approximation to the sum of a generated +10.000-volt±1-millivolt offset supply and the ±10-volt full-scale output from the data amplifier. The offset binary number produced is linear to within 0.0075 percent full scale, with a resolution of 2.4414 millivolts per bit. Conversion speed is 20 microseconds per bit. The device is a conventional successive-approximation analog-to-digital converter, with the two most significant bits of the ladder network trimmed to remove errors due to voltage drops across the switches.

The signals are amplified by a differential-input single-ended-output two-stage amplifier, with differential and common-mode impedances exceeding 50 and 20 megohms, respectively, at frequencies below 5 kilohertz. The common-mode rejection ratio is greater than 120 decibels over the same frequency range. The characteristics most important to the ratio technique are linearity, which is within 0.005 percent full scale, and short-term stability, which is better than 0.001 percent for 5 seconds at a maximum rate of temperature change of 0.01°C per second. The common-mode rejection ratio becomes important when bridge current is sensed at 8-volt excitation levels.

Constant-current sources are supplied to each base of the differential input pair to compensate for the bias current required by the matched semiconductors, but the more usual constant-current-source common-emitter supply is replaced with a variable current source that maintains the combined collector currents constant. The differential output from the collectors connects to an operational amplifier, the output of which feeds back to the emitters of the

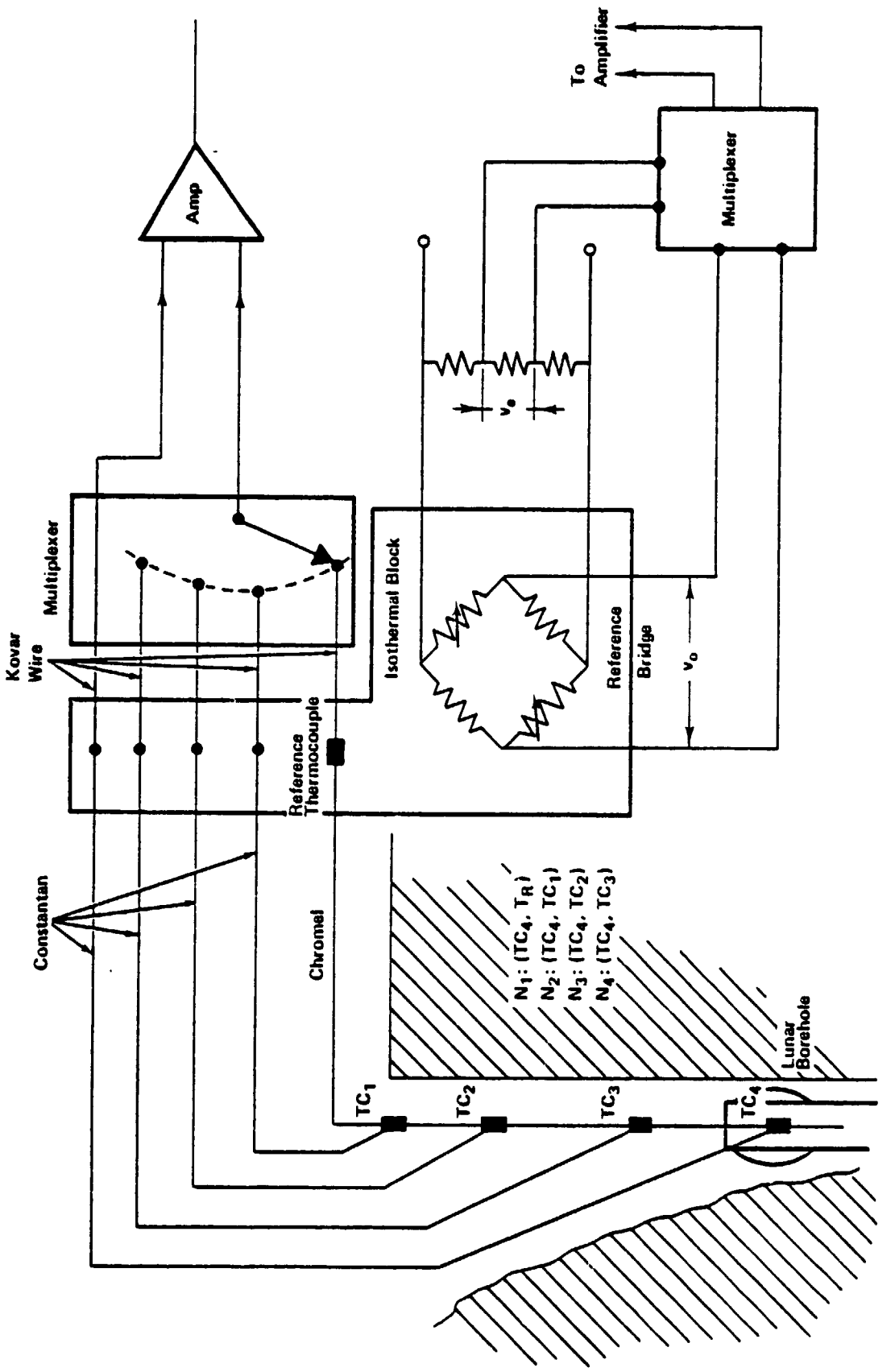

Appendix C-Figure 7

input stage to force the total of the collector currents to divide equally between the two halves of the differential pair. Stable operating points are thus established independently of common-mode inputs over a wide temperature range. The first-stage gain is 100. After filtering, the signal is applied to the input of the second-stage amplifier, which normally operates with a gain of 2.88. The total amplifier gain of 288 is used for all bridge measurements.

Thermocouple measurements require an input range of ±10 millivolts rather than ±34 millivolts. During thermocouple sequences, therefore, the second-stage gain is changed from 2.88 to 10 by switching a field-effect transistor to introduce a potential divider in the feedback path of the second stage.

THERMOCOUPLE MEASUREMENTS

Eight constantan and two chromel wires from the thermocouple junctions in the probe cables connect to Kovar leads at an isothermal block inside the electronics package. The Kovar leads convey the thermocouple voltages to the multiplexer. The isothermal block also contains a platinum/Evanohm bridge thermometer with two constant-value resistance arms. A schematic representing one probe-cable set of thermocouple junctions and the reference-temperature bridge is presented in Figure 7.

Thermocouple measurements of absolute temperature have an inherent accuracy an order of magnitude lower than platinum resistance measurements, in part because of thermocouple instability but primarily because of difficulties in measuring low-level voltage sources. Since the ratio technique is not applicable to thermocouple measurements, a calibration method is used to establish system gain and offset during the measurement sequence that determines the isothermal block temperature with the bridge thermometer.

Measurements on the reference-temperature bridge follow the same pattern as those on the probe bridges, except that the amplitude of excitation is

attenuated to give a ±10-millivolt full-scale output, which is the range of the thermocouple voltages. An amplifier nominal gain of 1000 is selected for reference-bridge and thermocouple measurements. To find system gain and error offset values, it is assumed that the attenuated positive and negative bridge-excitation voltages v_e are of known, equal, and opposite magnitudes since they are derived from the precisely controlled pulsed-power supply and are connected to the bridge by short leads within the electronics package.

The sensed excitation signals v_e^+ and v_e^- are converted by the analog-to-digital converter to binary numbers N_1 and N_3 in accord with the relationships

$$N_1 = [(v_e^+ + v_{off})G]/\mu$$

$$N_3 = [(v_e^- + v_{off})G]/\mu$$

where v_{off} is error offset voltage referred to the amplifier input, G is system gain, and μ is the digit resolution unit of 2.4414 millivolts. Gain is found from

$$G = \mu(N_1 - N_3)/(v_e^+ - v_e^-)$$

when the offset voltages cancel. To find the error offset voltage v_{off}, the offset binary outputs N_1 and N_3 are converted to positive and negative numbers by subtracting offset count 4096. If $N_1' = (N_1 - 4096)$ and $N_3' = (N_3 - 4096)$, then $v_{off} = \mu(N_1' + N_3')/2$.

The use of known balanced inputs in the reference-bridge measuring sequence thus establishes system gain and offset. The measured outputs are converted through electronics calibration data, and the bridge voltage ratio is then used to solve iteratively a third-order calibration equation for reference-

bridge temperature and hence for isothermal-block and reference-thermocouple temperature. Measurements of thermocouple voltages made shortly thereafter (in the sequence N_1, N_2, N_3, N_4, as shown on the Figure 7 schematic) are processed, using calculated gain and offset values, to arrive at true thermocouple voltage outputs.

The output from the chromel/constantan reference junction in the isothermal block is measured relative to only one of the junctions in the cable - that inside the hollow of the gradient sensor at the top of the probe. The remaining three junctions in each probe cable are also measured relative to this top junction. The double-referencing arrangement is designed to center the mean of the thermocouple-output extremes close to 0 volts for maximum measurement resolution. The predicted temperature range for the thermocouple junction at the top of the probe is 200°K to 260°K; the full-scale thermocouple range is 90°K to 350°K, and the isothermal-block temperature is controlled to between 278°K and 328°K.

The voltage/temperature characteristics of the thermocouples are described by calibration correction factors applied to standard tables of the National Bureau of Standards (NBS) (Adams and Davisson, 1965).

PACKAGE CONSTRUCTION AND THERMAL CONTROL

The heat-flow instrument operates from a 29-volt d.c. supply and requires data-interlace and mode-control signals from the ALSEP Central Station. The unit is otherwise self-contained with respect to logic and power management for all the sensor measurements and for probe-heater control.

In the deployed configuration, a ribbon cable made up of 40 flat copper conductors in a plastic film extends from the instrument package across 9 meters of the lunar surface to the ALSEP Central Station. This cable is connected to an astromate connector, which the astronaut mates with the Central Station

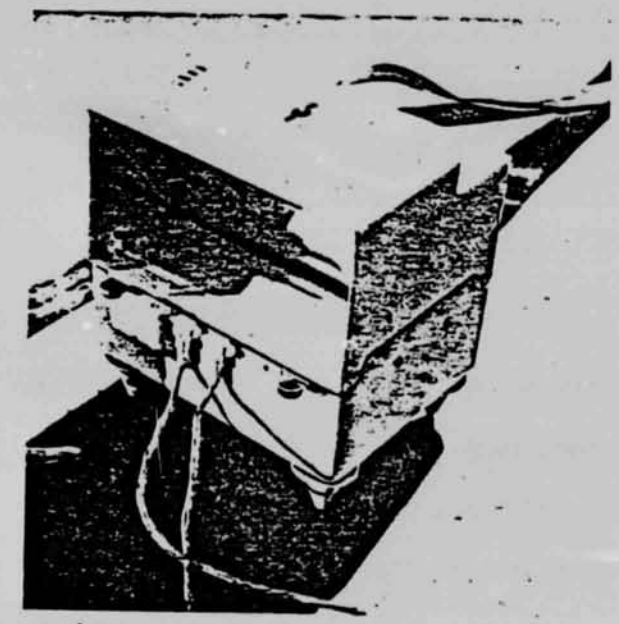

Figure 8 Heat-Flow-Instrument Package

outlet for power to and communication with the heat-flow instrument.

The two probe cables are each made up of 35 unshielded conductors, interwoven for a uniform stress distribution so that the weight of the astronaut can be supported without degradation in cable performance. These cables are very flexible, exhibiting little residual torque when extended, and they are covered with a woven Teflon sleeve to provide a low coefficient of friction during deployment. Heat leaks from the cables on the lunar surface to the probes and the electronics package are small since the conductors are made from low-thermal-conductivity wire.

The complete surface package, shown in Figure 8, weighs 7.0 pounds (3.2 kilogram) and is 9.5x10.0x11.0 inches (24x25x28 centimeters) in size, including the feet. The astromate connector, ribbon cable, and spool weigh 1.4 pounds (0.6 kilogram).

Electronics Package

The electronic circuitry shown in Figure 9, is made up of five multilayer printed-circuit boards, joined in a stack by interlocking spacers bonded to each board. The stack is 2.5x7.6x5.6 inches (6x19x14 centimeters) in size, the boards consisting of up to twelve layers, each 0.004 inch (0.1 millimeter) thick. The layers of circuit tracks are interconnected through plated holes in the composite board, and as many as 210 component subpackages are mounted on one board. The components are in physical contact with a heavy printed-circuit conductor, which forms a heat path to the interlocking spacers. Column screws pass through the spacers to a metal plate, which serves both as a thermal control plate and as a support for the board stack. A d.c./d.c. converter for the instrument power supplies is packaged on a board that is bonded to the thermal control plate. Heating elements are also mounted in good thermal contact with the plate. A short length of Manganin cable (at left in Figure 9) provides thermal insulation from the copper conductors in

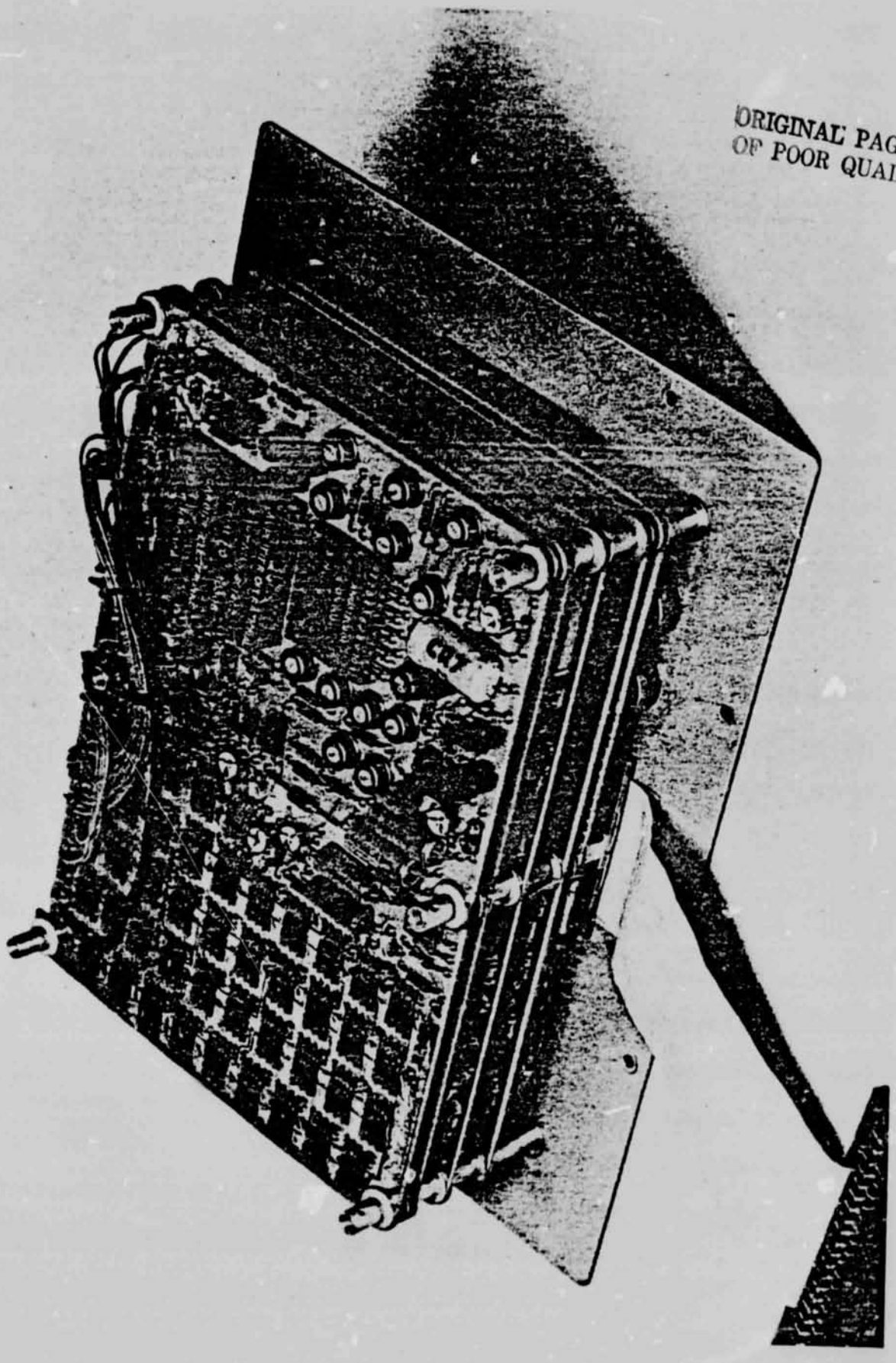

Appendix C-Figure 9

the ribbon cable. Bonded to the thermal control plate at the other side of the unit is a 70-pin isothermal connector to which the two probe cables are soldered. When the unit is assembled, the board stack is enclosed by a metal cover with a compressible, electrically conducting gasket to provide a barrier to electromagnetic interference.

The electronics unit weighs 3.3 pounds (1.5 kilograms).

Thermal Control Design

A thermal insulation bag, shaped as a container for the metal cover surrounding the board stack, is hooked by velcro pads to a low-thermal conductivity mounting ring fitted around the inside edge of the thermal plate. The bag is constructed of twelve layers of closely spaced high-reflectivity shields having very low transverse conductivity; bridal-silk netting separates the layers and covers the inside and outside of the bag. The infrared emissivity of the 1/4-mil aluminized Mylar used for the shields is approximately 0.02.

The electronics assembly is supported and protected by a thin fiberglass outer case, which is connected to the mounting ring by low-conductivity joints. When the unit is standing on the feet on this outer case, the well-insulated electronics compartment is situated beneath the exposed thermal control plate. Internally generated heat is conducted to the plate and radiated from a spectrally selective surface coating (S-13G) having a high infrared emittance ($\epsilon_{IR} = 0.9$) and a low absorptance ($\alpha_s = 0.2$) at frequencies where solar power is most intense.

The thermal plate is protected from direct solar radiation by a sunshield fitted over the assembly as shown in Figure 8. The sunshield is an insulated box with one open side, which is placed to face away from the equator with its edge aligned in the east/west direction. The numbered marks on the sunshield are used as a shadowgraph with the shadow cast by the handling tool, which fits into the center socket. A specular reflector slopes from the top edge of the

lunar night is 10.5 watts. Should the 29-volt operational supply be switched off under abnormal circumstances, a separate survival line can be activated to a part of the thermal-plate heater for a power dissipation of 4 watts.

The thermal control system is designed for instrument deployments between lunar latitudes of ±45 degrees.

CALIBRATION AND TESTING

To ensure that the heat-flow instrument will meet its performance requirements, the calibration and test program is extensive and thorough. Indeed, a substantial part of the large array of calibration and test apparatus used was developed specifically for this purpose. The sensors, probes, and electronics are subjected to worst-case mission environments and calibrated as subunits before assembly as flight instruments. The subassembly calibrations are verified by tests on the complete unit, which then undergoes a further series of tests closely simulating all the conditions anticipated for travel to and operation on the moon. The stability of the instrument following exposure to such critical environments as system vibration is carefully checked.

Sensor Calibration

The platinum resistance thermometers are calibrated as a bridge by a comparison method. Intercomparisons of NBS standards indicate that accuracies afforded by this method approach those obtained by absolute fixed-point calibration. Each sensor is immersed, along with a standard thermometer, in an isothermal bath of trichloroethylene. The baths have separate temperature controls so that temperatures can be independently set for each thermometer of the differential bridge. The standard thermometers are interchanged for several measurements to determine offset. The degree Kelvin is established from NBS-calibrated standard thermometers. Secondary absolute-value resistance standards of 1000 ohms, referred to an NBS standard, are maintained as a reference for the electrical measurements.

To check for random errors, each gradient bridge is calibrated at 42 points, which are least-squares fitted to equations (6) and (7) or 8 and 9 to yield the constants in these equations. The standard deviation of the least-squares fit to the data points in equation (6) does not exceed $0.48 \times 10^{-3^{o}}$K for any of the sensor assemblies tested, and more than 60 such assemblies have been produced. The gradient bridges are calibrated at differential temperatures of +20, +10, +2, 0, -1, -2, -10, and -20°K at absolute temperatures of 200, 212.5, 225, 237.5, and 250°K. The equivalent differential-temperature drift of some randomly selected gradient sensors tested periodically at 200°K and 270°K over a 3-year period is approximately $0.3 \times 10^{-3^{o}}$K. The average absolute-temperature drift for individual sensor elements over the same 3-year period has been found to be $0.5 \times 10^{-3^{o}}$K. The ring sensors are calibrated at a minimum of 14 points to calculate 12 calibration constants.

Thermal-plate reference-temperature bridges in the electronics package are calibrated at -20, 0, +25, +50, and +90°C to yield the constants X_1, X_2, X_3 and X_4 in the relationship

$$V_0/V_E = X_1 + X_2(T_R) + X_3(T_R)^2 + X_4(T_R)^3$$

where T_R is the reference-bridge temperature and V_0/V_E is the bridge voltage ratio. During reference-bridge calibration at 0°C, all eight cable thermocouple junctions are immersed in an isothermal bath for calibration at 90, 200, 250, and 350°K.

Electronic Testing and Calibration

Testing of the electronics data chain involves adjustment by resistance-value selection for zero off-set, common-mode rejection, and gain. A calibration factor is found for each measuring channel by calibrating the channel as it will be used - that is, by performing ratio measurements. A set of resistance

networks, calibrated to an accuracy of 0.002 percent, substitute for bridge and line resistances to simulate high-sensitivity and low-sensitivity ratios and bridge resistance. The various types of measurement are made through separate channels. Calibration is performed at nine different differential-ratio amplitudes and five levels of bridge resistance, and at least ten measurements are made for each of the input ratios. The mean $\bar{m}$ and standard deviation σ of the output ratios for a constant input are calculated, and a linear calibration factor is found from the mean values corresponding to ratios near the limits of channel range (n = 1 and n = 9 in Figure 10). The ideal transfer function of the channel is the calibration factor. The error at any point n is defined as the difference between the ideal output $R_1(n)$ and the mean output $\bar{m}$ (n), summed with the standard deviation $\sigma(n)$. To verify system linearity, these measurements are made at temperature intervals throughout the operating range of the heat-flow instrument. A maximum error of 0.0375 percent full scale is specified, but the typical maximum for instruments tested to date is 0.02 percent. Calibration factors are modified for the actual bridge-lead resistances. Thermocouple channel accuracy is also checked by multiple measurements at nine points throughout the $\pm$10 millivolt input range.

Probe Performance Testing

Assembled probes are characterized over ambient- and differential-temperature operating ranges in a temperature-gradient apparatus or gradient chamber, which has an overall height of 11 feet (3.4 meters) and a diameter of 2 feet (0.6 meter). The probes are inserted in a gradient tube 2.5 centimeters in internal diameter, in which a positive or negative temperature field can be developed. A liquid-nitrogen bath surrounds the gradient-tube assembly to provide a constant-temperature heat sink for heat introduced in developing average and linear differential temperatures. A double-vacuum shell minimizes heat leaks and permits the probe to be inserted without unduly disturbing the thermal equili-

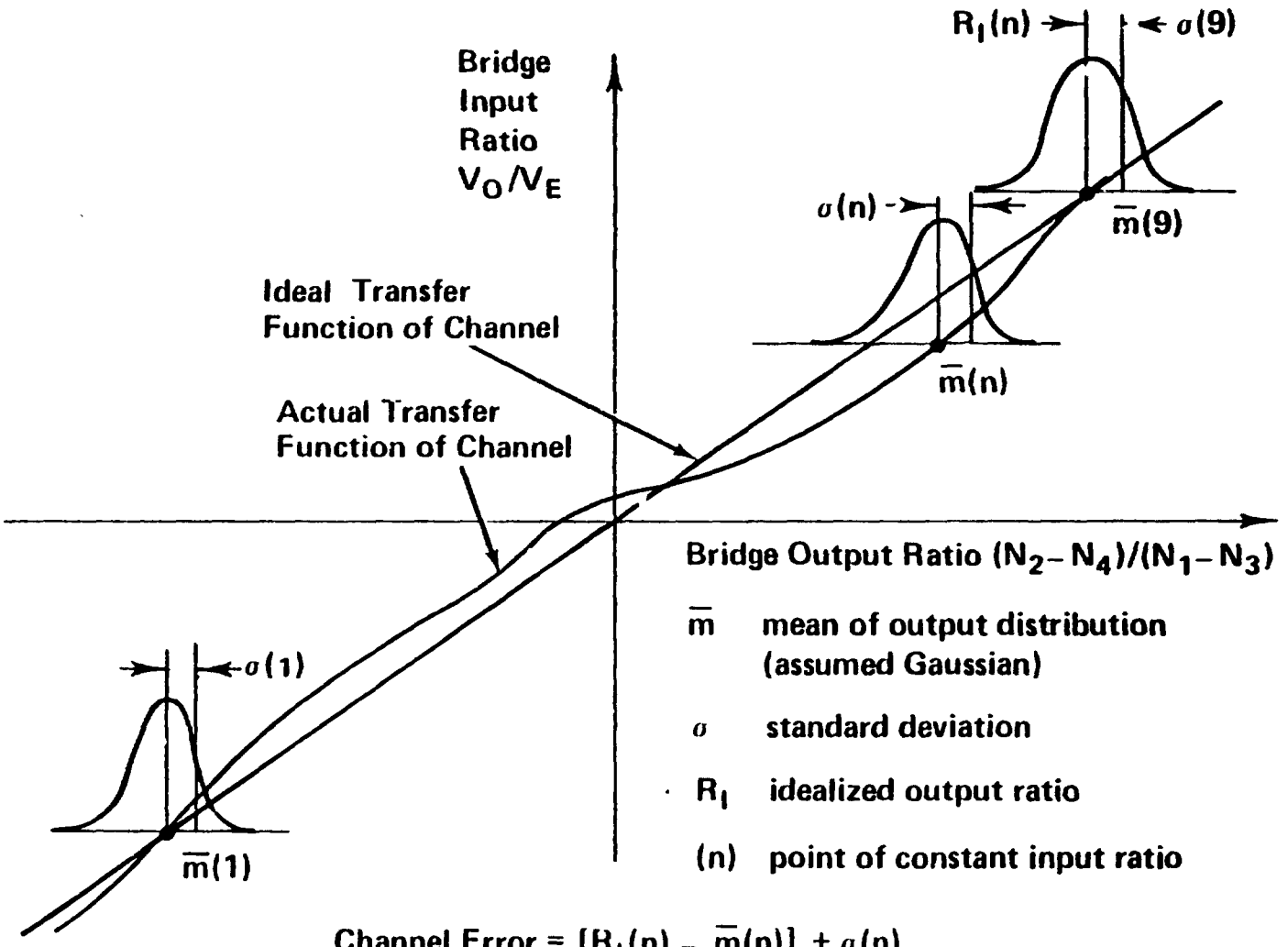

Channel Error = $[R_I(n) - \bar{m}(n)] + \sigma(n)$

Appendix C-Figure 10

brium. Thermocouples and thermopiles in the gradient tube, along with associated readout instrumentation, provide temperature measurements to accuracies that approximate those of the heat-flow instrument. Probe-measured differential temperature is compared with apparatus-measured differential temperature in the form of a "shorting" ratio, which is approximately a linear function of the absolute temperature along the gradient, the probes being radiatively coupled to the gradient tube. This shorting ratio varies from bridge to bridge, depending on small differences in probe construction. The probes are tested at mean ambient temperatures of 205, 225, and 245°K, with linear gradients of 0, 2, and 18°K across each probe half-section. At least five tests are performed with each flight-instrument probe, including two in which the probe is integrated with the electronics. Gradient-chamber tests at 0°K check the zero offset of the gradient bridges and determine the offset values for the ring bridges, the cables of which are shortened during probe assembly. Each of the probe heaters is turned on at the 0.002-watt level by the electronics to characterize the "low-conductivity" performance of the probe in an infinitely conducting environment, which the gradient-tube apparatus represents since it is an almost perfect heat sink.

Thermal conductivity testing is also performed in an apparatus that simulates the properties of the lunar regolith. The thermal conductivity test apparatus is a 10.5-by 3-foot (3.2-by 0.9-meter) Dewar flask, with inner-vessel-wall cooling to the temperature range 200°K to 250°K. A probe boretube extends into a bed of glass microbeads in the inner container. The outer cavity and the boretube are evacuated, and the thermal conductivity of the glass-bead bed is varied over the anticipated lunar range by controlling the gas-filling pressure. Two such thermal conductivity test units have

been constructed to permit the simultaneous testing of the two probes of a heat-flow instrument.

The Heat-Flow Instrument Testing

For functional testing of the probes and the heat-flow instrument as a whole, thermal similators are used to provide a stable temperature environment for the probes in the lunar-temperature operating range. Each simulator is an insulated container 8 feet (2.5 meters) deep, filled with solid carbon dioxide and ethanol, in which a heavy-metal double boretube is vertically situated. The ethanol fluid stabilizes at the temperature of the subliming dry ice that it surrounds. Since the temperature of sublimation is a function of pressure, the fluid temperature increases with depth to impose a gradient along the boretubes. Thermocouples and thermopiles within the metal block measure the temperature profile along the tubes. The laboratory thermal-simulator apparatus has a compartment for the electronics package so that the whole instrument can be operated in a vacuum. When inserted into the boretubes, the two probes of the instrument are in a similar, uncontrolled but slowly changing temperature field, and comparisons can be made of processed measurements on the probe bridges at given heights in the bath.

A similar simulator has been built into an adjunct to a 27- by 20-foot (8.3- by 6.2 meter) thermal vacuum chamber. During ALSEP system testing, the heat-flow electronics package is deployed inside the main chamber, with the probes situated in the stabilized thermal-simulator boretubes. The entire ALSEP system, including the heat-flow instrument, is exposed to the temperature conditions of lunar dawn, lunar noon, and lunar night in a vacuum of 5×10^{-8} Torr. Cold space is simulated in the chamber by pumping liquid nitrogen under pressure through black, optically tight panels. The sun is represented by carbon arc lamps and dust degradation on instrument surfaces is simulated by subjecting them to additional infrared radiation.

TABLE 4. Apollo 16 Heat-Flow Instrument Test Results in Lunar-Night Environment[a]

Sensor Data	Upper Gradient Bridge (°K)	Lower Gradient Bridge (°K)	Upper Remote Bridge (°K)	Lower Remote Bridge (°K)
Absolute temperature, mean difference[b]	-0.002	-0.020	-0.028	-0.036
Absolute temperature standard deviation[c]	0.016	0.037	0.034	0.032
High sensitivity temperature differential, mean difference[b]	0.001	-0.001	0.003	0.002
High sensitivity temperature differential, standard deviation[c]	0.0002	0.0002	0.0021	0.0010
Low sensitivity temperature differential, mean difference[b]	0.001	-0.003		
Low sensitivity temperature differential, standard deviation	0.002	0.002		
Cycles	8	8	10	10

[a] Test performed on 26 July, 1971.

[b] Mean difference in readings of two opposed sensors

[c] Standard deviation of difference in readings of two opposed sensors about the mean difference

Table IV presents a comparison of thermal-simulator temperature measurements made in a changing temperature environment by the heat-flow-instrument probes and electronics package during simulated lunar-night testing of the Apollo 16 ALSEP system. The means of the differences between the temperatures measured by adjacent bridges, corrected for bridge shorting ratio, and the standard deviations from the means are tabulated. The very small differences noted may have been caused by differences in the transient responses of the two probes, by different probe responses to nonlinear gradients, or by slightly different temperature fields, the result either of inherent differences between the apparatus boretubes or of different times of measurement. Outside of these factors, the probe-measurement differences reflect the consistency of total instrument calibration, stability, and signal processing.

The low-sensitivity measurements on the upper gradient bridges illustrate an effect of data averaging that is generally seen in heat-flow-instrument test results. Although resolution in the $\pm 20^{\circ}$K range is ten times less than in the high-sensitivity range, a fact reflected by the standard deviations, the averages are about the same in the two ranges. The number of measurements that do not follow this pattern decreases as the number of data cycles increases. Thus, system resolution is effectively increased by multiple-measurement averaging in both the low and the high sensitivity ranges. Use of this technique can result in an effective resolution better than analog-to-digital-conversion quantization would allow for a single measurement.

During the simulated lunar-night test in which these results were obtained, the probe cables were lying in an uncontrolled temperature zone. There is little value, therefore, in comparing thermocouple readings 2, 3, and 4. However, the mean of the measurement differences for the thermocouples situated at the top of the probes (0.073°K) relative to the single-measurement resolution of 0.17°K

again demonstrates the data-averaging effect. The readings also provide a good comparative check of the thermocouples.

INSTRUMENT PACKAGING

All the components of the heat-flow instrument are pictured in Figure 11. These include a packing container for the probes and an emplacement tool used by the astronaut to insert the probes into the borestems. Overall package design is strongly influenced by the requirement for deployability by a suited astronaut, as evidenced by the various pull rings, handles, and carry straps seen in the photograph.

The probes are folded, with two molded packing pieces secured by nylon cloth and velcro pads holding the sections slightly apart. They are stored for transportation in two thin aluminum containers, which are carried to separate deployment sites on the lunar surface, each with one probe inside. The probes are held within the containers in nylon bags by soft foam bulkheads, so spaced along the folded probe as to suppress the first free-bending mode of the probe. The cables are coiled around the inside of the probe containers in troughs formed by an inner wall on each side.

One probe container has provision for stowing the collapsed emplacement tool - four telescoping fiberglass tubes that lock when extended to give a tool length of 224 centimeters. A slotted piece of fiberglass at the end of the smallest-diameter tube fits over the probe cable to implement probe deployment. The tool is white, with markings at 2-centimeter intervals and a bright orange band to indicate the depth to which the probe should be pushed.

The two probe containers fit together to form a single package, strengthened by the emplacement tool inside. The package is covered with white thermal-control paint and secured by velcro straps with pull rings. A complete probe-container assembly is 3.4x4.5x25.5 inches (8.6x11.4x64.8 centimeters) in size, excluding

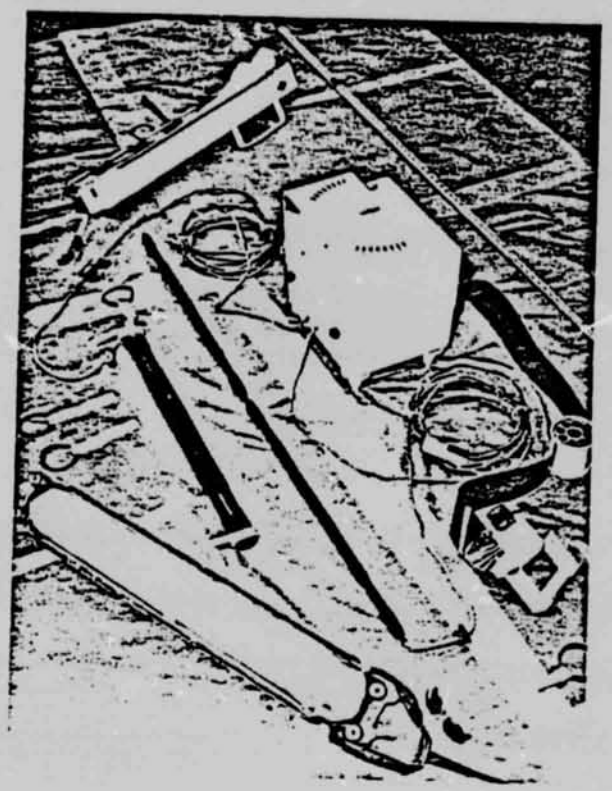

Figure 11 Apollo 16 Heat-Flow-Instrument Components

Appendix C-Figure 11

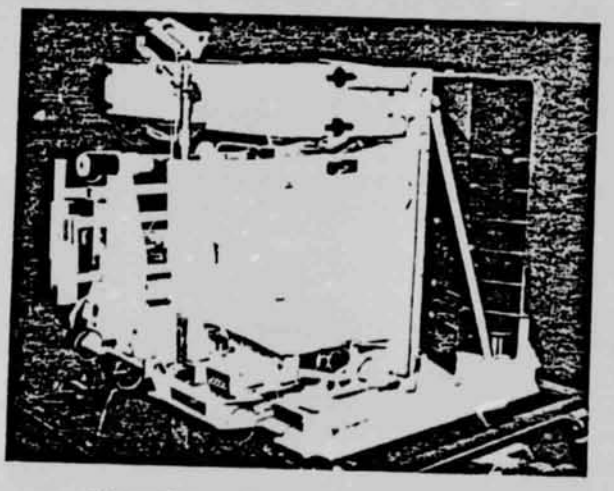

Figure 12 ALSEP Subpackage 2 Heat-Flow-Instrument Subpallet

Appendix C-Figure 12

handles, and weighs 3.5 pounds (1.6 kilograms).

Carried to the moon in an equipment bay of the Lunar Module, the heat-flow instrument is mounted via quick-release fasteners to a subpallet, which stands vertically on a pallet as shown in Figure 12, supported by energy-absorbing mounts. The electronics package has shock-absorbing washers fitted to the four lugs protruding from the mounting ring. The probe package is secured through tubes at the four corners of the box. The astromate connector and cable (coiled inside the reel) are seen in the figure beneath the electronics package. The nylon cover on the electronics package, which serves to protect the thermal control surfaces from lunar dust, is removed before final leveling and alignment of the instrument on the moon.

References

Adams, R.K. and E.G. Davisson (1965) Smoothed thermocouple tables of extended significance (°C), ORNL 3649, Oak Ridge National Laboratory, Oak Ridge, Tennessee, v. 2, Sect. 2.6

Callendar, H.L. (1871) On the construction of platinum thermometers; Phil. Mag. (London), v. 32, n. 194, p. 105-113, July

Callendar, H.L. (1887) On the practical measurement of temperature; Phil. Trans. (London), p. 161-230, June

'Heat Flow Electronics' (1969) Final report on subcontract 0243, prepared by Gulton Industries, Inc., Data Systems Division, Albuquerque, New Mexico, for The Bendix Corporation, Aerospace Systems Division, Ann Arbor, Michigan, January

Klaven, L., L. Lofgren and P. Felsenthal (1970) A rugged, stable differential platinum resistance thermometer; Rev. Scientif. Instr., v. 41, n. 4, p. 541-544, April

Langseth, M.G., Jr. (1968) 'Lunar Heat Flow Experiment' presentation before the American Astronautical Society Conference, Ann Arbor, Michigan, AAS68-207, American Institute of Aeronautics and Astronautics, New York, N.Y.

Langseth, M.G., Jr., et al. (1970) Apollo 13 lunar heat flow experiment, Science v. 168, n. 3928. p. 211-217, 10 April

Langseth, M.G., Jr., K.A. More and W.E. Johnson (1968) An experiment to measure heat flow from the interior of the moon; Bendix Techn. Jour., v. 1 n. 1, p. 33-34, Spring

'Lunar Heat Flow Probes for the ALSEP Heat Flow Experiment' (1969) Final report on subcontract 0242, prepared by Arthur D. Little, Inc., Cambridge, Massachusetts, for The Bendix Corporation, Aerospace Systems Division, Ann Arbor, Michigan, April

Nathanson, D. and R. Merrian (1970) Performance prediction and analysis of the lunar heat flow probes; Final report submitted by Arthur D. Little, Inc., Cambridge, Massachusetts, to Lamont-Doh Geological Observatory, Columbia University, Palisades, New York, January

Robertson, D., and K.A. Walch (1962) Calibration techniques for precision platinum resistance thermometers; in, C.M. Herzfield (ed.-in-chief) and F.G. Brickwedde (ed.), Temperature: Its Measurement and Control in Science and Industry, Reinhold Publishing Corp., New York, Vol. III, Part I.

Siemens, C.W. (1871) On the increase of electrical resistance in conductors with rise of temperature; Proc. Roy. Soc. (London), v. 1871, p. 444, April

U.S. Patent 3,114,125, dated 18 April 1961, granted to Rosemount Engineering Company, Minneapolis, Minnesota.

*